DISSERTATION

SUBMITTED TO THE

COMBINED FACULTY OF

NATURAL SCIENCES AND MATHEMATICS

OF THE

RUPERTO–CAROLA–UNIVERSITY OF HEIDELBERG

GERMANY

FOR THE DEGREE OF
DOCTOR OF NATURAL SCIENCES

Put forward by

JORGE ABREU VICENTE

Born in: Vigo, Spain

ORAL EXAMINATION: JANUARY 25th, 2017

Molecular cloud structure at Galactic scales

Referees:

Prof. Dr. Thomas Henning
Dr. Simon Glover

"Science is our best tool to generate a Universal language that transcend individual differences."

Marcelo Gleiser

"The Island of Knowledge"

Zusammenfassung
Molekülwolken sind die Geburtsorte der Sterne und spielen eine wesentliche Rolle für die Entwicklung von Galaxien. Trotz ihrer großen Bedeutung für die Entstehung von Sternen und die Entwicklung von Galaxien sind die physikalischen Eigenschaften von Molekülwolken kaum erforscht. Besonders aktiv wird diskutiert, welche Prozesse die Entstehung, die Struktur und die Entwicklung von Molekülwolken bestimmen, und damit insbesondere auch, welche Prozesse die Sternentstehungsaktivität regulieren. Vor Beginn dieser Forschungsarbeit wurden beobachtungsbasierte Studien der Struktur von Molekülwolken und präzise Messungen der Sternentstehungsaktivität in diesen nur für Objekte in der näheren Umgebung unseres Sonnensystems durchgeführt, wodurch diese nur begrenzt Aufschluss über grundlegende Eigenschaften in anderen Bereichen der Milchstraße geben. Deshalb ist es notwendig diese Beobachtungen auf weiter entferntere Regionen auszudehnen. Diese Dissertation widmet sich der Bestimmung von Randbedingungen durch Beobachtungen, sodass ein vollständiges Bild über die Prozesse entsteht, welche für die Struktur und Entwicklung von Molekülwolken, und auch für die Sternentstehung in unserer Galaxie relevant sind. Wir präsentieren die erste systematische Studie über die Struktur und Entwicklung von Molekülwolken, die auch Molekülwolken in nahegelegenen Spiralarmen mit einbezieht. Des Weiteren präsentieren wir eine Erhebung über Filament-artige Molekülwolken, welche nach aktuellem Stand der Forschung in Verbindung mit der Spiralstruktur der Galaxie stehen. Schließlich stellen wir eine neue Technik vor, welche die Qualität von existierenden Beobachtungsdaten verbessert, um damit präzisere Randbedingungen zu erhalten, was wesentlich ist für die Untersuchung der Struktur von Molekülwolken.

Abstract
Molecular clouds are the sites were stars are born and they play a crucial role in galactic evolution. Despite their main role on star formation and galaxy evolution, physics of molecular clouds are still poorly understood. Particularly, the processes controlling the formation, structure, and evolution of molecular clouds are still a matter of debate and so are the processes that regulate their star–forming activity. Previous to the beginning of this thesis, observational studies of molecular cloud structure and accurate measurements of star–forming activity in molecular clouds existed only for the Solar neighborhood, proving a very limited range of Galactic environments. Extending these studies to larger distances is crucial. This thesis is dedicated to provide the observational assets needed to obtain a Galactic picture of the processes involved in the molecular cloud structure and star–formation. We present the first systematic study of molecular cloud structure and evolution including molecular clouds in nearby spiral arms. We present a census

of filamentary–shaped molecular clouds that are thought to be connected to the spiral Galactic structure. Finally, we also develop a new technique that improves the quality of the existing observational data to obtain more accurate observational assets, crucial in the study of molecular cloud structure.

Acknowledgements

A doctoral thesis is far more than hard individual work during the PhD studies. I honestly think that a thesis cannot be successfully written if there is lack of synergy between supervisors and students. For this reason, I would like to begin the acknowledgments by my supervisors, Prof. Dr. Thomas Henning and Dr. Jouni Kainulainen. A significant part of this work is definitely theirs and their labor as supervisors was fantastic. I would also like to thank Dr. Amy Stutz, who during last year became a third supervisor and was crucial for one of the chapters of this thesis. I thank the Deutsche Forschungsgemeinschaft (DFG) for their financial support via the Sonderforschungsbereich (SFB) 881 "The Milky Way System". I also thank to Prof. Dr. Henrik Beuther who was the connection with the SFB 881 project and was also very supportive during my thesis. I also want to thank to Dr. Simon Glover for accepting being referee of this thesis and part of my thesis Committee.

I would like to mention that the offices of JK, TH, AS, and HB were open to me at any time, as it was the office of Dr. Christian Fendt. The work of CF as coordinator of the International Max Planck Research School in Heidelberg (IMPRS–HD) is simply amazing. Undoubtedly he owns a significant part of the success that the IMPRS–HD program, which I also thank, has generated over the years. I am very proud of being part of the IMPRS. I also thank to the students of my IMPRS generation, student representatives, and members of the MPIA that made this PhD a memorable three–plus year experience.

But the road to this thesis is not only the MPIA. This road began 31 years ago and many people have contributed in different manners to this thesis. First, I want to thank to every teacher I had, from the elementary school to the my Master degree in Granada. Specially to Ismael, Mónica, Miguel Ángel, Félix, Rosa, Novoa, and Antxon.

I thank Esteban and Denise. They were a central part of my life in Heidelberg. Furthermore, Denise was who show me how to use the IRAM 30m telescope in Granada, where we shared another two great years. Thanks to Esteban who presented my IMPRS application on time. Otherwise, these lines would not be possible. And speaking about the application process, it was Raquel who talked me about the IMPRS-HD program and encouraged me to apply on a moment on which my astronomy career was at its lowest point. Unfortunately, she is not here anymore, but she is also a part of this thesis and any further work related with it. Thanks also to all the people that made these three years in the wonderful city of Heidelberg a great experience: Alberto, Elena, Laura, Arsela, MJ, Juan, Laura, Onix, and the Bad Dürkheim team. Alberto and Elena deserve their own mention on this list. Elena for all the lunch time conversations at MPIA, for all the good times out of the institute, and for a great support. Alberto, for all those *weinfests* and great moments like the bike travel from Heidelberg to Cologne. I also want to thank Fran, Denise, Esteban, Alex, Alicia, Frederiq, Uwe, Ahitamy, and Mikel for the great moments shared every first weekend of August in our Holy Land of Wacken. And speaking about Wacken, thanks to Steward for introducing me, around 20 years ago, into the crazy world of the rock and metal music. Music was a very important way to relax my brain during the hard moments. Thank you to the three rock bands, and their members, on which I was involved and that defined different moments of my life: Heissel (Steward, Luis, Lucas, Tito, Xavi, Nani, Coe), Hypnosis (Dani, Pablo, Charlie), and MILF (Fran, Guillermo, Gabriele, Ahitamy).

My years in Granada were key on my road. I want to thank "Núcleo Duro" for all those great nights watching Real Madrid games, although none of us were together for the last two Champions. I thank also to Rebeca, Willy, Manuel, Ignacio, Juan Luis, Manolo, Frederiq, Juan, Paco, and Sandra from the IRAM 30m telescope. Those years could not be understood without Alicia, who was my partner during eight years and a very important part of who I have become. I thank to Ahitamy and Sergio for all the great moments from La Laguna and Granada. I thank the best flatmate ever, the other father of our first son (Neutrón), for all those PP Fridays, Guitar–beer weekends and sharing infinite projects during our years in Granada.

There are much more people in previous years that are somehow part of this thesis. Jose Manuel, Anna, Raquel, Necho, Coral, Tavi, Beli, Rafael, Maria, Marcos, Geli, Maria, Pablo, Costas, Casal, Madrina, Padrino, Encarna, Eva, Uska, Sara, ... I can't name everyone.

My Grandparents, Benito and Carmen, who sadly passed during the years of this Thesis. This work is also yours. Of course, I thank to my parents. Because they built the pillars of these 31 years that are somehow written on the next 200 pages. You are the best parents I could ask for. Thank you also to Neutrón, who is taking care of them while I am abroad. Finally, I would like to thank the huge support that Diana gave me during the hard

last year, on which this thesis became more than an obsession. She was always there supporting me and understanding the situation. Thank you also to my new German family for making me feel at home since the first day. And speaking about family, I can't finish these lines without saying thank you to the small Alma (I feel necessary clarifying that here Alma stands for a future baby, and that the name has nothing to do with Atacama, although I wouldn't mind to have two Almas in the near future. It will refer to a telescope in the reminder of this thesis), who is still not here, but is already helping from inside Diana. I will wait for you after defending this thesis "Peque".

Contents

List of Figures

List of Tables

Dedicated to Alma, Diana and my Parents

Chapter 1

Introduction

The fact that star formation occurs in the coldest and densest regions of molecular clouds has been widely accepted and demonstrated for decades (cf. Lada and Lada, 2003; Tielens, 2005; Draine, 2011a; Hennebelle and Falgarone, 2012; André et al., 2014a; Dobbs et al., 2014; Molinari et al., 2014a, see in Fig. 1.1). During their lives, stars transform hydrogen and helium into heavy elements (e.g. carbon, nitrogen, oxygen), ejecting them into the interstellar medium (ISM) at the end of their lives. The mass ejection processes (e.g. supernovae explosions) inject momentum and enrich the chemical composition of the ISM. The enriched ISM will form new generations of stars, richer in heavier elements than the previous ones. The molecular clouds play a catalytic role in this cyclic connection between the ISM and stars: they block the external radiation, providing the cold environment that the molecular clouds need to undergo in gravitational collapse and form new stars. This cycle drives the chemical, morphological, and dynamical evolution of galaxies. The study of molecular clouds is therefore crucial not only to understand the processes involved in star formation, but also to understand the evolution of galaxies as a whole.

Despite their main role in star formation and galaxy evolution, the physics of molecular clouds are still poorly understood. The processes controlling the formation, structure, and evolution of molecular clouds are still a matter of debate and so are the processes that regulate their star–forming activity. Molecular clouds are very complex systems governed by several physical processes. The simple theoretical models used to describe the internal structure of molecular clouds tend to fail due to the (at least partially) stochastic nature of the processes involved. Molecular clouds are not isolated objects. They form and evolve inside diffuse envelopes of atomic gas, subjected to the galactic environment. Molecular clouds are hierarchically structured, suggesting that the relative importance of the physical processes involved in molecular cloud evolution are likely to change, depending on the scales at which we study the molecular clouds. To obtain a full observational picture of molecular clouds we must perform observations at scales of the entire molecular cloud (~ 100 pc) down to scales relevant for star formation (~ 0.1 pc), but also from molecular clouds subjected to different Galactic environments. This is very challenging from an observational point of view, since a big number of molecular clouds must be observed using different observatories for each of the needed scales. Great theoretical efforts have also been made in the last years to improve our knowledge of molecular cloud evolution and its connection to star formation (see Dobbs et al., 2014, for a review), resulting in sets of simulations with very different parameters. Most of these simulations are able to generate molecular clouds with physical properties and star–forming activities consistent with observations. The only way to disentangle which of the theories is correct is to improve the observational data against which theories are tested and thus further developed.

This Thesis is dedicated to improving the observational data of molecular clouds, obtaining physical properties of statistically significant samples of molecular clouds within the Galaxy, and developing observational techniques that will be further used to improve the quality of observational data of the entire Milky Way.

1.1 Overview on the ISM

The ISM is a heterogeneous mixture of gas, dust, and cosmic rays that fills the space between stars. It accounts for approximately the 10% of the Milky Way mass integrated over 15 kpc of the Galactic center (Draine, 2011a). Based on models of primordial nucleosynthesis, hydrogen is the main component of the ISM, accounting for the $\sim$90% of the total particle number and $\sim$70% of its total mass. The helium is the second most abundant atom, accounting for $\sim 9\%$ of the total by particle number and $\sim 28\%$ by mass (Steigman, 2007). Heavier elements account only for 0.12% of particles or 1.5% of mass. The dust particles are composed of large fractions of heavy atoms and account for 1% of the total mass of the ISM. Despite their tiny mass fraction in

FIGURE 1.1: Infrared (left) and optical (right) images of the Orion A molecular cloud. The infrared image was taken with *Spitzer*/IRAC and it shows the protostars in green, and hot gas in red. The dark filamentary structure on which the protostars are seen is part of the molecular cloud on which the stars are born. The optical image was taken with the NOAO/AURA/NSF. The protostars observed in the infrared are completely obscured by the dust in the the molecular cloud at optical wavelengths. *Credit: NASA, JPL-Caltech, T. Megeath*

the ISM, dust particles play a main role on its chemical evolution and star formation: they act as catalysts in important reactions such as the formation of the H_2 molecule, the most abundant of the Universe, and they play a crucial role in attenuating the stellar radiation, allowing molecular clouds to reach the conditions necessary to the onset of star formation (Draine, 2011a; Glover and Clark, 2012).

The ISM is an open system with no thermodynamic equilibrium so that the gas temperatures and densities vary over huge dynamic ranges, ($10 \leq T[\mathrm{K}] \leq 10^{5.5}$, $10^{-3} \leq n[\mathrm{cm}^{-3}] \leq 10^{6}$). For this reason and for simplicity of study, the ISM is usually divided into different phases characterized by the dominant state of its main component: hydrogen. The different phases and their properties are summarized in Table 1.1, as extracted from Draine (2011a). It is worthy to note that this classification may vary among different literature sources (e.g. Tielens, 2005).

TABLE 1.1: Phases of the ISM based on Draine (2011a)

Phase	Main H state	T [K]	$n_0[\mathrm{cm}^{-3}]$	Volume [%]
Coronal gas	H II	$> 10^{5.5}$	$\sim 4 \times 10^{-3}$	50
Ionized medium	H II	10^4	$0.3 - 10^4$	10
Warm neutral medium	H I	$\sim 5 \times 10^3$	0.6	40
Cool neutral medium	H I	~ 100	30	1
Molecular clouds	H_2	$10 - 50$	$10^3 - 10^6$	0.1

In this thesis we will focus on the molecular clouds, in which the star formation takes place. However, it should be noted that the different phases by no means correspond to fixed boundaries defining closed systems. The ISM is an open system on which each phase is in constant exchange with the others. For example, the molecular clouds can create stars massive enough to ionize their hydrogen atoms, generating H II regions in their surroundings. The transition from H II regions to molecular clouds necessarily pass through an atomic phase. The Orion star–forming region in Fig. 1.1 is a very good example of the interplay between the molecular, atomic, and ionized phases of the ISM.

1.2 Molecular clouds

The study of molecular clouds is important not only because they are one of the main components of the ISM, but also because they are the places where stars are born (e.g., Lada and Lada, 2003; McKee and Ostriker, 2007; Hennebelle and Falgarone, 2012; Dobbs et al., 2014). In molecular clouds the hydrogen is found mainly in its molecular state, H_2, and it is the main component of molecular clouds, although it is not the only molecule discovered in the ISM. Almost 200 different molecules have been discovered to date[1]. Unfortunately, the symmetry of the H_2 molecule results in a lack of a permanent dipole moment making it unobservable at typical temperatures of molecular clouds[2] ($T \sim 10 - 20$ K). To overcome this issue, astronomers

[1] `https://www.astro.uni-koeln.de/cdms/molecules`

[2] Molecules with null dipole moment are not able to emit radiation via rotational transitions, which emit in the domain of the sub– and mm wavelengths. The reason is that the dipole moment vector must change to emit photons. If there is no dipole moment, the rotation cannot generate photons. However, the H_2 molecule can be observed at IR wavelengths on its vibrational transitions.

need to find a molecule that traces the molecular gas to study molecular clouds. The best option to study physical properties of molecular clouds is the CO molecule, which will be used in the Chapter 4 of this thesis.

Molecular clouds were discovered via observations of the CO molecule (Penzias et al., 1972; Wilson, Jefferts, and Penzias, 1970) which is the second most abundant in the Universe after H_2 (H_2/CO$\simeq 1.1 \times 10^{-4}$ Pineda et al., 2010). The high dissociation energy ($h\nu \sim 11.2$ eV) of the CO molecule allows it to live in the surfaces of molecular clouds, where the ultraviolet radiation of the interstellar radiation field is still intense. The low rotational levels of the CO molecule are efficiently populated via collisions with H_2 molecules due to their characteristic temperatures similar to the kinetic temperature of molecular clouds ($T_k \sim 10$ K). In addition, the CO molecule has a small coefficient of spontaneous emission for rotational transitions, becoming these easily thermalized at typical densities of molecular clouds. Under these conditions, the excitation temperature of the CO molecule is similar to the kinetic temperature of the molecular clouds (Rohlfs and Wilson, 2004). Due to its high abundance and population of low rotational levels, the CO molecule is optically thick. The combination of observations of the CO molecule with less abundant, optically thin, isotopologues (e.g., ^{13}CO, C^{18}O, C^{17}O) is useful to study the physical parameters of molecular clouds .

Inferring molecular gas masses from CO observations needs a calibration factor that converts the integrated CO emission into the total gas mass of H_2. This factor is known as the CO-to-H_2 conversion factor, X_{CO}. In the Milky Way, this factor has a mean value $X_{CO} = 2 \times 10^{20}\,\mathrm{cm}^{-2}$ / K / km / s^{-1} (Bolatto, Wolfire, and Leroy, 2013), with an uncertainty of $\pm 30\%$. However, deviations from the X_{CO} canonical value exist in different environments: low metallicity galaxies have larger X_{CO} values (e.g., Leroy et al., 2011; Schruba et al., 2012; Bolatto, Wolfire, and Leroy, 2013); starburst galaxies and galactic centers, including the Milky Way, show smaller X_{CO} values (Bolatto, Wolfire, and Leroy, 2013). Furthermore, there is observational and theoretical evidence of the existence of H_2 gas not associated to CO emission, known as CO-dark gas (Grenier, Casandjian, and Terrier, 2005; Wolfire, Hollenbach, and McKee, 2010; Smith et al., 2014; Glover and Smith, 2016; Tang et al., 2016). This CO-dark gas is generally located in the surfaces of molecular clouds (see also Sect. 1.2.2). The X_{CO} dependence of the environment and the presence of CO-dark gas therefore limits our ability to obtain accurate molecular gas masses from CO observations alone. Furthermore, the CO molecule is not suitable to study the densest regions of molecular clouds since at low temperatures it freezes out into dust grains (Langer et al., 1989; Tielens, 2005; Bergin and Tafalla, 2007; Hollenbach et al., 2009; Draine, 2011a). CO is therefore a good tracer of general properties of molecular clouds, but its ability to trace the molecular gas is limited to a small dynamical range of temperatures and densities.

An alternative tracer of molecular gas that can be used to study physical properties of molecular clouds at higher dynamical ranges is the interstellar dust. The interstellar dust was discovered by Trumpler (1930) by attenuation of the optical radiation emitted by distant open clusters. The spectrum of the thermal emission from interstellar dust grains at far–infrared (FIR) wavelengths can be described by a modified black body function:

$$I_\nu = B_\nu(T_{\rm obs})\tau_0 \left(\frac{\nu}{\nu_0}\right)^\beta , \tag{1.1}$$

where ν is the frequency, I_ν is the intensity at each frequency, $B_\nu(T_{\rm obs})$ is the blackbody function at the observed temperature, τ_0 the optical depth at the reference frequency ν_0, and β is the dust spectral index. In case that observations at different wavelengths are available for the same region, these can be fitted with Eq. 1.1 to obtain the observed temperature of the emitting dust (e.g., Gordon et al., 2010; Kramer et al., 2010; Ragan et al., 2012a; Launhardt et al., 2013a; Schneider et al., 2013a; Schneider et al., 2015b). Furthermore, the dust emission is optically thin at FIR wavelengths and it can be used to derive the mass of molecular gas if a gast–to–dust ratio is assumed (Draine, 2011a, and references therein) using

$$M_{gas} = M_{dust} R = R \frac{F_\nu d^2}{\kappa_\nu B_\nu(T_{obs})} \tag{1.2}$$

where M_{gas}, M_{dust} are the masses of molecular gas and dust, R is the dust–to–gas ratio, F_ν is the observed flux, d is the distance to the cloud, and κ_ν is the absorption coefficient of the dust. Furthermore, dust emission emits in diffuse regions without CO emission, and also in the dense regions of molecular clouds where the CO is frozen out (Tielens, 2005; Draine, 2011a).

The dust can also be used to infer molecular gas masses at near– and mid–infrared (NIR, MIR) wavelengths. In both cases the extinction that the dust produces in the radiation from objects in the background is used to estimate the column density of dust and gas (Lombardi and Alves, 2001; Lombardi, Alves, and Lada, 2006; Lombardi, 2009; Kainulainen et al., 2009a; Kainulainen et al., 2011c; Kainulainen and Tan, 2013). The dust is therefore a good alternative to the CO to estimate general properties of molecular clouds. In Chapters A.6 and 4 of this thesis, dust emission is used to obtain physical parameters in molecular clouds fitting observational data with Eq. 1.1 and Eq. 1.2. In Chapter 3 we present a method to improve the FIR data provided by the *Herschel* Space observatory (Pilbratt et al., 2010a), improving the accuracy of the physical parameters of molecular clouds estimated using the *Herschel* data.

1.2.1 Molecular clouds in the Galaxy

The properties of the CO molecule and its isotopologues to trace the molecular clouds have been used in the last decades to carry out Galactic surveys to study the properties of molecular clouds in the Galaxy. Since the first surveys, published three decades ago (Dame et al., 1987; Solomon et al., 1987), the Galactic plane has been surveyed in many of the CO isotopologues several times: (Dame, Hartmann, and Thaddeus, 2001), the GRS survey (Jackson et al., 2006), COHRS (Dempsey, Thomas, and Currie, 2013), ThrUMMS (Barnes et al., 2015), and SEDIGISM (Schuller et al. subm.).

These surveys show that the 20% of the total mass of the ISM in the Milky Way is in form of molecular gas. Although most of the molecular gas ($4 \times 10^8\,\mathrm{M}_\odot$ Roman-Duval et al., 2016) is found in molecular clouds ("dense molecular gas"), a significant fraction of the Galactic CO emission has been found to originate in "diffuse molecular gas" often not identified as molecular clouds. This "diffuse molecular gas" represents 25% of the total molecular gas mass ($1.5 \times 10^8\,\mathrm{M}_\odot$ Dame, Hartmann, and Thaddeus, 2001; Hennebelle and Falgarone, 2012; Roman-Duval et al., 2016). In this Thesis I study the molecular clouds. In the reminder of this Thesis I will therefore refer only to the "dense molecular gas" which originated in molecular clouds. Typical molecular cloud sizes range from a few parsecs up to $\approx 50 - 100$

pc the sizes of the largest molecular clouds known, commonly named giant molecular clouds (GMCs). The masses of molecular clouds have typical values of $10^3 - 10^6\,\mathrm{M}_\odot$, with the mass spectrum of molecular clouds with $> 10^4\,\mathrm{M}_\odot$ following a power law $M^{-\gamma}$, where $\gamma < 2$, with slight variations between galaxies (Dobbs et al., 2014, and references therein). The gas temperatures in molecular clouds have typical values of 10–50 K (Tielens, 2005; Draine, 2011a).

Molecular clouds are concentrated within $\sim 50\,\mathrm{pc}$ of the Galactic midplane (Sanders, Solomon, and Scoville, 1984; Langer, Pineda, and Velusamy, 2014). The density of molecular clouds peaks in the inner Galaxy, on a ring-like structure of about 5 kpc with a hole of ∼4 kpc in diameter in the Galactic center (the Galactic molecular ring: Solomon and Rivolo, 1989)[3]. Observations of GMCs in nearby spiral galaxies show that most of the GMCs are located in spiral arms (e.g. M33, M51, see also Fig. 1.2; Gratier et al., 2010; Egusa, Koda, and Scoville, 2011; Schinnerer et al., 2013a), with the most massive molecular clouds often related to H II regions (Hennebelle and Falgarone, 2012). However, some molecular clouds are also found in inter–arm regions (Egusa, Koda, and Scoville, 2011; Schinnerer et al., 2013a). In Chapter 4 I present a study of giant filamentary–shaped molecular clouds and study their properties relative to their spiral– or inter–arm connections.

1.2.2 The creation of molecular clouds

To form a molecular cloud, a chemical transition from H I to H_2 must occur. The transition from the atomic to the molecular medium takes place in the surfaces of molecular clouds, frequently referred to as photo dissociation regions (PDRs: see Fig. 1.3, Wolfire, Tielens, and Hollenbach, 1990; Hollenbach and Tielens, 1997; Kaufman et al., 1999; Tielens, 2005; Röllig et al., 2007; Draine, 2011a). In the atomic medium, the stellar radiation field has far-ultraviolet (FUV) photons that can dissociate the H_2 molecules and keep the carbon atoms in an ionized state. The gas temperatures in these regions are higher than 100 K. The H_2 molecule is formed on the surfaces of dust grains from H I atoms. However, the H_2 molecules are dissociated unless

[3]The existence of the Galactic Ring has recently been questioned by Dobbs and Burkert (2012), who proposed a two symmetric spiral arm pattern for the Milky Way as an explanation of observations.

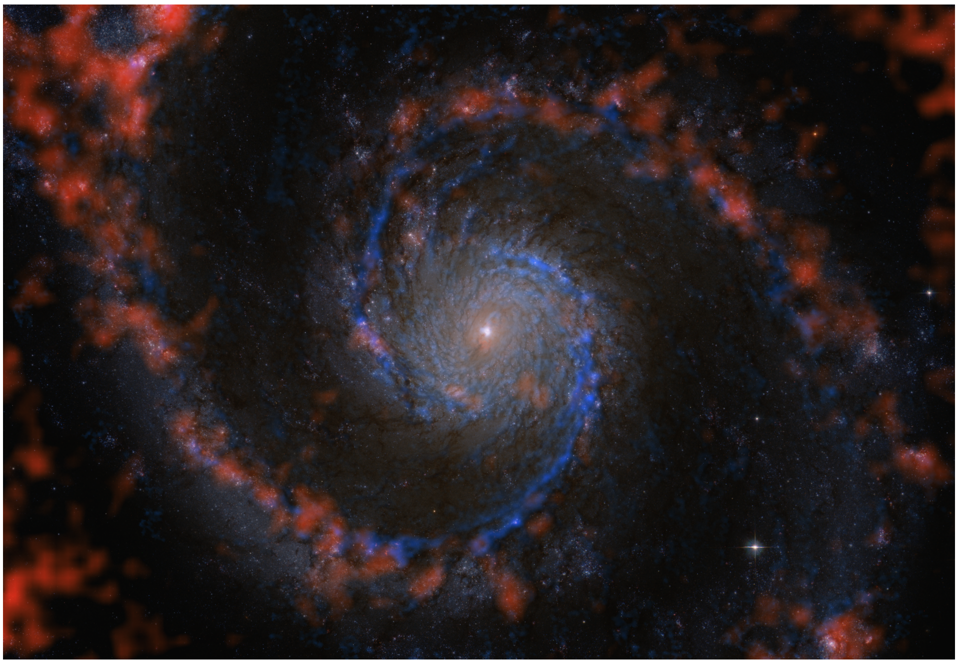

FIGURE 1.2: Background, optical image of M51 obtained by the HST telescope. The blue feature shows the CO(1-0) line emission obtained with the IRAM 30m telescope and the red feature shows the H I emission obtained with the EVLA. *Credit: PAWS team/IRAM/NASA HST/T.A. Rector (University of Alaska Anchorage).*

the interstellar dust generates an effective shield against the FUV radiation. This happens at visual extinctions of $A_V \approx 1 - 3\,\mathrm{mag}$[4] depending on the PDR models used (Wolfire, Tielens, and Hollenbach, 1990; Hollenbach and Tielens, 1997; Kaufman et al., 1999; Tielens, 2005; Röllig et al., 2007). Dust is therefore crucial in the creation of molecular gas: it absorbs FUV photons that can dissociate the H_2 molecule and acts as a catalyst in the formation of the H_2 molecule.

This superficial H_2 layer coexists with ionized carbon since the FUV photons are energetic enough ($6 \leq h\nu \leq 13.6\,\mathrm{eV}$) to keep the carbon atoms ionized. These regions of the PDRs are observed and studied using mainly the [C II] cooling line at 158 μm , and they have typical temperatures of $\approx 50\,\mathrm{K}$. The carbon atoms will remain ionized until the H_2 molecules and the dust create an effective shield against carbon–ionizing photons, at visual extinctions $A_V \approx 3 - 5\,\mathrm{mag}$ and gas temperatures $T \approx 20\,\mathrm{K}$, again depending on specific PDR models (Wolfire, Tielens, and Hollenbach, 1990; Hollenbach

[4]Note that the visual extinction and the column density are basically the amount of material between the emitting object and the observer and that they are related: $N_{\mathrm{H}_2} = 0.94 \times 10^{21}\, A_V\, \mathrm{cm}^{-2}\, \mathrm{mag}^{-1}$. In this Thesis, both magnitudes will be used.

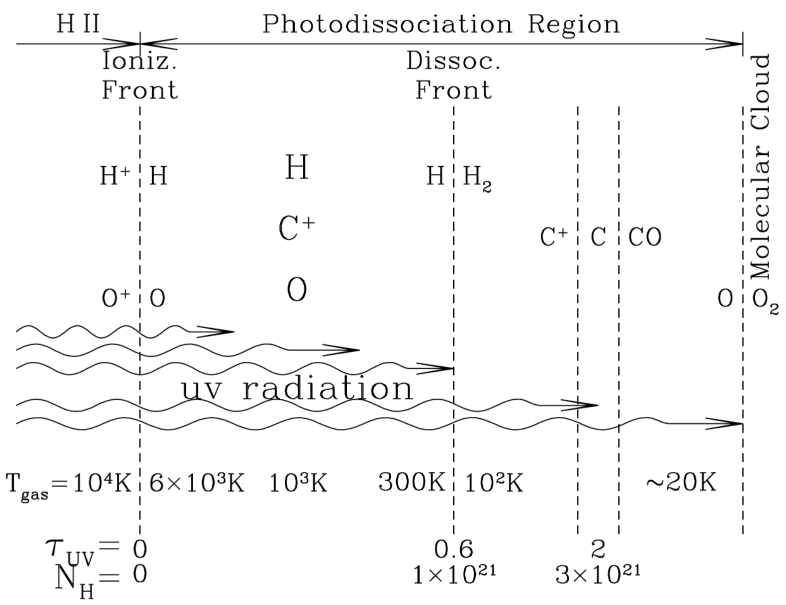

FIGURE 1.3: A schematic structure of a PDR *Credit: Draine (2011a)*

and Tielens, 1997; Kaufman et al., 1999; Tielens, 2005; Röllig et al., 2007). The carbon atoms transition rapidly from their ionized state to the neutral state, and then form the CO molecules via different chemical reactions (Langer, 1976; Hollenbach and Tielens, 1997; Tielens, 2005). The PDR models tend to consider the molecular clouds starting at $A_V \approx 10$ mag, where the oxygen becomes molecular (see Fig. 1.3). However, in this Thesis I will consider as molecular clouds the dense molecular gas associations traced by bright CO emission or dust.

1.2.3 Internal structure of molecular clouds

The internal structure of molecular clouds can be used to infer the physical processes acting on them. The continuous improvement of the observational data obtained from molecular clouds, from the first CO surveys in the late 80's (Dame et al., 1987; Solomon et al., 1987) to the latest molecular cloud surveys (Dame, Hartmann, and Thaddeus, 2001; Jackson et al., 2006; Dempsey, Thomas, and Currie, 2013; Barnes et al., 2015), show that at every scale they are composed of a high number of dense, small–scale, structures located inside less abundant, large–scale, diffuse envelopes.

The smallest structures known in molecular clouds are the cores. Cores have sizes of ~ 0.1 pc and are the immediate sites of star–formation (Bergin and Tafalla, 2007; Draine, 2011a; Hennebelle and Falgarone, 2012; Dobbs et al., 2014; André et al., 2014a). The cores are local high–density peaks ($10^4 - 10^6\,\mathrm{cm}^{-3}$) with typical masses between $0.3 - 100\,\mathrm{M}_\odot$ and they are expected to undergo gravitational collapse to form single or low multiplicity stellar systems (di Francesco et al., 2007; Ward-Thompson et al., 2007; Draine, 2011a). The reason of this expectation is that the core mass function is similar to the stellar initial mass function shifted by a factor of $\sim 0.3 - 0.7$ (Motte, Andre, and Neri, 1998; Testi and Sargent, 1998; Alves, Lombardi, and Lada, 2007; Enoch et al., 2008; Könyves et al., 2010; André et al., 2014b). This difference is interpreted as the fraction of the mass of the cores that is converted into stars (i.e., the core–to–star efficiency, Matzner and McKee, 2000). Some cores have been observed isolated and are known as Bok globules or cometary globules (Barnard, 1927; Bok and Reilly, 1947). However, cores are usually embedded in larger structures known as clumps. The clumps have sizes up to ~ 2 pc, densities of $10^4 - 10^5\,\mathrm{cm}^{-3}$, and they may contain up to thousand solar masses. These are responsible for the formation of stellar cluster associations including massive OB stars (Beuther et al., 2007; Tan, 2007; Tan et al., 2014). Note that the observational definitions of core and clump have always been the subject of discussion (e.g., Evans, 2008). The definition adopted here for cores and clumps follows the nomenclature used in Bergin and Tafalla (2007). The cores and clumps are often divided into starless (pre–stellar) or star–forming (proto–stellar), based on the presence or absence of MIR sources, adopted as presence of protostars (e.g., Tackenberg et al., 2012). In Chapter A.6 I study the density structure of starless clumps.

The cores and clumps are often embedded in filamentary structures (e.g., André et al., 2014b; Könyves et al., 2015, and references therein, see also Fig. 1.1). In a study of cores in the Aquila molecular cloud it was found that 75% of the starless cores are associated to filamentary structures, and that they are also the dominant structure in the dense gas ($A_V > 7\,\mathrm{mag}$, $n \sim 10^4\,\mathrm{cm}^{-3}$) of the molecular cloud (Könyves et al., 2015). The interstellar filaments are surrounded by more diffuse gas that fills most of the volume of molecular clouds (e.g., Schneider et al., 2013b; André et al., 2014b; Könyves et al., 2015). The ubiquity of filaments in molecular clouds and their close relation to star formation make their study crucial to understand the whole processes of molecular cloud evolution and star formation. A more detailed introduction to interstellar filaments can be found in Sect. 1.3. Furthermore, in Chapter 4 we present a census of filamentary structures in molecular clouds and their main physical properties.

The differences between the structures presented in this section are mainly their spatial scales and densities. Each of the structures described here may be subjected to different physical processes (introduced in Sect. 1.2.4). Studying the density structure of molecular clouds will therefore help to understand the different proccesses involved in shaping their structure. We do this study in Chapter A.6, where we study the column density distribution of a statistically significant sample of molecular clouds.

1.2.4 Processes acting in molecular clouds

As stated in Sect. 1.2.3, the molecular clouds are highly filamentary and clumpy. Theoretical works show that there are several physical processes that can generate this kind of structure: global gravitational collapse (Larson, 1985; Burkert and Hartmann, 2004; Heitsch et al., 2008; Zamora-Avilés, Vázquez-Semadeni, and Colín, 2012; Zamora-Avilés and Vázquez-Semadeni, 2014), supersonic turbulence without gravity (Passot, Pouquet, and Woodward, 1988; Padoan et al., 2001; Falgarone and Passot, 2003; Hennebelle, 2013), and colliding flows (Vázquez-Semadeni et al., 2006; Banerjee et al., 2009; Tasker and Tan, 2009; Vázquez-Semadeni et al., 2011; Tasker, 2011). These theories have been studied in magnetized and non–magnetized media.

Molecular clouds are inevitably turbulent. Their Reynolds number is $\mathrm{Re} = Lv/\nu_{turb} \sim 10^9$, where L is the characteristic linear scale of the molecular clouds, v is velocity and $\nu_{turb} \sim 10^{16}$ cm^{2}s^{-1} is the viscosity of molecular clouds. Larson (1981) found a relationship between the velocity dispersion and size of molecular clouds in the Milky Way that suggests that, at large scales, the molecular clouds are governed by turbulent motions. Similar results were found in more recent studies of molecular clouds within the Milky Way (Heyer et al., 2009; Lombardi, Alves, and Lada, 2010; Roman-Duval et al., 2011) and in nearby galaxies (Bolatto et al., 2008). Furthermore, the typical velocity dispersions observed in molecular clouds are $\sigma_V \gtrsim 1\,\mathrm{km/s}$. These large velocity dispersions are larger than the sound speed at typical molecular cloud conditions, $\sigma_s \approx 0.2\,\mathrm{km/s}$, meaning that the turbulence in molecular clouds is supersonic. Interestingly, the dense cores of molecular clouds, those intimately linked to star formation, depart from the Larson (1981) scaling relationships and show subsonic turbulence (Goodman et al., 1998; Caselli et al., 2002). However, the turbulence decays too fast in molecular clouds to be able to explain the large velocity dispersions observed, leading to the question: which are the processes that drive turbulence in the molecular clouds? The turbulence in molecular clouds can be internally and externally driven. The main processes injecting internal turbulence in molecular clouds are: jets and outflows observed in protostars (e.g., Machida, Inutsuka, and Matsumoto, 2008; Price, Tricco, and Bate, 2012); radiation and ionization fronts from high-mass stars, that may generate shocks and blow up the maternal cloud (e.g., Krumholz, 2007; Offner et al., 2009; Commerçon et al., 2011). The processes generating this internal turbulence could explain the observed core-to-star efficiency of $\sim 50\%$ due to the ejection of gas from the protostars (Alves, Lombardi, and Lada, 2007; André et al., 2010a; Dobbs et al., 2014). However, these internal turbulence processes alone do not explain the large scale turbulence of molecular clouds. The processes responsible of injecting large scale turbulence in molecular clouds must be externally driven: galactic shears, supernovae explosions, and gravitational infall motions are the most likely drivers of large scale turbulence in molecular clouds (Mac Low and Klessen, 2004; Gressel, 2010; Van Loo, Butler, and Tan, 2013; Padoan et al., 2016).

Another plausible explanation to the large velocity dispersions observed over large scales in molecular clouds is the global collapse scenario (Goldreich and Kwan, 1974; Vázquez-Semadeni et al., 2007; Heitsch et al., 2008; Vázquez-Semadeni et al., 2009; Heitsch, Ballesteros-Paredes, and Hartmann, 2009; Hartmann, Ballesteros-Paredes, and Heitsch, 2012; Zamora-Avilés, Vázquez-Semadeni, and Colín, 2012; Zamora-Avilés and Vázquez-Semadeni, 2014). In this scenario, molecular clouds are described as a hierarchy of structures at different densities with continuous accretion from the most diffuse to the most dense structures. The gas motions of such a system are enough to explain the large velocity dispersions observed in molecular clouds. The initial phases of this scenario are turbulence dominated, since it builds up on the collision of warm gas clouds, with gravity becoming more important as time evolves. Observations show hints of accreting gas inflows at small scales in the densest regions of molecular clouds (e.g., Schneider et al., 2010; Kirk et al., 2013a). Simulations of molecular clouds following this scenario show that they form huge amounts of stars during their first $\sim 20 - 30$ Myr of life, and that the feedback from these stars disrupts the cloud rapidly (e.g., Zamora-Avilés, Vázquez-Semadeni, and Colín, 2012; Zamora-Avilés and Vázquez-Semadeni, 2014). This model is able to reproduce the low star–forming efficiency observed in the MW, and it would also explain why so few of the molecular clouds known have no star–forming activity. These clouds would be on a very early stage of evolution that could be turbulence–dominated, but that should last about a Myr. This model works for molecular clouds up to 10^5 solar masses, but it is still not clear its ability to explain more massive molecular clouds.

1.2.5 Star formation in molecular clouds

Several decades ago, Schmidt (1959) used observations of molecular clouds within the MW to find an empirical correlation between the surface density of the star–forming rate (SFR, $\Sigma_{\rm SFR}$) and the total gas surface density ($\Sigma_{\rm g}$)

$$\Sigma_{\rm SFR} \propto \Sigma_{\rm g}^n, \tag{1.3}$$

with a most likely value for the power–law index $n = 2$. Years later, Kennicutt (1998) made an analogous study in around 100 nearby galaxies finding that the power-law index was $n = 1.4$. This is known as the Kennicutt–Schmidt (KS) law. In more recent years, both works have been revisited with more sensitive observations of molecular clouds in the Milky Way and nearby galaxies. These works study the correlation of the SFR and the gas surface density, dividing it into atomic and molecular gas surface densities (Leroy et al., 2008; Bigiel et al., 2008; Krumholz, McKee, and Tumlinson, 2009). It was found that the SFR surface density only correlates with the molecular gas, suggesting that stars are formed in the molecular clouds (see Fig. 1.4).

However, observations of molecular clouds in the Milky Way have shown that the KS law is scale–dependent and it breaks down at molecular cloud

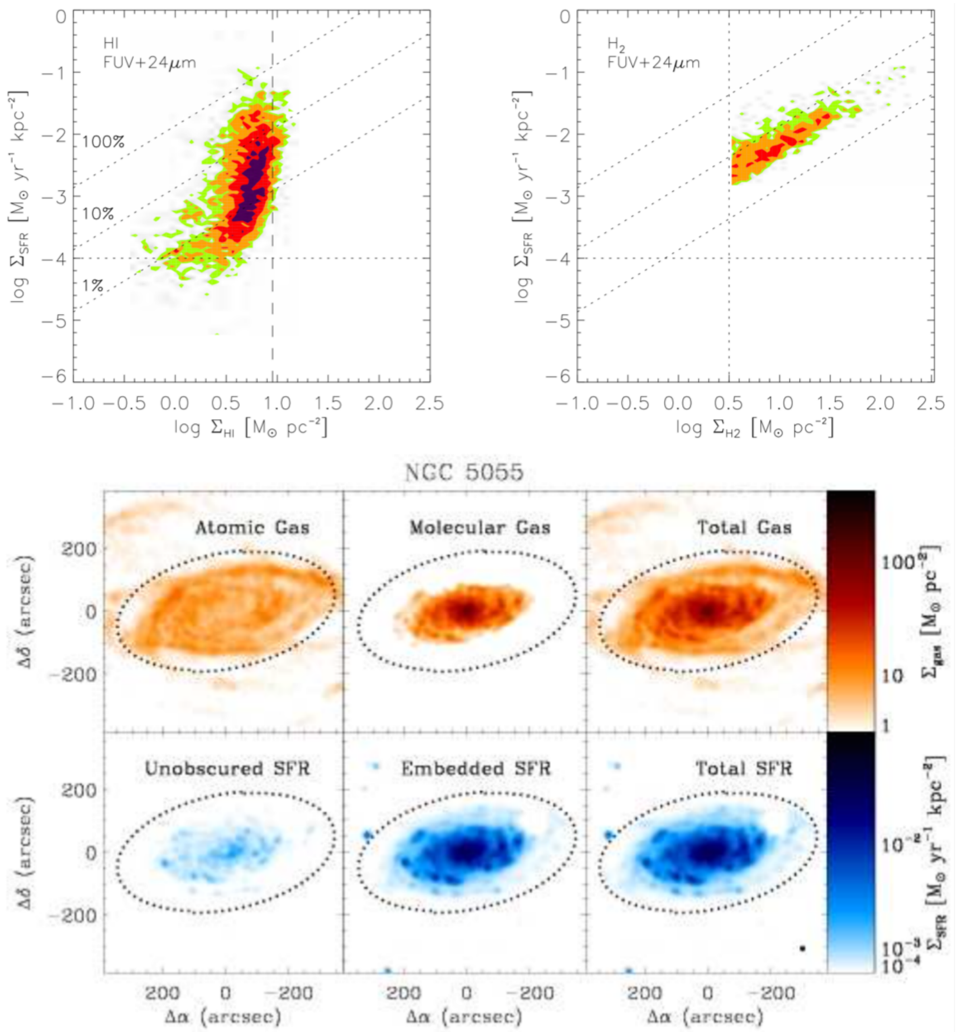

FIGURE 1.4: *Top:* The Kennicutt–Schmidt law observed in nearby galaxies for atomic (left) and molecular (right) gas. The vertical axis shows the logarithmic surface density of the SFR, derived from FUV and 24 μm emission. The horizontal axis show the logarithmic surface density of the atomic (left) and molecular (right) gas. *Credit: Bigiel et al. (2008)*. *Bottom:* Distributions of the atomic gas, molecular gas, total gas, and SFR in the galaxy NGC 5055. The SFR shows a clear spatial correlation with the molecular gas. *Credit: Leroy et al. (2008)*

scales (Heiderman et al., 2010a; Lada, Lombardi, and Alves, 2010a; Gutermuth et al., 2011a). Lada, Lombardi, and Alves (2010a) realized that the observable two–dimensional structure of the observed molecular clouds have a major role in controlling their SFR. Particularly, they found that the SFR surface density correlates linearly with the surface density of molecular gas (Σ_{gas}) weighted by the fraction of dense gas (f_{DG}) in molecular clouds

$$\Sigma_{SFR} = f_{DG}\Sigma_{gas}, \tag{1.4}$$

where f_{DG} is the fraction of the dense gas mass in molecular clouds ($\Sigma_{gas} \gtrsim 116\,\mathrm{M_{\odot}pc^{-2}}$) to the total molecular gas mass. They tested their result in molecular clouds of nearby galaxies and found that this linear scaling law exists for molecular cloud masses ranging over several orders of magnitude, from single clouds to molecular gas masses averaged over entire galaxies (Lada et al., 2012a). Furthermore, Gutermuth et al. (2011a) found the correlation $\Sigma_{SFR} \propto \Sigma_{gas}^{2}$ studying the relationship between molecular gas surface densities and the surface density of young stellar objects (YSOs) in eight nearby molecular clouds. Combining both results is found that the amount of dense gas in molecular clouds depends linearly on the surface density of molecular gas ($f_{DG} \propto \Sigma_{gas}$). These works suggest that the SFR of molecular clouds is set by their fractions of dense gas, which at the same time are set by the surface density of molecular gas mass. We note that Krumholz, Dekel, and McKee (2012) found another empirical correlation under which the surface density of SFR is proportional to the gas surface density weighted by the free–fall time (t_{ff}) of molecular clouds $\Sigma_{SFR} \propto \Sigma_{gas}/t_{ff}$. This correlation is able to fit data of MW and nearby galaxies over five orders of magnitude. These results are challenged in the Chapter A.6 of this thesis.

Another open issue in the study of the SFR of molecular clouds is how SFR changes with the evolution of the clouds. Let's consider the ρ–Ophiucus and Pipe molecular clouds. Both have similar molecular gas surface densities, but the dense gas fraction and the SFR in Ophiucus are 15 times larger than in the Pipe, that has almost no star-forming activity (Lombardi, Alves, and Lada, 2006; Wilking, Gagné, and Allen, 2008). This result highlights an outstanding open question: will the Pipe ever become ρ–Ophiucus? In other words: are the Pipe and Ophiucus molecular clouds governed by different physical processes or is the Pipe at an early evolutionary state than ρ–Ophiucus on which the star formation is still not important? Related to these questions: what are the physical processes that drive the evolution of molecular clouds and regulate their star–forming activity? These are outstanding currently open questions in the study of molecular clouds and star formation. In Chapter A.6 we address these questions studying a statistical significant sample of Galactic molecular clouds subjected to different Galactic environments and in different evolutionary phases.

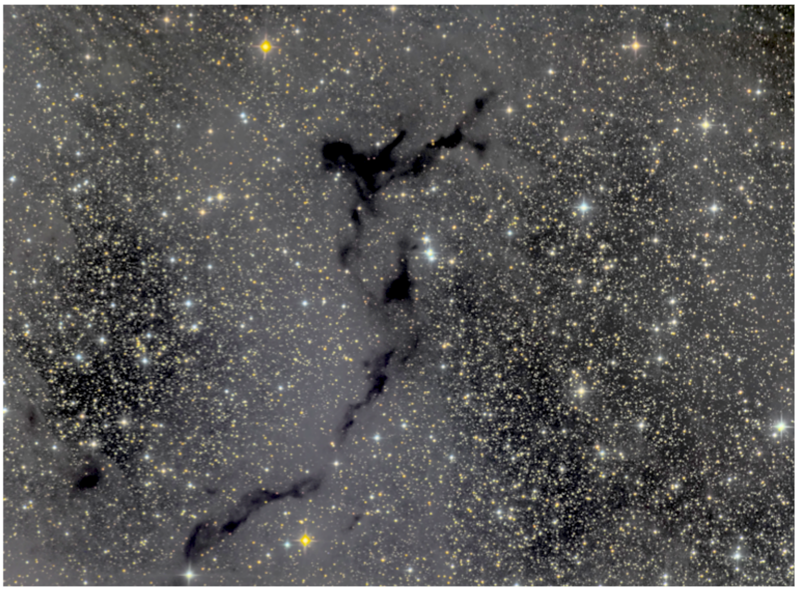

FIGURE 1.5: Optical image of Barnard 150 (Barnard, 1919). *Credit: http://www.pbase.com*

Another open question in molecular clouds is their lifetime. If molecular clouds would form stars through free-fall collapse, MC lifetimes should be on the order of a few Myr. However, observational lifetime estimates suggest that molecular clouds can be live up to 100 Myr (Koda et al., 2009; Kawamura et al., 2009; Meidt et al., 2015). Furthermore, if the stars were created on free-fall timescales, the average SFR in the MW would be 100 solar masses per year while observations show it to be about 1 solar mass per year. The star–forming efficiency is therefore very low in molecular clouds. They convert only about 1% of their gas into stars on a given free–fall time (Krumholz, Dekel, and McKee, 2012). Interestingly, the star–forming efficiency is found to be constant over wide ranges of molecular cloud properties (Krumholz, Dekel, and McKee, 2012), suggesting a universal gas depletion timescale. There should therefore be other processes involved with molecular cloud evolution and regulating their star–forming activity (Krumholz, Dekel, and McKee, 2012, see also Sect. 1.2.4). In Chapter A.6 we use the column density distribution of molecular clouds at different evolutionary states to estimate their evolutionary time–scales based on a free–fall semi–analytical model from Girichidis et al. (2014).

1.3 Interstellar filaments

As stated in Sect. 1.2.3, molecular clouds are highly filamentary in structure and contain a significant amount of the dense cores intimately linked to star formation. Studying interstellar filaments is therefore crucial to understand the whole processes of molecular cloud evolution and star formation. The existence of interstellar filaments has been known for a long time (see B150 in Fig. 1.5, Barnard, 1919). The first observations, at optical wavelengths, show the interstellar filaments as dark regions of the sky devoid of stars. With the development of the FIR– and radio–astronomy, the filaments and molecular clouds could begin to be studied (Schneider and Elmegreen, 1979; Bally et al., 1987; Uchida et al., 1991; Abergel et al., 1994; Chini et al., 1997; Falgarone, Pety, and Phillips, 2001; Hily-Blant and Falgarone, 2007; Nutter et al., 2008; Peretto and Fuller, 2009; Beuther et al., 2011; Hacar et al., 2013; Kainulainen et al., 2013a). Filaments are observationally defined by André et al. (2014b) as "any elongated ISM structure with an aspect ratio larger than $\sim 5-10$ that is significantly overdense respect to its surroundings".

The recent *Herschel* observations, thanks to its outstanding sensitivity, show that molecular clouds are built up by complex filamentary networks that permeate the ISM in a wide variety of environments and over a wide range of scales (e.g., André et al., 2010b; Molinari et al., 2010a; Arzoumanian et al., 2011; Palmeirim et al., 2013; Schneider et al., 2012a; Kirk et al., 2013b; Kirk et al., 2013a; André et al., 2014b; Stutz and Kainulainen, 2015). Filaments are ubiquitous in molecular clouds, no matter whether these clouds are quiescent or harbor star-forming activity (e.g., Molinari et al., 2014b). These filaments are the dominant structures in the dense regions of molecular clouds. More than half of the molecular cloud masses enclosed at $A_V > 7$ mag is in form of filaments (Könyves et al., 2015). Observations show that most of the star–forming cores, protostars, and young stellar clusters are associated to filaments, suggesting that they play a major role in star formation (e.g., Myers, 2009; André et al., 2014b; Dobbs et al., 2014; Molinari et al., 2014b; Könyves et al., 2015; Stutz and Gould, 2016; Kainulainen et al., 2016, see also Fig. 1.1). The young stellar OB cluster associations are preferably found in regions where several filaments collide (Kirk et al., 2013b; André et al., 2014b).

The current filament models are built on the linear perturbation theory of

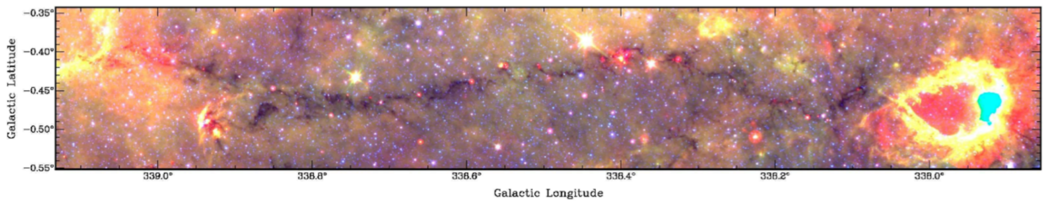

FIGURE 1.6: Mid–infrared image of *Nessie* obtained from the GLIMPSE survey (Benjamin et al., 2003). *Credit: Jackson et al. (2010)*

self–gravitating, thermally supported, equilibrium cylinders (Inutsuka and Miyama, 1992; Fiege and Pudritz, 2000a; Fiege and Pudritz, 2000b; Fischera and Martin, 2012b). The fundamental physical parameter of these models is the critical line-mass, that assuming a typical gas temperature of 10K along the filament, is $M_{crit} \approx 16\mathrm{M}_{\odot}\mathrm{pc}^{-1}$. Filaments with higher line-masses are expected to fragment on a series of periodically spaced fragments (Inutsuka and Miyama, 1992; Fischera and Martin, 2012b). These fragments would then fragment into smaller filaments, until they reach sizes comparable to the Jeans length, $L_J \approx 0.1$ pc (Arzoumanian et al., 2011; Palmeirim et al., 2013; Kainulainen et al., 2013b; André et al., 2014b). The critical line-mass can exhibit slight variations due to influence of magnetic fields (Heitsch, 2013a), external pressure (Fischera and Martin, 2012b; Fischera and Martin, 2012a; Heitsch, 2013b), and accretion (Heitsch, 2013a; Gómez and Vázquez-Semadeni, 2014). Filaments within molecular clouds of the Solar neighborhood have line-masses close to the critical value (Schmalzl et al., 2010; Arzoumanian et al., 2011; Palmeirim et al., 2013; Hacar et al., 2013; André et al., 2014b). These filaments have widths of $L_J \approx 0.1$ pc (Arzoumanian et al., 2011; Palmeirim et al., 2013) which are surprisingly similar to the typical sizes of the molecular cores ultimately linked to star formation (Myers, 2009; Arzoumanian et al., 2011; Kainulainen et al., 2013c; André et al., 2014b).

Filaments with $M_{line} > 100\mathrm{M}_{\odot}\mathrm{pc}^{-1}$ have also been observed in the Galaxy, challenging the equilibrium model presented above (Hernandez et al., 2012; Kainulainen et al., 2013b; Stutz and Gould, 2016). The existence of these filaments suggests that their evolution is not governed by the same kind of processes involved in the filaments with line-masses near the critical value. This class of filament has typical total masses $M > 10^5\,\mathrm{M}_{\odot}$, and are commonly associated to high-mass stars and star-clusters. The study of these massive filaments is therefore important to better understand the high–mass star formation process. However, only the example of Orion A has been studied in the Solar neighborhood (Bally et al., 1987; Uchida et al., 1991; Polychroni et al., 2013; Takahashi et al., 2013; Stutz and Kainulainen, 2015; Kainulainen et al., 2016; Stutz and Gould, 2016; Teixeira et al., 2016). The over–critical line–mass filaments are usually located at larger distances in the Galactic plane (Jackson et al., 2010; Henning et al., 2010a; Beuther et al., 2011; Kainulainen et al., 2013b; Ragan et al., 2015). In Chapter 4 we present a census of high mass filaments that populate the Fourth galactic quadrant.

Recently, Jackson et al. (2010) published the discovery of an 80 pc long filament, known as *Nessie*. *Nessie* has super critical line mass and it is associated with the Scutum-Centaurus spiral arm, and its discovery has initiated the study of a family of giant molecular filaments (GMFs) in the Milky Way. In addition to *Nessie*, four other GMFs had been discovered and studied early on (Beuther et al., 2011; Kainulainen et al., 2011a; Battersby and Bally, 2014; Li et al., 2013; Tackenberg et al., 2013). All these five GMFs were identified first as absorption features against the MIR background of the Galaxy and confirmed to be phisically continuous objects using additional spectral line information. The existence of such filaments raises the question whether they could be connected to the large-scale, Galactic spiral arm structure. A systematic Galactic census of GMFs, characterizing their occurrence and properties, is required to answer this question. Such a census is show in Chapter 4.

The first systematic census of GMFs was carried out by Ragan et al. (2014, hereafter, R14). Their study is only focused on the first Galactic quadrant. The reason why they didn't perform a more extended census is that by the time they did their study, no systematic spectral line survey (mandatory to confirm the absorption features as connected physical entities) at sufficient resolution was available for the fourth quadrant. R14 identified a series of filamentary NIR and MIR extinction features. They used ^{13}CO spectral information to search for low-density gas bridges connecting the extinction features. Their goal was to find the longest possible extent of the gas connecting filamentary structures. They found seven GMFs with lengths between 50-230 pc and masses on the order of 10^4-10^5 $M_\odot$. They used the Milky Way spiral-arm model of Vallée (2008) to investigate the connection of the GMFs in the Galactic structure. They found that, unlike Nessie, six out of eight of their GMFs lie in inter-arm regions, rather than in spiral arms.

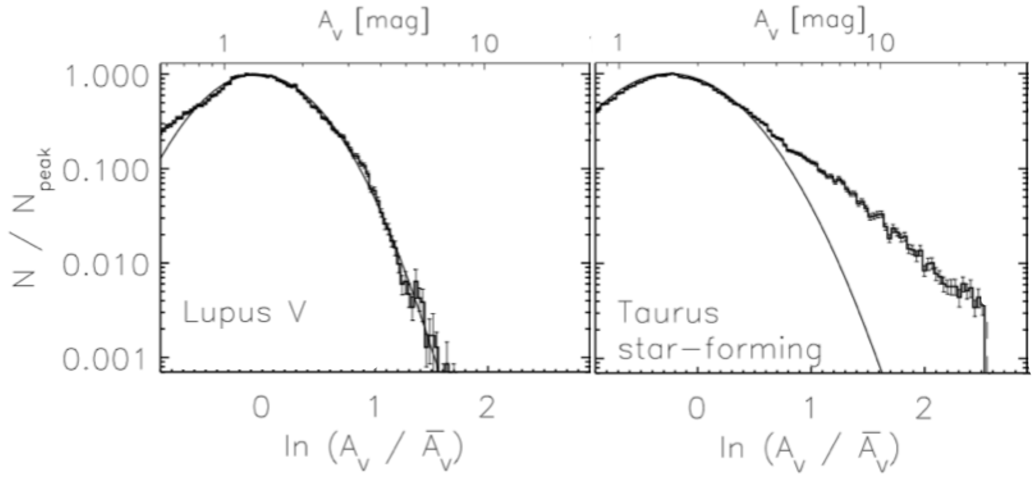

FIGURE 1.7: Logarithmic mean normalized N–PDFs, in units of visual extinction, for the quiescent molecular cloud Lupus V (left) and the star–forming molecular cloud Taurus (right). *Credit: Kainulainen et al. (2009a)*

Recently, Wang et al. (2015) identified GMFs from a different perspective. They used dust emission from *Herschel* to identify nine GMFs with masses and lengths similar to those found by R14. Generally, both filament-finding methods do not identify the same filaments; if they do so, the size of the structures is not necessarily the same. Using a more recent model of the spiral structure of our Galaxy (Reid et al., 2014), they found much higher coincidence between their GMFs and spiral arms than R14 (who used the Vallée, 2008, model), with seven out of nine filaments located in Scutum-Centaurus and Sagittarius spiral arms. The tentative connection between the GMFs and the Galactic spiral structure, together with the intimate connection between filaments and star formation, makes GMFs outstanding objects to study the star formation process on a Galactic environment. In Chapter 4 we present a census of the GMFs in the fourth Galactic quadrant and study the connection between our newly identified GMFs and those previously known and the Galactic spiral structure.

1.4 Probability density function of column densities: a key tool to study cloud–shaping processes and evolution of molecular clouds

As stated in Sect. 1.2.4, molecular clouds are inevitably turbulent. Furthermore, large scale properties of molecular clouds show that this turbulence is supersonic (e.g., McKee and Ostriker, 2007). This supersonic turbulence is expected to affect to the internal structure of molecular clouds. Statistical measurements of the internal structure of molecular clouds are therefore expected to have imprinted signs of this supersonic turbulence, and also of other physical processes involved in shaping the molecular cloud structure. A particularly important statistical tool to study the density structure of molecular clouds is the probability density function (PDF). The PDF describes the relative likelihood of a continuous variable to have a given value. Applied to observational data of column density, they describe the probability of a given pixel to have a column density between $N(H)$ and $N(H) + \Delta$, with Δ the sampling interval of the PDF. In the following, we will refer to the column density probability density functions as N–PDFs, and to the volume density PDFs as ρ–PDFs.

The ρ–PDFs are key in the current star–formation theories that use the ρ–PDFs regardless whether they study the initial mass function (Padoan and Nordlund, 2002; Hennebelle and Chabrier, 2008; Hennebelle and Chabrier, 2009; Elmegreen, 2011), the star formation efficiency (Federrath and Klessen, 2013), the KS law (Elmegreen, 2002b; Elmegreen, 2002a; Krumholz and McKee, 2005; Tassis, 2007; Ostriker, McKee, and Leroy, 2010), or the SFR (Krumholz and McKee, 2005; Padoan and Nordlund, 2011). All these theories integrate the ρ–PDFs over a critical density, which is characteristic for each model, to obtain the SFR of molecular clouds. Ultimately, the SFR depends on the virial parameter (gravity), turbulent forcing parameter[5], sonic Mach number (turbulence), and magnetic fields (Federrath and Klessen, 2013; Padoan et al., 2014).

[5]A dimensionless parameter with values between 0.3 and 1 that indicates whether the turbulence is solenoidal, compressive or mixed.

Simulations predict that turbulence-dominated gas develops a log-normal N-PDF (Federrath and Klessen, 2013); such a form is predicted for the ρ-PDF of isothermal, supersonic turbulent, and non-self-gravitating gas (Vazquez-Semadeni, 1994; Padoan, Jones, and Nordlund, 1997; Scalo et al., 1998; Ostriker, Stone, and Gammie, 2001; Padoan and Nordlund, 2011; Ballesteros-Paredes et al., 2011; Federrath and Klessen, 2013). Log-normal ρ-PDFs can, however, result also from processes other than supersonic turbulence such as gravity opposed only by thermal-pressure forces or gravitationally-driven ambipolar diffusion (Tassis et al., 2010).

Unfortunately, observers cannot measure the ρ–PDFs, but only their two dimensional analogous, N-PDFs. However, both PDFs can be related, assuming statistical isotropy (Brunt, 2010; Brunt, Federrath, and Price, 2010). The N-PDFs are therefore useful tools for inferring the role of different physical processes in shaping the structure of molecular clouds. The log-normal N-PDF is defined as

$$p(s;\mu,\sigma_s) = \frac{1}{\sigma_s\sqrt{2\pi}} exp\left(\frac{-(s-\mu)^2}{2\sigma_s^2}\right), \tag{1.5}$$

where $s = \ln(A_V/\overline{A_V})$ is the mean-normalized visual extinction (tracer of column density, see Section 2.2.3), and μ and σ_s are the mean and standard deviation of the distribution. The log-normal function has typical widths $\sigma_s = 0.3 - 0.4$ (Kainulainen et al., 2009a). It has been suggested that the determination of the width can be affected by issues such as unrelated dust emission along the line of sight to the cloud (Schneider et al., 2015c). Deviations from a log–normal function are expected in the ρ-PDFs and N-PDFs. Specifically, deviations are expected at high densities, where the overdensities created by the supersonic motions eventually become self–gravitating entities (Klessen, 2000; Klessen and Burkert, 2000; Kritsuk, Norman, and Wagner, 2011; Girichidis et al., 2014).

Observations of the N-PDFs in a sample of 23 nearby molecular clouds show two kinds of N-PDFs (Kainulainen et al., 2009a). A few molecular clouds have N-PDFs consistent with log–normal functions (left panel in Fig. 1.7), while most of them show deviations from a log–normal function at large column densities (right panel in Fig. 1.7). The functional shape of the N-PDF deviations from a log–normal function is still subjected to debate. Some works describe it as a power–law tail (Kainulainen et al., 2009a; Russeil et al., 2013; Schneider et al., 2013b; Schneider et al., 2014), while other works use a second, wider, log–normal function (e.g., Kainulainen et al., 2011c; Kainulainen and Tan, 2013). The description of the shapes of the low-column density regimes of both kinds of N-PDFs is still under debate. The papers cited above describe the low-column density regimes as log-normal functions. In contrast, Alves, Lombardi, and Lada (2014) and Lombardi, Alves, and Lada (2015) argue that a power-law function fits the observed N-PDFs throughout their range, and that the log–normal shape at low column densities is due to observational effects (see also Schneider et al., 2015c). The origin of these differences remains unclear. Interestingly, the molecular clouds with log–normal N-PDFs have small or null star–forming activity, while the molecular clouds that deviate from log–normal N-PDFs are actively forming stars. These observations agree with a picture where the molecular clouds are initially subjected to supersonic turbulence (log–normal N-PDFs) that creates a series of density enhancements that eventually become self–gravitating and form stars (log–normal and power–law tail N-PDFs, or double log–normal N-PDFs). The study of N-PDFs is therefore important not only to study the physical processes involved in shaping molecular clouds, but also to study their evolution and star–forming activity. The N-PDFs are widely used in Chapter A.6 of this Thesis.

1.5 Framework of this Thesis

Despite the importance of the molecular clouds and star formation in the evolution of galaxies as a whole, a complete understanding of the physical processes involved in the molecular cloud evolution, structure and star formation is still missing. Current theories use very different parameters and physical processes to explain the existing observational data. However, all these theories are able to simulate realistic molecular clouds with properties in agreement with observational evidence. The observational assets available at the beginning of this thesis were not enough to distinguish between the different theories. Improving the observational statistical assets is therefore imperative to improve our knowledge of the processes controlling molecular cloud evolution, structure and star formation.

Previous to the beginning of this thesis, observational studies of molecular cloud structure and accurate measurements of SFR existed only for molecular clouds in the Solar neighborhood (Goodman, Pineda, and Schnee, 2009; Kainulainen et al., 2009a; Lada, Lombardi, and Alves, 2010a; Kainulainen et al., 2011c; Lada et al., 2012a; Kainulainen and Tan, 2013; Kainulainen, Federrath, and Henning, 2013; Schneider et al., 2013b; Kainulainen, Federrath, and Henning, 2014). The Solar neighborhood represents a tiny portion of the MW and therefore these works can only probe a very limited range of Galatic environments. Furthermore, molecular clouds in the Solar neighborhood probe a limited range of molecular cloud masses $M < 10^5$ $M_\odot$and only Orion among them harbor high mass star formation (Lada, Lombardi, and Alves, 2010a). This observational picture prohibits the development of a global picture of the factors that control the molecular cloud evolution, structure, and star formation processes.

Extending these studies to larger distances is crucial for three principal reasons. First, studying the more massive and distant molecular clouds will allow us to sample the entire molecular cloud mass spectrum present in the Galaxy. Second, larger numbers of molecular clouds over all masses provide statistically meaningful samples. Finally, extending to larger distances is necessary to study the possible effect of the Galactic structure on the mass distribution statistics.

This thesis is dedicated to providing the observational assets needed to paint a Galactic picture of the processes involved in the molecular cloud structure and star–formation. We also develop a new technique that improves the quality of the existing observational data to obtain more accurate observational assets, crucial in the study of molecular cloud structure.

The questions which aim to be answered in this thesis are: which are the physical parameters that shape the molecular clouds? What are the key parameters that determine the star–forming activity of molecular clouds? Do these parameters change with molecular cloud evolution? How does the Galactic environment affect to the star–forming activity and structure of molecular clouds? In the next sections I describe the projects used to answer these questions.

1.5.1 Molecular cloud structure: from local to Galactic scales

Despite their utility, a complete, a global understanding of the N-PDFs of molecular clouds is still missing. The most important weakness in previous studies is that previous works only analyze relatively nearby molecular clouds, $d \lesssim 1.5\,\mathrm{kpc}$ (Goodman, Pineda, and Schnee, 2009; Kainulainen et al., 2009a; Lada, Lombardi, and Alves, 2010a; Kainulainen et al., 2011c; Lada et al., 2012a; Kainulainen and Tan, 2013; Kainulainen, Federrath, and Henning, 2013; Schneider et al., 2013b; Kainulainen, Federrath, and Henning, 2014). A larger statistical sample of molecular clouds at larger distances and subject to different Galactic environments is needed to obtain a Galactic picture of the molecular cloud structure. Furthermore, a statistically significant sample of molecular clouds in the Galactic plane will likely contain examples of molecular clouds at different evolutionary stages. This allows to study the changes that molecular cloud evolution induces in the N-PDFs.

In Chapter A.6 I present the first systematic study of the relationship between the column density distribution of molecular clouds within nearby Galactic spiral arms and their evolutionary status as measured from their stellar content. I analyze a sample of 195 molecular clouds located at distances below 5.5 kpc, identified with the ATLASGAL survey (Schuller et al., 2009a; Csengeri et al., 2014a) data. Three different evolutionary classes are defined within this sample: starless clumps, star-forming clouds with associated young stellar objects, and clouds associated with H II regions. We compare the variations on the column density statistics of this sample of molecular clouds with their evolutionary stages and masses. Furthermore, we use the results connecting the SFR of molecular clouds to their fraction of dense gas and to their total gas mass surface densities (Sect. 1.2.5). Finally, I estimate the evolutionary timescales of three groups of clouds using a free–fall semi analytical model (Girichidis et al., 2014).

1.5.2 Improving the observational studies of column density statistics of molecular clouds: A Fourier method to combine *Planck* and *Herschel* data.

Herschel, thanks to its outstanding sensitivity and ability to observe the FIR continuum, has revolutionized our ability to obtain the column density and temperature distributions of molecular clouds (e.g., Kramer et al., 2010; Launhardt et al., 2013b; Russeil et al., 2013; Schneider et al., 2013b; Lombardi et al., 2014; Schneider et al., 2014; Schneider et al., 2015d; Schneider et al., 2015a; Stutz and Kainulainen, 2015; Pokhrel et al., 2016; Zari et al., 2016).

Large areas of the sky have been surveyed with the FIR bolometers of *Herschel* (PACS (Poglitsch et al., 2010a) and SPIRE (Griffin et al., 2010)): e.g., the Galactic plane has been entirely observed in the HiGal Survey (Molinari et al., 2010a); the Gould Belt Survey observed molecular clouds in the Solar neighborhood (André et al., 2010b); also nearby galaxies such as M31 (Fritz et al., 2012), M33 (Kramer et al., 2010), and the Large Magellanic Cloud (Meixner et al., 2010) have been surveyed. These surveys provide observations of the FIR continuum at five wavelengths from 70 μm to 500 μm , allowing one to obtain line–of–sight averaged column densities and temperatures via Eq. 1.1 and Eq. 1.2. Furthermore, the stability of space-based observations allows for the recovery of extended emission down to much fainter flux levels and over larger scales than those accessible with ground-based sub-mm data (like ATLASGAL in Chapter A.6). Simultaneously, the *Herschel* data probe higher column densities at higher resolution than those commonly accessible with near-infrared (NIR) extinction measurements (but see also Stutz et al., 2009; Kainulainen et al., 2011a).

However, even given the wealth of information that the *Herschel* continuum data provide, large portions of the data remain to be scientifically exploited. An obstacle to obtain accurate column density maps is that *Herschel* did not measure the total power background emission levels. Such measurements may be particularly important for data acquired in regions with strong background emission such as the Galactic plane. The lack of a proper background measurements results in relative fluxes throughout the scan maps. A robust method to obtain an absolute background calibration in the PACS and SPIRE flux maps is a requirement for extracting accurate column density and temperature maps from *Herschel* data.

Obtaining such total power corrections is not trivial. The most common procedure used to calibrate the *Herschel* fluxes is by adding a constant–offset derived from *Planck* (Planck Collaboration et al., 2014a) data (e.g., Bernard et al., 2010; Zari et al., 2016), as has been done for SPIRE (see Section 6.10 in SPIRE data reduction guide). This method assume that the background corrections are constant over the whole mapped areas. However, the background emission levels may vary within the observed area, especially in cases where the maps are large. Adopting a constant–offset derived from *Planck* to correct the *Herschel* fluxes is therefore an over-simplification, as it is demonstrated in Chapter 3.

In Chapter 3, I present a method that uses the the large scale emission observed by *Planck* and the small scale emission observed by *Herschel* in the Fourier space. Combining both datasets in the Fourier space assures that the complete spatial information that *Planck* data provides at large scales is transferred to the newly calibrated *Herschel* maps. This method is presented and evaluated for three different test–case regions. With this method, we will be able to obtain the most accurate column density and temperature maps to date, thus improving our ability to study the column density structure of molecular clouds (Sect. 1.5.1, Chapter A.6). Furthermore, the method presented in Chapter 3 can be applied to any dataset combination with the same properties (very different resolution). Thus, providing a standard tool to improve any observational datasets.

1.5.3 A census of the GMFs for further study

In Sect. 1.3 it was shown that filaments are the dominant structures in the dense regions of molecular clouds and that they have a close relationship to star formation. Recently, a series of tens–of–parsec long filamentary structures known as GMFs were discovered. Their lengths suggest that GMFs might be affected by the Galactic rotation and connected to the Galactic spiral structure. Thus, offering outstanding opportunities to study the molecular cloud structure and star formation on a Galactic environment. However, even the most basic physical properties (e.g., mass, size) of the GMFs are still very poorly understood. Owing to the relatively low number of known GMFs and uncertainties in the Galactic models, the relation of GMFs to the Galactic structure remains an open question. Extending the census of GMFs is key to obtain a Galaxy-wide piture of the physical properties of the GMFs, as a mandatory starting point to study further implications.

In Chapter 4, I extend the current census of GMFs to the fourth Galactic quadrant. The GMFs are first identified as NIR/MIR extinction features and confirmed as physically connected structures using spectral line information. A sample of nine newly identified GMFs and their physical properties are presented. The GMFs identified in this thesis, together with previous samples, are placed in the Galactic context using a model of the spiral-arm pattern of the Galaxy (Reid et al., 2014). Finally, the different methods used so far to identify the GMFs (Ragan et al., 2014; Wang et al., 2015; Zucker, Battersby, and Goodman, 2015) are compared to understand observational biases on their identification.

Chapter 2

Relationship between column density distribution and evolutionary class of molecular clouds

Adapted from Abreu-Vicente, J., Kainulainen, J., Stutz, A., Henning, Th., Beuther, H. (2015) Astronomy & Astrophysics, Volume 581, id.A74

2.1 Introduction

As it was shown in Sect. 1.2.3, the column density distribution of MCs has been found to be sensitive to the relevant physical processes (Hennebelle and Falgarone, 2012). The study of the density structure of clouds that are at different evolutionary stages can therefore help to understand which physical processes are dominating the cloud structure at those stages. The Column density probability density functions (N-PDFs) are useful tools for inferring the role of different physical processes in shaping the structure of molecular clouds.

Previous observational works show that non-star-forming molecular clouds show N-PDFs consistent with log–normal functions while star–forming molecular clouds have excess compared to the log–normal function at high column densities (Kainulainen et al., 2009a; Kainulainen et al., 2011c; Kainulainen, Federrath, and Henning, 2014; Kainulainen and Tan, 2013; Schneider et al., 2013b, see also Fig. 1.7). It is generally accepted that this excess at high column densities is well described by a power-law function in their high-column density regimes. However, some works also claim that this excess can be described by a second, wider, log–normal function (e.g., Kainulainen et al., 2011c; Kainulainen and Tan, 2013). The description of the shapes of the low-column density regimes of both kinds of N-PDFs is still a matter of debate. The papers cited above describe the low-column density regimes as log-normal functions (Eq. 1.5). In contrast, Alves, Lombardi, and Lada (2014) and Lombardi, Alves, and Lada (2015) argue that a power-law function fits the observed N-PDFs throughout their entire range. Furthermore, the properties of the log–normal shape of the N-PDFs at low column densities is affected by observational effects such us line–of–sight contamination from unrelated molecular clouds (Schneider et al., 2015c).

Simulations predict that turbulence-dominated gas develops a log-normal N-PDF (Federrath and Klessen, 2013); such a form is predicted for the volume density PDF (hereafter ρ-PDF) of isothermal, supersonic turbulent, and non-self-gravitating gas (Vazquez-Semadeni, 1994; Padoan, Jones, and Nordlund, 1997; Scalo et al., 1998; Ostriker, Stone, and Gammie, 2001; Padoan and Nordlund, 2011; Ballesteros-Paredes et al., 2011; Federrath and Klessen, 2013). Log-normal ρ-PDFs can, however, result also from processes other than supersonic turbulence such as gravity opposed only by thermal-pressure forces or gravitationally-driven ambipolar diffusion (Tassis et al., 2010).

Another interesting measure of the density structure of molecular clouds is the dense gas mass fraction (DGMF) that describes the mass enclosed by regions with $M(A_V \geq A'_V)$, relative to the total mass of the cloud, $M_{\rm tot}$.

$$dM' = \frac{M(A_V \geq A'_V)}{M_{\rm tot}}. \tag{2.1}$$

The DGMF has been recently linked to the star-forming rates of molecular clouds: Heiderman et al. (2010b) and Lada, Lombardi, and Alves (2010a) and Lada et al. (2012a) showed, using samples of nearby molecular clouds and external galaxies, that there is a relation between the mean star-forming rate (SFR) surface density ($\Sigma_{\rm SFR}$) and the mean mass surface density ($\Sigma_{\rm mass}$) of MCs: $\overline{\Sigma}_{\rm SFR} \propto f_{\rm DG}\overline{\Sigma}_{mass}$, where $f_{\rm DG} = \frac{M(A_V > 7.0\,{\rm mag})}{M_{\rm tot}}$ (see also Sect. 1.2.5). Furthermore, in a sample of eight molecular clouds within 1 kpc, a correlation $\Sigma_{\rm SFR} \propto \Sigma^2_{\rm mass}$ was reported by Gutermuth et al. (2011b). Combining these two results suggests $f_{\rm DG} \propto \Sigma_{\rm mass}$. In other words, the amount of dense gas and the SFR in molecular clouds are set by their surface density of total molecular gas.

Despite their utility, a complete, global understanding of the N-PDFs and DGMFs of molecular clouds is still missing. As stated in Sect. 1.5.1, the most important weakness in previous studies is that they only analyze relatively nearby molecular clouds ($d \lesssim 1.5\,\mathrm{kpc}$), probing a very limited range of Galatic environments. Under this conditions, the development of a global picture of the factors that control N-PDFs across different Galactic environments is not possible. Extending N-PDF studies to larger distances is imperative for three principal reasons. First, studying the more massive and distant MCs will allow us to sample the entire MC mass range present in the Galaxy. Second, larger numbers of MCs over all masses provide statistically meaningful samples. Finally, extending to larger distances is necessary to study the possible effect of the Galactic structure on the mass distribution statistics.

Another issue in the observational study of column density structure in molecular clouds is that different observational techniques sample the N-PDFs and DGMFs differently. Previous works have employed various methods: CO line emission only samples N-PDFs between $A_V \approx 3{-}8$ mag (Goodman, Pineda, and Schnee, 2009). NIR extinction traces column density at wider, but still narrow, dynamic range, $A_V \approx 1 - 25$ mag (Lombardi and Alves, 2001). Kainulainen and Tan (2013) and Kainulainen, Federrath, and Henning (2013) used a novel extinction technique that combines NIR and MIR data, considerably increasing the observable dynamic range, $A_V = 3 - 100$ mag. Schneider et al. (2013b) and Lombardi, Alves, and Lada (2015) used *Herschel* FIR data to sample N-PDFs at $A_V < 100$ mag.

In this chapter, we employ the ATLASGAL (Schuller et al., 2009a; Csengeri et al., 2014a) survey to study a large sample of molecular clouds in the Galaxy. The ATLASGAL survey traces submillimeter dust emission at 870 μm. Submillimeter dust emission is an optically thin tracer of interstellar dust, and hence a direct tracer of gas if a canonical dust-gas mass ratio is assumed. The submillimeter observing technique employed in the ATLASGAL survey filters out diffuse emission on spatial scales greater than 2.5′, hence making the survey most sensitive to the densest material of the interstellar medium in which star formation occurs. With this data set we can observe the cold dense interiors of molecular clouds in both the near and far sides of the Galactic plane. We use this data sample to study the N-PDFs and DGMFs of molecular clouds at different evolutionary classes.

2.2 Data and methods

The ATLASGAL (Schuller et al., 2009a; Csengeri et al., 2014b) survey is a systematic survey of the inner Galactic plane at sub-mm wavelengths. ATLASGAL has observed the Galactic plane region between Galactic longitudes $l \leq \pm 60^\circ$ and Galactic latitudes $b \leq \pm 1^\circ$ at 870 μm using the LABOCA bolometer (Siringo et al., 2009) in the Atacama Pathfinder Experiment (APEX) telescope.

ATLASGAL offers an angular resolution of $19.2''$. The rms may vary within the different regions observed by ATLASGAL, but it is consistently below 50 mJy/beam. The observing and reduction procedures employed in the ATLASGAL survey filter out diffuse emission on angular scales greater than 2.5′, hence making the survey most sensitive to the densest material of the ISM in which star formation occurs. With this data set we can observe the cold dense interiors of molecular clouds in both the near and far sides of the Galactic plane.

In this chapter we use ATLASGAL data to identify MCs in the Galactic plane region between $l \in [9^\circ, 21^\circ]$ and $|b| \leq 1^\circ$, where the rms of the survey is 50 mJy/beam. We selected this area, because extensive auxiliary data sets were available for it: specifically, starless clumps have already been identified by Tackenberg et al. (2012). We classified the identified molecular cloud regions in three groups based on their evolutionary classes: starless clumps (SLCs), star-forming clouds (SFCs), and H II regions. In the following, we describe how each class is defined and how we estimated the distance to each region.

2.2.1 Source selection

We identified molecular cloud regions based primarily on ATLASGAL dust emission data. As a first step, we defined objects from ATLASGAL data simply by using 3σ emission contours (0.15 Jy/beam) to define the region boundaries. Then, we used distances available in literature (see Sect. 2.2.2) to group together neighbouring objects located at similar distances (within the assumed distance uncertainty of 0.5 kpc), i.e., those that are likely associated with the same molecular cloud. As a next step, we expanded the boundaries of the regions down to their lower closed flux contours. The reason to do this is that the column density PDFs only describe the column

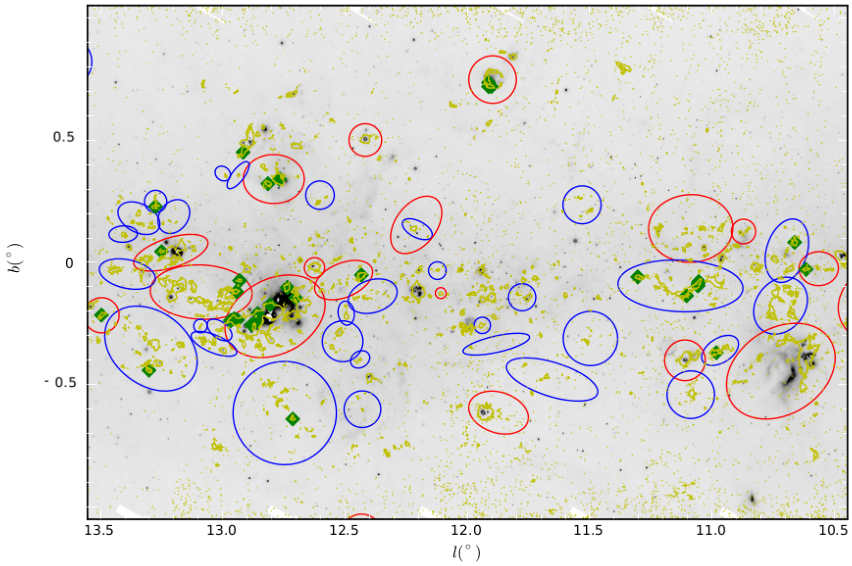

FIGURE 2.1: MIPSGAL 24 μm map of the Galactic plane between $10.5\,\mathrm{deg} < l < 13.5\,\mathrm{deg}$. Yellow contours indicate the 3σ (0.15 Jy/beam) emission level of the ATLASGAL data. Red and blue ellipses show the H II regions and SFCs, respectively. SLCs are shown with green filled diamonds. Similar maps are shown in Appendix A.2.

density distribution properly at values equal or higher than the lowest close contour on which the N-PDFs are calculated. Finally, each region created in this manner was classified either as a SLC, SFC, or H II region using information about their stellar content available in literature. An example of the region definition is shown in Fig. 2.1 (see also Appendix A.2). We identify a total of 615 regions, 330 of them with known distances and classified either as SLC, SFC, or H II regions (Fig. 2.2). Throughout this chapter we refer to each of the ellipses shown in Fig. 2.1 with the term *region*. In the following we explain the definition of the three evolutionary classes in detail.

H II regions are defined as regions hosting previously cataloged H II regions. We used the catalogues Wood and Churchwell (1989), Lockman (1989), Garay et al. (1993), Bronfman, Nyman, and May (1996), Lockman, Pisano, and Howard (1996), Forster and Caswell (2000), and Urquhart et al. (2013b). We identified 114 H II regions in the considered area. Distances are known for 84 of them (74%). Two thirds (57) of the H II regions with distance estimates lie at near distances ($d < 5.5\,\mathrm{kpc}$). If we assume the same distribution for the 30 H II regions with unknown distances, 20 of them would be located at near distances. Nevertheless, we exclude these regions from our analysis. We summarize the number of regions with and without known distances in Table 2.1 (see also Sect. 2.2.2).

The star-forming clouds (SFCs) are defined as the subset of regions devoid of H II regions but containing young stellar objects (YSOs) and protostars. Here the presence of YSOs and protostars is assumed to be a clear indication of ongoing star formation. For this purpose, we used the YSO catalogues of Dunham et al. (2011) and Tóth et al. (2014). The former search signs of active star formation in the Bolocam Galactic Plane Survey (Aguirre et al., 2011, BGPS) using the GLIMPSE Red Source catalogue (Robitaille et al., 2008), the EGO catalogue (Cyganowski et al., 2008), and the RMS catalogue (Lumsden et al., 2013a). They found 1341 YSOs in the area $l \in [9°, 21°]$ and $|b| \leq 0.5°$ and it is >98% complete at the 0.4 Jy level (Dunham et al., 2011). Tóth et al. (2014) present a catalog of 44001 YSO candidates, 2138 in the area $l \in [9°, 21°]$ and $|b| \leq 1°$, with a reliability of 90% in the YSO classification. All the regions showing spatially coincident YSOs were classified as SFCs. We only require one YSO to classify a region as SFC, but our SFCs have more than one. The probability of classifying a SFC as a region without YSOs due to completeness issues in the YSOs catalogues is therefore very low. We identified 184 SFCs, 126 of them with known distances. The 80% (99) of the SFCs with known distances lie at $d < 5.5$ kpc and are therefore studied here. Assuming the same SFC distribution for the SFCs with unknown distances, we estimate that the 80% (46) of the SFCs with no distance estimates would be located at near distances.

Finally, we adopted the starless clump catalog from Tackenberg et al. (2012) to define our sample of SLCs. They present a SLC sample with peak column densities $N > 10^{23}\,\mathrm{cm}^{-2}$. The properties of this SLC sample were specifically chosen in order to detect potential high-mass star progenitors. Tackenberg et al. (2012) used uniform criteria to classify their SLC sample: absence of GLIMPSE and/or 24 μm MIPSGAL sources. Tackenberg et al. (2012) identified 120 SLCs with known distances[1] in the Galactic plane area studied. All SLCs are located inside our previously defined H II regions or SFCs (see Fig. 2.1).

We note a caveat in the above evolutionary class definition scheme. Our scheme makes an effort to capture the dominant evolutionary phase of the region, but it is clear that not all the regions are straightforward to classify. In principle, the distinction between H II regions and SFCs is well defined; it depends on whether the regions host an H II region or not. However, eight

[1]We adopt only regions with solved kinematic distance ambiguity (KDA) as sources with known distances.

regions harbor only UCH II regions whose extent is tiny compared to the full extent of those regions (#34, #54, #192, #195, #233, #246, #247 and #390). Since our aim is to capture the dominant evolutionary phase, we classified these regions as SFCs.

We also note that our evolutionary class definition is based only on the stellar content of the regions. The SLCs exhibit no indications of star-forming activity, SFCs have star-forming sources, H II region have formed massive stars. However, we emphasize that we cannot assume that all the SLCs will definitely form stars. Similarly, we cannot assume that all the star-forming content within SFCs will become massive enough to create H II regions, although some of them will. Therefore we do not aim to draw a *sequential* evolutionary link between these three classes of regions. Instead, the estimated time-scales for each class instead aim to identify independent evolutionary time-scales for each observational class.

2.2.2 Distance estimates and convolution to a common spatial resolution

We adopted distances to each region from literature. The two main literature sources used were Ellsworth-Bowers et al. (2013) and Wienen et al. (2012). The former catalog measures kinematic distances of molecular clumps identified with sub-mm dust emission. They solve the kinematic distance ambiguity (KDA) using Bayesian distance probability density functions. They use previous data sets to establish the prior distance probabilities to be used in the Bayesian analysis. This method has a 92% agreement with Galactic Ring Survey based distances. In total, 68 out of 330 regions have counterparts in Ellsworth-Bowers et al. (2013). Wienen et al. (2012) measured the kinematic distances to dense clumps in the ATLASGAL survey using ammonia observations. We obtained distance estimates for 80 regions from this catalog. We also used other catalogs based on kinematic distances (Walsh et al., 1997; Simon et al., 2006; Rudolph et al., 2006; Roman-Duval et al., 2009; Urquhart et al., 2013b; Tackenberg et al., 2012), and in a three-dimensional model of interstellar extinction (**2009ApJ...706..727M**). A detailed discussion on the methods for distance estimates is beyond the scope of this thesis. We therefore refer to the cited papers for a detailed discussion on them. Table 2.2 shows the number of distance estimates adopted from each literature source. In regions with more than one distance estimate, we estimated the distance averaging the different values. For all but six of the studied regions ($\sim 96\%$) the distance ambiguity was solved in at least one of the cited papers. Regions with different KDA solutions in literature (i.e. with several clouds along the same line-of-sight) were removed from our sample to avoid line-of-sight contamination. For the remaining six regions we used maps from the GLIMPSE and MIPS surveys to search for dark shadows against background emission (e.g., Stutz et al., 2010a; Ragan et al., 2012a). The near distance was adopted for regions associated with IRDCs.

Since all the SLCs of our sample are embedded in H II regions or SFCs (see Section 2.2.1), we compared the distance estimates for the SLCs and for their hosting regions. In every but one case, the distance estimates of the SLCs and their hosting SFCs or H II regions were in good agreement. In the only inconsistent case, the SLC was located at the far distance in (Tackenberg et al., 2012) and its hosting SFC was located at the near distance. Since the KDA solutions of the SLC and its hosting SFC differ, we removed out both regions from the final sample (see also previous paragraph).

Figure 2.2 shows the distance distribution of our sample. A vast majority ($\sim$ 80%) of our regions is located within 5 kpc distance. There is a gap between 6 and 10 kpc, coinciding with the central hole of the Galactic molecular ring (Solomon and Rivolo, 1989)[2]. At the far side of the Galaxy, there are three density enhancements that coincide with the Sagittarius, Norma, and Perseus spiral arms (Fig. 2.3).

We study only regions within 5 kpc since the highest source density of our sample is located there. Assuming an error in distance determination of about 0.5 kpc, we also included regions located between 5 kpc and 5.5 kpc. We convolved the ATLASGAL data of all closer regions to a common 5 kpc distance resolution using a Gaussian kernel of $FWHM = \sqrt{(19.2'')^2(\frac{5\,\mathrm{kpc}}{d\,\mathrm{kpc}})^2 - (19.2'')^2}$. This convolution was done for each region individually. At the distance of 5 kpc, the $19.2''$ resolution of the ATLASGAL translates to about 0.5 pc. We therefore do not resolve the dense cores ultimately linked to star formation that have typically a size of $\sim$0.1 pc (Motte and Hennebelle, 2009; Ragan, Henning, and Beuther, 2013).

[2]We note that the existence of the Galactic Ring has recently been questioned by Dobbs and Burkert (2012), who proposed a two symmetric spiral arm pattern for the Milky Way as an explanation of observations.

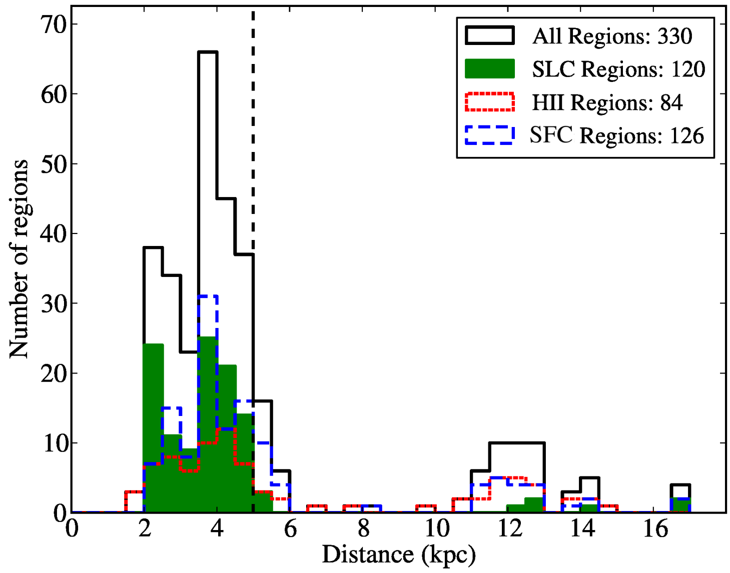

FIGURE 2.2: Distance distribution of the molecular cloud regions. Black solid line shows the total number of regions. Red dotted line shows the HII regions, the blue dashed line the SFCs, and green filled area the SLCs. Black dashed vertical line at 5 kpc shows the common distance to which we have smoothed the data.

When smoothing maps to a common distance, some of the smaller SLCs were washed out by strong emission gradients likely associated with nearby strong sources. This artificially increases the SLCs column densities. To minimize the effect, we inspected each SLC by eye, discarding those that were significantly affected by strong gradients. Appendix A.3 shows the SLCs included in the final sample.

The total number of regions studied in this chapter, and the number of regions in each evolutionary class, are listed in Table 2.1.

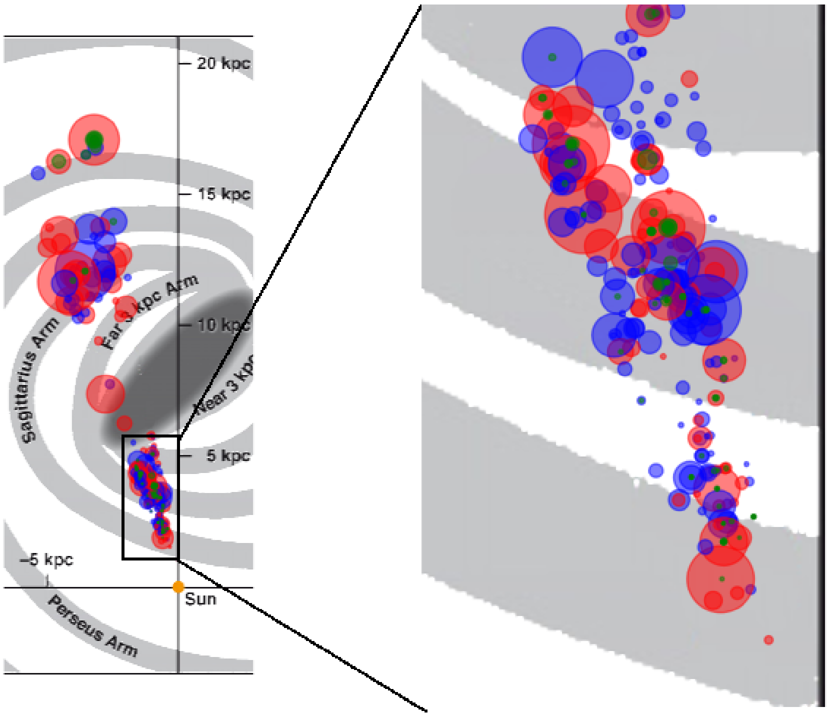

FIGURE 2.3: Artist impression of face-on view of the Milky Way (R. Hurt, SSC-Caltech, MPIA graphic, Tackenberg et al. 2012). H II regions are shown as red circles, star-forming clouds as blue circles and starless clumps as green circles. Circle sizes are proportional to region sizes. The right panel shows a zoom to the region enclosed by the black rectangle in the left panel, where the source density is highest.

TABLE 2.1: Completeness of each evolutionary class

	H II	SFCs	SLCs	No class
Total	114	184	210	107
Known d^a	84	126	120	—
$d < 5.5$ kpc	57	99	111	—
$d > 5.5$ kpc	27	27	9	—
miss. $d < 5.5$ kpc^b	20	18	102	87
miss. $d > 5.5$ kpc^b	10	8	8	20
Studied	57	99	31^b	—

a) Only SLCs with KDA solved and, if more than one distance estimate, agreement between different literature sources.
b) Number of regions lost due to lack of distance estimates. We assume homogeneous distribution of the sources along the Galactic plane area studied.
c) We only studied isolated SLCs (see Sect. 2.2.2)

TABLE 2.2: Literature sources from which distances were obtained

Reference	H II	SFCs	SLCs
1	7	50	11
2	19	6	18
3	23	1	7
4	39	23	18
5	7	11	5
6	14	26	5
7	—	13	—
8	17	—	5

(1) Ellsworth-Bowers et al. (2013); (2) Tackenberg et al. (2012); (3) Urquhart et al. (2013b); (4) Wienen et al. (2012); (5) Roman-Duval et al. (2009); (6) **2009ApJ...706..727M** (7) Simon et al. (2006); (8) Walsh et al. (1997).

TABLE 2.3: Regions studied in this thesis

ID	Type	RA (J2000)	DE (J2000)	Radius (″)	Maj. Ax (″)	Min. Ax (″)	Angle (°)	d^b (kpc)	σ_D^c (kpc)	Ref.
2	SFC	18:05:35.91	-20:52:28.00	90	—	—	—	3.2	—	1
3	SFC	18:05:47.64	-21:00:32.00	90	—	—	—	4	—	1
4	HII	18:06:15.12	-20:31:36.50	150	—	—	—	5.5	0.4	3
5	SFC	18:06:46.98	-20:59:04.10	180	—	—	—	4.5	—	1
7	HII	18:06:52.03	-21:04:27.35	180	—	—	—	4.8	<0.1	4,6
8	SFC	18:06:53.75	-21:18:46.50	150	—	—	—	4.4	—	1
11	SFC	18:07:34.17	-20:26:03.30	150	—	—	—	2.6	—	1
13	SFC	18:07:42.18	-21:23:02.20	200	—	—	—	4.7	0.3	1
16	SFC	18:07:55.85	-20:28:26.60	220	—	—	—	2.5	—	1
27	HII	18:08:53.62	-18:16:08.10	350	—	—	—	3	0.1	4,2
28	SFC	18:08:59.71	-20:11:29.40	150	—	—	—	2	—	4
29	HII	18:09:23.23	-20:08:38.60	150	—	—	—	3.6	0.1	4,3
31	SFC	18:09:24.38	-20:01:35.70	220	—	—	—	2.3	0.4	1,4
30	HII	18:09:01.33	-19:48:33.30	—	290	250	-60	5.2	—	2
33	HII	18:09:05.33	-19:28:00.80	150	—	—	—	2.5	—	3

(1) Ellsworth-Bowers et al. (2013); (2) Tackenberg et al. (2012); (3) Urquhart et al. (2013b); (4) Wienen et al. (2012); (5) Roman-Duval et al. (2009); (6) **2009ApJ...706..727M** (7) Simon et al. (2006); (8) Walsh et al. (1997).

a) These regions have not previous solution for the KDA, but they show shadows against the NIR background radiation, so we located them at the near distance solution. **b)** The distance shown in this table is the result of averaging all the distance estimates available for each source. **c)** The dispersion of all the distance estimates available for each region, when more than one distance estimates are available.

2.2.3 Column density and mass estimation

Column densities of molecular gas were calculated via

$$N_{\mathrm{H_2}}[\mathrm{cm^{-2}}] = \frac{RF_\lambda}{B_\lambda(T_{Dust})\mu m_{\mathrm{H}}\kappa\Omega}, \tag{2.2}$$

where F_λ and $B_\lambda(T)$ are respectively the flux and the blackbody radiation as a function of temperature, T, at 870 μm. The quantity μ is the mean molecular weight (assumed to be 2.8) of the interstellar medium per hydrogen molecule, m_{H} is the mass of the hydrogen atom, Ω is the beam solid angle, and $R = 154$ is the gas-to-dust ratio (Draine, 2011b). We used a dust absorption coefficient $\kappa = 1.85\,\mathrm{cm^2g^{-1}}$ at $870\,\mu$m, which was calculated by interpolation of the Ossenkopf and Henning (1994a) dust model of grains with thin ice mantles and a mean density of $n = 10^6\,\mathrm{cm^{-3}}$. We assumed $T = 15\,\mathrm{K}$ for SLCs and SFCs (Wienen et al., 2012), in agreement with previous dust temperature estimations within infrared dark clouds (Peretto and Fuller, 2010, IRDCs) and in envelopes of star-forming cores (Stutz et al., 2010b; Launhardt et al., 2013a). For H II regions we assumed $T = 25\,\mathrm{K}$. This dust temperature is in agreement with the average dust temperatures in PDR regions surrounding H II regions ($T = 26\,\mathrm{K}$), where most of the FIR-submm dust emission of these objects comes from (Anderson et al., 2012). It also agrees with the mean temperature found in the central region of NGC6334 ($T \sim 24\,\mathrm{K}$), that is an expanding H II region (Russeil et al., 2013). For a better comparison with previous works, we present the column density data also in units of visual extinction using a conversion: $N_{\mathrm{H_2}} = 0.94 \times 10^{21}\,A_V\,\mathrm{cm^{-2}\,mag^{-1}}$ (Bohlin, Savage, and Drake, 1978). The rms noise of the ATLASGAL data (50 mJy) corresponds to $A_V = 4.5\,\mathrm{mag}$ for both the SFCs and SLCs and 2.2 mag[3] for H II regions. No saturation problems were found in the ATLASGAL survey. The optical depth is $<< 1$, therefore our measurements do not suffer from optical depth effects in the high-column density regime (Schuller et al., 2009a).

We estimated the total gas mass of each region from dust continuum emission, assuming that emission is optically thin:

$$M_g = \frac{Rd^2F_\lambda}{B_\lambda(T_{Dust})\kappa}, \tag{2.3}$$

[3]The difference in the rms values in terms of A_V is due to the temperatures assumed for each evolutionary class.

where d is the distance to the region. We assume the same values for the other listed quantities as we assume for the column density determination (Eq. 2.2). Masses of the regions cover three orders of magnitude (Fig. 2.4). The masses of the SLCs span $0.2 - 4 \times 10^3\,\mathrm{M}_{\odot}$, the SFCs $0.3 - 15 \times 10^3\,\mathrm{M}_{\odot}$, and the H II regions $0.2 - 200 \times 10^3\,\mathrm{M}_{\odot}$. Larger masses for H II regions and SFCs are expected since both have much larger sizes than SLCs (Fig. 2.1).

The derived mass and column density values depend on the assumed dust properties, specifically on $\kappa_{870\,\mu\mathrm{m}}$, R and T_{Dust}. Both $\kappa_{870\,\mu\mathrm{m}}$ and R are subject to uncertainties: $\kappa_{870\,\mu\mathrm{m}}$ values differ by $\sim 1\,$dex in different dust models (Shirley et al., 2005; Shirley et al., 2011). Eq. 2.2 and Eq. 4.5 assume isothermal clouds. This is clearly an oversimplification, increasing the uncertainty in the derived masses. Mass depends also on d^2, making uncertainties in distance a major contributor to the absolute uncertainties. If we adopt $\Delta d \sim 0.5\,$kpc, nearby regions will be more affected by distance uncertainties (50% at 1 kpc) than the most distant regions (10% at 5 kpc). This assumption agrees with the distance uncertainties reported by (Roman-Duval et al., 2009). We note that the absolute uncertainty in our derived column densities is very large, potentially larger than a factor 10. The relative uncertainties between the evolutionary classes can be influenced by the different temperature assumptions or intrinsic differences in the dust properties. The isothermal assumption introduces differences in the low-column density regime of the N-PDFs, but it has negligible effect in shaping the column density distribution at high-column densities (see App. 2.3.3). In the case of dust properties, we have no knowledge about any observational-based study suggesting changes in them in molecular clouds at different evolutionary phases. We therefore assume that the dust properties do not introduce relative uncertainties between the three molecular cloud classes defined.

2.2.4 Physical properties of the evolutionary classes

We define and analyze in this work three distinctive evolutionary classes of objects: SLCs, SFCs and H II regions. The objects in these classes are different in their physical characteristics. These differences originate dominantly from the fact that the H II regions and SFCs are typically extended regions (i.e., molecular clouds or even cloud complexes), while SLCs are smaller, "clump-like" structures. We quantify here the basic physical properties of

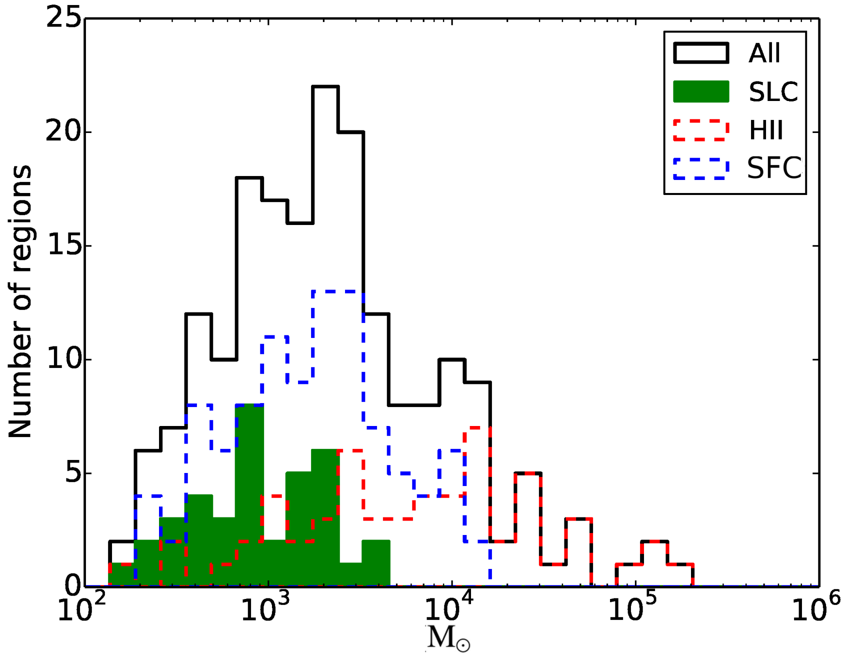

FIGURE 2.4: Mass distribution of the molecular cloud regions. Filled green area shows mass for starless clumps, dashed blue line shows star-forming clouds and red dashed line shows H II regions. Masses are given in solar mass units.

the objects in our three evolutionary classes. The properties are also listed in Table 2.4.

Figure 2.4 shows the mass distribution of our regions. The mass distribution of H II regions spans 3 dex from $10^2 - 10^5\,M_\odot$. SFCs have masses of $10^2 - 10^4\,M_\odot$, and SLCs show the most narrow mass range, $10^2 - 10^3 M_\odot$.

The spread of the distribution of mean column densities is $\overline{A_V} = 3 - 25$ mag and it peaks at $\overline{A_V} = 7$ mag (see Fig. 2.5). The $\overline{A_V}$ distribution differs in each evolutionary class. While most SFCs and SLCs have $\overline{A_V} \lesssim 10$ mag, a considerable number of H II regions show $\overline{A_V} > 10$ mag. We note that the mean column densities of our sample are overestimated due to the spatial filtering of ATLASGAL, and so is the peak of the $\overline{A_V}$ distribution. This effect is more important in H II regions and SFCs since they have larger areas and hence larger fraction of diffuse material that is filtered out than the SLCs.

Figure 2.5 also shows the size distribution of each class and of the total sample. The SLCs have the smallest sizes of the sample with a mean size of 1.4 pc and a range of sizes between 1 pc and 2.5 pc. The range of sizes of the SFCs is 2-15 pc, with a mean of 5.3 pc. The H II regions have the largest mean size of the three evolutionary classes, 7 pc, and also the largest spread,

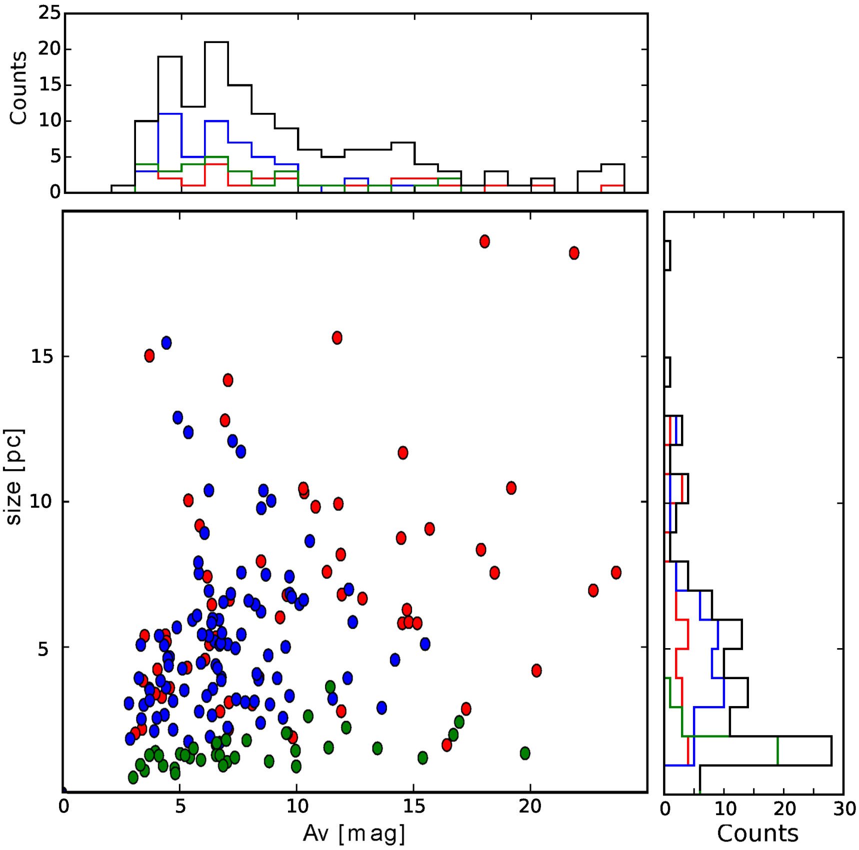

FIGURE 2.5: Mean column density, $\overline{A_V}$, and size distribution of all the regions. In the scatter plot we show the H II regions in red, the SFCs in blue and the SLCs in green. The histograms show the $\overline{A_V}$ and size distributions of each evolutionary class (same colors) and the whole sample (black).

2-18 pc.

2.3 Results

We use the column density data to study the column density distributions of the regions. In the following, we first analyze the *N*-PDFs and DGMFs. We also compare the column density distributions obtained with ATLASGAL with those obtained using *Herschel* data. We then examine the relationship between the total mass and the column density distribution of the regions.

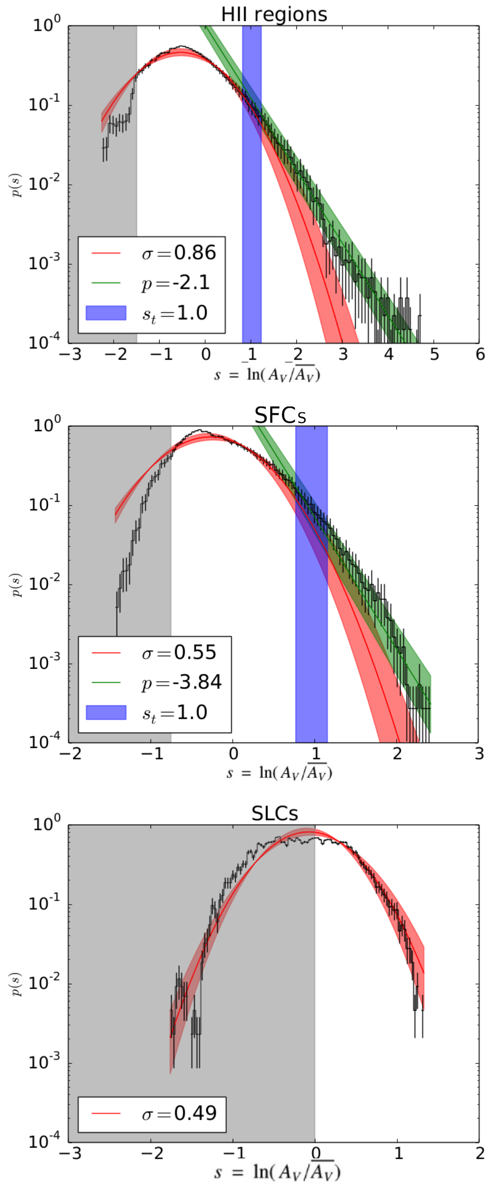

FIGURE 2.6: Total mean normalized column density PDFs of H II regions (top), SFCs (center) and SLCs (bottom). All panels: horizontal axis show mean normalized column densities, $s = \ln(A_V/\overline{A_V})$. Vertical error bars show Poisson standard deviation, $\sigma_{poisson} \propto \sqrt{N}$. The best-fit curves assuming a combination of log-normal and power-law functions are indicated, respectively, by red and green solid lines, with the fit errors indicated as shaded regions of the same colors. The gray shaded regions indicate data below the reliability limit. These data were excluded from the fit. Blue shaded regions show the range of values obtained for the mean-normalized column density value at which N-PDFs deviate from a log-normal to a power-law like function, s_t.

TABLE 2.4: Mean physical properties of the evolutionary classes

	H II	SFCs	SLCs
Mass [$M_\odot$]	18×10^3	2.7×10^3	1.2×10^3
$\overline{A_V}$ [mag]	10.6 ± 6.2	7.0 ± 2.5	8.2 ± 4.2
Size [pc]	7.0 ± 4.0	5.3 ± 2.7	1.4 ± 0.6

2.3.1 *N*-PDFs

We first analyze the total *N*-PDFs of the three evolutionary classes. To construct the *N*-PDFs, we used the mean normalized column densities $s = \ln(A_V/\overline{A_V})$ (see Eq. 1.5) of each region. We calculated $\overline{A_V}$ as the mean column density of all the pixels of each region. The resulting *N*-PDFs were then stacked together to form the total *N*-PDFs, shown in Fig. 2.6 as the black histogram. The three classes show clearly different *N*-PDFs: the H II regions have the widest (or shallowest) *N*-PDF, followed by a slightly narrower (or steeper) *N*-PDF of SFCs. The SLCs have the narrowest *N*-PDF.

Interpreting the low-column density shape of the *N*-PDFs requires taking into account two issues. First, ideally the *N*-PDF should not be affected by how exactly the field-of-view toward an individual region is cropped, i.e., it must include all column density values above a given level. Second, one must ascertain that the pixels are not dominated by noise or contamination from neighbouring regions. To fold these two limitations into one, we define a "reliability limit" of the *N*-PDFs as the minimum column density value above which all regions of the evolutionary class are well defined by a closed emission iso-contour (see Appendix A.3, A.4 and A.5). These levels are $s = -1.5, -0.75$, and 0 for H II regions, SFCs, and SLCs, respectively. These levels correspond typically to $A_V = 2, 4$, and 9 mag, all at least 1-σ above the noise level (50 mJy; see Section 2.2.3). The larger reliability limit in SLCs originates from the fact that they are embedded in H II regions and SFCs, being surrounded by emission levels higher than the map noise. The total number of pixels above these limits are 20×10^4, 9×10^4, and 10^4 for H II regions, SFCs, and SLCs, respectively. We note that this definition of the reliability limit is very conservative; it is set by the lowest iso-contour above which *all* regions of the evolutionary class show a closed contour. Most regions, however, have this limit at lower s values. We also note that systematic uncertainties such as the dust opacity uncertainty do not affect (or, are unlikely to affect) the relative shapes of the three classes with respect to each others.

To quantify the shapes of the *N*-PDFs shown in Fig. 2.6, we fit them, equally sampled in the log space, with a combination of log-normal (see Eq. 1.5) and power-law ($p(s) \propto cs^p$) functions. We used five free parameters in the fit: the width (σ_s) and mean (μ) of the log-normal function, the slope (p) and constant (c) of the power-law, and the break point between both functions (s_t). Furthermore, molecular cloud masses should be recovered when integrating the fitted function, representing an extra boundary condition to the fit. The fitting range was defined as all s values larger than the reliability limit. We weighted the data points by their Poisson noise. We obtained the uncertainties of the fitted parameters by fitting the *N*-PDFs using different bin sizes (Sadavoy et al., 2014). Results are summarized in Table 2.5.

SLCs are well described by a log-normal *N*-PDF ($\sigma_{s,SLC} = 0.5 \pm 0.1$). Even though the peak of the *N*-PDFs is below the reliability limit, it is well constrained by the fit because of the normalization factor in Eq. 1.5. The *N*-PDFs of H II regions and SFCs are inconsistent with a single log-normal function; they are better described by a combination of a log-normal function at low column densities and a power-law function at high column densities. The low-column density log-normal portion of H II regions is wider ($\sigma_{s,\mathrm{H\,II}} = 0.9 \pm 0.09$) than that of SFCs ($\sigma_{s,SFC} = 0.5 \pm 0.05$). The mean-normalized column densities at which the *N*-PDFs transition from log-normal to power-law is similar in both classes, H II regions and SFCs: $s_t = 1.0 \pm 0.2$. We also find differences in the power-law slopes of the *N*-PDFs. The power-law slope is clearly shallower for H II regions ($p = -2.1 \pm 0.1$) than for SFCs ($p = -3.8 \pm 0.3$).

2.3.2 Comparing ATLASGAL and Herschel

Every observational technique to estimate *N*-PDFs has its own limitations. The ATLASGAL data reduction process filters out extended emission from the maps in scales larger than 2.5′ (Schuller et al., 2009a). The FIR emission observed by *Herschel* (Pilbratt et al., 2010b) is very likely to be contaminated by emission from dust unrelated to the cloud of interest (Schneider et al., 2015c). We explore now how the *N*-PDFs derived with *Herschel* and ATLASGAL differ. We do this for one example object of each evolutionary class using the H II region M17 (#248), the SFC IRDC G11.11-0.12 (#54) and the SLC (#54c).

The *Herschel* data of the SFC the SLC were taken as part of the *Herschel* guaranteed time key program Earliest Phases of Star formation (Henning et al., 2010b; Ragan et al., 2012b, EPOS). The data of M17 was obtained from the *Herschel* program Hi-GAL (Molinari et al., 2010b). We used the three SPIRE (**2010A&A...518L...3G**) wavelengths (250 μm, 350 μm and 500 μm), reduced using `scanamorphos v23` (Roussel, 2013), and PACS 160 μm (Poglitsch et al., 2010b), reduced using `HIPE v12` (Ott, 2010). In the flux calibration process, the Planck zero-point correction was applied only to the M17 data.

We derived the column density and temperature maps for each of the three selected regions through a pixel-to-pixel modified greybody fit to the four *Herschel* continuum maps, all of them smoothed to a resolution of 36″. For consistency with the ATLASGAL data analysis, we adopted the dust opacity by interpolation of the Ossenkopf and Henning (1994a) dust model of grains with thin ice mantles and a mean density of $n = 10^6\,\mathrm{cm}^{-3}$. The mean uncertainty obtained in our greybody fitting technique for the temperature maps is $\sim 2.5\,\mathrm{K}$. The relative uncertainty of the column density maps is $\sim 40\%$. The column density maps are shown in Fig. 2.7.

The area over which a molecular cloud shows significant emission is different in ATLASGAL and *Herschel* column density maps. We face this issue by comparing the *N*-PDFs over two different areas: the area over which ATLASGAL shows significant emission, which we will refer to as dense gas area (white contours in Fig. 2.7 and panels in the mid row in the same figure). We also compare the *N*-PDFs derived from the entire areas shown in Fig. 2.7.

We now describe how the *N*-PDFs derived from *Herschel* and ATLASGAL data look like. In the SFC and the H II region *Herschel*-derived *N*-PDFs show a clear log-normal and power-law combination. This combination is seen in both cases of area selection: dense gas area and whole map. The ATLASGAL-derived *N*-PDFs of the SFC and the H II region also have power-law tails at high column densities but they do not show a log-normal distribution at low column densities. In both cases, *Herschel*-derived *N*-PDFs do not probe regions with $A_V \lesssim 10\,\mathrm{mag}$. Both, the ATLASGAL-derived and *Herschel*-derived *N*-PDFs of the SLC are unfortunately dominated by noise, making a comparison impossible. At 36″ of resolution the SLCs do not have enough pixels for an analysis.

The absence of column densities $A_V \lesssim 10\,\mathrm{mag}$ in the *Herschel* data-set is very likely related to the line-of-sight contamination. To compare *N*-PDFs of the datasets without this contamination, we subtracted the background emission from the *Herschel* column density maps. We estimated the magnitude of the line-of-sight contamination averaging the *Herschel*-derived column densities inside the white boxes shown in the top row of Fig. 2.7. We found $A_V^{\mathrm{bg}} = 11.2 \pm 1.2\,\mathrm{mag}$ in the SFC and SLC regions and $A_V^{\mathrm{bg}} = 7.0 \pm 1.6\,\mathrm{mag}$ in the H II region. The background-subtracted *N*-PDFs are shown in the fourth and fifth rows of Fig. 2.7 for the whole map and the dense gas area. The background subtraction significantly widens the *Herschel*-derived *N*-PDFs in the low column density regime. It has, however, very small effect in the high column-density regime, which is slightly flattened.

To estimate the difference between the fitted parameters in the datasets we fitted the power-law tails of the *N*-PDFs, following the same procedure as in Section 2.3.1. The fits were performed in the column density regimes $A_V > 30\,\mathrm{mag}$ and $A_V > 40\,\mathrm{mag}$ in the SFC and H II region respectively. In all cases, the power-law portion of ATLASGAL is somewhat shallower ($p_{\mathrm{HII,AG}} = -1.2$, $p_{\mathrm{SFC,AG}} = -2.0$) than that obtained for *Herschel* ($p_{\mathrm{HII,H}} = -1.6$, $p_{\mathrm{SFC,H}} = -2.3$). The power-law slopes obtained in this work for the SFC are shallower than those reported by Schneider et al. (2014). The difference is probably caused by the different column density ranges used to fit the power-law in the works. When the background component of *Herschel* is removed, the power-law tails flatten and become much more similar to those observed by ATLASGAL ($p^{\mathrm{bg}}_{HII,H} = -1.2$, $p^{\mathrm{bg}}_{SFC,H} = -1.9$). Using only the ATLASGAL emission area (middle row of Fig. 2.7) or the whole map (bottom row of Fig. 2.7) makes no significant difference in the slope of the power-law tails obtained. We conclude that the high-column density power-law parts of the *N*-PDFs are in good agreement between ATLASGAL and *Herschel*. The agreement is even better when the background contamination component of *Herschel* is removed. Note that a background correction to the *Herschel* column densities is usually necessary, as the diffuse Galactic dust component is significant at the Galactic plane. Therefore, one should consider the background subtracted *N*-PDF as a better estimate of the *N*-PDF of the cloud.

We identify the absence of log-normal components in the ATLASGAL-derived *N*-PDFs as an effect associated to the spatial filtering in the data reduction process. This effect is significant in both H II regions and SFCs, being less important in denser regions of molecular clouds where SLC objects lie. Spatial filtering is clearly seen at column densities $A_V \sim 10-20$ mag in Fig. 2.7, where the *Herschel*-derived *N*-PDFs shows a clear excess compared to the ATLASGAL-derived *N*-PDFs. Despite the significant differences shown by the *N*-PDFs derived at low column density regimes, the power-law tails at high column densities are in good agreement, showing the ATLASGAL-derived *N*-PDFs marginally flatter distributions than the *Herschel*-derived *N*-PDFs. Similar results are obtained when the ATLASGAL-derived and *Herschel*-derived DGMFs are compared.

2.3.3 Effects of the isothermal assumption on the *N*-PDFs

Obtaining column densities via dust emission maps at sub-mm wavelengths requires the use of the dust temperature (see Eq. 2.2). When only one wavelength is available, as in the case of this project, the most simple assumption is that the dust is isothermal. However, molecular clouds are not isothermal and the isothermal assumption can therefore generate artificial features in the column density distributions of the maps derived with this method. When several wavelengths are available, as in the case of *Herschel* observations, the line-of-sight averaged temperature and column density distributions can be simultaneously obtained via modified blackbody fitting to the FIR/sub-mm spectral energy distribution.

To study the temperature effects on the resulting *N*-PDFs we used the *Herschel* derived temperature distributions in the previous section to reconstruct the ATLASGAL column density maps of the same three regions. The results of this experiment are shown in Fig. 2.8. In the H II region, the isothermal assumption underestimates the low column density regimes of the *N*-PDF, which remain practically unaffected at $A_V > 40$ mag. The isothermal *N*-PDF of the SFC overestimates the low column density regime and remain similar to the *N*-PDF of the *Herschel*-derived temperature distribution at $A_V = 10 - 90$ mag. The isothermal *N*-PDF in the SLC is shifted to lower column densities.

The isothermal assumption is therefore valid in the high column density regime (i.e. in the power-law tail) of the H II region and the SFC examples shown here. We note that the relative temperature uncertainties are larger in the coldest regions (T$\sim 12 - 15$ K) of molecular clouds (i.e. in the densest regions) and these uncertainties could also result in the underestimate of the *N*-PDF observed at $A_V > 90$ mag in the SFC. Unfortunately, we cannot quantify the possible differences in the shape of the isothermal and the *Herschel*-derived temperature distribution *N*-PDFs of the SLC. The isothermal *N*-PDF therefore offers a more accurate reproduction of the *Herschel*-derived temperature distribution *N*-PDF in the column density regime of the power-law tail than at low-column densities.

2.3.4 Dense Gas Mass Fraction

In Section 4.1 we defined the DGMFs as the fraction of gas mass enclosed by regions with $M(A_V \geq A'_V)$, relative to the total mass of the cloud (see Eq. 2.1). Fig. 2.9 shows the mean DGMFs of each evolutionary class. Generally, H II regions exhibit larger reservoirs of high-column density gas than the SLC and SFC regions.

We quantified the shapes of the mean DGMFs by fitting them with a combination of exponential ($\propto e^{\alpha A_V}$) and power-law ($\propto A_V^{\beta}$) functions, leaving both exponents and the breaking point as free parameters and weighting each point by the Poisson standard deviation. Fit errors were calculated as in Section 2.3.1, resulting in parameter value uncertainties of 10%-15%. While the mean DGMF of the SLCs is well fitted by an exponential, H II regions and SFCs transition from an exponential to a power-law shape at $A_V \geq 20$ mag. This change is evidently linked to the change from log-normal to power-law shape in the *N*-PDF because the DGMFs are an integral of the *N*-PDF. H II regions show the shallowest mean DGMF ($\alpha = -0.06$), followed by SLCs ($\alpha = -0.11$) and SFCs ($\alpha = -0.14$). In the power-law portion of the DGMFs, H II regions are also shallower ($\beta = -1.0$) than SFCs ($\beta = -2.1$). The amount of mass enclosed by the power-law DGMF is 30% of the total mass in H II regions, almost a factor of three lower, 10%, for the SFCs.

The mean DGMF of H II regions above $A_V = 300$ mag is dominated by regions #4, #55 and #122 (see Table A.1). This flat tail is built up by less than 1% of the pixels in each of the mentioned regions, and hence, is not representative of the whole H II sample.

TABLE 2.5: Results of the best-fit parameters to the total N-PDFs and DGMFs.

	N-PDFs			DGMFs	
	σ_s^a	p^b	s_t^c	α^d	β^e
H II	0.9±0.09	-2.1±0.1	1.0±0.2	-0.06^f	-1.0
SFCs	0.5±0.05	-3.8±0.3	1.0±0.2	-0.14	-2.1
SLCs	0.5±0.1	—	—	-0.11	—

a) Standard deviation of the log-normal portion of the N-PDFs. **b)** Slope of the power-law portion of the N-PDFs. **c)** Transition from log-normal to power-law portion of the N-PDFs in mean-normalized column densities. **d)** Slope of the exponential portion of the DGMFs. **e)** Slope of the power-law portion of the DGMFs. **f)** Relative errors of DGMFs account for 10%.

TABLE 2.6: Mass intervals of each evolutionary class in Fig. 2.10

[M$_\odot$]	H II	SFCs	SLC
$M_{i.1}$	—	$< 10^3$	$< 10^3$
$M_{i.2}$	$1 - 2 \times 10^3$	$1 - 2 \times 10^3$	$1 - 2 \times 10^3$
$M_{i.3}$	$2 - 5 \times 10^3$	$2 - 5 \times 10^3$	$2 - 5 \times 10^3$
$M_{i.4}$	$0.5 - 1 \times 10^4$	$0.5 - 1 \times 10^4$	—
$M_{i.5}$	$> 10^4$	—	—

2.3.5 Relationship between the region's mass and column density distribution

Does the dense gas mass fraction of a region depend on its mass and from therein, affect the SFR - cloud mass relation presented by Lada et al. (2012a)? We analyze the DGMFs of each evolutionary class divided in five mass intervals (listed in Table 2.6) that have at least 9 regions each to answer this question.

Figure 2.10 shows the mean DGMFs of each mass interval for the three evolutionary classes. In all evolutionary classes, most massive regions have shallower DGMFs than those of less massive regions. We fit the mean DGMFs with exponential and power-law functions as described in Sect. 2.3.4. Most DGMFs could not be fitted well with the combination of both functions over their entire column density range. Only the DGMFs of the most massive SFCs and H II regions required two component functions; DGMFs of less massive regions are well described by an exponential alone. Exponents derived from this analysis are shown in Table 2.7.

TABLE 2.7: Slopes of the exponential and power-law fits to DGMFs, α, β for the mass ranges presented in Table 2.6.

	$M_{i.1}$	$M_{i.2}$	$M_{i.3}$	$M_{i.4}$	$M_{i.4}$
α(H II)	—	-0.25	-0.22	-0.06	-0.04
α(SFCs)	-0.29	-0.20	-0.18	-0.10	—
α(SLC)	-0.32	-0.19	-0.09	—	—
β(H II)	—	—	—	-0.59	-0.61
β(SFCs)	—	—	-1.03	—	—

In all evolutionary classes, the exponent of the exponential function, α, increases with mass (see Table 2.7). In order to further investigate this correlation, we repeated the same fitting procedure for each individual region. Results are shown in Fig. 2.11. Top panel of Fig. 2.11 shows the relationship between α and the mass of each region: $\alpha \propto M^{-0.43\pm0.05}$, that has a correlation coefficient $r = 0.64$ and a significance value $p = 0.18$. The fit parameters and their errors were obtained from a Monte-Carlo simulation of 10^6 cycles. On each cycle we selected a random sample of points and fitted the resulting data set. We adopt the average of the best fit parameters obtained on each cycle as the best fit values and their standard deviation as the error of the fit. It could be argued that the correlation between α and mass is dominated by the most massive ($M > 3 \times 10^4 M_\odot$) H II regions. To establish whether the correlation strength depends strongly on these few massive clouds we also explored this correlation without those extreme points. The correlation coefficient is somewhat lower in this case $r = 0.56$ and a significant value $p = 0.21$. However, there is no significant difference in the resulting fit ($\alpha \propto M^{-0.40\pm0.08}$). Power-law exponents of DGMFs also exhibit a correlation with mass: $\beta \propto M^{-0.16\pm0.03}$ (see middle panel of Fig. 2.11). The larger scatter seen in the data from the exponential fits relative to that seen in power-law fits may indicate that the power-law regimes of DGMFs are much better constrained than the exponential regimes.

2.4 Discussion

2.4.1 *N*-PDFs as a measure of the evolutionary stage of objects.

The total *N*-PDFs of different evolutionary classes exhibit clear differences; these differences can be linked to differences in the mechanisms that drive the evolution of objects within the various classes. The *N*-PDF of SLCs is well described by a single log-normal function (see Fig. 2.6). This agrees with previous observations of starless low-mass clouds (Kainulainen et al., 2009a) or starless regions of star-forming clouds (Schneider et al., 2012b; Schneider et al., 2013b; Russeil et al., 2013). In particular, this simple log-normal form agrees with predictions for turbulence-dominated media from numerical simulations (Padoan, Jones, and Nordlund, 1997; Vázquez-Semadeni and García, 2001).

In contrast, the total *N*-PDFs of star-forming clouds, i.e., H II regions and SFCs, show two components that can be described by log-normal and power-law functions. The power-law components of the *N*-PDFs of the H II regions are shallower than those of the SFCs. Previous studies have found that the power-law slopes are within $p = [-1.5, -3.3]$, with shallower slopes related to most active star-forming regions. In the only study with a resolution similar to ours, Russeil et al. (2013) found a non-star-forming region in NGC 6334 to have a steep *N*-PDF slope[4] ($p = -5.7$), moderately star-forming regions to have shallower slopes ($p = -3.3, -3.0$), and an H II region to have the shallowest slope ($p = -1.5$). Their trend to have shallower *N*-PDF in a cloud region that contains an H II region is similar to what we find in our work.

Theories and simulations that consider turbulent gas under the influence of gravity predict power-law-like tails for *N*-PDFs with exponents comparable to what is observed (Kritsuk, Norman, and Wagner, 2011; Federrath and Klessen, 2013), possibly featuring flattening of the power-law over timescales relevant for star formation (Ballesteros-Paredes et al., 2011; Federrath and Klessen, 2013; Girichidis et al., 2014). Kritsuk, Norman, and Wagner (2011) showed that a collapsing spherical cloud with a power-law density distribution, $\rho \propto r^{-\kappa}$, will have a power-law *N*-PDF with a slope of

[4] Russeil et al. (2013) quote the equivalent radial density profile (κ), which can be related with the slope of the power-law tail of the *N*-PDF via $p = -2/(\kappa - 1)$.

$p = -2/(\kappa - 1)$. The power-law slopes that we observe (see Table 2.5) indicate $\kappa = 1.9$ and 1.5 for the H II regions and SFCs, respectively. The former is very close to the value $\kappa = 2$ of a collapsing isothermal sphere (Shu, Adams, and Lizano, 1987), suggesting that the density distribution of H II regions may be dominated by self-gravity. The value of $\kappa = 1.5$ we find for SFCs can also be indicative of a collapse slowed down by turbulence-driving effects (Girichidis et al., 2014). We note a caveat in this analysis. Our SFCs and H II regions are unlikely to be close to spheres and their large sizes make them unlikely to be under general free-fall collapse. However, these regions are composed of numerous smaller ATLASGAL clumps (see Fig. 2.1) that may be closer to spherical symmetry, and we are averaging the emission of all these smaller clumps. Indeed, the density profile exponent of our SFCs is similar to that found by Beuther et al. (2002) in a sample of small high mass star-forming objects, which correspond to our definition of SFCs.

Recent works based on *Herschel* observations have explored possible effects of other processes (e.g. ionising radiation or shock compression) on the *N*-PDFs of H II regions (Schneider et al., 2012b; Schneider et al., 2013b; Tremblin et al., 2014). Tremblin et al. (2014) report *N*-PDFs with two log-normal components. They relate the log-normal component at low column-densities to the turbulent motions of the gas and the component at high-column densities to ionization pressure. They also suggest that the presence of these double-peaked *N*-PDFs depends on the relative importance of ionizing and turbulent pressures. The total *N*-PDFs of our H II regions, composed of 60 individual regions, does not exhibit such behavior. This could originate from a combination of several factors: *i)* the low-column density component detected by Tremblin et al. (2014) is at column densities of $A_v \lesssim 6$ mag. These column densities are generally filtered out from the ATLASGAL data; *ii)* the size-scales of the molecular clouds studied in Tremblin et al. (2014) and this work are different and it may happen that the ionisation front of the H II regions is not spatially resolved in our observations.

The above models offer an attractive possibility to link the observed *N*-PDF tails to self-gravitating gas in molecular clouds. However, it has not yet been shown observationally that the power-law parts would be definitely caused by self-gravity; an alternative interpretation has been proposed by Kainulainen et al. (2011b) who suggested that the overall pressure conditions in the clouds may play a role in producing the observed power-law-like behavior in low-mass molecular clouds.

2.4.2 Dense Gas Mass Fraction in molecular clouds

With our cloud sample, we are able to study the DGMFs of molecular clouds over a relatively wide dynamic range of column densities and separately in various evolutionary classes. The continuous DGMF functions (Eq. 2.1) allow for a more complete census of the dense gas in the clouds than the analysis of the ratios of two tracers, e.g., of CO emission and dust emission. We find that the DGMFs of H II regions are shallower than those of SFCs and SLCs. This suggests a direct relation between the star-forming activity of molecular clouds and their relative dense gas mass fraction. Similar results have also been previously found in nearby regions (Lada, Lombardi, and Alves, 2009; Lada, Lombardi, and Alves, 2010a; Kainulainen et al., 2009a; Kainulainen and Tan, 2013) and filmentary clouds (André et al., 2010a).

We detect a clear correlation between the DGMF slope and cloud mass (see Fig. 2.10). Previously, Battisti and Heyer (2014a) found no correlation between molecular cloud mass and the dense gas fraction in a large sample of molecular clouds. They defined the dense gas fraction as the ratio of dust emission-derived mass, traced with 1 mm flux, above $A_V = 9.5\,\mathrm{mag}$ to CO-derived mass: $f_{\mathrm{DG}} = M_{\mathrm{dust}}/M^{\mathrm{CO}}_{GMC}$. Their result imply that there is no correlation between the mass of CO-traced gas ($A_V \sim 3-8\,\mathrm{mag}$) and the mass of gas at column densities $A_V > 9\,\mathrm{mag}$. Unfortunately, we do not measure the CO mass of our MCs and therefore we cannot directly compare our results with those of Battisti and Heyer (2014a). The correlation we find between the molecular cloud masses and the slope of DGMFs suggests that the dense gas fraction depends on the mass of moderately dense gas ($A_V \gtrsim 10\,\mathrm{mag}$) rather than the CO mass of the clouds.

Lada, Lombardi, and Alves (2010a) and Lada et al. (2012a) suggested that star formation rates depend linearly on the amount of dense gas in molecular clouds: $\Sigma_{\mathrm{SFR}} \propto f_{\mathrm{DG}}\Sigma_{\mathrm{mass}}$, with $f_{\mathrm{DG}} = M(A_{\mathrm{V}} > 7\ \mathrm{mag})/M_{\mathrm{tot}}$. Combining this relation with Gutermuth et al. (2011b), who derived the relation $\Sigma_{\mathrm{SFR}} \propto \Sigma^2_{\mathrm{mass}}$, suggests $f_{\mathrm{DG}} \propto \Sigma_{\mathrm{mass}}$. We find that this correlation indeed exists in the range $\Sigma_{\mathrm{mass}} = 50-200\,\mathrm{M_{\odot}pc^{-2}}$ (see Fig. 2.11). At higher surface densities the relationship flattens at $f_{\mathrm{DG}} \cong 0.8$, suggesting that the maximum amount of dense gas that a MC can harbor is around 80% of its total mass. Consequently, the maximum Σ_{SFR} of a molecular cloud is reached at $f_{\mathrm{DG}} \cong 0.8$. This value depends on the definition of the column density threshold (A_V^{th}) of the dense gas becoming lower for higher values of $A_V^{\rm th}$. The spatial filtering of ATLASGAL data (see Appendix 2.3.2) results in overestimated $f_{\rm DG}$ values. We therefore propose $f_{\rm DG} \cong 0.8$ as an upper limit to the actual maximum $f_{\rm DG}$ of a MC. The overestimation of the $f_{\rm DG}$ values derived above can be studied using DGMFs. In general, DGMFs have been shown to follow an exponential function, $\propto e^{\alpha A_V}$, down to low column densities (Kainulainen et al., 2009a; Kainulainen and Tan, 2013). We adopted the α values calculated in Section 2.3.5 and integrated the exponential DGMF in the range $A_V = 0 - 7$ mag to obtain an estimate of $f_{\rm DG}$. The result is shown with crosses in bottom panel of Fig 2.11. The mean overestimation of $f_{\rm DG}$ in SFCs and H II regions is 2 and ~1.3 respectively. We did not include the SLCs in this experiment because their reliability limit is $A_V = 9$ mag and therefore they have $f_{\rm DG} = 1$ (i.e. all its mass is enclosed in regions $A_V > 7$ mag).

Our data can also help to understand the SFR - dense gas mass relation suggested by Lada et al. (2012a). The SFR - dense gas mass relation shows significant scatter of star formation rates for a given dense gas mass, about 0.6 dex (see Fig. 2 Lada et al. (2012a) and Fig. 2.12). This scatter shows that not all clouds with the same amount of dense gas form stars with the same rate. To gain insight into this, we calculated the dense gas mass fractions and star formation rates for our regions as defined by Lada et al. (2012a), i.e., $SFR = 4.6 \times 10^{-8} f_{\rm DG} M_{\rm tot}$ $\rm M_{\it sun} yr^{-1}$. Figure 2.12 shows the SFR - dense gas mass relation with data points from Lada, Lombardi, and Alves (2010a). The figure also shows the mean SFR of our regions in six mass bins, with error bars showing the relative standard deviation of $f_{\rm DG}$. The standard deviations are also listed in Table 2.8. The relative standard deviation of $f_{\rm DG}$ over the entire mass range of our regions is 0.71, which is slightly higher than the relative scatter of SFR in Lada et al. (2012a), $f_{\rm DG} = 0.56$. We conclude that the scatter in star formation rates for a given dense gas mass can originate from differences in dense gas fractions, i.e., in the total masses of clouds for a given dense gas mass. This, in turn, suggests that the dense gas mass is not the only ingredient affecting the star formation rate, but the lower-density envelope of the cloud also plays a significant role. However, we note the caveat that ATLASGAL filters out low-column densities , which may make the dense gas fractions we derive not comparable with those in Lada et al. (2012a), derived using dust extinction data.

TABLE 2.8: Statistics of $f_{\rm DG}$ in this work and in (Lada et al., 2012a).

$M_{\rm tot}$	$\overline{f_{\rm DG}}$	$\sigma/(\overline{f_{\rm DG}})$	# of regions
This work			
$< 0.8 \times 10^3$	0.24	0.22	13
$0.8 - 2.2 \times 10^3$	0.29	0.73	42
$2.2 - 6.0 \times 10^3$	0.31	0.64	39
$6.0 - 17 \times 10^3$	0.41	0.50	27
$17 - 46 \times 10^3$	0.58	0.33	10
$> 46 \times 10^3$	0.83	0.16	4
Entire range	**0.39**	**0.71**	**135**
(Lada et al., 2012a)			
$0.8 - 100 \times 10^3$	0.11	0.56	11

2.4.3 Evolutionary time-scales of the evolutionary classes as indicated by their *N*-PDFs

If *N*-PDFs evolve during the lives of molecular clouds, could they give us information about the evolutionary timescales of the clouds in the three classes we have defined? Girichidis et al. (2014) have developed an analytical model which predicts the evolution of the ρ-PDFs of a system in free-fall collapse. They estimate the relative evolution time-scale, $t_{\rm E}$, from the free-fall time at the mean density, $\overline{\rho}$, of the molecular cloud, $t_{\rm ff}(\overline{\rho})$, and the density at which the ρ-PDFs begin to show a power-law shape, $\rho_{\rm tail}$

$$t_{\rm E} = \sqrt{0.2\frac{\overline{\rho}}{\rho_{\rm tail}}}t_{\rm ff}(\overline{\rho}). \quad (2.4)$$

The model also predicts the mass fraction of gas in regions with $\rho > \rho_{\rm tail}$. We denote this mass as $M_{\rm dense}$.

Since our work is based on column densities instead of volume densities, we need to write Eq. 2.4 in terms of column densities. To this aim, we assume a ratio between 2D and 3D variances, $R = \sigma^2_{N/<N>}/\sigma^2_{\rho/\overline{\rho}}$. This relation is also valid for the ratios $\overline{\rho}/\rho_{\rm tail}$ and $\overline{A}_V/A_V^{\rm tail} = e^{-s_t}$, where $A_V^{\rm tail}$ is the column density value at which the *N*-PDF becomes a power-law and s_t is the mean normalized $A_V^{\rm tail}$. Then, Eq. 2.4 can be written as

$$t_{\rm E} = \sqrt{\frac{0.2}{\sqrt{R}}e^{-s_t}}t_{\rm ff}(\overline{A}_V). \quad (2.5)$$

TABLE 2.9: Evolutionary time-scales

	t_E [t$_{\rm ff}$]	t_E [Myr]	$M_{\rm dense}$ [%]	$\overline{\rho}$ [cm^{-3}]
H II	0.4 ± 0.1	0.7 ± 0.2	$30^{+0.05}_{-0.06}$	0.3×10^3
SFCs	0.4 ± 0.1	0.3 ± 0.1	$10^{+0.06}_{-0.04}$	1.5×10^3
SLCs	0.3 ± 0.1	$\lesssim 0.1 \pm 0.03$	—	4.7×10^3

This equation allows us to estimate the evolutionary time-scale of a molecular cloud using two observable quantities, namely $\overline{A}_V$ and $A_V^{\rm tail}$. The factor R is still not well constrained. Kainulainen, Federrath, and Henning (2014) obtained observationally a value of $R \sim 0.4$ while Brunt, Federrath, and Price (2010) obtained $R = [0.03, 0.15]$ in MHD turbulence simulations without gravity. In the following we use the observationally derived value, $R = 0.4$, to estimate the time-scales of our three evolutionary classes. We estimate the uncertainty in the time-scales as the relative uncertainty between $R = 0.4$ and $R = 0.15$, which is roughly 30%.

We find that our H II and SFCs classes have evolutionary time-scales $t_{E,\rm H\,II} = t_{\rm E,SFC} = 0.4 \pm 0.1 t_{\rm ff}$ and their relative mass of gas in regions with $s > s_t$ are $M_{\rm dense,H\,II} \sim 30 \pm 0.05\%$ and $M_{\rm dense,SFC} \sim 10 \pm 0.06\%$ where the uncertainties were obtained from the 1-σ uncertainties in s_t (see Section 2.3.1). Since the *N*-PDF of the SLCs has no power-law tail, we calculated an upper limit of their evolutionary time-scale by using the largest extinction in their *N*-PDFs as a lower limit, $s_t > 1.2$. We obtained $t_{E,SLC} < 0.3 \pm 0.1 t_{\rm ff}$.

The above relative time-scales can be used to estimate absolute time-scales if the free-fall time is known. We estimate the free-fall time of each evolutionary class as $t_{\rm ff} = \sqrt{3\pi/32G\overline{\rho}}$. The mean density of each class was estimated using their mean masses and effective radii[5] and assuming spherical symmetry. We find that the mean evolutionary time-scale for our H II regions is $t_{E,\rm H\,II} = 0.7 \pm 0.2\,$Myr, and the time-scale of SFCs is $t_{E,\rm SFC} = 0.3 \pm 0.1\,$Myr. SLCs have the shortest time-scales, $t_{E,\rm SLC} < 0.1 \pm 0.03\,$Myr. We note that the absolute time-scales are measured using the onset of the gravitational collapse in the molecular cloud as $t = 0$ and that they were specifically estimated independently for each of the three classes of clouds defined in this work.

Do the above results agree with previous time-scale estimations? The

[5]We define the effective radius as the radius of a circle with the same area as the projected area of a given cloud.

evolutionary time-scale of our SLC sample is within the range of collapse life-times derived in other studies. For example, Tackenberg et al. (2012) derived a life-time of 6×10^4 yr and Ragan, Henning, and Beuther (2013), $7-17\times10^4$ yr for the starless core phase. Furthermore, Csengeri et al. (2014a) found a time-scale of $7.5 \pm 2.5 \times 10^4$ yr for massive starless clumps in the Galaxy using ATLASGAL data. In all these studies, as well as in present chapter, the starless clumps are massive enough to be able to harbor high-mass star-forming activity. Similar evolutionary time-scales have also been found in regions that are more likely to only form low-mass stars, e.g., in Perseus (Walker-LaFollette et al., 2014). The SFC evolutionary time-scale is close to recent age estimates of Class 0+1 protostars, $\sim 0.5 - 0.4$ Myr (Dunham et al., 2014, Table 1). H II regions are subject to other physical processes apart from gravity, such as Rayleigh-Taylor (RT) instabilities involved in the expansion of the H II regions and shocks due to stellar feedback. These processes make this simple evolutionary model hardly applicable to them and we therefore do not discuss the evolutionary time obtained for H II regions further.

Finally, we mention several caveats associated with the time-scales derived above. The mean column density used in Eq. 2.5 corresponds only to the mean observed column density and not necessarily to the actual mean column density that should be used in Eq. 2.5. In addition, the factor, R, relating 2D and 3D variances of mean normalized densities is still not well constrained. Furthermore, this model assumes a single cloud undergoing free-fall collapse. While this assumption can be true for the SLCs, it is unlikely to be the case in SFCs. As mentioned in Section 2.4.1, we assume that the smaller ATLASGAL clumps which compose each SFC region are close to spherical symmetry. With these caveats, we only aim to study the evolutionary time-scales in terms of orders of magnitude. Considering these caveats, we conclude that the method of estimating evolutionary time-scale presented agrees with independently derived typical ages for SLCs and SFCs.

2.5 Conclusions

We have used ATLASGAL 870 μm dust continuum data to study the column density distribution of 330 molecular clouds molecular clouds that we divide in three evolutionary classes: starless clumps (SLCs), star-forming clouds (SFCs), and H II regions. Our large sample of molecular clouds allows us to study their column density distributions at Galactic scale for the first time. We study the column density distributions of the clouds over a wide dynamic range $A_V \sim 3 - 1000\,\mathrm{mag}$, spanning a wide range of cloud masses ($10^2 - 10^5\,\mathrm{M}_{\odot}$). In the following we summarize the main results obtained.

- The total N-PDFs of SLCs is well described by a log-normal function with a width of about $\sigma_s \sim 0.5$. The total N-PDF of SFCs and H II regions show power-law tails at high column densities, with H II regions having a shallower slope. These observations agree with a picture in which the density distribution of SLCs is dominated by turbulent motions. The SFCs are significantly affected by gravity, although turbulence may still play a role in structuring the clouds. The density distributions of H II regions are consistent with gravity-dominated media. Our statistical sample shows that this picture, earlier observed in clouds of the Solar neighborhood, is relevant also at Galactic scale.

- DGMFs of SLCs are well described by exponential functions with exponent $\alpha_{exp} = -0.1$. The DGMFs of H II regions and SFCs are better described by power-laws with exponents of $\beta = -1.0$ and $\beta = -2.1$ respectively. The DGMF shape depends on cloud mass, being shallower for the most massive clouds and steeper for the less massive clouds. This dependence exists in all evolutionary classes.

- We find an approximately linear correlation $f_{\mathrm{DG}} \propto \Sigma_{\mathrm{mass}}$ for $\Sigma_{\mathrm{mass}} = 50-200\,\mathrm{M}_{\odot}\mathrm{pc}^{-2}$, valid for all evolutionary classes. This relation flatens at $f_{\mathrm{DG}} \cong 0.8$ in MCs, suggesting that the maximum star-forming activity in MCs is reached at $f_{\mathrm{DG}} \cong 0.8$. We also find that the intrinsic scatter of f_{DG} is (~0.7 dex) is similar to the scatter seen in the relation SFR - dense gas mass of (Lada, Lombardi, and Alves, 2010a; Lada et al., 2012a). This suggests that both, the dense gas mass and the lower-density envelope of the cloud, play a significant role in affecting the star formation rate.

- We estimate the evolutionary time-scales of our three classes using an analytical model which predicts the evolution of the PDF of a cloud in free-fall collapse (Girichidis et al., 2014). We found $t_{\mathrm{E}} \lesssim 0.1\,\mathrm{Myr}$,

$t_{\mathrm{E}} \sim 0.3\,\mathrm{Myr}$, and $t_{\mathrm{E}} \lesssim 0.7\,\mathrm{Myr}$ for SLCs, SFCs, and H II regions, respectively. Both time-scales agree with previous, independent age estimates of corresponding objects, suggesting that molecular cloud evolution may indeed be imprinted into the observable *N*-PDF functions. H II regions show a complexity of physical processes that make this model hard to apply to them.

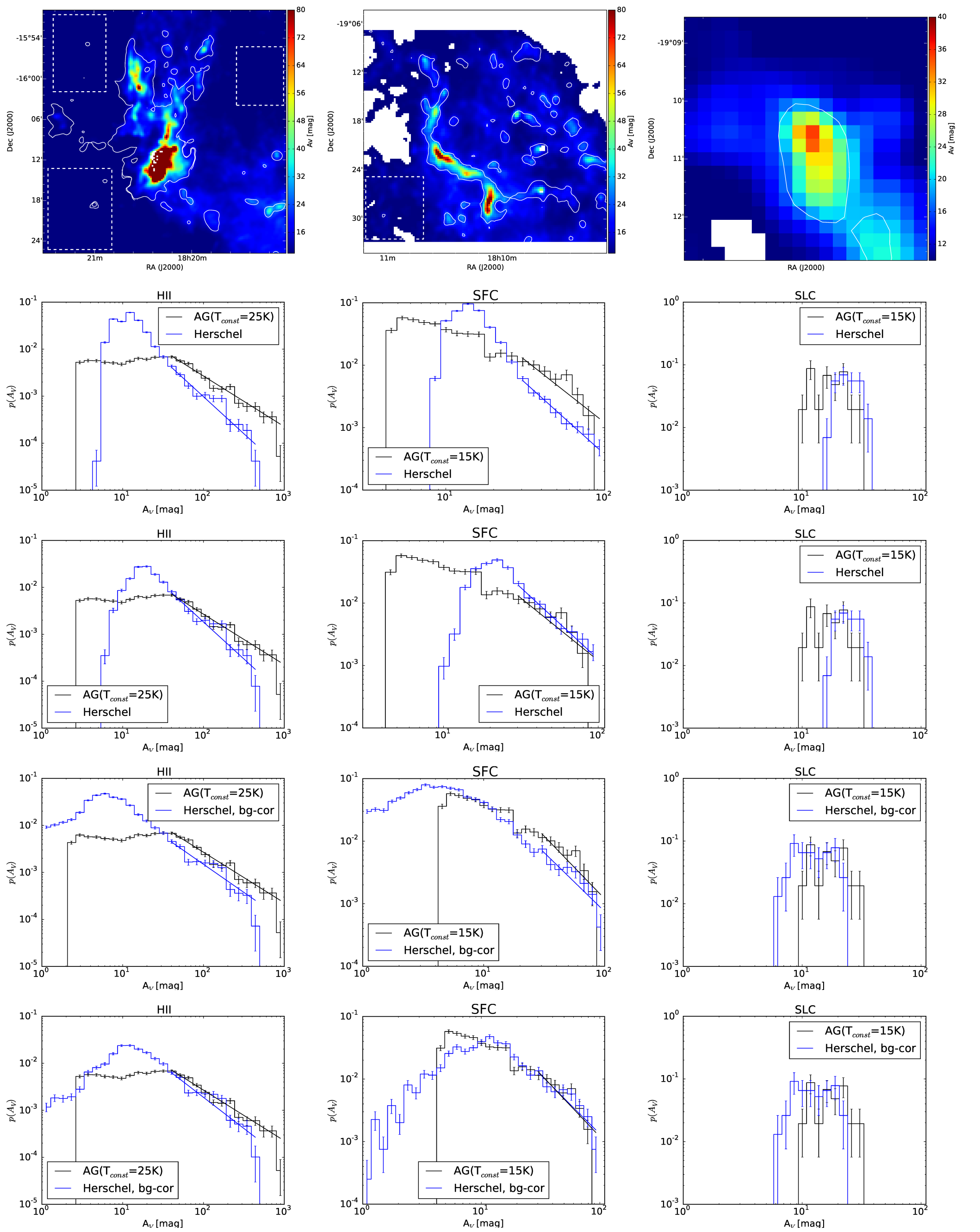

FIGURE 2.7: *Top row: Herschel*-derived column density maps of M17 (H II region), G11 (SFC) and #53c (SLC), in units of A_V. The white contours show the dense gas area (A_V >2 mag, 4.5 mag and 9 mag for the H II region, SFC and SLC respectively). The white dashed boxes show the regions where the background contamination of *Herschel* has been calculated. *Second row:* N-PDFs as seen by *Herschel* (blue) and ATLASGAL (black) in the maps shown in the top row. The vertical error bars show the Poison standard deviation. The solid lines show the best fit to the power-law tail. *Third row:* ATLASGAL-derived and *Herschel*-derived N-PDFs in the dense gas area. *Fourth row:* Background corrected ATLASGAL-derived and *Herschel*-derived N-PDFs in the whole map area of the top row. The background emission was estimated as the mean column density in the dashed boxes of the first row, seen by *Herschel*. *Bottom row:* Background corrected N-PDFs evaluated in the dense gas area.

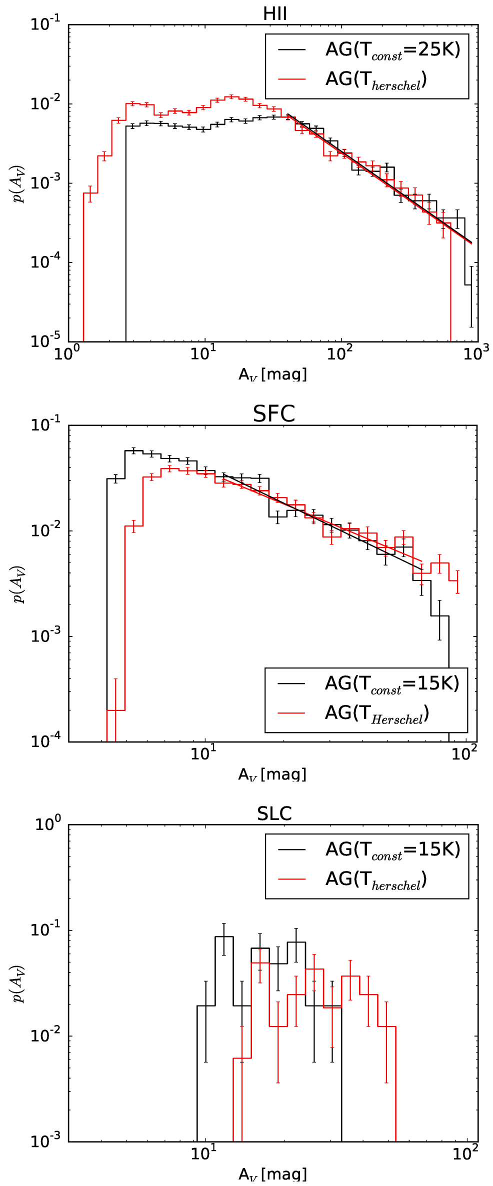

FIGURE 2.8: Isothermal ATLASGAL-derived *N*-PDFs (black) and *N*-PDFs derived using ATLASGAL emission maps together with *Herschel*-derived temperature maps (red). From left to right, H II region, SFC and SLC. The vertical error bars show the Poison standard deviation. The solid lines show the power-law fit to the data in the column density range covered by the lines.

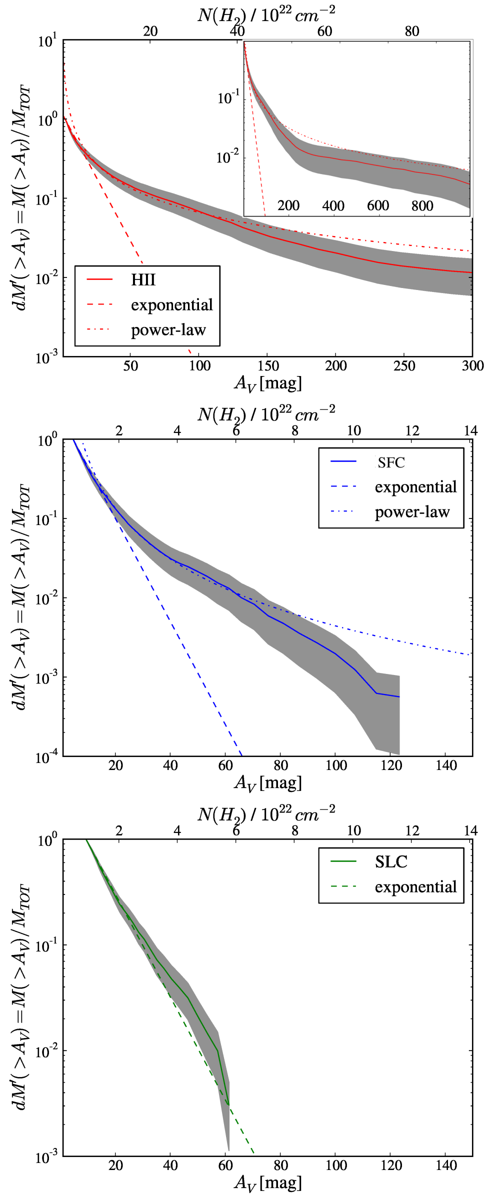

FIGURE 2.9: Mean DGMFs of H II regions, SFCs (center) and SLCs (bottom). Solid colored lines show mean normalized DGMFs. DGMFs were normalized to the reliability limit of each evolutionary class: $A_V = 2, 4, 9\,\mathrm{mag}$ for H II regions, SFCs and SLCs, respectively. Colored dashed lines show the fit of the DGMFs with exponential functions. Dashed-dotted colored lines show fits with power-law tails in the higher A_V range. Grey shaded regions show statistical poisson errors of the DGMFs. Small box in left panel shows the whole mean DGMF of H II regions up to $A_V = 1000\,\mathrm{mag}$.

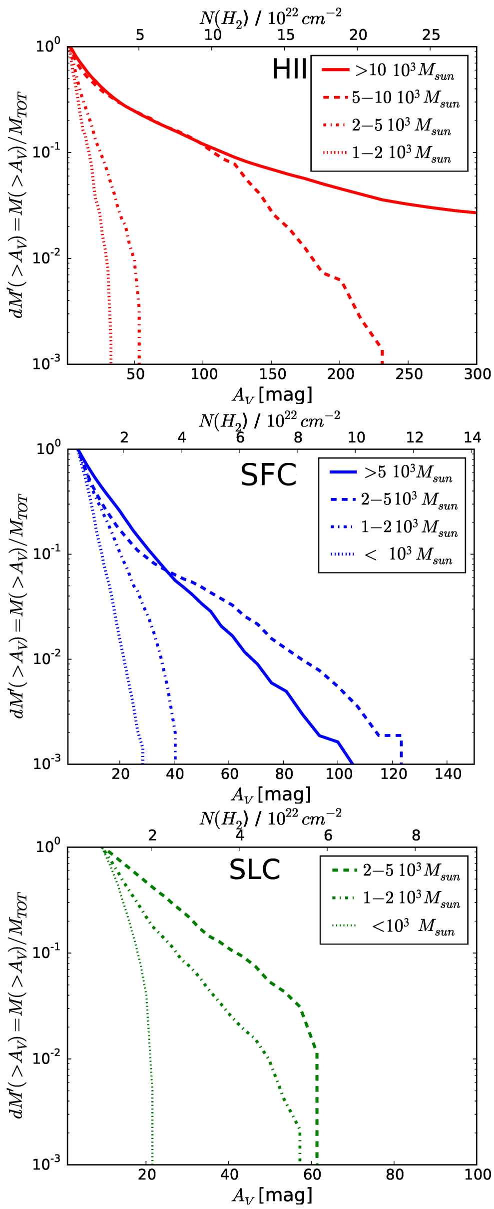

FIGURE 2.10: Mass-binned average DGMFs for each evolutionary class. Each line shows the DGMF for each of the mass intervals listed in the corresponding panel and defined in Table 2.6. Dotted lines, dotted-dashed lines, dashed lines, and solid lines progress from less to most massive bins, respectively. The DGMFs were normalized following the procedure described in Section 2.3.4 and shown in Fig. 2.9.

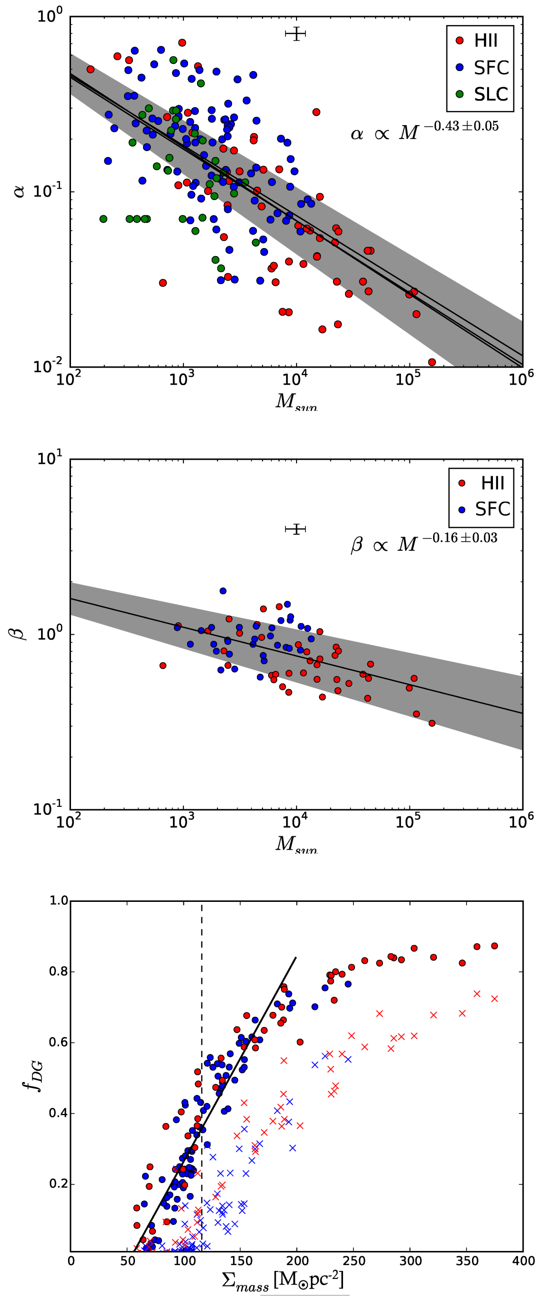

FIGURE 2.11: *Top:* relationship between the mass of the regions [$M_\odot$] and the exponent of the exponential fit to the DGMFs (α_{exp}). Black solid line shows the best fit to the data and the shaded region shows its σ error. The dotted and dashed lines show the best fit when the most massive H II regions are removed. Colors indicate the evolutionary class of each point as indicated. *Middle:* relationship between mass of the regions and the slope of the power-law range of the DGMFs. Black line shows the best fit to the data and the shaded region shows its σ error. *Bottom:* relationship between the mean gas mass surface density of the MCs, $\Sigma_{\rm mass}$, and the dense gas mass fraction of gas, $f_{\rm DG} = \frac{M(A_V > 7.0\,{\rm mag})}{M_{\rm tot}}$. The crosses show the $f_{\rm DG}$ obtained integrating the exponential regime of the DGMFs of each region in the range $A_V = 0 - 7\,$mag (see third paragraph in Sect. 2.4.2). Black line shows a linear fit to the data in the range $\Sigma_{\rm mass} = 50 - 200\,{\rm M_\odot pc^{-2}}$. Vertical dashed line at $\Sigma_{\rm mass} = 116\,{\rm M_\odot pc^{-2}}$ (Lada, Lombardi, and Alves, 2010a; Lada et al., 2012a) indicates the threshold for the dense gas.

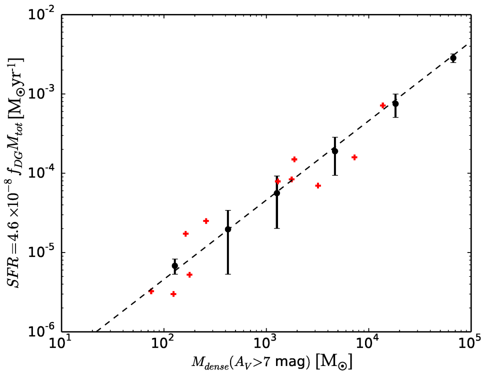

FIGURE 2.12: SFR as defined in Lada et al. (2012a) for different mass ranges of SFCs and H II regions. Red crosses show data from Lada et al. (2012a). Solid black vertical lines show the standard deviation, σ, for each mass bin for our study. Black dashed line shows the constant value $f_{\rm DG} = 1$.

Chapter 3

Obtaining more accurate column densities and temperatures: A Fourier–space combination of *Planck* and *Herschel*

This Chapter has been submitted for publication in the journal Astronomy & Astrophysics. Abreu-Vicente, J., Stutz, A. Robitaille, T., Henning, T. & Keto, E. (2016) submitted. Its current status is recommended for publication after further review. It has been uploaded to astroPh: arXiv:1605.03195.

In Chapter A.6 we present the first systematic study of the relationship between the column density distribution of molecular clouds within nearby Galactic spiral arms and their evolutionary status. As it was discussed in Sect. 2.2, Sect. 2.4.1, and Sect. 2.4.2, the ATLASGAL data is not sensitive to the more diffuse regions of molecular clouds. Observational studies of column density structure must be able to trace these regions since most of the molecular gas mass is located on them, and also because they are responsible for the log–normal part of the N–PDFs generally attributed to supersonic turbulent motions.

This chapter is intended to improve the observational estimates of column density structure in the diffuse regions of molecular clouds to which *Herschel* is sensitive.

3.1 Introduction

The *Herschel* Space Telescope PACS (Poglitsch et al., 2010a) and SPIRE (Griffin et al., 2010) photometers have surveyed large areas of the sky (e.g., André et al., 2010b; Gordon et al., 2010; Kramer et al., 2010; Meixner et al., 2010; Molinari et al., 2010a; Fritz et al., 2012; Draine et al., 2014; Stutz and Gould, 2016) in the far-infrared (FIR) and sub-millimeter (sub–mm) from 70 μm to 500 μm , measuring the cold dust emission largely inaccessible from the ground. Furthermore, the stability of space-based observations allows for the recovery of extended emission down to much fainter flux levels and over larger scales than those accessible with ground-based sub-mm data. Simultaneously, the *Herschel* data probe higher column densities at higher resolution than those commonly accessible with near-infrared (NIR) extinction measurements (but see also Stutz et al., 2009; Kainulainen et al., 2011a).

However, even given the wealth of information that the *Herschel* PACS and SPIRE continuum data provide, large portions of the data remain to be scientifically exploited. An obstacle to obtain accurate column density maps is that *Herschel* did not measure the total power background emission levels. Such measurements may be particularly important for data acquired in regions with strong background emission such as the Galactic plane. The lack of a proper background measurements results in relative fluxes throughout the scan maps. A robust method to obtain an absolute background calibration in the PACS and SPIRE flux maps is a requirement for extracting accurate column density and temperature maps from *Herschel* data.

Obtaining such total power corrections is not trivial. The most common procedure used to calibrate the *Herschel* fluxes is by adding a constant–offset derived from *Planck* (Planck Collaboration et al., 2014a) data (e.g., Bernard et al., 2010; Zari et al., 2016), as has been done for SPIRE (see Sect. 6.10 in SPIRE data reduction guide). However, see also Zari et al. (2016) for a near infrared extinction and *Planck* based calibration method. These method assume that the corrections are independent of angular scale. However, the background emission levels may vary within the observed area, especially in cases where the maps are large. Adopting a constant–offset derived from *Planck* to correct the *Herschel* fluxes is therefore an over-simplification, as we will demonstrate.

Here we present a method to apply the large scale *Planck* correction to the *Herschel* data. The Planck all-sky dust model (Planck Collaboration et al., 2014d) is currently the best available option for correcting the *Herschel* images at 160 μm to 500 μm because of the close match in wavelength coverage. The dust model obtained from *Planck* was derived using 353 GHz, 545 GHz, 857 GHz, and DIRBE/IRAS 100 μm data. The inclusion of the DIRBE/IRAS 100 μm data in the Planck model ensures that the cold peak of the spectral energy distribution near ~ 160 μm , is well constrained. We use a Fourier analysis similar to the "feathering" technique (e.g., Stanimirovic, 2002) often applied in interferometric analysis. However, our method also presents significant departures from the canonical feathering technique, such as the analysis of the relative noise in the images to be combined and the relative weighting function that we adopt.

In summary, here we essentially combine the *Planck* emission on large angular scales with *Herschel* emission on smaller, but still large, angular scales in Fourier space. We adopt a hyperbolic tangent weighting function that provides a smooth but sharp transition from from *Planck* Fourier modes to *Herschel* modes. While traditional Gaussian weights are usually adopted in the above mentioned feathering method, the advantage of using a hyperbolic tangent weighting function is that it provides control of the angular scale of the transition from *Planck* modes to *Herschel* modes. We determine the scale of the transition from *Planck* dominated power to *Herschel* dominated power base on two criteria: the relative noise in the two images to be combined, and the presence of excess power at large angular scales in the *Herschel* scan-maps. Combined, these prove to be critical considerations for the accurate combination of the data sets in question.

We apply our method to three fields observed by *Herschel* that span a wide range of Galactic environments: B68, Perseus, and the Galactic plane region at $l = 11^\circ$ (HiGal–11, including G11 and W31). We process the new absolute calibrated maps to obtain dust column density (N(H)) and temperature (T) maps. We compare our column density maps to those obtained from *Herschel* maps corrected based on a constant background and those obtained from a single sub-mm wavelength (e.g. ATLASGAL Schuller et al., 2009b; Csengeri et al., 2016). The data processed in this work will be made publicly available.

This chapter is organized as follows. In Section 3.3 we describe the steps required to prepare the publically available data for Fourier analysis. In Section 3.4 we describe the basic methodology that we will apply. In Sections

TABLE 3.1: *Herschel* observations

Name	Obs ID	RA (J2000) [hh:mm:ss]	DE (J2000) [°:′:″]	Project	Ref
Perseus-04	1342190326	03:29:39	+30:54:34	KPGT_ pandre_ 1	1 , 2
B68	1342204365	17:22:25	-23:50:53	KPGT_ pandre_ 1	1 , 3, 4
HiGal-11	1342218966	18:09:50	-19:25:22	KPOT_ smolinar_ 1	5

(1) André et al. (2010b); (2) Sadavoy et al. (2013); (3) Motte et al. (2010); (4) Motte et al. (2012); (5) Molinari et al. (2010a).

3.4.1, 3.4.2, and 3.4.3 we demonstrate the method on three specific fields. In Section 3.5 we compare the post-processed N(H) and T maps to the canonical "scalar offset" method. We present our conclusions in Section 3.6.

3.2 Interferometry, short spacing and feathering

The basics of the technique that will be used in this Chapter to combine the *Herschel* and *Planck* data have been originated in interferometry and they are explained in detail in Stanimirovic (2002).

Unlike in single dish observations, on which the data obtained recovers the image observed by the telescope, interferometers observe in the Fourier space (Ségransan, 2007). This means that if we want to reconstruct the image observed by the interferometer we need to sample the Fourier plane as much as possible. Lets assume an interferometer with six antennas, like the old IRAM Plateau de Bure interferometer in France, now known as NOEMA and with eight antennas. The top left panel of Fig. 3.1 shows the physical positions of the antennas in the ground. If the six antennas observe the same source at the same time, the uv–plane will be sampled as shown in the top right panel. Each cross belongs to the distance between two antennas. The blue and green crosses are symmetric respect to the origin of coordinates. If we keep observing the same source during a long time, the rotation of the earth will change the position of the telescopes respect to the source and the baselines in the uv–plane, improving the coverage of the latter, as shown in the bottom left panel of Fig. 3.1. The uv–plane data more distant from the origin (indicated with the red arrows), is responsible for reconstructing the small scales of the image. In other words, the smaller details, it defines the resolution of the image. Unfortunately, antennas must be separated and

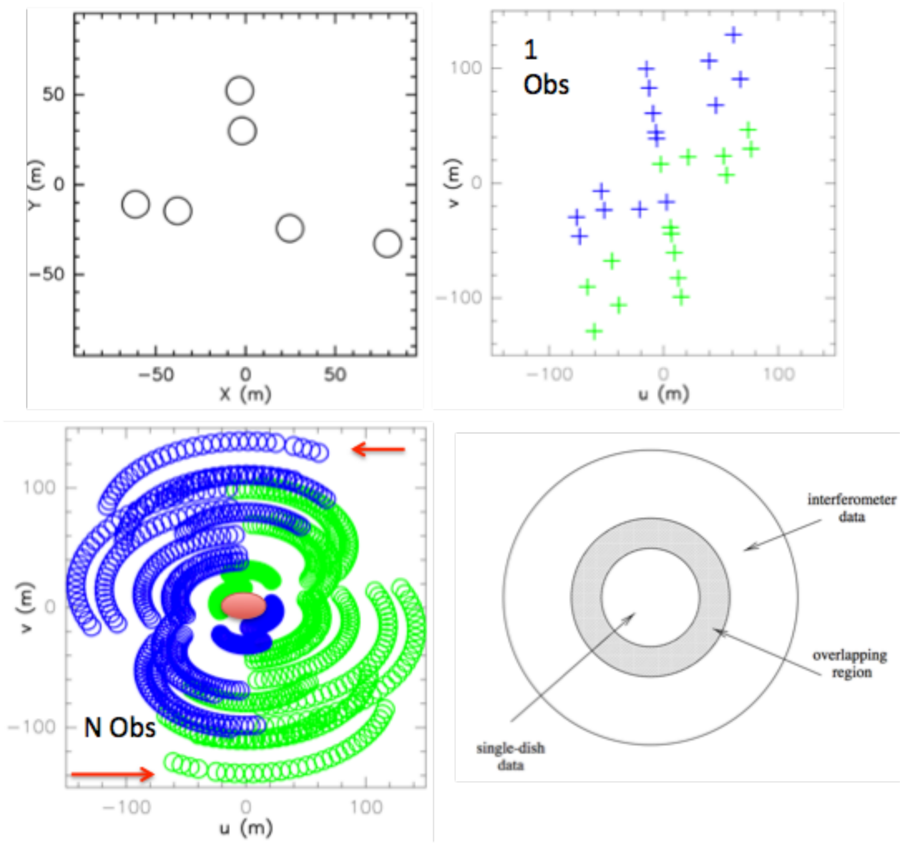

FIGURE 3.1: Scheme of an interferometer and the uv–plane coverage. Images courtesy of J. Pety (IRAM). Image in the bottom right fromSégransan (2007).

there is no way of sampling the origin of the uv–plane (in red in Fig. 3.1). To do this, the distance between two antennas should be zero meters. This implies a limitation to interferometry. The small scales in the uv–plane correspond to the largest scale of the image that we can obtain. To obtain the large scale information, the interferometers need what is known as short spacing observations. That is observe the same source with a single dish telescope. These observations sample the origin of the uv–plane, allowing the recovery the large scale information of the source observed.

The interferometric and single dish observations are combined as shown in the scheme of the bottom right panel of Fig. 3.1. The process of this combination is known as feathering and is similar to that used in this chapter to combine the *Planck* and *Herschel* datasets. In this analogy, the *Herschel* data are the interferometric (high resolution) observations and the *Planck* data represent the single-dish (low resolution) observations. The procedure is similar to that used in Csengeri et al. (2016) to recover extended emission of

ATLASGAL data. See Stanimirovic (2002) for an explanation of the formalism as applied to interferometry.

In short, we combine *Herschel* and *Planck* data in the Fourier space. We generate the FT of the *Herschel* (FT_H) and *Planck* (FT_P) maps and add them, weighted by their correspondent *uv*–scale ($\kappa = \sqrt{u^2 + v^2}$) dependent functions, to obtain the FT of the combined image, FT_C:

$$FT_C = FT_H w_H(\kappa) + FT_P w_P(\kappa). \tag{3.1}$$

We then calculate the combined FT to obtain the *Herschel* and *Planck* combined images. Due to several issues found during its application, and described in detail in the following sections, we needed to modify the standard feathering technique of Stanimirovic (2002).

3.3 Data and intial processing

In this chapter we use public *Herschel* and *Planck* (Planck Collaboration et al., 2014b) archive data. Here we describe the data and initial processing steps that are required before applying our method to recover the large angular scale emission from the *Planck* data.

3.3.1 *Herschel* data

The Herschel Space Observatory (*Herschel* , Pilbratt et al., 2010b) is a European Space Agency (ESA) and NASA funded space-based far-infrared (FIR) telescope with a 3.5 m mirror. It has three on-board instruments capable to perform spectral and continuum observations at wavelengths between 55 μm and 672 μm . In this Thesis I focus only on the bolometer capabilities of the Photodetecting Array Camera and Spectrometer (PACS Poglitsch et al., 2010b) and Spectral and Photometric Imaging Receiver (Griffin et al., 2010, SPIRE).

The *Herschel* data used in this chapter were retrieved from the *Herschel* science archive. We select parallel mode observations carried out with the PACS (Poglitsch et al., 2010a) and SPIRE (Griffin et al., 2010) photometers. We use the level 2.5 data products. These data products are optimized for extended emission reconstruction as well as the principle observing mode used for large-scale surveys (i.e., the parallel mode). We therefore focus exclusively on these products in this chapter. We use the red (160 μm) channel of PACS, and the three wavelengths of SPIRE (250 μm, 350 μm, and 500 μm). These maps have native pixel scales (and beam sizes) of 3.2″ (11.8″), 6″ (18.2″), 10″ (24.9″) and 14″ (36.3″) respectively. The data products used in this chapter are listed in Table 3.1. We refer the reader to the references in this table for further observational details. While the archive PACS/160 μm data are

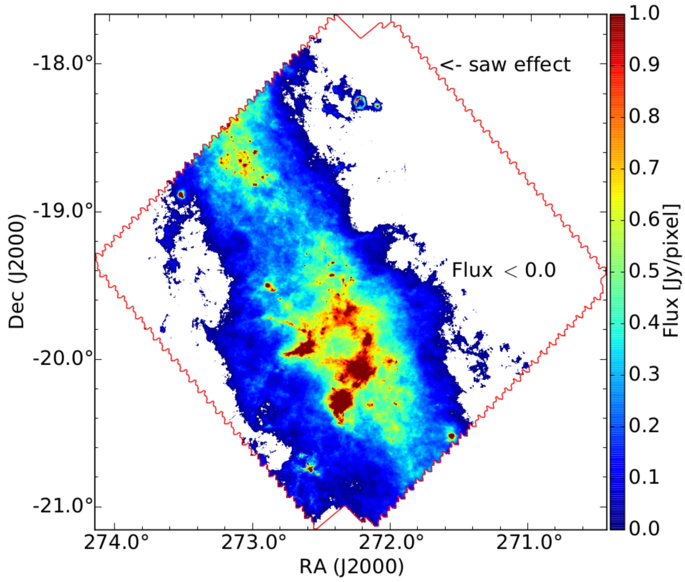

FIGURE 3.2: *Herschel* / PACS 160 μm map of HiGal–11. The negative values are shown in white. The red contour indicates the irregular boundary of the *Herschel* map.

not corrected for total power with *Planck* , the SPIRE data do include such a correction. Previously, the *Planck* corrections have been carried out by adding a single number to the image which effectively shifts the zero-point to higher values[1]. This scalar correction assumes that the *Herschel* data are only missing the "total power" component in the reconstructed maps due to the nature of measurements acquired with bolometers. What has not been investigated previously is the possibility that the *Herschel* data may also be corrupted at large angular scales corresponding to low-order but non-zero Fourier modes in the images. Here we develop a method that is capable of recovering this multi–scale emission while also accounting for the effects of noise in the images.

[1]For the SPIRE case, this procedure is described in detail in the instrument handbook: `herschel.esac.esa.int/Docs/SPIRE/spire_ handbook.pdf`.

3.3.2 *Planck* all-sky dust model

The *Planck* satellite has observed the entire sky at nine different frequencies in the range 30 – 857 GHz (Planck Collaboration et al., 2014b). One of the mission data products is an all-sky model of the foreground dust emission, obtained from a modified blackbody (MBB) fit to *Planck* observations at 353, 545, and 857 GHz, complemented with IRAS 100 μm (Thomas, 1986) observations (Planck Collaboration et al., 2014d). This model estimates the dust optical depth, temperature, and spectral index with a resolution of 5′ (30′ for the spectral index, β). The results of this modelshould be used only within the frequency range 353–3000 GHz. At shorter wavelengths the dust emission is known to contain a non-thermal component due to stochastically heated grains (e.g. Draine et al., 2007; Draine, 2011a; Planck Collaboration et al., 2014d; Meisner and Finkbeiner, 2015).

3.3.3 Initial processing

Cropping the edges of *Herschel* observations

In the main step of this method we combine the *Planck* and *Herschel* data in the Fourier space. Fourier Transforms (FTs) are sensitive to any spatial patterns on the maps. As we show in Fig. 3.2, the original *Herschel* maps have two main spatial patterns: a “saw” effect in the field edges, and a zero–padding outside of the observed region. The first step of our method consists of rotating and cropping the *Herschel* maps to eliminate these edge effects. Unfortunately, the general field geometry of *Herschel* data is not well described by a rectangular field. We therefore must find the best combination possible between removing "zero-padding" and "saw" effects and keeping the larger amount of data possible. The *Herschel* /SPIRE and *Herschel* /PACS observations in parallel mode have an intrinsic pointing offset[2]. We therefore treat both instruments separately and define different effective regions for each instrument.

[2] See *Herschel* handbook for further details.

From the *Planck* dust model to predicted intensities

We use the *Planck* all-sky foreground dust emission model (see Section 3.3.2) to reconstruct a FIR spectral energy distribution (SED) at the observed *Herschel* wavelengths. This model provides the optical depth at $\nu_0 = 353\,\mathrm{GHz}$ (τ_0), the dust temperature (T_{obs}), and the dust spectral index (β) for each sky pixel based on a modified black-body (MBB) fit the observed fluxes. We obtain the SED following the *Planck* analysis via

$$I_\nu = B_\nu(T_{\mathrm{obs}})\tau_0 \left(\frac{\nu}{\nu_0}\right)^\beta, \tag{3.2}$$

where I_ν is the intensity at each frequency, and $B_\nu(T_{\mathrm{obs}})$ is the blackbody function at the observed temperature. We convert these SEDs into *Herschel* simulated observations, integrating them over the respective *Herschel* filter response functions for extended sources. The *Herschel* pipeline assumes a flat νS_ν calibration within each bandpass. We therefore obtain the monochromatic *Planck* fluxes (S) as follows:

$$S = \frac{\int I_\nu \, R_\nu \, \mathrm{d}\nu}{\int \left(\frac{\nu}{\nu_0}\right)^2 R_\nu \, \mathrm{d}\nu}, \tag{3.3}$$

where I_ν is the intensity obtained in Eq. 3.2, R_ν is the spectral response function for each *Herschel* bandpass, and ν_0 the effective central frequency of each bandpass (Robitaille et al., 2007). We repeat this step for each pixel of the *Planck* all-sky dust emission model, obtaining four maps of simulated emission at the targeted *Herschel* wavelengths. These maps are initially extracted from the *Planck* healpix data format at a 75″ pixel scale. In a later step these images are regrided and rotated to the reference frame of the *Herschel* images at their respective wavelengths (pixel scales for *Herschel* data are listed above). This regriding operation is a strict requirement to carry out the Fourier analysis presented below. However, we caution that regriding from 75″ to e.g., 3.2″ in the case of the 160 μm image causes subtle but significant artifacts in the *Planck* maps. We account for these artifacts in the analysis presented in this chapter. For simplicity, we refer to this data cube as the *Planck* data cube.

We investigate how the uncertainties of the parameters T_{obs}, β, and τ_0 propagate to our simulated flux maps. To estimate the effect of uncertainties

TABLE 3.2: Uncertainties in flux values as propagated from the *Planck* dust model.

λ [μm]	$\sigma_T = 8\%$	$\sigma_\beta = 8\%$	$\sigma_\tau = 10\%$
160	42%	5%	10%
250	29%	4%	10%
350	22%	4%	10%
500	15%	3%	10%

Uncertainties in the model fluxes for fiducial MBB parameters of $T_{\rm obs} = 20$, $\beta = 1.7$, and $\tau_0 = 1e-4$.

we use the standard deviations of $T_{\rm obs}$, β, and τ_0 derived for the whole sky, which are respectively 8%, 8%, and 10% (Planck Collaboration et al., 2014d). We apply these values to an MBB function independently and estimate how much the flux varies at the four wavelengths of interest. In Table 3.2 we show the results for the representative fiducial MBB parameters $T_{\rm obs} = 20$, $\beta = 1.7$, and $\tau_0 = 1e{-}4$. At every wavelength, the temperature uncertainties dominate on our simulated maps, with the effects being larger at shorter wavelengths.

3.4 Combining *Herschel* and *Planck* fluxes: methodology

As stated above, we use the *Planck* foreground emission component model (Planck Collaboration et al., 2014d) to generate flux maps at each of the *Herschel* wavelengths we consider in this chapter, namely 160 μm , 250 μm , 350 μm , and 500 μm . Our goal is to derive *Planck* –based multi–scale corrections for the *Herschel* images at each wavelength before deriving dust column density and temperature maps. In this section we summarize our basic methodology. In the subsequent sections we analyze in detail three regimes that must be treated differently based on the specific properties of the images, namely noise and power at large angular scales.

At a given wavelength, *Planck* and *Herschel* provide independent estimators of the image at all scales. For *Planck* , the estimator of the deconvolved image Fourier transform is $= \mathcal{F}(\textit{Planck}\ ) \times e^Q$. Here,

$$Q = \frac{\pi^2}{\ln 16}\left[(n/S_x)^2 + (m/S_y)^2\right]\mathrm{FWHM}^2, \tag{3.4}$$

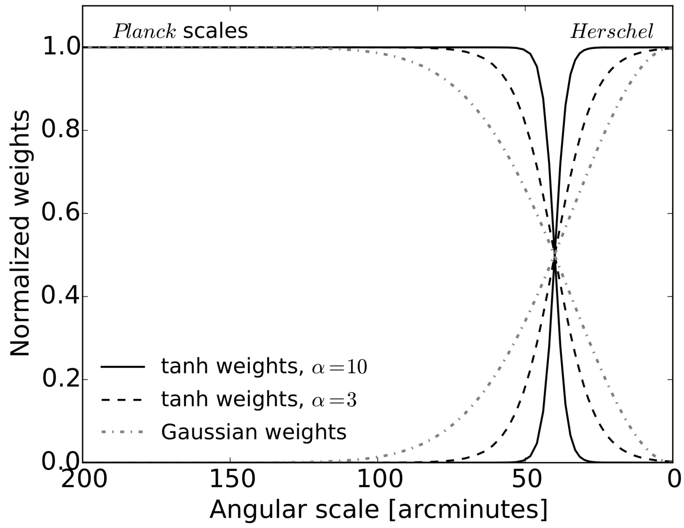

FIGURE 3.3: Hyperbolic tangent weighting function used to combine the *Herschel* and *Planck* (Eq. 3.6). The black solid line shows the hyperbolic tangent weights with $\alpha = 10$, while the dashed line assumes $\alpha = 3$. For comparison, the gray dashed-dotted line shows Gaussian weights. All curves assume $\kappa_{eff} = 40'$.

is the *Planck* beam transfer function[3] assuming a perfectly Gaussian beam, n and m are the Fourier modes, S_x and S_y are the dimensions of the box (size of the image), and FWHM is the *Planck* beam size. However, in reality observed beams are not pure Gaussians. And *Planck* is no exception. Indeed, the beam profiles at the various observed frequencies have been carefully quantified and are known to contain significant sidelobe power (Planck Collaboration et al., 2014c). Since the *Planck* foreground emission model is the result of the combination of various non-Gaussian beams (including the IRAS 100 μm data), we do not expect that the beam window function will obey Eqn. 3.4 assuming the reported model FWHM = 5′. Instead, we empirically measure the beam transfer function, as described in detail in the following sections.

Assuming that the beam transfer function has been characterized, then if we consider only the *Planck* image, application of the e^Q factor would effectively amount to image deconvolution. However, it is well known that applying this correction on scales smaller than the beam results in noise amplification. Nevertheless, mathematically it is important to keep track of this factor because in fact this suppression of the *Planck* emission is significant even on scales that are significantly larger than the *Planck* beam, as we will

[3]https://wiki.cosmos.esa.int/planckpla/index.php/Effective_Beams

show below. Formally, the way to implement the Fourier combination of *Herschel* and *Planck* data (or any similar data set) is the following:

$$I_k = H_k(1 - w_k) + P_k e^Q w_k, \tag{3.5}$$

where k→(n,m) indicates the Fourier modes, w_k is the weighting function, and $I_k, H_k,$ and P_k are the Fourier transforms of the total, *Herschel* , and *Planck* images, respectively.

While Eq. 3.5 is true in general, there is no universal choice of w_k because the weighting of the images depends on the individual qualities and characteristics of the images (e.g., noise, systematics, etc.). The most basic feature of the weights in our case is the requirement that $w_0 = 1$. That is, the final combined image must contain the *Planck* $k = 0$ information that the *Herschel* data are at least partially lacking. This is mathematically identical to the previously applied "scalar offset" correction (e.g., Bernard et al., 2010; Lombardi et al., 2014; Zari et al., 2016). That is, the scalar offset method corresponds to applying *only* the zero–mode correction in the Fourier domain. However, our method will also capture low order modes that may contain significant power in *Planck* and in some cases be corrupted in the *Herschel* data. We show in Table 3.3 that overall the *Herschel* images contain more noise than the *Planck* images. However, the application of the e^Q factor will greatly amplify the noise in the *Planck* images, causing the *Planck* noise to completely overwhelm the *Herschel* signal at small scales. The noise amplification is exponential and thus huge at angular scales similar than the *Planck* beam size. We do not wish to equally weight noisy data with good quality data. Thus, the elevated noise in the deconvolded *Planck* data, combined with their low resolution ($\sim 5'$), lead us to adopt a transition from *Herschel* to *Planck* at the largest scales possible.

Generically, to implement Eq. 3.5 we must choose a functional form for the *Planck* weights (w) that satisfies $w_0 = 1$, is continuous, and suppresses the *Planck* information on small scales where *Planck* noise is most amplified. We define w as the hyperbolic tangent function (see Fig. 3.3):

$$w = \frac{e^{-x}}{e^x + e^{-x}}; \qquad x \equiv \alpha \left(\frac{\kappa}{\kappa_{eff}} - 1 \right), \tag{3.6}$$

where α is the factor defining the steepness of transition from 1 to 0 in the weights and κ_{eff} is the optimum scale identified for the transition between

Planck and *Herschel* . The adopted value of α is somewhat arbitrary, but since we wish to implement a relatively sharp transition between *Planck* and *Herschel* , we adopt $\alpha = 10$ (see Fig. 3.3) for all images and wavelengths. κ_{eff} should be generically fixed for all images but adjustable for special cases. In general we find that a $\kappa_{eff} = 40'$ satisfies the requirements of our method (see Sect. 3.4.1 and Sect. 3.4.2); however, an important exception applies to noisy fields (see Sect. 3.4.3).

TABLE 3.3: *Planck* and *Herschel* image sizes, noise properties, constant–offsets, and fit parameters.

Region	λ	S_x	S_y	rms$_{Planck}$ [a]	rms$_{Herschel}$ /rms$_{Planck}$ [a]	*Herschel* $(m,n)=0^b$	*Planck* $(m,n)=0^b$	FWHM$_{eff}$ [c]	γ_{eff} [c]	κ_{eff} [d]
	[μm]	[′]	[′]	[Jy/arcsec^2]		[Jy/arcsec^2]	[Jy/arcsec^2]	[′]		[′]
HiGal–11	160	124	124	9.4e-1	28.4	1.7e-2	3.6e-2	5.13	3.16	40
	250	124	124	6.5e-1	6.9	2.3e-2	2.4e-2	5.05	0.60	40
	350	124	124	1.5e-1	8.7	1.1e-2	1.1e-2	5.16	0.52	40
	500	124	124	4.9e-2	7.3	3.9e-3	3.9e-3	5.11	1.53	40
Per-04	160	138	138	5.7e-2	36.5	2.2e-4	1.3e-3	5.95	-1.81	40
	250	138	138	4.5e-2	13.4	1.2e-3	1.2e-3	5.55	-2.90	40
	350	138	138	2.5e-2	8.2	7.5e-3	7.5e-3	5.23	-0.85	40
	500	138	138	1.0e-2	5.7	3.2e-4	3.4e-4	4.59	4.32	40
B68[e]	160	72	72	2.2e-2	8.9	1.1e-3	1.8e-3	···	···	∞
	250	72	72	1.2e-2	2.5	1.2e-4	1.3e-4	···	···	∞
	350	72	72	4.7e-3	2.6	7.1e-4	7.2e-4	···	···	∞
	500	72	72	2.1e-3	2.3	2.9e-4	2.9e-4	···	···	∞

[a] The noise is measured within the following angular scale ranges for each wavelength: 160 μm $\rightarrow (6,12)''$; 250 μm $\rightarrow (8,18)''$; 350 μm $\rightarrow (12,24)''$; 500 μm $\rightarrow (14,36)''$. The *Planck* noise is measured in the original model images *before deconvolution*; after deconvolution the noise is amplified exponentially with the Fourier modes.

[b] *Herschel* and *Planck* image zero-mode amplitude per pixel in the Fourier domain. To obtain the "scalar offsets", the two must be subtracted.

[c] Beam transfer function best-fit parameters (see Equation 3.4).

[d] Adopted angular scale for the transition between *Planck* and *Herschel* .

[e] For B68, the data are too noisy to permit an accurate determination of the *Planck* effective beam transfer function (Equation 3.4) and thus too noisy to apply our multi-scale combination method.

In what follows we show representative examples of *Planck* and *Herschel* data–sets that each belong to one of these three distinct categories:
The good – HiGal–11: This field does not suffer from elevated noise levels of artifacts and thus is considered "well behaved". We discuss this field first because it allows us to present the basic method in the absence of additional complexities.
The bad – Perseus: We find that this field exhibits large scale spurious power in the *Herschel* data despite obeying the expected behaviour at intermediate and small scales. We use the scale at which this spurious power appears to define $\kappa_{eff} = 40'$.
The ugly – The Pipe: We show that this region is too noisy, particularly at 160 μm , to apply a multi-scale *Planck* correction without significantly degrading the *Herschel* data. In this case, we simply apply the $(n, m) = 0$ corrections.

3.4.1 The good: HiGal–11

We begin by presenting the full analysis of the 160 μm image. Later we discuss the 250 μm , 350 μm , and 500 μm image reconstruction.

HiGal–11 at 160 μm

Figure 3.4 shows the low–order Fourier modes of the *Planck* image generated at 160 μm . We note that in general the conversion between Fourier modes and angular scales is given by

$$\theta = [(n/S_x)^2 + (m/S_y)^2]^{-1/2}, \tag{3.7}$$

where as above, n and m are the Fourier modes, and S_x and S_y are the dimensions of the box (or angular size of the image in each dimension). In the particular case of a square image geometry such as this one, the conversion between angular scale and Fourier modes is purely circular, $\theta \propto [n^2 + m^2]^{-1/2}$, and both axis scales can be shown meaningfully on the same plot. In the left panel of Fig. 3.4 we highlight obvious artifacts which are caused by the requirement to regrid the *Planck* data to the same pixel–scale as that of the *Herschel* data. These artifacts correspond to horizontal and vertical structures in the image of the Fourier modes; see right panel of Fig. 3.4. As can be seen in Fig. 3.4 the Fourier moduli are clearly signal-dominated

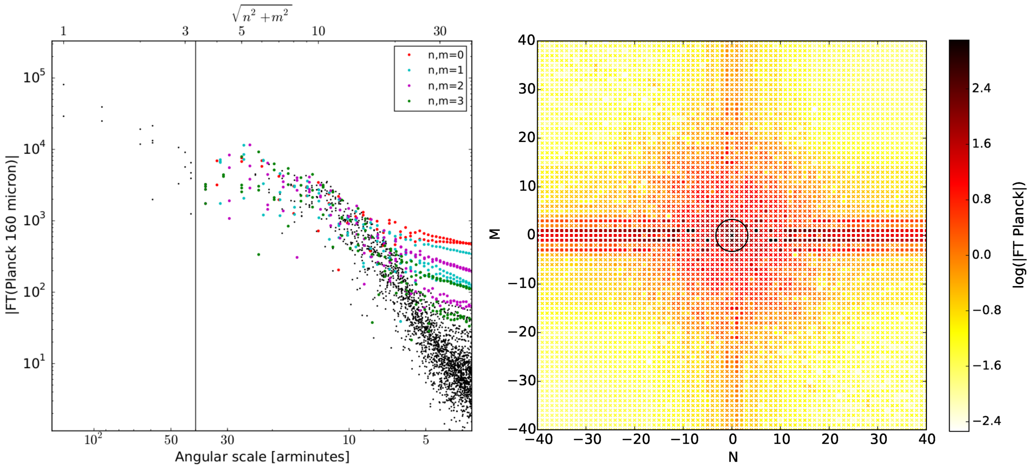

FIGURE 3.4: *Left:* 160 μm HiGal–11 *Planck* Fourier moduli as a function of angular scale (bottom abcissa) and Fourier mode radius (top abcissa). We highlight the lowest order modes affected by the pixel regriding requirements with the indicated colors; the corresponding points are indicated in the left panel as squares. The vertical line indicates $\kappa_{eff} = 40'$ (see text). *Right:* Fourier moduli amplitude image. The pixels corresponding to low-order artifacts are shown as filled squares, which are highlighted in various colors in the left panel. These artifacts follow well–defined vertical and horizontal tracks and are caused by regriding the *Planck* model image to a much finer pixel scale. These artifacts do not propagate into the lowest order modes (the modes inside the indicated circle) and are excluded from the beam transfer function analysis (see text). The size of the circle indicates κ_{eff}, that is, the *Planck* Fourier modes that we use in the image combination.

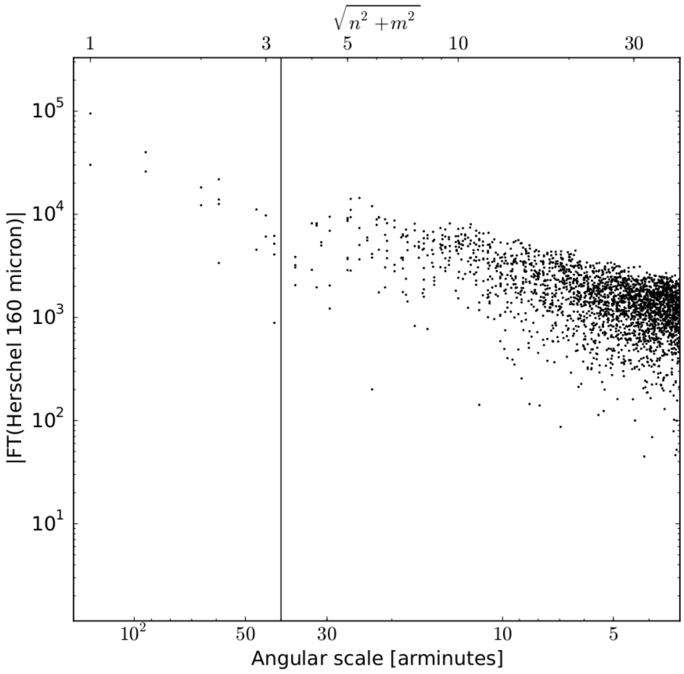

FIGURE 3.5: 160 μm HiGal–11 *Herschel* Fourier moduli as a function of angular scale (bottom) and Fourier mode radius (top).

at large angular scales. Therefore these artifacts can be safely ignored if the method is restricted to analyzing only the low–order modes (largest angular scales). This therefore drives the choice of κ_{eff} to large values (but see below and Sect. 3.4.2 for further justification). We find no obvious artifacts in the *Herschel* images (Fig. 3.5).

However, fundamentally, the noise properties of the images must be understood in order to choose a well-motivated κ_{eff}. For example, if the image providing the estimate of the large–scale power is very noisy, then ideally κ_{eff} should be as large as possible so as to include the least amount of noise in the final combined image. The noise per pixel in an image can be estimated from the rms scatter in the Fourier moduli as $\sigma = \mathrm{rms}|\mathcal{F}(I)|/(N)$, where I is the image and N is the number of pixels. We measure the $\mathrm{rms}|\mathcal{F}(I)|$ between angular scales of 6″ to 12″, a range determined by the region within which the moduli distributions are flat as a function of scale (that is, at or below the beam resolution) for both *Planck* and *Herschel* . In the case of *Planck* the regriding artifacts discussed above make an insignificant contribution to the rms scatter. We present the noise estimates in Table 3.3. From these measurements it is clear that the *Herschel* data are noisier than the *Planck* data. However, the *Planck* noise amplification induced by the transfer function (see Sect. 3.4) results *Planck* data being far noisier than *Herschel* data. Thus, we conclude that we must choose κ_{eff} to be as large as possible. However, there is an upper limit imposed on κ_{eff} by the *Herschel* data. This scale is $40'$, and is discussed in Sect. 3.4.2.

In Fig. 3.6 we show the ratio of the *Planck* to *Herschel* Fourier moduli. The key features of this diagram are:

1 The *Planck* effective beam response function does not follow the shape of a Gaussian with 5′ FWHM, but instead is consistent with a larger FWHM.

2 There is no evidence for a multiplicative calibration missmatch between *Planck* and *Herschel* .

3 There is no evidence for a systematic constant–offset between *Planck* and *Herschel* , which may be expected due to contamination from e.g., stochastic heating of dust grains.

With an understanding of the existing low–order mode artifacts in the *Planck* and *Herschel* images we can proceed to measure the *Planck* model effective beam transfer function (e.g., Eq. 3.4) as follows. While the quoted *Planck* model beam is a Gaussian with 5′ FWHM, we test this assumption by directly fitting the ratio of the *Planck* to *Herschel* Fourier moduli as a function of scale (Fig. 3.6). The fact that the *Planck* beam is much larger than even the largest *Herschel* beam (see Sect. 3.3) permits us to measure the effective *Planck* beam transfer function. In Fig. 3.6 the ratio of the moduli does not behave as we would expect for a Gaussian beam: the green curve illustrates the beam transfer function for a Gaussian with FWHM = 5′. This curve provides a poor characterization of the ratio behaviour at all relevant scales and clearly demonstrates that the *Planck* model beam is significantly larger than the quoted value and has significant power at large scales. Some of this behaviour may arise from non-Gaussian beam profiles such as side lobes. While in this work we are particularly concerned with the large angular scale correction for *Planck* and not errors on small scales where *Herschel* will dominate, we cannot simply apply Eq. 3.4 to correct the *Planck* Fourier amplitudes as these do not provide a satisfactory fit on any scale.

We therefore adopt an empirical approach to measuring the *Planck* effective beam window function. We assume a function similar to that shown in

Eq. 3.4, but with an additional term that provides more power on larger angular scales:

$$Q' = pFWHM^2(x^2 + \gamma x); \qquad x \equiv [(n/S_x)^2 + (m/S_y)^2]^{1/2}, \qquad (3.8)$$

where $p = \pi^2/\ln 16$, and $FWHM$ and γ are free parameters. We then fit this function to the distribution of Fourier moduli ratios, and obtain the fit shown in Fig. 3.6 as the red line. Here we adopt an iterative fitting approach designed to exclude noisy data as we have found that outliers can bias the results. We begin by excluding points that are flagged in Fig. 3.4 as artifacts caused by the regriding of the *Planck* image. We then re–fit Eq. 3.8 excluding all points that lie more that one rms away from the original fit. The best–fit values obtained for FWHM and γ are listed in Table 3.3. We note that the values of the individual parameters of the Q' fit cannot be taken at face value. That is, the *Planck* 160 μm beam FWHM values are not equal to those listed in Table 3.3. The reason for this is that the two terms in Eq. 3.8 are degenerate. Significant departures at 160 μm from the nominal 5′ Gaussian beam profile quoted by the *Planck* collaboration may be rooted in complexities in the IRAS 100 μm beam. This analysis tentatively suggests that this aspect of the *Planck* foreground dust model could be improved in the future.

Once we characterize the *Planck* effective beam window function by fitting Eq. 3.8, we proceed with Eq. 3.5 and Eq. 3.6 to obtain a combined *Herschel* and *Planck* 160 μm image. As stated above and further explained in Section 3.4.2, we adopt a value of $\kappa_{eff} = 40'$. Figure 3.7 shows the resulting image. For simplicity we will refer to images combined with our multi–scale method as *feathered images*. For comparison with previous work, we also generate a "combined image" that includes only the $(m, n) = 0$ *Planck* information, which is equivalent to applying a constant–offset to the *Herschel* image. We list the $(m, n) = 0$ values in Table 3.3. We refer to images processed in this fashion as *constant–offset images*. Figure 3.8 shows the difference between and ratio of the feathered image and the constant–offset image for HiGal–11 at 160 μm . The feathered image has more emission in the diffuse regions off of the Galactic plane, and the differences can exceed 40% over significant areas of the image. Contrary, the feathered image tends to show $\sim 10\%$ lower fluxes on the Galactic plane areas. The feathered and constant–offset images agree on compact objects. Furthermore,

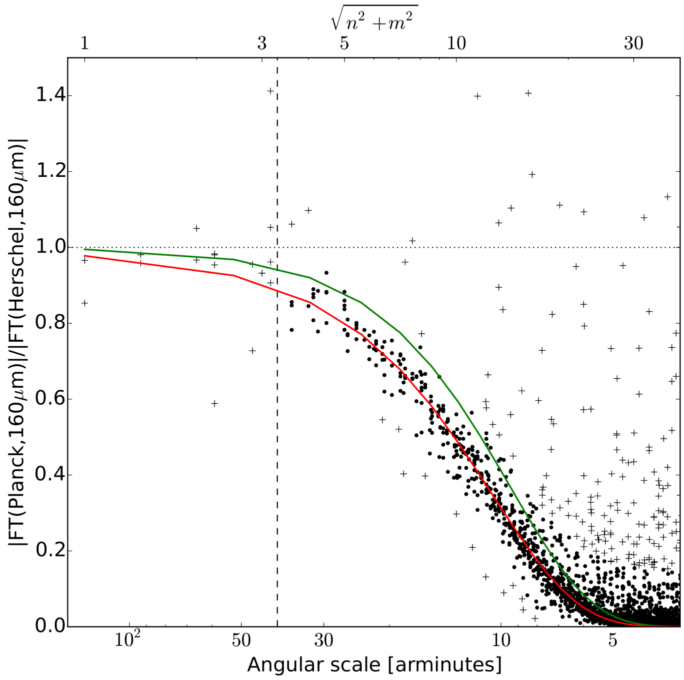

FIGURE 3.6: 160 μm HiGal–11 ratio of Fourier moduli as a function of angular scale (bottom) and Fourier mode radius (top). $\kappa_{eff} = 40'$ (see text) is indicated with a dashed vertical line. The red curve shows the best-fit to the filled circles and represents the effective beam transfer function for *Planck* ; that is, in the absence of calibration differences, if the *Planck* resolution were the same as that of *Herschel* the beam transfer function would be equal to unity (the dotted line). +-symbols indicate points that we exclude from the beam transfer function determination. The green curve illustrates the expected beam transfer function for a pure Gaussian with FWHM of 5′ as shown in Eq. 3.4, and clearly fails to characterize the observed behaviour.

these figures illustrate non–uniform and scale dependent nature of the signal in the *Planck* low–order modes. Note that the difference between the feathered and the constant–offset images should have a resolution on the order of $\kappa_{eff} = 40'$ (Fig. 3.8 left).

HiGal–11 at 250 μm , 350 μm , and 500 μm

Here we repeat the same procedure outlined above on the 250 μm , 350 μm , and 500 μm images. Because all three wavelengths exhibit very similar behavior we highlight the 250 μm example. We refer the reader to Table 3.3 for further details on the individual image parameters and effective beam transfer functions (Eq. 3.8) at each wavelength.

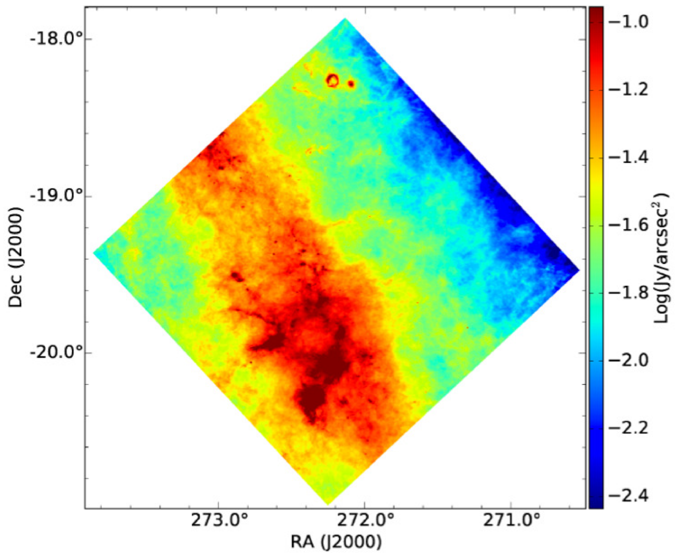

FIGURE 3.7: Combined 160 μm image of HiGal–11, shown on a log scale to highlight low emission regions at large scales where our method has the most impact.

Figure 3.9 shows our analysis of the 250 μm HiGal–11 image. The behaviour at 250 μm is very similar to the 160 μm behaviour described in detail above. The only exception to this can be seen in the bottom right panel of Fig. 3.9, which shows that the 250 μm *Planck* model effective beam transfer function (red curve) is much more similar to the theoretical expectation (green curve) than at 160 μm . We speculate that the increasing agreement between the theoretical expectation for the beam transfer function and the measured one with wavelength may be tied to irregularities in the IRAS 100 μm data which are included in the *Planck* emission model. Overall, we find that the *Herschel* /SPIRE data are very well behaved as an ensemble and that our method is robust in this regime.

Figure 3.10 shows the feathered 250 μm image (top panel) and the difference between the feathered and the constant offset image (bottom panel). Again, we observe a similar behavior as that found at 160 μm . More large scale emission is recovered in the feathered image, and this emission is clearly a function of scale. That is, the constant background image over-emphasizes the Galactic plane. The flux level discrepancy between the two versions of the background treatment reaches the 40% level, similar to the 160 μm case.

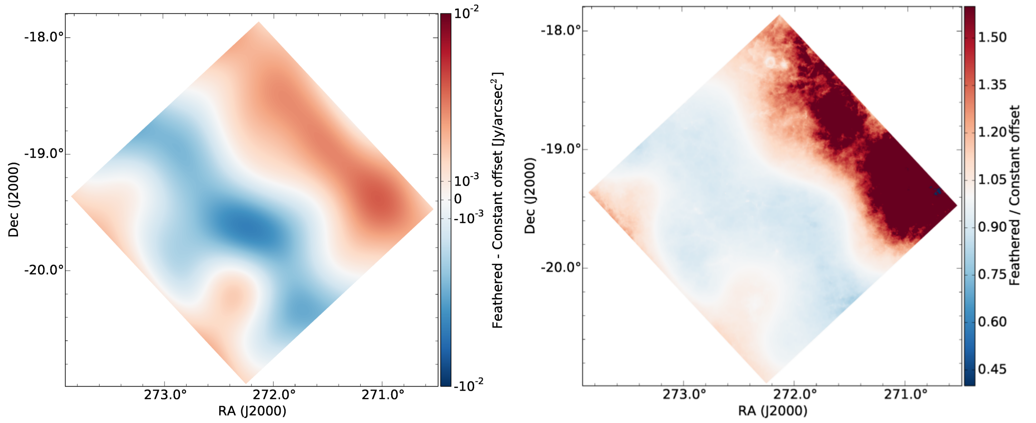

FIGURE 3.8: *Left:* Difference between the feathered image (our method) and the constant–offset image. *Right:* Ratio of the feathered image over the constant–offset image. The feathered image has more emission in the diffuse regions off of the Galactic plane, and the differences can exceed 40% over significant areas of the image. Furthermore, these figures illustrate non–uniform and scale dependent nature of the signal in the *Planck* low–order modes.

3.4.2 The bad: Perseus

With one very important exception, we find that this region of Perseus (covering NGC1333) behaves in a similar fashion as HiGal–11 (see Sect. 3.4.1). Inspection of the ratio of Fourier moduli shown in Fig. 3.11 immediately reveals that while the *Herschel* amplitudes behave well at $\sim$ small angular scales, they are too large compared to the *Planck* amplitudes at scales above $\sim 50'$. This behavior is clear at 160 μm and may be present at 250 μm while the two longest wavelengths apear to remain unaffected. That is, despite the very regular and theoretically expected behaviour of the effective beam transfer function (red curve in Figure 3.11 and Eq. 3.8) at scales below $\sim 40'$, the ratio of moduli exhibits a clear deficit on large scales at 160 μm . Given that the ratio obeys theoretical expectations on small scales, the probable culprit for this large-scale excess is the *Herschel* image reconstruction software. We note that if the *Planck* model image were to suffer from contamination of stochastically heated dust grain emission detected by IRAS at 100 μm , this would effectively drive the ratio to values > 1. Instead, here we find the opposite behavior, and only on the largest scales. In fact, we find no evidence for either excess emission in the *Planck* model in any of the regions we have investigated or evidence for a calibration mismatch between the flux scaling. We note that our adopted ($\kappa_{eff} = 40'$) is larger than the resolution of the the dust emisivity power-law index, β, maps (30′)

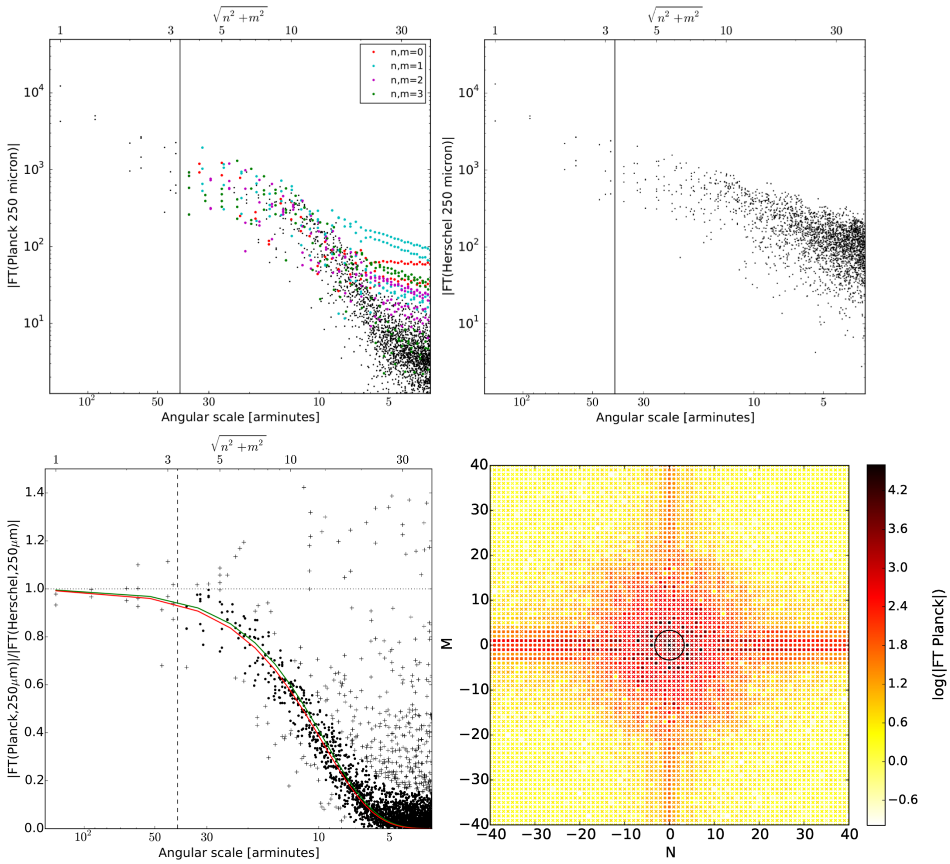

FIGURE 3.9: *Top Left:* 250 μm HiGal–11 *Planck* Fourier moduli as a function of angular scale (bottom abcissa) and Fourier mode radius (top abcissa). The lowest order modes, which are affected by the pixel regriding requirements, are highlighted with the indicated colors; the corresponding points are indicated in the bottom left panel as squares. The vertical line indicates $\kappa_{eff} = 40'$. *Top Right:* 250 μm HiGal–11 *Herschel* Fourier moduli. *Bottom Right:* Same as Figure 3.6 for the 250 μm HiGal–11. In contrast to the 160 μm behaviour the green curve, which illustrates the expected beam transfer function for a pure Gaussian with FWHM of $5'$, is similar to the best fit we obtain by fitting Eqn. 3.8, illustrated with the red curve. *Bottom Left:* Fourier moduli amplitude image. The pixels corresponding to low-order artifacts are shown as filled squares, which are highlighted in various colors in the top left panel. Similar to the 160 μm behaviour, these artifacts follow well–defined vertical and horizontal tracks and are caused by regriding the *Planck* model image to a much finer pixel scale. These artifacts do not propagate into the lowest order modes (the modes inside the indicated circle) and are excluded from the beam transfer function analysis (see text). The size of the circle indicates κ_{eff}, that is, the *Planck* Fourier modes that we use in the image combination.

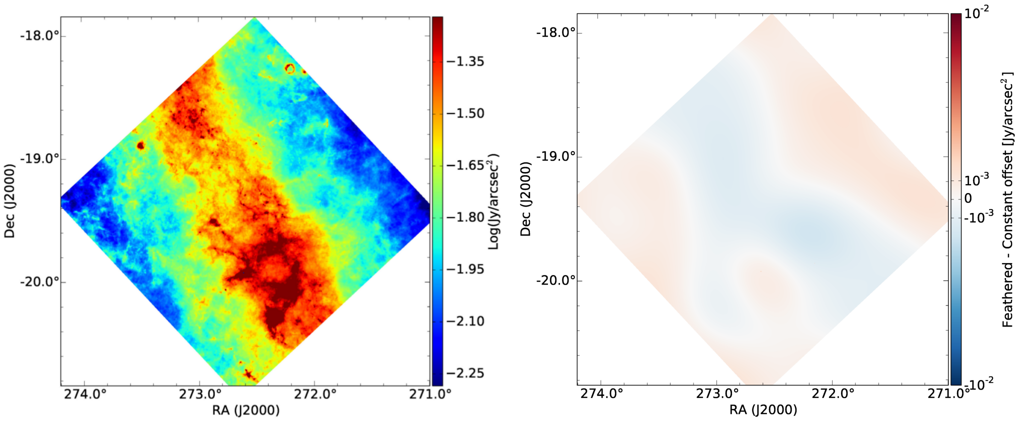

FIGURE 3.10: *Top:* Feathered 250 μm image of HiGal–11, shown on a log scale. *Bottom:* Difference between the feathered image (our method) and the constant–offset image.

adopted by the *Planck* dust emission model (see Sect. 4.2). We therefore do not expect to be biased by the worse resolution of this parameter compared to $T_{\rm obs}$ and τ_0.

Speculatively, the *Herschel* /PACS image reconstruction software may be introducing subtle but systematic large-scale power that may potentially be related to the noise properties of the particular image or the observing mode. Perhaps the most likely culprit is the fact that the observed area in this case contains significant emission at the map edges (see Fig. 3.12). It is well beyond the scope of this chapter to address possible problems in the *Herschel* /PACS reduction software. Instead, by construction and with our careful choice of $\kappa_{eff} = 40'$, our method simply removes these corrupted *Herschel* modes from the combined image and replaces them with those of *Planck* . Thus our choice of κ_{eff} is no choice at all: We are driven to choose the largest possible κ_{eff} by the requirement to not degrade the *Herschel* images with the noisier *Planck* data (see above). And we are constrained on the large scales by the requirement to exclude the *Herschel* power when it is corrupted.

3.4.3 The ugly: B68 region of the Pipe Nebula

Figure 3.13 shows the ratio of the 160 μm *Planck* -to-*Herschel* Fourier moduli. The ratios exhibit large scatter that we attribute to noise in the images. Furthermore, there is evidence for an excess in the *Herschel* amplitudes at large scales, as found in the case of the Perseus example shown above.

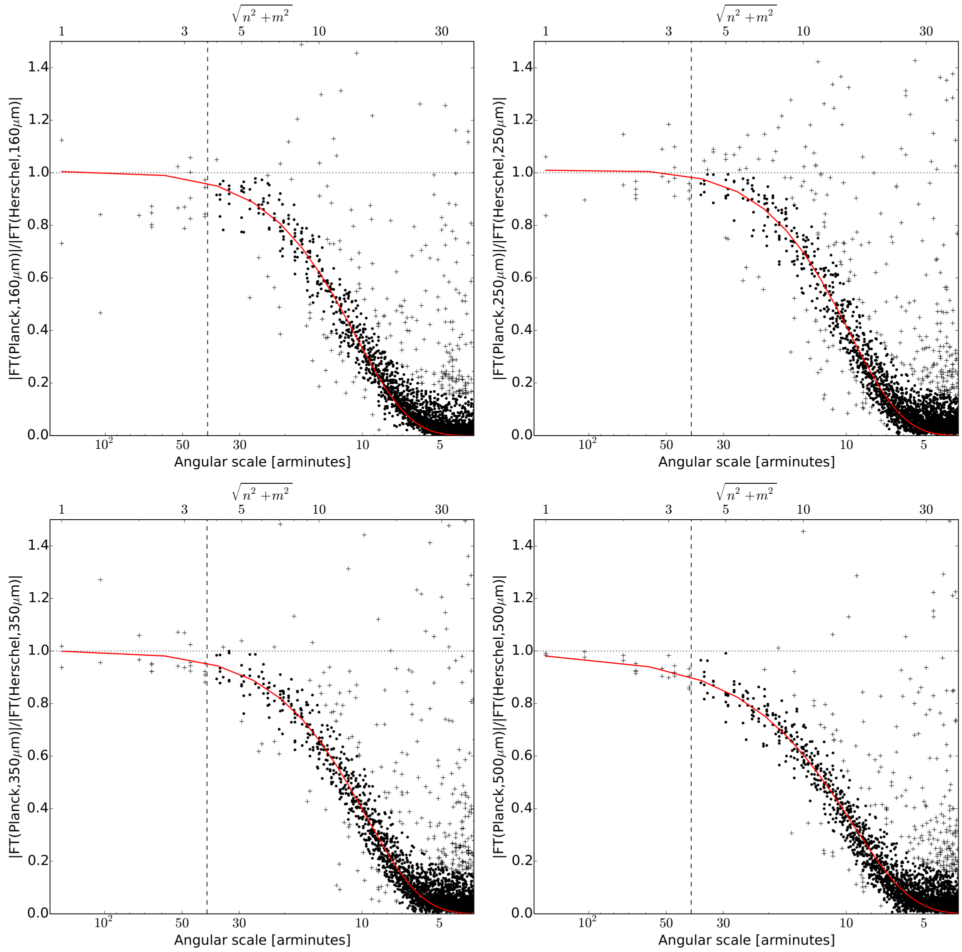

FIGURE 3.11: Same as Figure 3.6. Left → right: 160 μm → 500 μm ratio of *Planck* to *Herschel* Fourier moduli. The red curve indicated the effective beam transfer function obtained from fitting Eq. 3.8. The vertical dashed line indicates $\kappa_{eff} = 40'$ (see Eq. 3.6). The specific value of $\kappa_{eff} = 40'$ is imposed by the large angular scale ratio deficit at 160 μm (which may also be present at and 250 μm).

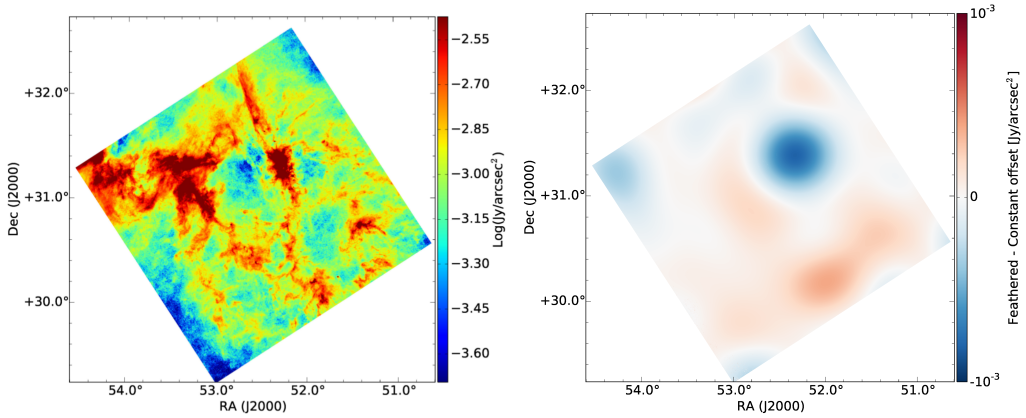

FIGURE 3.12: *Top:* Perseus 160 μm feathered image. *Bottom:* Difference between the feathered and the constant offset images.

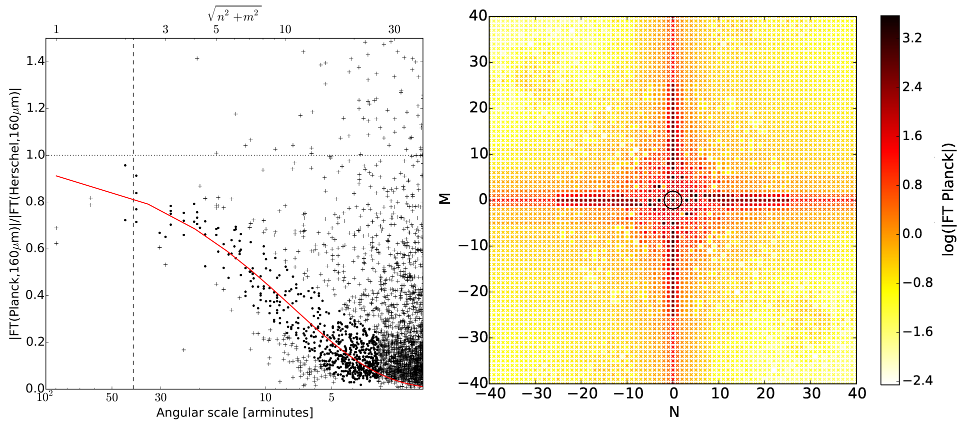

FIGURE 3.13: *Top:* Same as Fig. 3.6 for the B68 field at 160 μm . The ratio is dominated by noise-induced scatter, and thus a reliable fit to the Eq. 3.8 cannot be obtained (red curve illustrated the nominal fit the data). *Bottom: Planck* Fourier moduli amplitude plot; our adopted value of $\kappa_{eff} = 40'$ is illustrated with the black circle.

However, given the noise-induced inaccuracies in the determination of the *Planck* beam transfer function as well as the limitations imposed by the relatively small filed size (this is the smallest region we analyze in this chapter), we adopt the following approach. We simply apply the zero-mode correction to the 160 μm image.

The implications of the B68 case are important for future *Herschel* image reconstruction. Fundamentally, this method is both noise and field-size limited. As shown in Table 3.3, the 160 μm *Herschel* -to-*Planck* noise ratio is approaching unity for B68 and in fact B68 has the lowest ratio of the 160 μm fields considered here. As noted above, this ratio directly affects our ability to measure the *Planck* effective beam transfer function, and the same will be true in other regions. Second, small observed field sizes are not ideal; we cannot obtain accurate reconstructed (feathered) images in cases where the field size is of order $\sim 4\times\kappa$ or smaller because the artifacts in the *Planck* image become dominant over the signal in the modes of interest, that is, the largest *Planck* modes (see Fig. 3.13).

We emphasize the fact that we cannot correct what appears to be large-scale spurious power in the B68 *Herschel* image. Similar to the Perseus case, the B68 region also exhibits large scale power; however, due to the observed field size, the number of Fourier modes in this regime is small. Furthermore, inspection of Fig. 3.13) may tentatively indicate that this spurious power is even more prominent than in the Perseus case. This may indicate that the origin of this excess power is indeed rooted in the *Herschel* archive reduction software noise treatment. In light of our discovery, we therefore caution that low column density and low flux regions at large scales in the *Herschel* images of nearby low-mass (and thus low signal) regions are likely subject to systematic bias. In future applications of our method we will analyze each individual field to determine the quality of the *Planck* effective beam transfer function fit to decide if the data can be treated with a multi-scale approach or if we are limited to the less complete"scalar offset" method. We note that for the purposes of this chapter and the specific application to B68, we adopt the "scalar offset" method for all wavebands, as indicated in Table 3.3.

3.5 Column density and temperature maps: comparison between the feather method and the constant background method

In this section we compare our column density and temperature maps obtained with our "feathered" flux maps to those obtained with constant–offset corrected maps. We explain in Sect. 3.5.1 the procedure used to get the column density and temperature maps. We do the comparison for the regions HiGal–11 (Sect. 3.5.3) and Perseus (Sect. 3.5.4).

3.5.1 N(H) and temperature fitting: modified black-body fitting

We provide a brief summary here and refer the reader to Stutz and Kainulainen (2015) and Stutz et al. (2010a) for further details.

We convolve the feathered data to the beam of *Herschel* 500 μm (FWHM $\sim 36''$) using convolution kernels from Aniano et al. (2011). We then re–grid the data to a common coordinate system, using an $14''$ pixel scale. With the surface densities of the four wavelengths we obtain an SED for each pixel. We fit each pixel SED using an MBB function:

$$S_\nu = \Omega\, B_\nu(\nu, T_\mathrm{d})\,(1 - e^{-\tau(\nu)}), \tag{3.9}$$

where Ω is the beam solid angle, $B_\nu(T_\mathrm{d})$ is the *Planck* function at a dust temperature T_d, and $\tau(\nu)$ is the optical depth at frequency ν. We define the optical depth as $\tau(\nu) = N_\mathrm{H}\, m_\mathrm{H}\, R_{gd}^{-1}\, \kappa(\nu)$, where $N_\mathrm{H} = 2 \times N(\mathrm{H_2}) + N(\mathrm{H})$ is the total hydrogen column density, m_H the mass of the hydrogen atom, κ_ν the dust opacity, and R_{gd} the gas–to–dust ratio, assumed to be 110 (Sodroski et al., 1997). We use the dust opacities listed in the column 5 in Table 1 of Ossenkopf and Henning (1994b): dust grains with thin ice mantles after 10^5 years of coagulation time at an assumed gas density of 10^6 cm^{-3}. The systematic effects introduced when assuming a different dust model are discussed in Stutz et al. (2013) and Launhardt et al. (2013b). The choice of dust model, along with the adopted R_{gd} value, likely dominate the systematic uncertainties.

We use a two-step method for applying the color and beam size corrections to the pixel SEDs. We fit the uncorrected fluxes to obtain a first estimate of the temperature. We then use this temperature to apply the corrections as described in the SPIRE and PACS instrument handbooks. We then repeat the fit to the corrected SED.

3.5.2 Effects of the 160 μm in the MBB fit

Here we adopt a simple Monte Carlo (MC) analysis with the goal of assessing the effects of *(a)* noise, *(b)* the filter bandpass, and *(c)* the exclusion of 160 μm on the derivation of temperature and column densities. We generate a set of idealized MBB spectra over a range of temperatures (from 10 K to 44 K), at fixed N(H) $= 5\times10^{21}$ cm^{-2}, adopting the Ossenkopf and

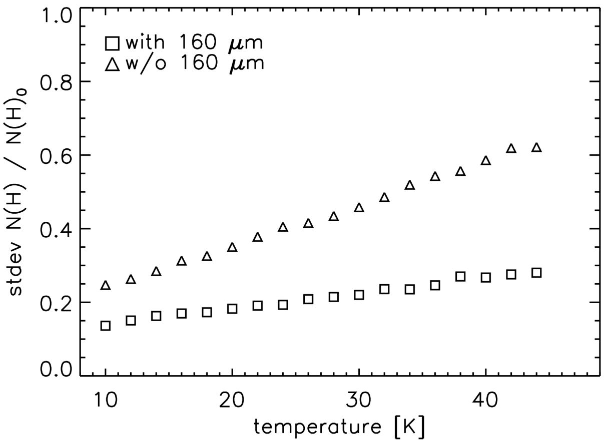

FIGURE 3.14: Fractional error in the best-fit N(H) value as a function of temperature for a fiducial N(H) value of 5×10^{21} cm^{-2}. Squares indicate the Monte Carlo results including 160 μm data while triangles indicate results including only the three SPIRE wavelengths.

Henning (1994b) dust model with β = 1.8. After integrating these models over the *Herschel* filter bandpasses, we run 2000 realizations of these SEDs with a Gaussian noise of fractional error 10%, matching the reported *Herschel* noise levels. Figure 3.14 shows the resulting scatter in the best-fit N(H) values, which depend on the model input temperature. Figure 3.15 shows the scatter in the best-fit temperature values. While the best-fit temperature error increases dramatically with the exclusion of the 160 μm data, the N(H) errors are well behaved but inflated relative to the run including the 160 μm data: for temperatures below 20 K, the fractional N(H) error is < 40% and < 20% when we exclude or include the 160 um data,respectively. Figure 3.16 shows the N(H) error as a function of N(H) and input model temperature. Both trials with and without the 160 μm recover the underlying N(H) values to within ~40% below ~30 K.

N(H) results both with and without 160 μm data show systematic offsets and a temperature dependence on the errors, as expected. However, including the 160 μm better reflects the input N(H) values for all temperatures. Even though the high temperature points are in the Rayleigh—Jeans limit, the exclusion of the 160 μm systematically biases the N(H) values upwards (Pokhrel et al., 2016; Zari et al., 2016). Below ~20 K the results between including and not including the 160 μm yield similar N(H) values. Nevertheless, these results highlight that 160 μm data should be included

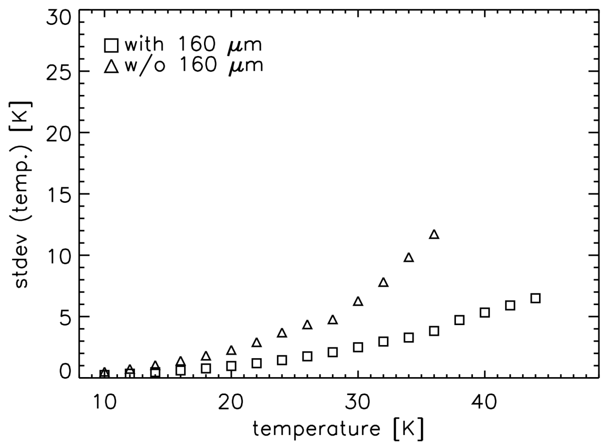

FIGURE 3.15: Same as Fig. 3.14, showing the error on the best fit temperature.

when possible. However, when 160 μm data data are unavailable or unsuitable, the magnitude of the error on N(H) decreases with temperature, and is arguably irrelevant below $\sim 30\,\mathrm{K}$ given the absolute error budget on the column densities (see e.g., Launhardt et al., 2013b). We note that these tests yield approximate estimates of the effect of excluding the 160 μm data because here we do not include uncertainties associated with e.g., color corrections and a more realistic noise model.

3.5.3 HiGal–11

We have shown in Sect. 3.4.1 and Sect. 3.4.2 that the *Herschel* data corrected with a constant–offset tend to underestimate the fluxes in diffuse regions compare to our flux "feathered" maps, while both agree well in regions with strong emission. These results are general for the four *Herschel* wavelengths, being specially important at 160 μm and 250 μm . With these results we would expect the column densities of the diffuse regions to be overestimated by *Herschel* , and therefore the temperatures to be underestimated. This is exactly what we find in the HiGal–11 field, as it is shown in Fig. 3.17 and Fig. 3.18. In strong emitting (i.e. dense) regions we see agreement in both, column density and temperature maps, as shown with the white regions in the ratio map, the similar high column density tails of the histograms, and the surface density points follow the identity at large column

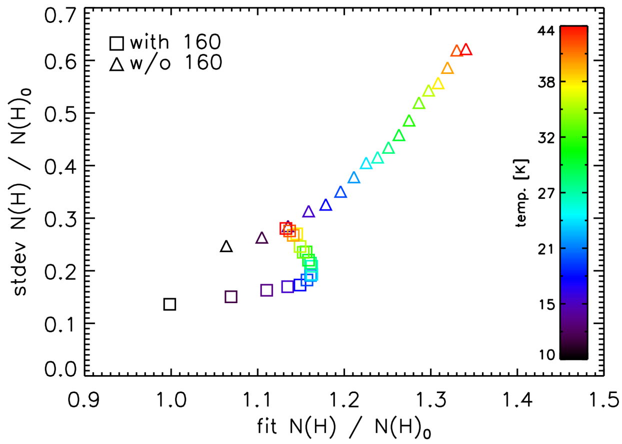

FIGURE 3.16: Fractional N(H) errors versus fractional systematic offset in the best fit N(H) values. Color indicates the input temperature. Symbols are the same as Fig. 3.15 and Fig. 3.16.

densities (and temperatures). The constant–offset maps do not measure column densities lower than $10^{22}\,\mathrm{cm}^{-2}$. The inverse effect is seeing in temperatures: the constant–offset temperatures below 20 K tend to be significantly lower than our "feathered" temperatures (see Fig. 3.18).

The map regions with discrepancies larger than the 30% between both methods fill the 15% of the region. This result highlights the importance of a proper treatment of the *Herschel* data, specially in diffuse regions, since the column densities are directly related with the mass of the dust, and therefore total mass of the molecular clouds observed, intimately linked to physical parameters as the gravitational potential.

3.5.4 Perseus

The "feathered" and constant–offset maps of Perseus, for column density and temperature, are similar in strong FIR emitting regions (see Fig. 3.19 and Fig. 3.20). In contrast with the case of the HiGal–11, there is not a clear difference between column densities at temperatures at the very low regimes. However, the latter shows a big scatter between two maps as seen in the surface density plot of Fig. 3.20. The temperature difference map shows that in general, the constant–offset and "feathered" temperatures agree within 2 K in Perseus. The differences in column densities are concentrated on the gas surrounding the NGC 1333 region. These differences account for more than 30% at intermediate ($10^{22}\,\mathrm{cm}^{-2}$) column densities.

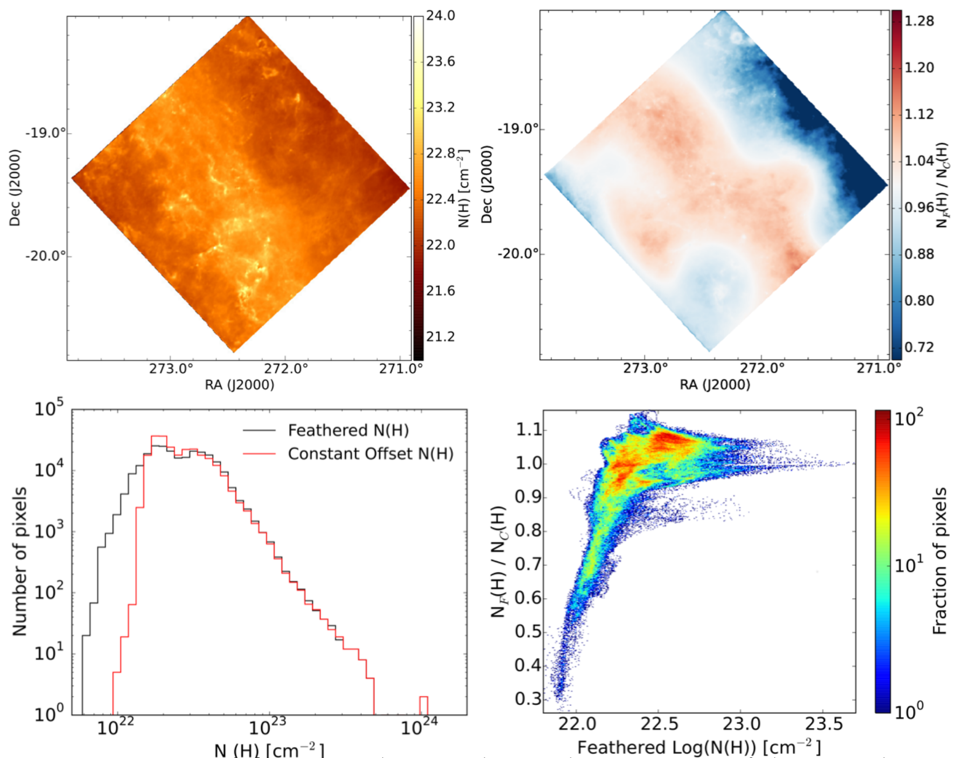

FIGURE 3.17: *Top left:* Logarithmic column density map of the HiGal–11 obtained with our method. *Top right:* Ratio of our "feathered" and the constant–offset column density maps. *Bottom left: Histograms of the "feathered" (black) and the constant–offset (red) column density maps. Bottom right:* Ratio of "feathered" and constant–offset corrected column densities $N_F(H)/N_C(H)$ function of the "feathered" column density.

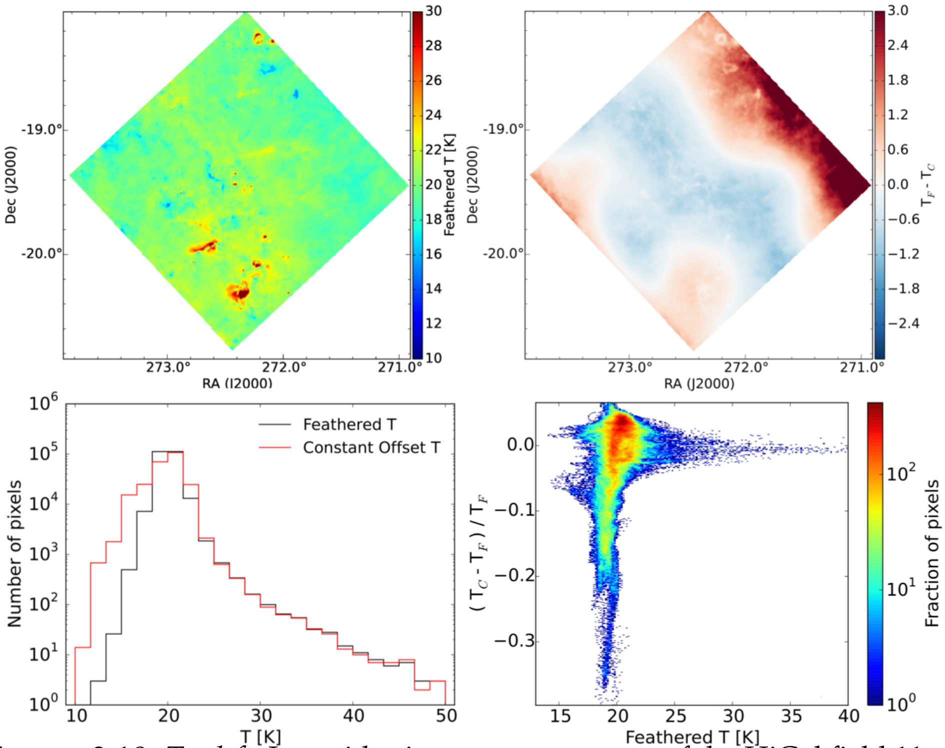

FIGURE 3.18: *Top left:* Logarithmic temperature map of the HiGal field 11 obtained with our method. *Top right:* Ratio of our "feathered" and the constant–offset temperature maps. *Bottom left: Histograms of the "feathered" (black) and the constant–offset (red) temperature maps. Bottom right:* Residuals, $T_C - T_F/T_F$, of the "feathered" and constant–offset temperature maps as function of the "feathered" temperature.

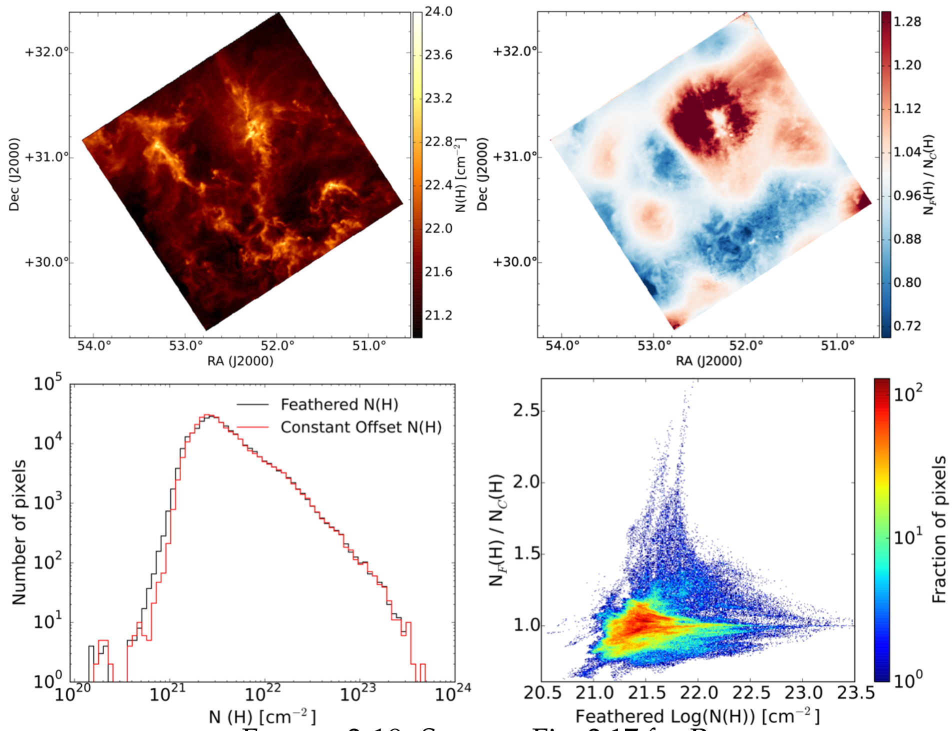

FIGURE 3.19: Same as Fig. 3.17 for Perseus.

As in HiGal–11, we note the importance of a proper treatment of the column density data. Note the amount of mass that the constant offset corrections miss in the surrounding area of NGC 1333, leading to total mass underestimates of the region, biasing the determination of physical parameters on it.

3.6 Conclusions

At a given wavelength, *Planck* and *Herschel* provide independent estimators of an image at all scales. Here we present a multi-scale method that maximizes the relative Fourier information in the *Planck* and *Herschel* images to produce combined total-power emission maps at 160 μm , 250 μm , 350 μm , and 500 μm . These combined maps, which we refer to as "feathered images" are then post-processed into column density and temperature maps. We apply our method to three fields that span a range of noise properties, field sizes, and Galactic environments. We compare both our feathered flux maps and resulting N(H) and T maps to previous methods and conclude the following.

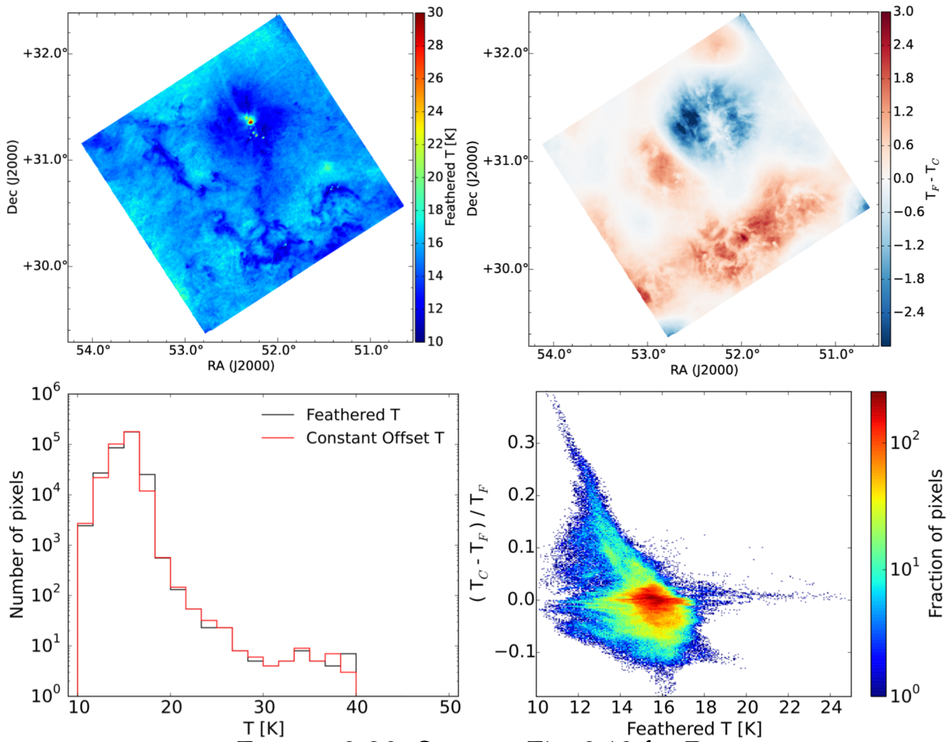

FIGURE 3.20: Same as Fig. 3.18 for Perseus.

3.6.1 Image fathering

The previous approach to this problem can be summarized as follows: it applies a constant–offset correction to the entire image at a given location on the sky through the comparison of the mean flux levels in the *Planck* model versus *Herschel* observations. This method is mathematically identical to including only the (0,0) Fourier modes of *Planck* in the *Herschel* image. Here we develop a method such that the scale dependence of the *Planck* correction can be quantified and included in the *Herschel* maps. We find that

1 The *Planck* corrections are indeed scale dependent. That is, the (0,0) Fourier modes do not fully capture the behaviour of the missing *Herschel* emission on large scales.

2 We measure the effective *Planck* beam transfer function for each image in order to deconvolve the *Planck* data before combining it with *Herschel* . We find that the effective *Planck* beam transfer function never matches a 5′ Gaussian function; at 160 μm the departures can be significant. In general, as the wavelength increases so does the agreement with the nominal 5′ Gaussian beam quoted for the *Planck* model.

3 Noise must be analyzed on a case-by-case basis to understand the scale at which the *Planck* and *Herschel* data should be combined. We adopt one well-motivated effective scale for combining the images. However, we allow for departures from this generic choice in specially noisy cases.

4 Elevated image noise inhibits our ability to measure an accurate beam transfer function.

5 The fact that the deconvolved *Planck* foreground emission model images are generically noisier than the *Herschel* observations drives us to adopt a large angular scale (κ_{eff}) for combining the two image estimators.

6 No generic set of weights can be determined independently for the problem of combining images. We adopt hyperbolic tangent weights for the cases where the effective *Planck* beam can be measured reliably. For cases that are either too noisy or the field size is too small, we apply only the zero-mode Fourier corrections.

7 Alarmingly, we discover evidence for a large angular scale ($\theta > 40'$) excess of power in the *Herschel* images of Perseus and the B68 region of the Pipe Nebula. In the case of Perseus our method corrects this spurious emission. In the case of B68 at 160 μm the observations are too noisy to fully correct this. Tentatively, the presence of the large-scale excess of *Herschel* flux appears related to the overall signal-to-noise in a given observation and thus may be related to the noise treatment in the *Herschel* reduction and image reconstruction software. We find no evidence for such an excess in the galactic plane region near $l = 11\,\mathrm{deg}$ (the HiGal–11 field).

We apply this method to the specific case of *Planck* and *Herschel* , but it can of course be generically applied to any combination of image estimators containing radically different angular resolutions. The two most critical assessments to be made when applying this technique is a relative noise estimate and a measurement of the effective beam transfer function of the images to be combined.

3.6.2 Column density and temperatures

In the HiGal–11, our “feathered” column densities exhibit higher (lower) N(H) values in (out of) the Galactic plane region, compared to the “constant–offset” method. In general, a similar effect is seen in Perseus in the areas surrounding NGC 1333, which also exhibits higher N(H) values compared to previous methods. We show that N(H) values calculated based on the "constant–offset" method can be discrepant by factors of $\sim 50\%$ or more, but typically span variations of $\sim 30\%$ over significant portions of the images.

In general, our "feathered" column densities recover more low column material, and the discrepancies with the previous method are most significant at the lower end of the column density distribution, near N(H) $\sim 10^{22}$ cm^{-2}. Above this value, we find generally acceptable agreement with previous methods. As most molecular cloud mass resides at low N(H) values,a proper treatment of the column densities and temperatures is needed to better constrain fundamental physical parameters such as the gravitational potential.

Chapter 4

A sample of giant molecular filaments

Adapted from: Abreu-Vicente, J., Ragan, S., Kainulainen, J., Henning, Th., Beuther, H., Johnston, K., (2016) Astronomy & Astrophysics, Volume 590, id.A131.

In Chapter A.6 we present a statistical study of molecular cloud structure in the Galactic plane. In Chapter 3 we present a technique that will improve the observational assets obtained in Chapter A.6. In this Chapter we perform a census of molecular clouds that contain large ($L > 50$ pc) filamentary structures, that are known to be the dominant structures in dense regions of molecular clouds and be intimately connected to the immediate sites of star formation (Sect. 1.3). The length and location of these giant molecular filaments (GMFs) make them outstanding objects to study the connection of the molecular cloud structure and star formation to the Galactic environment. In this chapter we present a census GMFs, estimate their properties, and study their locations relative to the Galactic structure.

4.1 Introduction

Filaments are omnipresent in molecular clouds, no matter whether these clouds are quiescent or harbor star-forming activity (e.g., Molinari et al., 2014b). Understanding the physical origin and evolution of filaments is therefore needed to explain the whole process of star formation.

The discovery of "Nessie" (Jackson et al., 2010; Goodman et al., 2014), an 80 pc long filament associated with the Scutum-Centaurus spiral arm, has initiated the study of a family of giant molecular filaments (GMFs) in the Milky Way (see Sect. 1.3). After this discovery, a series of works have searched for other GMFs in the MW (Ragan et al., 2014; Wang et al., 2015;

Zucker, Battersby, and Goodman, 2015). These works have revealed other ≈ 20 GMFs that are located in spiral– and inter– arm regions of the Galactic plane (see Sect. 1.3). Owing to the relatively low number of known GMFs and uncertainties in the Galactic models, the relation of GMFs to the Galactic structure remains an open question. Extending the census of GMFs to other quadrants is key to obtain a Galaxy-wide piture of the physical properties of the GMFs.

One key problem in identifying GMFs is that column density data (extinction or emission) alone are not sufficient; spectral line data are needed to ascertain that the structure has a continuous velocity pattern (and hence is likely a continuous object in three dimensions). In short, the extinction patterns must be connected by a molecular gas tracer, usually ^{13}CO, and exhibit velocity coherence (i.e., the velocities of the filaments must have no steep jumps, but rather show continuous velocity gradients, if any). The requirement of having ^{13}CO data greatly hampers building a systematic census of GMFs: an unbiased ^{13}CO survey exists only for the first Galactic quadrant (Jackson et al., 2006, Galactic Ring Survey, GRS hereafter). The GRS covered the region $17^{\circ} \leq l \leq 55^{\circ}$ and $b \leq |1^{\circ}|$. The recent three-mm Ultimate Mopra Milky Way Survey (Barnes et al., 2011; Barnes et al., 2014, ThruMMS)[1] presents a good opportunity to trace molecular cloud dynamics in the fourth Galactic quadrant. This ongoing survey covers the fourth quadrant in ^{12}CO, ^{13}CO, C^{18}O, and CN.

In this chapter, we extend the current census of GMFs to the fourth Galactic quadrant. We identify the GMFs as NIR/MIR extinction features that are connected structures in ^{13}CO data as probed by the ThruMMS survey. We present a sample of nine newly identified GMFs and their physical properties. We place the results in the Galactic context with the help of models of the spiral-arm pattern of the Galaxy. Finally, we compare the different filament-finding methods to better understand their limitations and complementarity with each others.

[1]http://www.astro.ufl.edu/ peterb/research/thrumms/

4.2 Data and methods

4.2.1 ^{12}CO and ^{13}CO data

We use the ^{13}CO(J=1–0) observations of the ThrUMMS survey DR3 (Barnes et al., 2011; Barnes et al., 2014) to test the velocity coherence of the filament candidates. We also use the data to estimate the distance to the GMFs and to obtain their total masses. This ongoing survey is observing the fourth Galactic quadrant at latitudes $|b| < 1\,\mathrm{deg}$ in ^{12}CO, ^{13}CO, C^{18}O and CN with an angular resolution of $72''$ and an approximate rms of 1.5 K km/s. ThruMMS offers full spectral coverage of the ^{13}CO line at a spectral resolution $\sim 0.3\,\mathrm{km/s}$. The observations of ^{12}CO and ^{13}CO are mostly complete at $|b| < 0.5°$. However, less than 25% is complete at Galactic latitudes $|b| > 0.5°$.

4.2.2 Dust continuum at $870\,\mu\mathrm{m}$ as a dense gas tracer

We employ the ATLASGAL survey (Schuller et al., 2009b; Csengeri et al., 2014b) to trace the dense gas component of the GMFs. This survey observed cold dust emission in a large area ($-80° \leq l \leq 60°$) of the Galactic plane at $870\,\mu$m, with a FWHM of 19.2$''$ and a $rms \sim 50\,$mJy/beam. Although dust emission at sub-mm wavelengths does not generally trace only dense gas, ATLASGAL filters out large scale (2.5$'$) emission, thus making the observations specially sensitive to the densest gas component, generally located in the cold interior of molecular clouds.

4.2.3 Velocity data for the dense gas tracer

Unfortunately, with only ATLASGAL data, we cannot know whether the emission arises from a GMF or from a different point along the line-of-sight. We need extra spectral information. We employ several catalogs of star formation signposts to confirm that the dense gas is associated with the GMF. We search for counterparts of these catalogs with ATLASGAL clumps and compare the velocity of the sources with those of the GMFs.

We use the sources with radio recombination line counterparts in the WISE catalog of H II regions (Anderson et al., 2014), the Red MSX Survey (Lumsden et al., 2013b, RMS), and the catalogs of NH_3 (Purcell et al., 2012) and clumps H_2O masers (Walsh et al., 2011) of the HOPS survey.

In addition, we use a series of follow-up studies of the ATLASGAL survey: the catalogs of CO depletion and isotopic ratios (Giannetti et al., 2014), methanol massers (Urquhart et al., 2013a), and massive star-forming clumps (Urquhart et al., 2014). Further, we use the the catalog of dense clumps from the MALT90 survey (Foster et al., 2011; Foster et al., 2013; Jackson et al., 2013). We list the dense gas tracers associated to the GMFs in Table B.3.

4.2.4 Identifying giant molecular filaments

We identify the filament candidates following the same procedure as in R14. The first step is to identify filamentary extinction features by-eye at MIR and NIR wavelengths in the Galactic plane (see Fig. 4.1 and Appendix B). In this step, we use available data from GLIMPSE (Benjamin et al., 2003) and 2MASS (Skrutskie et al., 2006) surveys[2], representing wide, unbiased and continuous coverage of the Galactic plane at MIR and NIR wavelengths.

A group of 5 coauthors inspected the data by eye searching for the extinction features. The GMF candidates must satisfy two conditions: *1)* the extinction features must have a projected length of $\gtrsim 1^{\circ}$, and *2)* the group members, in pairs of two persons, must independently confirm the extinction feature as a filament-like structure. Massive episodes of star-formation can disrupt filaments, so we allow for gaps in the extinction structures if signs of massive star-formation are present (e.g., H II regions). We note that the photodissociation regions surrounding H II regions have strong PAH emission. As a result, NIR extinction features may coincide with emission at MIR wavelengths (e.g, 8 μm) if there are H II regions or strong radiation sources nearby (Draine, 2011a). Following this procedure, we find 12 GMF candidates within the fourth Galactic quadrant. The candidates are listed in Table 4.1. In the next section, we explore whether the GMF candidates are physically connected using line emission data.

4.2.5 Velocity coherence of the candidates

To avoid projection effects caused by physically unrelated molecular clouds along the line-of-sight, we only consider the candidates listed in Table 4.1 as GMFs once it is confirmed that they are velocity coherent structures. Very

[2]Both surveys can be visualized in web interfaces at: *http://www.alienearths.org/glimpse/* and *http://aladin.u-strasbg.fr/AladinLite/*

TABLE 4.1: Filament candidates in the fourth Galactic quadrant.

Candidate ID	$l_{\rm ini}$ [°]	$l_{\rm end}$ [°]	$b_{\rm ini}$ [°]	$b_{\rm end}$ [°]
F358.9-357.4	358.9	357.4	-0.4	-0.4
F354.7-349.7[a]	354.7	349.7	0.4	0.5
F343.2-341.7	343.2	341.7	0.0	0.4
F341.9-337.1	341.9	337.1	-0.2	-0.4
F335.6-333.6	335.6	333.6	-0.2	0.4
F329.3-326.5 [a]	329.3	326.5	-0.3	0.0
F329.4-327.1 [b]	329.4	327.1	-0.3	1.4
F326.7-325.8 [b]	326.7	325.8	0.9	-0.2
F324.5-321.4	324.5	321.4	-0.5	0.1
F319.0-318.7	319.0	318.7	-0.1	-0.8
F309.5-308.7	309.5	308.7	-0.7	0.6
F307.2-305.4	307.2	305.4	-0.3	0.8

a) These filament candidates have not been confirmed as GMFs because they are not velocity coherent. **b)** There is only ThruMMS coverage for the part of the filament.

long filaments are likely to show velocity gradients due to the differential rotation of the Galaxy. These gradients depend on the location of the filament in the Galaxy. For this reason, we do not restrict the velocity range of the filament candidates, but rather require them to show continuous velocity variations, without steep jumps. The filaments satisfying this requirement are considered velocity coherent.

We test the velocity coherence of the candidates using ^{13}CO observations of the ThrUMMS survey (see Sect. 4.2.1). We create position-velocity (PV) diagrams for each GMF candidate integrating the full spectral coverage collapsed over the whole latitude axis. In this step, we used the function `sum` of `python`. In the cases in which the PV diagrams show a series of different PV-components, we create ^{13}CO integrated intensity maps for each component. We then compare the extinction features with the ^{13}CO integrated intensity maps. If they represent a single ^{13}CO structure, then the filament candidates are labeled GMFs.

The following candidates are eliminated because their extinction features have no single coherent ^{13}CO velocity component: F354.7-349.7 and F329.3-326.5. The candidates F329.4-327.1 and F326.7-325.8 could not be confirmed because of the lack of proper coverage in the ThrUMMS data.

The remaining nine candidates were classified as GMFs.

The spiral arms are seen as seen as a single ^{13}CO component with a wide-velocity range in the PV diagrams (see Fig. 4.1 and Appendix B). If our GMFs lie inside spiral arms, then it is possible that we are integrating over the full spiral arm, thus overestimating the velocity range of the GMF. We do a fine tuning of the velocity range of the GMFs. We created position-velocity (PV) diagrams over a line following the identified extinction features for each candidate. This process can be done with the `python` tool, `Glue`[3]. These PV diagrams are shown in the bottom panels of Fig. 4.1–B.8. We also show in Table B.2 the l–b–v tracks of each filament.

4.2.6 Biases in the extinction-based filament finding method

We acknowledge that this method is necessarily subjective. We make an effort to reduce the subjectivity by requiring that at least three group members agree with the filament identification. In addition, some GMFs that could have been potentially identified may have been missed by our search approach.

Our filament finding method is biased towards the identification of quiescent structures (R14). Even though we allow for gaps in filaments if they carry signs of massive star formation, such violent episodes can disrupt molecular clouds, making them difficult (if not impossible) to be identified as GMFs.

The observation of extinction features against NIR and MIR background requires intense background emission to have enough contrast to identify extinction features. This is true at low Galactic latitudes, where the star density is high, but it is not the case at high latitudes. In general, this is not a severe issue in this work since we target specifically the Galactic plane. However, the region $325° < l < 320°$ shows low background emission at MIR wavelengths. The identification of extinction features in this region is therefore more difficult due to the lack of contrast between the background and the dense foreground structures.

[3]http://www.glueviz.org/

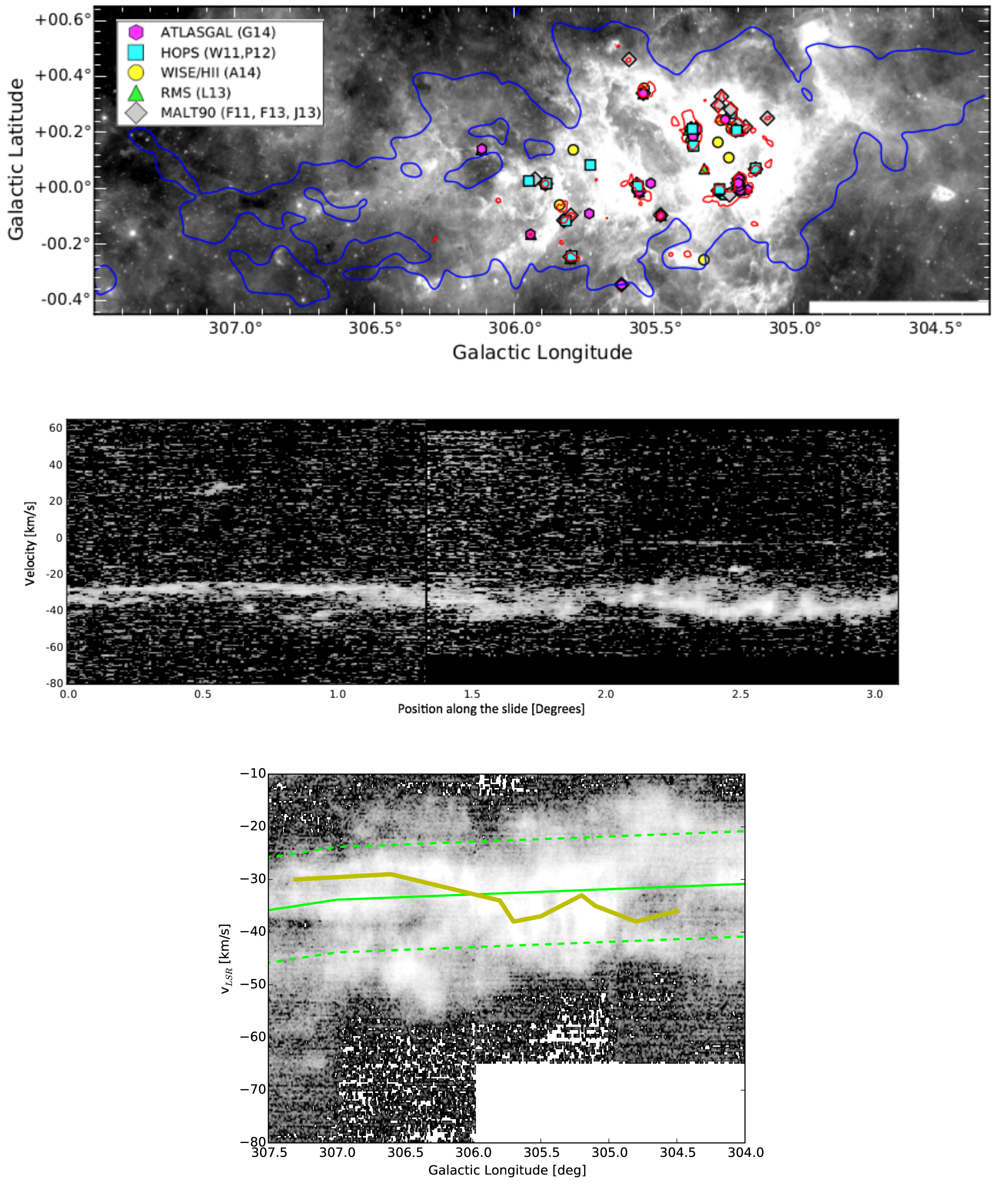

FIGURE 4.1: *Top:* Grayscale GLIMPSE 8 μm image of the GMF 307.2-305.4. The blue contours show the ^{13}CO integrated intensity of 2 K /km/s, integrated over the velocity range [-45,-25] km/s. The red contours show the ATLASGAL emission at a contour level of $F_{870\,\mu\mathrm{m}} = 250$ mJy/beam. The filled geometric objects show all the dense gas measurements from different surveys with v_{LSR} within the velocity range indicated in Table 4.2. Gray diamonds show MALT90 (Foster et al., 2011; Foster et al., 2013; Jackson et al., 2013) survey measurements, yellow circles belong to the spectral catalog of H II regions in the WISE survey (Anderson et al., 2014), The RMS survey (Lumsden et al., 2013b) is represented by green triangles, the cyan squares show NH_3 clumps from HOPS survey (Purcell et al., 2012), and the pink hexagons show spectral follow-ups of the ATLASGAL survey (Giannetti et al., 2014; Urquhart et al., 2013a; Urquhart et al., 2014). *Middle:* Position-velocity diagram of the ^{13}CO line of the GMF 307.2-305.4, obtained from a slice following the extinction feature (black line in top panel) used to identify GMF 307.2-305.4. *Bottom:* PV diagram of the ^{12}CO emission between $|b| \leq 1°$. The yellow line shows GMF 307.2-305.4 in the PV space. The green solid line shows the Scutum-Centaurus arm as predicted by Reid et al. (2014) and the dashed green lines show ± 10 km/s of the velocity of the spiral arm.

4.2.7 Estimating the total and dense molecular gas masses

4.2.8 Total molecular gas mass

To calculate the total gas mass of the filaments, we first obtain the column densities of ^{13}CO. We do so following a standard scheme in which the kinetic temperature of the ^{13}CO, $T_{^{13}\mathrm{CO}}$, is assumed to be the same as that of ^{12}CO, and equal to the kinetic temperature, T_k (e.g., Rohlfs and Wilson, 2004). We obtain T_k from the brightness temperature of the optically thick line ^{12}CO, $T_{\mathrm{B},^{12}\mathrm{CO}}$,

$$T_\mathrm{k} = \frac{5.5}{\ln(1 + \frac{5.5}{T_{\mathrm{B},^{12}\mathrm{CO}}+0.82})}, \tag{4.1}$$

with $T_{\mathrm{B},^{12}\mathrm{CO}}$ obtained from the peak of the ^{12}CO emission. The optical depth of the ^{13}CO line, $\tau_{^{13}\mathrm{CO}}$, is obtained via

$$\tau_{^{13}\mathrm{CO}} = -\ln\left[1 - \frac{T_{^{13}\mathrm{CO}}/5.3}{(e^{\frac{5.3}{T_\mathrm{k}}} - 1)^{-1} - 0.16}\right]. \tag{4.2}$$

We integrate the ^{13}CO spectra with peaks over $1.5\,\mathrm{K}$[4] to obtain the total column density of ^{13}CO

$$N_{^{13}\mathrm{CO}} = 3.0 \times 10^{14}\frac{T_\mathrm{k}e^{\frac{5.3}{T_\mathrm{k}}}\int \tau_{^{13}\mathrm{CO}}(\nu)\mathrm{d}\nu}{1 - e^{\frac{-5.3}{T_\mathrm{k}}}}. \tag{4.3}$$

For consistency with R14, we convert $N_{^{13}\mathrm{CO}}$ into ^{12}CO column densities, $N_{^{12}\mathrm{CO}}$, using a ^{12}CO/^{13}CO ratio that varies with galactocentric distance following the linear relation $^{12}\mathrm{CO}/^{13}\mathrm{CO} = 5.41R_\mathrm{gal}[\mathrm{kpc}] + 19.3$ (Milam et al., 2005). The galactocentric distances of the filaments are listed in Table. 4.2. Finally, the ^{12}CO column densities are converted into column densities of molecular gas following: $N_{^{12}\mathrm{CO}}/N(\mathrm{H}_2) = 1.1 \times 10^{-4}$ (Pineda et al., 2010). We find that ^{13}CO integrated intensities of 1.5 K / km/s correspond to $N(\mathrm{H}_2) \sim 1.3 \times 10^{21}\,\mathrm{cm}^{-2}$.

Finally, we obtain the total molecular gas mass of the GMFs via

$$M_\mathrm{total} = N_{^{13}\mathrm{CO}}m_{\mathrm{H}_2}N_\mathrm{pix}A_\mathrm{pix}d^2, \tag{4.4}$$

[4] This value represents the rms of the ^{13}CO spectra.

where m_{H_2} is the mass of the molecular hydrogen, N_{pix} and A_{pix} the number and area of the pixels inside the GMF respectively, and d the distance to the GMF (See Sect. 4.3.2).

4.2.9 Dense gas mass

We used the ATLASGAL data to estimate the dense gas mass of the GMFs. We required the ATLASGAL emission to be detected at 5σ (250 mJy/beam) for consistency with R14. This emission is equivalent to $N(\mathrm{H}_2) = 7 \times 10^{21}\,\mathrm{cm}^{-2}$. We estimate the dense gas mass of each GMF via

$$M_{\mathrm{dense}} = \frac{Rd^2 F_{870\mu\mathrm{m}}}{B_{870\mu\mathrm{m}}(T_{dust})\kappa}, \tag{4.5}$$

where $F_{870\mu\mathrm{m}}$ is the ATLASGAL flux, d is the distance to the filament, and $B_{870\mu\mathrm{m}}(T_{\mathrm{dust}})$ is the blackbody radiation at 870 μm as a function of temperature, T_{dust}, which we assume $T_{\mathrm{dust}} = 20\,\mathrm{K}$. $R = 150$ is the gas-to-dust ratio (Draine, 2011a). We used a dust absorption coefficient $\kappa = 1.42\,\mathrm{cm}^2\mathrm{g}^{-1}$ at $870\,\mu\mathrm{m}$, extrapolated from the dust model of Ossenkopf and Henning (1994b) for dust grains with thin ice mantles and a mean density of $n \sim 10^5\,\mathrm{cm}^{-3}$.

It is possible that the ATLASGAL emission along the line-of-sight of a filament is not related to the GMF, but rather with molecular clouds at different distances. To avoid this line-of-sight confusion we use spectral information of the star-forming signposts introduced in Sect. 4.2.3. If any of these signposts is associated to an ATLASGAL clump in projection and its v_{LSR}[5] lies inside the velocity range of the GMF, then we assume that this ATLASGAL clump is part of the GMF. If we found no star-forming signposts in an ATLASGAL clump, we also assume it to be part of the GMF. If the v_{LSR} of the signposts associated with ATLASGAL emission is outside the range of velocities of the GMF, then the associated ATLASGAL clumps are neglected.

[5]LSR stands for local standard of rest.

4.3 Results

4.3.1 Physical properties of the GMFs

In this section we present physical properties of the GMFs: length, velocity gradient, total mass, dense gas mass, and dense gas mass fraction.

4.3.2 Kinematic distance, length and velocity gradient

Before obtaining the mass and length of the GMFs, we estimate their kinematic distances using ^{13}CO data. We fit the spectrum of each GMF with a Gaussian and define the $v_{\rm LSR}$ as the centroid of the fit. We used the model of the Galactic spiral arm pattern by Reid et al. (2014) to convert $v_{\rm LSR}$ into kinematic distances, assuming the standard Galactic parameters. Our filament-finding method favors identification of nearby filaments. Although infrared dark clouds (IRDCs) can be seen against the MIR background at both sides of the Galaxy, only those in the near side would appear as clear extinction features at NIR wavelengths (Kainulainen et al., 2011a). Our extinction method is therefore limited to find filaments up to ∼8 kpc distance (Kainulainen et al., 2011a). We therefore assumed the near kinematic distances to our GMFs. The velocities and distances to the GMFs are listed in Table 4.2. We find distances between 2.2–3.7 kpc. These are similar to previously identified GMFs. For comparison with the kinematic distances, we also list in Table 4.2 the distances derived from dust extinction (Marshall, Joncas, and Jones, 2009). We estimated the mean extinction distance to the GMFs as the average of every counterpart in Marshall, Joncas, and Jones (2009) associated to the GMFs and assume their standard deviation as the uncertainty. In general we obtain larger distances using this method. This is consistent with a systematic offset of 1.5 kpc between kinematic and extinction derived distances, already reported in Marshall, Joncas, and Jones (2009).

We estimate the angular length of the GMFs using a line that follows the extinction and emission features at $8\,\mu$m from end to end of the significant ^{13}CO emission (≥1.5 K km/s) of each filament (see Fig. 4.1 and Appendix B). The significant emission is estimated measuring the noise of the CO integrated intensity maps. We find angular lengths between 1° and 3°. The angular length is converted into physical length using the distances previously estimated. No corrections are applied for the projection effects.

These lengths are therefore lower limits. We found GMF projected lengths between 40–170 pc, with a mean of $\sim$100 pc. These values are similar to the filaments identified by R14.

We estimate the projected velocity gradient of the GMFs as $\nabla v = (v_{\rm ini}$-$v_{\rm end})/l$, where $v_{\rm ini}$ and $v_{\rm end}$ are the velocity centroids at both ends of the GMF and l is the projected length of the GMF. Most of the GMFs exhibit projected velocity gradients throughout their extent, except the GMF 324.5-321.4, that shows no projected velocity gradient over its 120 pc size. We found projected velocity gradients between 0–120 km/s kpc^{-1} (see Table 4.2). We emphasize that these velocity gradients are projected. We did not correct them from projection effects. Therefore, these gradients offer a pure observational measure and should not be directly connected to velocity gradients introduced by Galactic rotation or shear motions.

TABLE 4.2: Regions studied in this chapter

Filament ID	l	b	θ	$v_{\rm ini}, v_{\rm LSR}, v_{\rm end}$	d^{d}_{kin}	d_{ext}	L	$\langle \nabla v \rangle$	$R_{\rm gal}$	$\langle z \rangle$
GMF	[°]	[°]	[°]	[$\mathrm{km\,s^{-1}}$]	[kpc]	[kpc]	[pc]	[$\mathrm{km\,s^{-1}\,kpc^{-1}}$]	[pc]	[pc]
307.2-305.4	[307.4,304.7]	[-0.3,0.6]	3.1	-29, -35, -39	3.1±0.7	5.7 ± 0.9	168	59	7.2	20
309.5-308.7	[309.6,308.6]	[-0.7,0.7]	1.5	-41, -43, -47	3.7±0.7	4.7 ± 0.3	97	62	6.8	25
319.0-318.7	[319.0,317.3]	[-0.8,0.2]	2.6	-35, -40, -44	2.8±0.4	4.9 ± 0.4	73	123	6.7	25
324.5-321.4	[324.3,321.4]	[-0.3,0.2]	3.1	-32, -32, -32	2.2±0.4	—[c]	119	0	6.9	7
324.5-321.4b[a]	[322.7,321.4]	[-0.2,0.2]	1.0	-32, -32, -32	2.2±0.4	2.9 ± 0.3[c]	38	0	6.9	21
335.6-333.6a	[335.8,332.2]	[0.0,-0.6]	2.0	-46, -50, -53	3.4±0.3	4.5 ± 0.5	119	59	5.7	7
335.6-333.6b	[332.8,331.6]	[-0.2,-0.2]	1.4	-48, -50, -51	3.3±0.3	5.8 ± 0.5	81	39	5.8	13
341.9-337.1	[342.2,340.2]	[-0.1,-0.2]	2.1	-43, -44, -48	3.5±0.3	5.1 ± 0.5	128	31	5.3	7
343.2-341.7	[342.8,341.7]	[0.0,0.5]	1.5	-43, -41, -41	3.4±0.3	4.9 ± 0.3	89	22	5.3	33
358.9-357.4	[358.1,357.4]	[-0.4,-0.3]	1.6	5, 7, 8	—[b]	2.9 ± 0.3	81	37	5.6	3

Column 1: GMF identification; Cols. 2-3: Galactic latitude and longitude ranges of the GMFs; Col. 4: Angular length of the filament from end to end; Col. 5: $v_{\rm ini}$ and $v_{\rm end}$ represent the velocity centroid of the ^{13}CO emission at the ends of the filament. $v_{\rm LSR}$ is the velocity centroid of the ^{13}CO emission along the entire GMF. This value is used to estimate the kinematic distance to the GMF; Col. 6: Kinematic distances and uncertainties, obtained from the Galactic model of Reid et al. (2014); Col. 7: Distances obtained from dust extinction models (Marshall, Joncas, and Jones, 2009). The distances were obtained as the mean of all the counterparts in the catalog (Marshall, Joncas, and Jones, 2009), overlapping the GMFs. The uncertainties show the standard deviation.; Col. 8: Projected length of the filaments; Col. 9: Projected velocity gradient of the filaments, obtained

as the ratio $(v_{\rm end} - v_{\rm ini})$/length; Col. 10: Galactrocentric radius; Col. 11: Mean height above the Galactic midplane in the middle of the filament. **a)** Most conservative definition of GMF324.5-321.4 (See Sect. B.1.4). **b)** We avoid the use of kinematic distance in this GMF since it lies in the Galactic center region. **c)** No Marshall, Joncas, and Jones (2009) counterparts in this filament. **d)** We used the kinematic distances to sources, except for GMF 358.9-357.4.

4.3.3 Dense gas mass fraction (DGMF)

We estimate the total molecular gas mass and the dense gas mass of the GMFs following the procedures described in Sect. 4.2.8 and Sect. 4.2.9. We obtain total molecular cloud masses in the range of $[1.4, 9.4] \times 10^5\,\mathrm{M}_\odot$. We found dense gas masses between $[2.1, 310] \times 10^3\,\mathrm{M}_\odot$.

We calculate the dense gas mass fraction (DGMF) of the GMFs as the ratio of the dense to total molecular gas masses of the GMFs. This quantity has been recently connected to the star-forming rate of molecular clouds (Heiderman et al., 2010a; Lada, Lombardi, and Alves, 2010b; Lada et al., 2012b; Abreu-Vicente et al., 2015). In general, we find DGMFs between 1.5% and 15%. However, the filament GMF 335.6-333.6 shows a larger DGMF, 37%. This large value is related to the massive H II complex G333, from which most of the ATLASGAL emission of the GMF arises (see Fig B.4). The DGMF of this filament agrees with values found in massive ($\geq 10^5\,\mathrm{M}_\odot$) H II regions in the Galactic plane (Abreu-Vicente et al., 2015). The lower DGMF values found in the other filaments are consistent with those found in the GMF sample of R14 and other large molecular filaments (Battersby and Bally, 2014; Kainulainen et al., 2013a). These values are also characteristic for local star-forming clouds (Kainulainen et al., 2009b; Lada, Lombardi, and Alves, 2010b; Lada et al., 2012b) and high-mass star-forming clumps (Johnston et al., 2009; Battisti and Heyer, 2014b).

The main uncertainty in our dense gas mass estimates is the distance to the filaments. This is also the case for the total gas mass. Unfortunately, the ThruMMS data has a non-uniform noise coverage that may lead to lose significant ^{13}CO emission in some of our GMFs, limiting our ability to measure their total gas mass. In addition, five of the GMFs are only partly covered by the ThruMMS data. As a consequence of these issues, we can only measure lower limits of the actual total gas mass in most of our GMFs, resulting in upper limits for the DGMFs. These are indicated in Table 4.3. We also show these regions in (see Fig. 4.1 and Appendix B).

4.3.4 Giant molecular filaments in the Galaxy

What is the role of the GMFs in the Galactic spiral structure? Do they belong to the spiral arms or to inter-arm regions? We explore the answer to these questions in Fig. 4.2, in which we show the v_{LSR} of the three inner spiral

TABLE 4.3: Masses and associations of the GMFs

GMF	M(^{13}CO) [10^4 M$_\odot$]	M(AGAL) [10^4 M$_\odot$]	DGMF [%]	Assoc.	Arm
307.2-305.4	82	8.7	10.6	G 305	Cent
309.5-308.7	> 81	1.7	< 2.1	RCW 179	Cent
319.0-318.7	55	1.6	2.9	...	Cent
324.5-321.4	> 14	0.21	< 1.5	G321.71	...
324.5-321.4b	4.2	0.21	5.0	G321.71	...
335.6-333.6	> 84	31	< 36.9	RCW106	Cent
335.6-333.6b	16	2.2	15.0	...	Cent
341.9-337.1	> 94	5.7	< 6.1	...	...
343.2-341.7	> 20	0.85	< 4.3	...	...
358.9-357.4	> 28	2.6	< 9.3	...	Cent

Column 1: GMF identification; Col. 2: total gas mass of the GMF; Col. 3: Dense gas mass of the GMF; Col. 4: Dense gas mass fraction, estimated as the ratio between Col.2 and Col.3 ; Col. 5: known star-forming regions or molecular clouds along the GMF.; Col. 6: Spiral arm association, if any.

arms in the fourth quadrant as function of their galactic longitude following Reid et al. (2014). For simplicity, since our filament finding method is more likely to reveal filaments in the near side of the Galaxy (Sect. 4.3.2), we only show the near distance solutions of the spiral arms. We measure the velocities at the ends of the filaments and plot them in Fig. 4.2. We find that six out of nine of our GMFs are connected to the Centaurus spiral arm, while three GMFs lie in inter-arm regions.

We also re-examine the locations of the GMFs identified by R14 using the Reid et al. (2014) model. We find that three out of their seven GMFs are connected to spiral arms (see Fig. 4.2), two of them to the Sagittarius arm and a third one to the Scutum arm. If we put together the GMF samples of R14 and this work we find that nine out of 16 GMFs are related to spiral arms. The percentage of spiral arm filaments higher in the fourth quadrant (67%) than in the first (<50%). In the first quadrant the GMFs are associated to the Sagittarius and Scutum arms, while in the fourth quadrant they are preferentially connected to the Centaurus arm.

The higher fraction of spiral arm filaments found by us compared to R14 is affected by our use of the Reid et al. (2014) model instead of the Vallée (2008) model. One of the main differences between Vallée (2008) and (Reid et al., 2014) is that the latter compare their model with typical spiral arm tracers such as H II regions or massers while this step is not done in the former work. The velocities of the Sagittarius arm, the closest spiral arm in the first quadrant, are significantly different in Vallée (2008) and (Reid et al., 2014) models.

Now we study the relative orientations of the GMFs compared to the spiral arms. Here we analyze together the GMF samples of this work and R14. Figure 4.3 shows that there are seven GMFs connected to the Scutum-Centaurus arm, two to the Sagittarius arm and there are seven GMFs located in inter-arm regions. Four of the GMFs connected to spiral arms in Fig. 4.3 are connected only by one of their ends. We now address whether the uncertainties are large enough to place part of a filament in an inter-arm region even if it lies within a spiral arm.

There are three main sources of error that play a role in the location of the filaments: the spiral arm width, the velocity resolution of the ^{13}CO spectra, and the uncertainty in the kinematic distance. The latter is by far the most important. The distance uncertainties of our GMFs, obtained from the Reid et al. (2014) model, range between [0.7–0.3] kpc (see Table. 4.2). These uncertainties are larger than the widths of the Scutum-Centaurus and Sagittarius spiral arms, 0.17 kpc and 0.26 kpc respectively, in the Reid et al. (2014) model. The estimates of the exact location of the filaments, based on these kinetic distances alone, are not enough to claim are not enough to claim that the GMFs are located in spiral arms, inter-arm regions or connect both.

We now complement this study with PV diagrams of the ^{12}CO emission, integrated between $|b| \leq 1°$. If a GMF lies inside a spiral arm, its velocity should be consistent with that of the spiral arm. A spiral arm appears in a PV diagram as a strong single component. We overlay a line showing the velocity of the GMF as function of its Galactic longitude on the PV diagram. If this line falls completely inside ^{12}CO emission of any spiral arm, we could say that the GMF is completely within it. If it falls outside, we can confirm that the GMF is located in an inter-arm region. We show the results of this experiment in the bottom panels of Fig. 4.1–B.8. These figures confirm that every GMF connected to a spiral arm in Fig. 4.3 has velocities consistent with the arm over its whole extent. These data offer no support for the hypothesis that some of the GMFs could be a spur (i.e., a filament connecting spiral-arms with inter-arm regions observed in external galaxies.) Similarly, the inter-arm GMFs show velocities not consistent with the spiral arms. We note that the spiral arm positions of some of our GMFs are independently confirmed by previous works, focused on particular H II regions or IRDCs within them (see App. B.1).

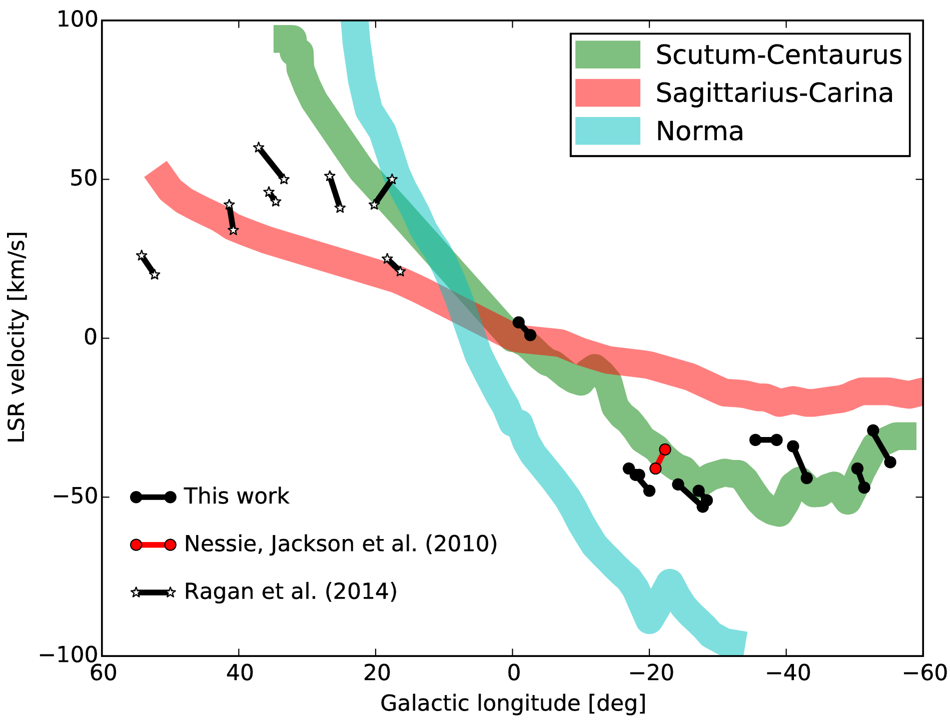

FIGURE 4.2: LSR velocities of the Norma (cyan), Scutum-Centaurus (green) and Sagittarius-Carina (red) spiral arms as function of galactic longitude, as estimated by Reid et al. (2014). The width of the lines, 8 km/s, is equivalent to the spatial width of the filaments from (Reid et al., 2014). For simplicity, we only show the near kinetic distances of the spiral arms. Each line segment represents a GMF, taking the $v_{\rm LSR}$ values from the ends of the filaments. The line segments ended with black circles show GMFs of our sample while those with white stars belong to R14. We also show Nessie, with a red line ended in red circles.

4.4 Discussion

4.4.1 Comparing large-scale filament finding methods

Three methods have been used so far to systematically search for tens-of-parsec scale filaments. Two of them, based on identification of the filaments as extinction features against the MIR/NIR background of the Galactic plane, have been used by R14, Zucker, Battersby, and Goodman (2015), and this work. In this work and in R14 we look for the largest filamentary

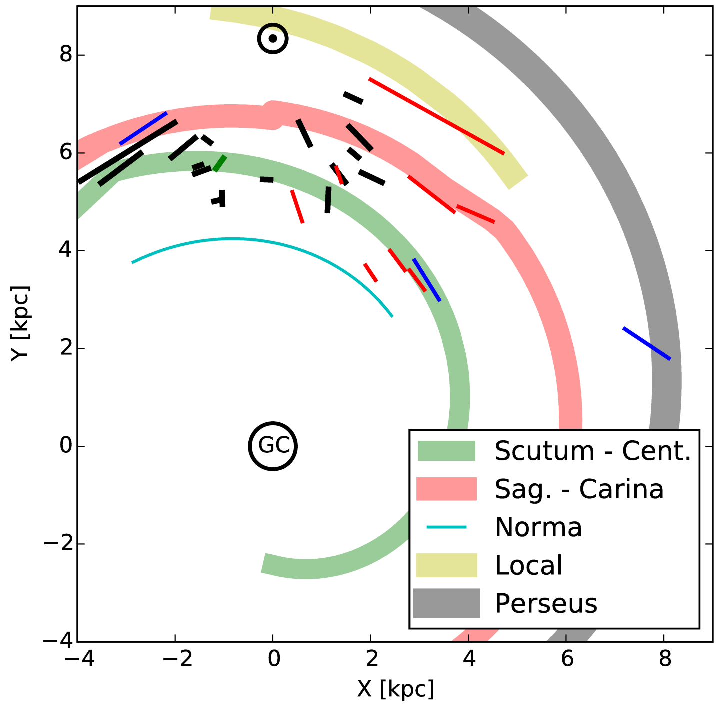

FIGURE 4.3: Face-on view of the Milky Way spiral arm structure following the Reid et al. (2014) model. We show the Norma (cyan), Scutum-Centaurus (green), Sagittarius-Carina (red), Local (yellow), and Perseus (Gray) spiral arms. The width of the spiral arms shows the width estimated by Reid et al. (2014). The circled GC represents the Galactic Center and $\odot$ represents the Sun. The black lines represent the GMF samples of this work (at negative X values) and R14 (at positive X values). The red lines show the filament sample from Wang et al. (2015), based on *Herchel* emission data. The green line shows Nessie (Jackson et al., 2010; Goodman et al., 2014). The blue lines represent other previously known filaments (Beuther et al., 2011; Battersby and Bally, 2014; Li et al., 2013).

structures in the Milky Way, irrespective of their relative orientation with respect to the galactic midplane or spiral arms. The filaments revealed by both works are known as GMFs. Instead, Zucker, Battersby, and Goodman (2015) search explicitly for Nessie analogues (i.e., filaments within spiral arms and parallel to the Galactic midplane). They refer to these filaments bones. The third method identifies the filaments as extended emission features at far-infrared (FIR) wavelengths using *Herschel* data (Wang et al., 2015). We will refer to these as emission-identified filaments. In principle, this naming scheme does not imply that the physical properties of the objects are different, nor that they should be called differently.

We compare first the GMFs and the bones. In the galactic plane areas covered by Zucker, Battersby, and Goodman (2015), R14, and this work there are nine bones, including Nessie, and 16 GMFs, seven from R14 and nine from this chapter. At first look, the bones should be a sub-group of the GMFs in which only GMFs (or sub regions within them) parallel to the Galactic mid-plane and inside spiral arms would be identified as bones. However, only three bones correspond to our GMFs. The filaments 10, 8 and 5 in Zucker, Battersby, and Goodman (2015) are sub-regions of the GMF 335.6-333.6, GMF 358.9-357.4, and GMF 20-17.9, respectively. The main reasons why only three out of nine bones of Zucker, Battersby, and Goodman (2015) overlap with the GMFs is because these bones have angular lengths clearly below 1°, which is one of our GMF requirements. This property makes the bones and GMFs not directly comparable to each other.

We now compare the extinction and emission-identified filaments. Only three out of nine emission filaments in Wang et al. (2015) have also been identified in extinction. These filaments, labeled in Wang et al. (2015) as G339, G11, and G26, correspond respectively to Nessie, the filament 6 in Zucker, Battersby, and Goodman (2015), and the GMF 26.7-25.4 in R14. The emission-identified filaments can be missed as extinction filaments because of lack of contrast between the filament and the MIR/NIR background. On the other hand, extinction filaments may not be identified in emission due to background and foreground confusion along the line-of-sight. Despite these differences both methods are likely to reveal quiescent structures in the early stages of star-formation. We conclude that the extinction and emission filament finding methods compliment each other well, finding filaments that can only be identified using one of both methods.

Do the physical properties of the filaments identified with the three different techniques agree? The bones have lengths between 13 pc and 52 pc and are the smallest of the three samples. The lengths of the emission-identified filaments (37–99 pc) are comparable to those of the GMFs (see Table 4.2). The bones and emission-identified filaments have masses on the order $M =\sim 10^3 - 10^4\ \mathrm{M}_{\odot}$, and with the GMFs being the most massive large-scale filaments (see Table 4.3). The masses of the emission-identified filaments and the bones are comparable to the dense gas masses of the GMFs. This is a selection effect. The masses of the bones are obtained over an area equivalent to the extinction feature and not over the full ^{13}CO emission as it is the case for our GMFs[6]. The similarity between the masses of the emission-identified filaments and the dense gas mass of the GMFs is a consequence of the dense gas material traced by the FIR continuum at 350 μm and 500 μm. The area covered by this emission is limited to dense regions that are surrounded by more diffuse ^{13}CO emission. The masses of the emission filaments and bones are therefore comparable only to the dense gas mass of the GMFs rather than to the total mass.

The direct comparison of the physical properties of the different kind of large filaments found so far is not straightforward. Each of the techniques used so far measures the filament properties on its on way. We encourage the use of the technique used in this chapter to obtain the bulk properties of long filaments in the future, so that they can be compared to the existing sample.

Do these filament techniques preferentially find spiral- or inter-arm filaments? In this discussion we do not include the bones since they lie within spiral arms by definition. Seven out of nine (78%) emission-identified filaments lie in spiral arms (Wang et al., 2015), as shown with the red filaments of Fig. 4.3. This percentage is lower for the extinction filaments (11 out of 18, 61%). Although the percentage of spiral arm emission-identified filaments is larger than that of extinction filaments, we acknowledge that with the small number of statistics we have this different may not be significant.

4.4.2 Dense gas mass fraction and its variation with the filament location

R14 found a tentative anti-correlation between the DGMF of the filaments and their distance to the Galactic midplane. They also found that the filament with highest DGMF in their sample was located in a spiral arm. This is also the case of the large-scale filament with the highest DGMF known to date, Nessie, with a DGMF$\sim 50\%$ (Goodman et al., 2014). However, we note that the dense gas mass estimates in Goodman et al. (2014) are made using HCN and not using sub-mm dust emission as in R14 or this work. The results of R14 have however poor statistics due to the low number of GMFs in

[6]Not to mention that they are generally smaller than the GMFs and the emission-identified filaments

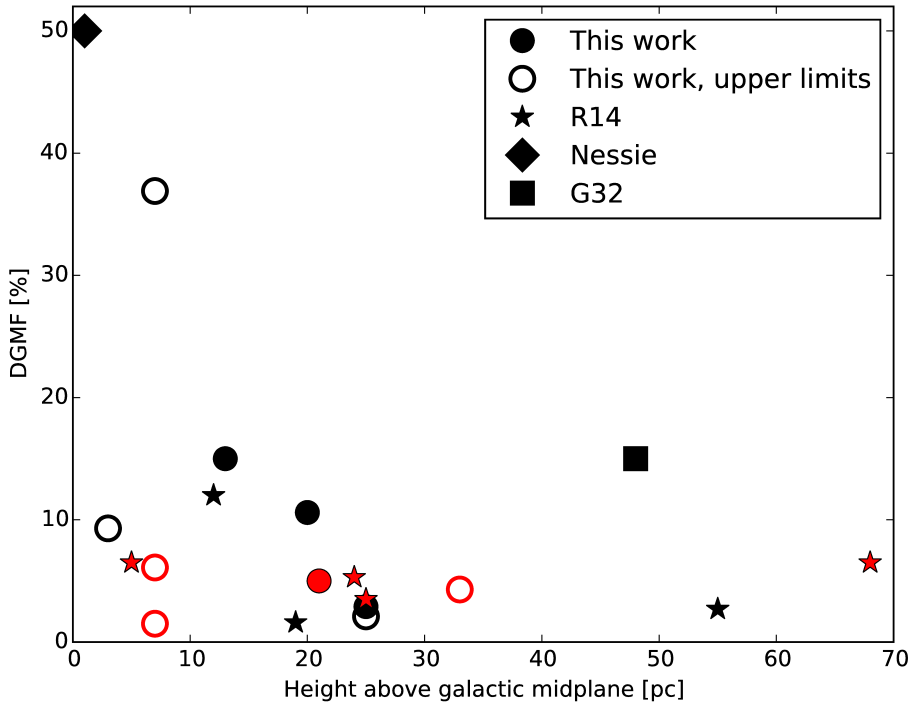

FIGURE 4.4: Dense gas mass fraction of filaments as a function of the offset above the Galactic mid-plane. The full circles show our GMF sample. The open circles show upper limits to the DGMF in our GMF sample. The black stars show the GMF sample of R14, the diamond indicates Nessie and the square the filament G32 (Battersby and Bally, 2014). The black symbols indicate GMFs within spiral arms while the red ones show inter-arm GMFs.

their sample. We explore this relationship further with our extended GMF sample.

The GMFs lie preferentially above the physical galactic midplane, which is located at about $b = -0.35°$ in the fourth quadrant. In Fig. 4.4 we show the relationship between the height above the galactic plane, z, and the DGMFs of the GMF samples of this work, R14, Battersby and Bally (2014) and Nessie. It shows no correlation at all between z and the DGMFs. The two filaments with the largest DGMFs lie close to the galactic midplane. However, the scatter in the DGMFs at any z, and particularly at $z < 10\,\text{pc}$, is also very high. We therefore conclude that there is no evidence for correlation between the height above the galactic plane and the DGMF of the filaments. However, in this work we only cover z scales of a few tens of parsecs, while we are able to study kilo-parsec scales along the line of sight. We cannot rule out the possibility of a DGMF-z relation at larger scales.

Another interesting points to look at are the difference in the DGMFs of spiral arm filaments and inter-arm filaments and the difference in DGMFs within different spiral arms. We found that the DGMF of the GMFs that belong to the Scuttum-Crux arm is $13.0 \pm 10.1\,\%$, while that of the GMFs in the Sagittarius arm is $2.1 \pm 0.5\,\%$, where the uncertainties are the standard deviation of the mean DGMFs. However, only two GMFs lie in the Sagittarius arm, generating a very poor statistical sample. Now we compare the DGMFs of arm and inter-arm GMFs. We estimate the mean DGMFs for every giant filament (GMF or emission) with DGMF estimates. We find that the mean DGMF in spiral arm filaments is $14.3 \pm 15.5\,\%$ while this value is lower in the inter-arm filaments, $4.8 \pm 1.7\,\%$. We note the big scatter in the DGMF of the spiral arm filaments, due mainly to Nessie and GMF 335.6-333.6, with DGMFs of 50% and 37% respectively. We performed an independent-samples t-test to compare the DGMFs of spiral- and inter-arm GMFs. We used the task `ttest-ind` from the package `scipy` in `Python`. This task returns the t-value and also a p-value[7] that is an indication on the significance of the means. We found a significant difference in the DGMFs of spiral-arm ($14.3 \pm 15.5\,\%$) and inter-arm GMFS ($4.8 \pm 1.7\,\%$), with t=2.02 and p=0.07. We can therefore assume that the mean DGMF of the spiral arm GMFs is higher than that of the inter-arm filaments. This is in agreement with observations in external galaxies, where the amount of dense gas is larger in the spiral arms than in inter-arm regions (Hughes et al., 2013; Schinnerer et al., 2013b). The connection between the DGMF and the star-forming activity of molecular clouds (Kainulainen et al., 2009b; Lada, Lombardi, and Alves, 2010b; Lada et al., 2012b; Abreu-Vicente et al., 2015) and this result suggest that the spiral arm filaments have larger star-forming potential than the inter-arm filaments. In other words, the star-forming activity of the GMFs depend on its Galactic location with respect to the spiral arms.

The masses of our GMFs, and also those of R14, are consistent with the definition of giant molecular clouds (GMCs). Stark and Lee (2006) found, using a sample of 56 GMCs (defined by them as molecular clouds with $M > 10^5\,\mathrm{M}_\odot$), that all GMCs were related to spiral arms. Only a 10% of less massive clouds were found to be unrelated to spiral arms. Following the GMC definition of Stark and Lee (2006), we found that five out of 14

[7] If the p-value returned by `ttest-ind` is lower than 0.10, then both means are significantly different.

GMFs consistent with GMC masses are in inter-arm regions. We therefore find that most of the GMCs in the Galaxy are related to spiral arms, as it was found by (Dame et al., 1986). Although the GMC population is enhanced in the spiral arms, the star-forming activity is not significantly enhanced on them (Eden et al., 2012; Eden et al., 2013; Moore et al., 2012). Our results agree with a picture on which a non-negligible amount GMCs can be found outside spiral arms, as also seen in external galaxies (Schinnerer et al., 2013b). Also in external galaxies, Foyle et al. (2010) have reported significant star-forming activity in inter-arm regions.

4.5 Conclusions

We have used the 2MASS, GLIMPSE, and ThruMMS surveys to extend the GMF catalog initiated in R14 to the fourth Galactic quadrant. We inspected visually the NIR/MIR images to look for filamentary extinction features of at least one degree in angular length. We then used spectral ^{13}CO information from the ThruMMS survey to confirm that those features are continuous in velocity.

- We present a sample of nine newly identified GMFs. The projected lengths of the new GMFs range from 38 pc to 168 pc. Total masses as traced by ^{13}CO are between $4 \times 10^4\ \mathrm{M}_\odot$ and $9.4 \times 10^5\ \mathrm{M}_\odot$. We also used the cold dust emission at 870 $\mu\mathrm{m}$ to estimate the dense gas mass of the GMFs and found that it ranges from $2.1 \times 10^3\ \mathrm{M}_\odot$ to $3.1 \times 10^5\ \mathrm{M}_\odot$.

- The ratio of the dense and total gas masses is the DGMF, which ranges between 1.5% and 37%. The largest is related with the H II complex G333 in the GMF 335.6-333.6. This value agrees with the DGMFs of massive (>$10^5\ \mathrm{M}_\odot$) molecular clouds with H II regions found in Abreu-Vicente et al. (2015). The other values, between 1.5% and 15%, are consistent with typical DGMFs found in molecular clouds (Battisti and Heyer, 2014b; Abreu-Vicente et al., 2015).

- We explored the role of the GMFs identified by us and R14 in the Galactic context. Adopting the Reid et al. (2014) Galactic model, we find that nine out of 16 GMFs are connected to spiral arms. Seven out of these nine filaments are connected to the Scutum-Centaurus arm and two to the Sagittarius arm. Three GMFs of R14 are related to spiral arms when the Reid et al. (2014) model is used, while only one is if Vallée (2008) model is used.

- We find no correlation between the DGMFs of GMFs and the distance from the Galactic midplane. This result disagrees with the tentative correlation found by R14. However, we note that we only observed GMFs within a few tens of parsecs of the Galactic midplane. We found that the DGMFs of the spiral arm GMFs are larger than those of the inter-arm GMFs. This result agrees with observations of external galaxies showing that the DGMFs of molecular clouds within spiral arms have larger DGMFs than inter-arm clouds (Hughes et al., 2013; Schinnerer et al., 2013b). The DGMF has a direct relationship with the star-forming activity (Kainulainen et al., 2009b; Lada et al., 2012b). This result therefore suggests that the star-forming potential of the GMFs is tightly connected to their relative position to the Galactic spiral arms.

- We compared the different methods used to date to identify large filaments: filaments identified as extinction features (GMFs and bones) and emission-identified filaments. The GMFs and the emission-identified filaments have comparable sizes and are generally larger than the bones. The total masses of the bones and the emission filaments are comparable to the dense gas masses of our GMF sample. This result is an observational effect since both, bones and emission filaments, search preferentially dense gas. Emission filaments are more preferentially connected to the spiral arms than our GMFs. Due to the different biases of the extinction and emission filament finding methods, each method can identify filaments that are missed by the other.

Chapter 5

Summary, conclusions, and a look into the future

5.1 Summary and conclusions

This thesis intended to improve observational constraints to better understand the molecular cloud evolution and its relationship with star formation and Galactic structure. The main questions to be addressed were: which are the physical parameters that shape the molecular clouds? What are the key parameters that determine the star–forming activity of molecular clouds? Do these parameters change with molecular cloud evolution? How does the Galactic environment affect to the star–forming activity and structure of molecular clouds? Here I present first the summary of the different projects used to answer these questions and the main results obtained. I will then address how this thesis has improved our understanding of those questions. Finally, I describe a series of observational projects that are needed to finally answer these questions.

5.1.1 Column density structure and evolutionary state of molecular clouds

In Chapter A.6 we presented the first study of the relationship between the column density distribution of molecular clouds within nearby Galactic spiral arms and their evolutionary status as measured from their stellar content. We analyze a sample of 195 molecular clouds located at distances below $5.5\,$kpc, identified from the ATLASGAL 870 μm data. We define three evolutionary classes within this sample: starless clumps, star-forming clouds with associated young stellar objects, and clouds associated with H II regions. The main results obtained with this project are listed below:

- The N–PDFs of molecular clouds in the Galactic plane are different for the three evolutionary classes defined in Chapter A.6: the N–PDFs of the starless clumps are well described by a log–normal function; the N-PDFs of the star–forming clouds and H II regions show a power–law tail at high column densities, with the power–law of the H II regions shallower than in the star–forming clouds. The power–law tails are likely showing that gravity has important roles in the star–forming clouds and H II regions. Our statistically significant sample shows that this picture, earlier observed in clouds of the Solar neighborhood, is relevant also at Galactic scales. Note that, although it is very tempting, drawing an evolutionary track of the N–PDFs with our data alone has to be done with caution: the starless clumps are only small portions of molecular clouds, so they cannot be directly compared. In addition, not every star–forming cloud in our sample is expected to generate H II regions in the future. Comparing our results with previous findings, however, suggests that the starless clouds are dominated by turbulent motions and that star–forming clouds have both turbulent– and gravity– dominated motions. H II regions are also expected to have turbulent– and gravity–dominated motions. However, the feedback from stars in these regions is important and can be significantly affecting the high column density regime of the N–PDFs.

- The dense gas mass fractions of the H II regions are larger than those of the star–forming clouds and the starless clumps show the lowest values. For each evolutionary class, more massive clouds show larger dense gas mass fractions. Molecular clouds dominated by the global collapse scenario are expected to show this behavior. However, we can't rule out any of the other scenarios with the data currently in hand.

- We find an approximately linear correlation $f_{\rm DG} \propto \Sigma_{\rm mass}$ for $\Sigma_{\rm mass} = 50 - 200\,{\rm M_{\odot}pc^{-2}}$, valid for all evolutionary classes. This relation flattens at dense gas mass fractions of 80%, suggesting that the maximum star-forming activity in molecular clouds is reached when the 80% of the molecular cloud mass is enclosed at gas surface densities

$A_V > 7$ mag. The molecular clouds of our sample with $f_{DG} = 0.8$ are H II regions, pointing to feedback from stars as the main reason why this factor is not higher. This result can be a valuable asset to be included in the theories of star formation.

- The scatter in the dense gas mass fractions of our molecular cloud sample is similar to the scatter observed in the SFR - total gas mass relation of (Lada, Lombardi, and Alves, 2010a; Lada et al., 2012a), suggesting that both, the dense gas mass and the lower-density envelope of the cloud, play a significant role in affecting the star formation rate.

- We estimate the evolutionary time-scales of our three classes using an analytical model which predicts the evolution of the PDF of a cloud in free-fall collapse (Girichidis et al., 2014). For each region we find time–scales in agreement with previous independent age estimates of corresponding objects, suggesting that molecular cloud evolution may indeed be imprinted into the observable *N*-PDF functions. Furthermore, this result would also point to molecular clouds dominated by a global collapse scenario.

5.1.2 A fourier space method for combining *Herschel* and *Planck* data

We present a Fourier method to combine 160 μm , 250 μm , 350 μm , and 500 μm publicly available *Herschel* data with the *Planck* foreground thermal dust emission model. The method eliminates the pervasive negative fluxes present in the *Herschel* 160 μm archive data while preserving the angular scale dependence of the background flux at all wavelengths. We apply our method to three regions spanning a range of Galactic environments and image noise properties: Perseus, the B68 region of the Pipe Nebula, and the Galactic plane region around $l = 11°$ (HiGal–11). For each region we post-process the combined dust continuum emission images to generate column density and temperature maps and compare them with the previous constant–background corrected maps. We list the main results of this work:

- We show that the background emission applied to the *Herschel* data is scale dependent and therefore a constant offset correction fails at keeping the spatial background structure.

- We discover evidence for a large angular scale ($\theta > 40'$) excess of power in the *Herschel* images of Perseus and the B68 region of the Pipe Nebula. Tentatively, the presence of the large-scale excess of *Herschel* flux appears related to the overall signal-to-noise in a given observation and thus may be related to the noise treatment in the *Herschel* reduction and image reconstruction software.

- In the HiGal–11, our "feathered" column densities exhibit higher (lower) N(H) values in (out of) the Galactic plane region, compared to the "constant–offset" method. In general, a similar effect is seen in Perseus in the areas surrounding NGC 1333, which also exhibits higher N(H) values compared to previous methods. We show that N(H) values calculated based on the "constant–offset" method can be discrepant by factors of $\sim 50\%$ or more, but typically span variations of $\sim 30\%$ over significant portions of the images.

- In general, our "feathered" column densities recover more low column material, and the discrepancies with the previous method are most significant at the lower end of the column density distribution, near N(H)$\sim 10^{22}$ cm^{-2}. Above this value, we find generally acceptable agreement with previous methods. As most molecular cloud mass resides at low N(H) values a proper treatment of the column densities and temperatures is needed to better constrain fundamental physical parameters such as the gravitational potential.

- We apply this method to the specific case of *Planck* and *Herschel* , but it can of course be generically applied to any combination of image estimators containing radically different angular resolutions. The two most critical assessments to be made when applying this technique is a relative noise estimate and a measurement of the effective beam transfer function of the images to be combined.

5.1.3 A sample of giant molecular filaments

In Chapter 4 we perform a systematic search of GMFs in the fourth Galactic quadrant and determine their basic physical properties. We identify GMFs based on their dust extinction signatures in the NIR and MIR and the velocity structure probed by ^{13}CO line emission. We estimate the basic physical properties of the GMFs. We use the ^{13}CO line emission and ATLASGAL dust emission data to estimate the total and dense gas masses of the GMFs. We combine our sample with an earlier sample from literature and study the Galactic environment of the GMFs.

- We present a sample of nine newly identified GMFs with projected lengths of 38 pc to 168 pc, total molecular masses between $4 \times 10^4\,\mathrm{M}_\odot$ and $9.4 \times 10^5\,\mathrm{M}_\odot$, and dense gas masses ranging from $2.1 \times 10^3\,\mathrm{M}_\odot$ to $3.1 \times 10^5\,\mathrm{M}_\odot$.
- The dense gas mass fraction of the GMFs are consistent with the values found for the molecular clouds studied in Chapter A.6.
- We explored the role of the GMFs identified by us and R14 in a Galactic context. Adopting the Reid et al. (2014) Galactic model, we find that roughly half of the GMFs are related to Galactic spiral arms.
- The spiral arm GMFs show larger dense gas mass fractions than the inter–arm GMFs. This result agrees with observations of external galaxies showing that the dense gas mass frations of molecular clouds within spiral arms are larger than in inter-arm clouds (Hughes et al., 2013; Schinnerer et al., 2013b). As shown in Chapter A.6, the dense gas mass fraction is directly connected to the SFR of the molecular clouds (Kainulainen et al., 2009b; Lada et al., 2012b). This result therefore suggests that the star-forming potential of the GMFs is tightly connected to their relative position to the Galactic spiral arms.

5.1.4 Conclusion

In the three different projects of this thesis we were able to successfully improve the existing observational constraints needed to challenge the theories of molecular cloud structure, evolution, and star formation. The results obtained can be used to partially answer the questions targeted in this thesis.

In Chapter A.6 we obtain results that tentatively point towards molecular cloud evolution driven by global collapse. However, the results obtained cannot be used to rule out any of the other scenarios. Also in Chapter A.6 we find that the amount of dense gas in molecular clouds is related with the total mass of the molecular clouds, suggesting that the molecular cloud masses directly influence in the star–forming activity of molecular clouds.

In other words, both–, the dense gas and the diffuse envelopes of molecular clouds are related to the star formation, with the dense gas having a more dominant influence. Furthermore, we find a limit to the dense gas mass fraction of molecular clouds of 80%. The reason for this is still to be found, although the fact that the clouds showing a 80% of dense gas are H II regions points to feedback from stars disrupting the dense gas. This result could be an important observational asset to be included in the theories of star formation.

In Chapter 4 we find that the giant molecular filaments located in spiral arms have larger amounts of dense gas than those located in inter–arm regions. Together with the results obtained in Chapter A.6, this suggests that the molecular clouds and giant molecular filaments in the spiral–arms have more important star–forming activity than those in inter–arm regions.

In Chapter 3 we present a method to improve our ability to improve the study of column density structure presented in Chapter A.6. This method can be used, not only in the specific datasets of Chapter 3 (*Herschel* and *Planck*), but also in any combination of datasets observing at the same wavelengths and with very different angular resolutions.

5.2 A look into the future

The results of this thesis point towards the global collapse scenario as being responsible for shaping molecular cloud structure during molecular cloud evolution. However, this result is only suggestive. Even larger samples of molecular cloud structure and a close connection between observations and simulations are imperative to confirm this trend.

To obtain such a sample there are two projects that can be seen as natural follow ups of this thesis. First, and this is an already ongoing project together with Amy Stutz, the *Herschel* data archive must be re–calibrated using the method presented in Chapter 3. We have currently re–calibrated half of the Gould Belt survey and a portion of 40 degrees in Galactic longitude of the HiGal Survey. We aim to fully re–calibrate both surveys early in 2017. **The lack of Herschel successor means that our data release will be the most accurate FIR continuum data set in the years to come**.

Once the *Herschel* re–calibrated dataset is available, a study of molecular cloud structure similar to that present in Chapter A.6 will be available for the whole Galactic plane. My plan is to lead such a project and use the observational assets obtained to challenge the predictions of the global collapse model for molecular cloud evolution in collaboration with Enrique Vázquez–Semadeni (e.g., Zamora-Avilés, Vázquez-Semadeni, and Colín, 2012). Furthermore, this observational dataset could be used to challenge the existing theories of star–formation.

In this thesis, I only present a census of the giant molecular filaments. These objects have still not been studied in depth. Since these objects challenge the theories that present the filaments as equilibrium cylinders (see Sect. 1.3), the obvious first step is to study the main parameters on which these theories are based: the line–mass and the mode of fragmentation of the filaments. Two test case filaments with super critical line masses are currently being studied with ALMA data (Orion A and G357, both with projects lead by Jouni Kainulainen). However, these are two isolated cases. Extending these studies systematically to the currently known giant molecular filaments will be needed to understand the physical processes that govern the evolution of these filaments.

Finally, the extent of the giant molecular filaments, up to 120 pc, assures that they can be resolved with ALMA observations of nearby Galaxies if they exist. Observing these filaments in external galaxies would help to understand their Galactic role. Furthermore, this could be a first step towards a Galactic model of star formation.

All these projects can be performed using the observational facilities currently available. The next five–to–ten years will undoubtedly bring new observational assets that will challenge the existing theories of molecular cloud evolution and star formation. However, to be successful in our road to reveal these processes we need to improve the synergy between theories, simulations, and observations. In addition, complementing the findings in the Milky Way with those of nearby galaxies is mandatory to understand the process of star–formation on a global scale.

Appendix A

Extra material for Chapter A.6

A.1 Regions studied

A.2 MIPSGAL 24μm maps with ATLASGAL contours and regions

A.3 ATLASGAL maps from starless clumps

A.4 H II regions

A.5 star-forming clouds

A.6 Full table of regions in Chapter A.6

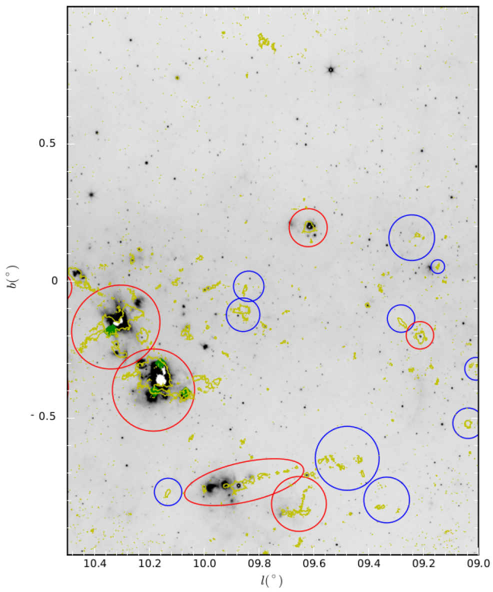

FIGURE A.1: Greyscale MIPSGAL 24μm map of the Galactic plane region comprised between Galactic longitudes $l = 9\,\mathrm{deg} - 10.5\,\mathrm{deg}$. Overlayed yellow contours show 3σ level (0.15 Jy/beam) isocontours of ATLASGAL survey. Red circles and ellipses show our defined H II regions while molecular cloud regions are shown in blue. Starless clumps are shown as green filled circles. In all cases, size of region markers matches their sizes.

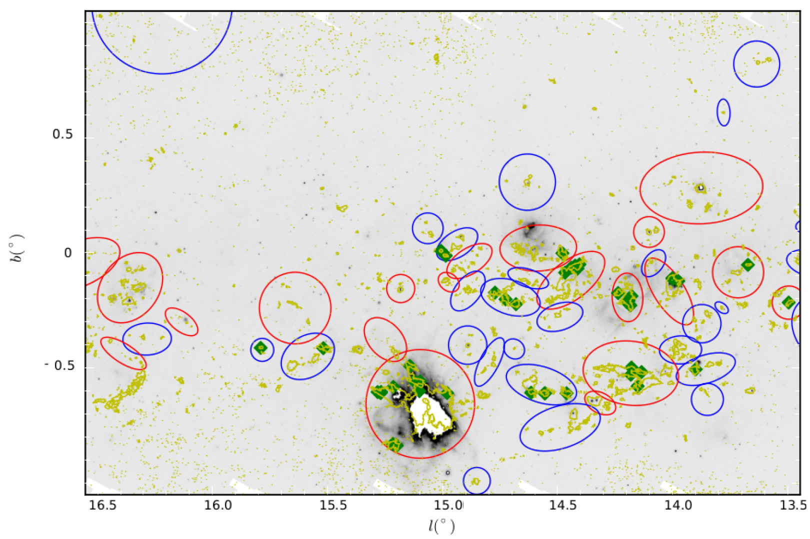

FIGURE A.2: Same as Fig. A.1 for Galactic longitudes $l = 13.5\,\mathrm{deg} - 16.5\,\mathrm{deg}$.

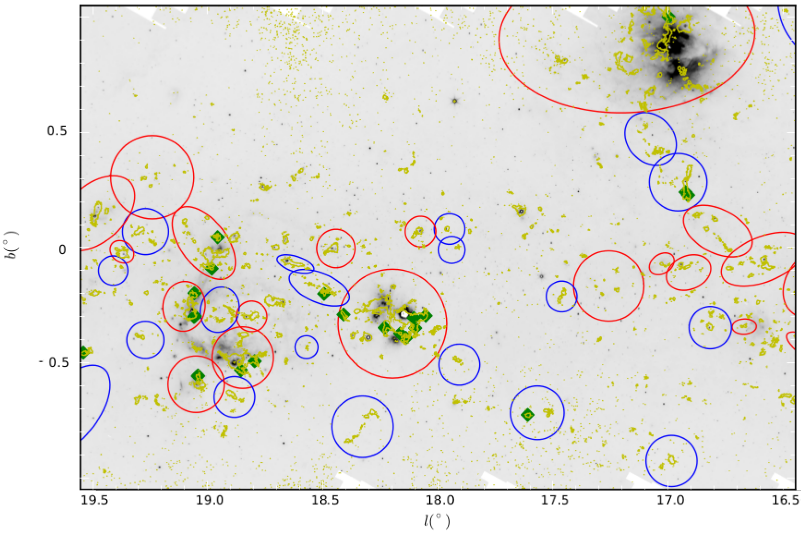

FIGURE A.3: Same as Fig. A.1 for Galactic longitudes $l = 16.5\,\mathrm{deg} - 19.5\,\mathrm{deg}$.

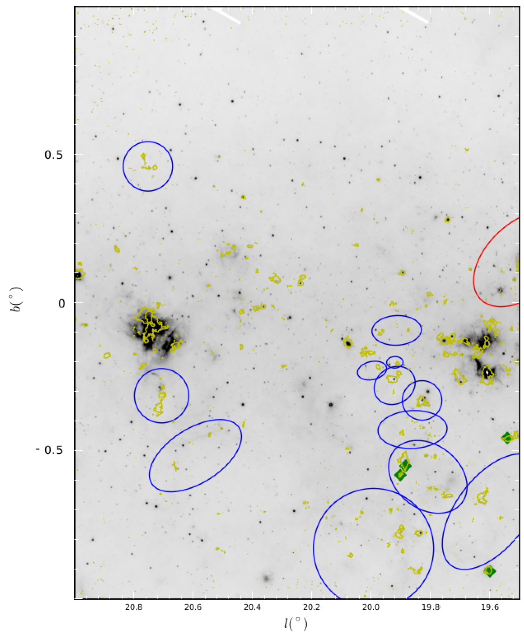

FIGURE A.4: Same as Fig. A.1 for Galactic longitudes $l = 19.5\,\mathrm{deg} - 21\,\mathrm{deg}$.

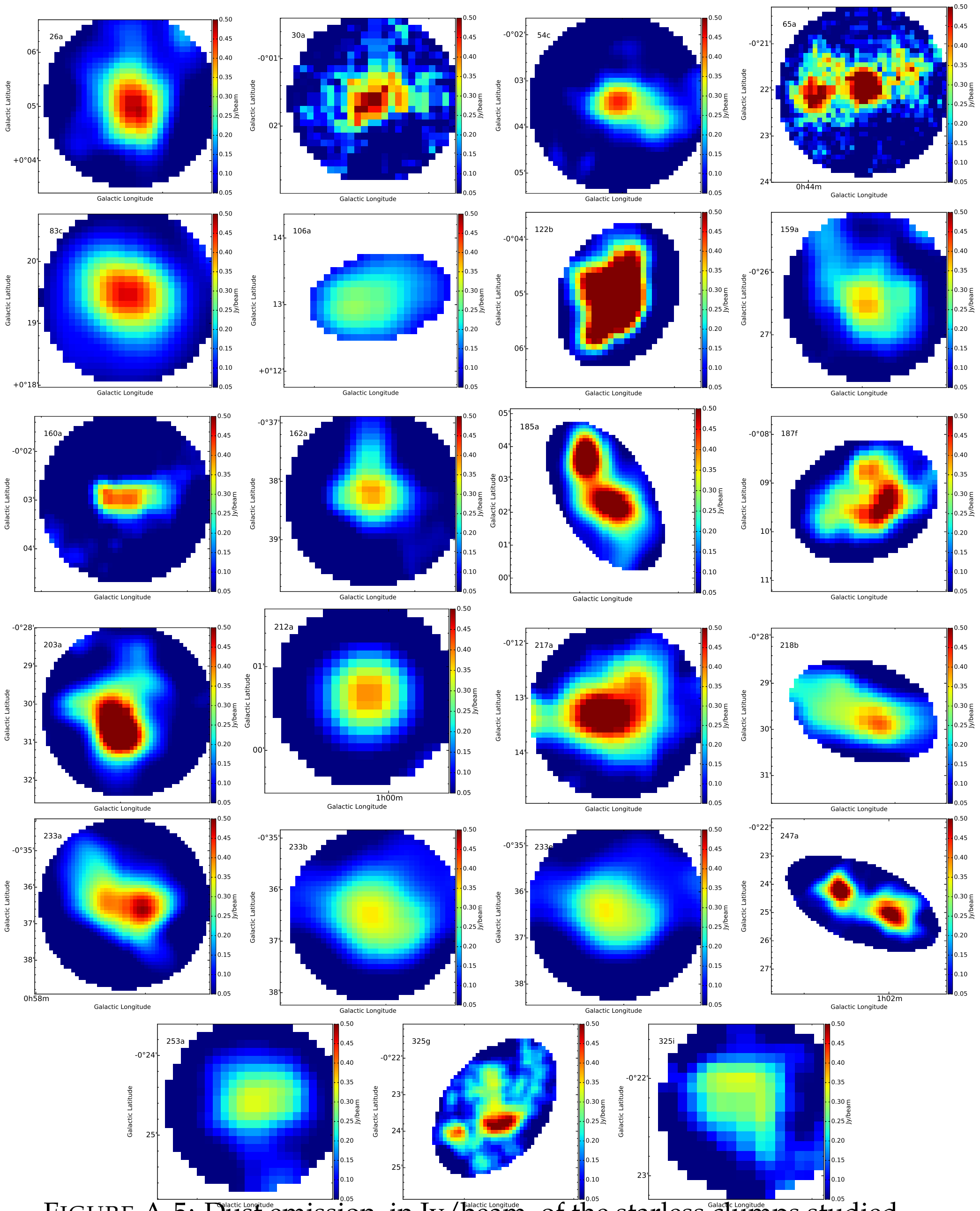

FIGURE A.5: Dust emission, in Jy/beam, of the starless clumps studied.

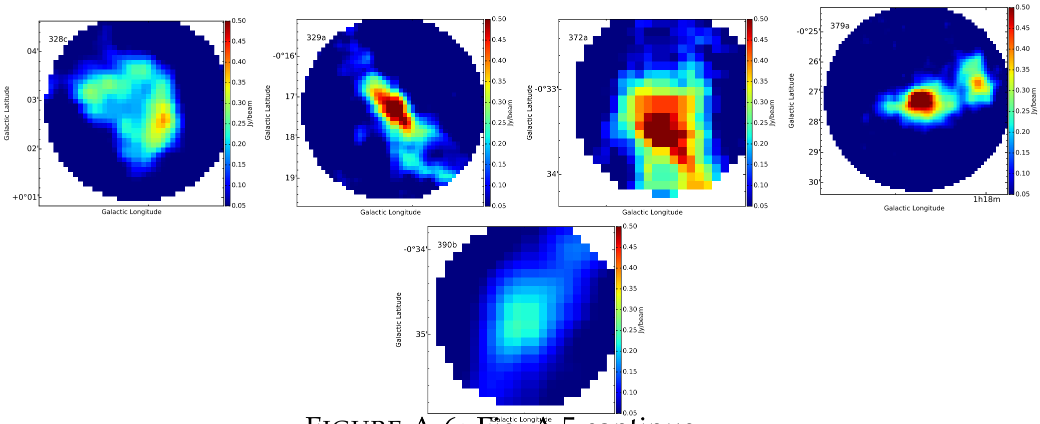

FIGURE A.6: Fig. A.5 continue.

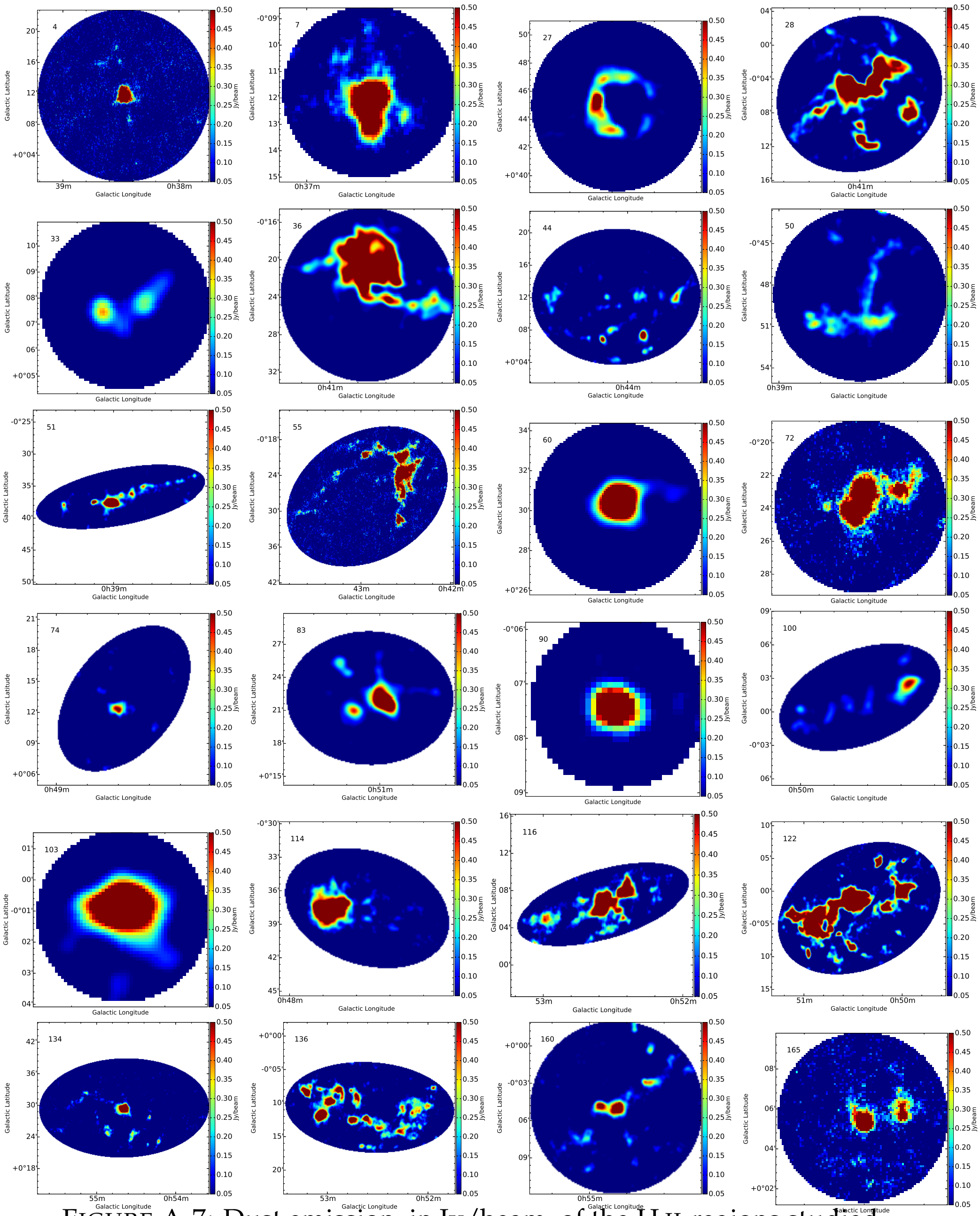

FIGURE A.7: Dust emission, in Jy/beam, of the H II regions studied.

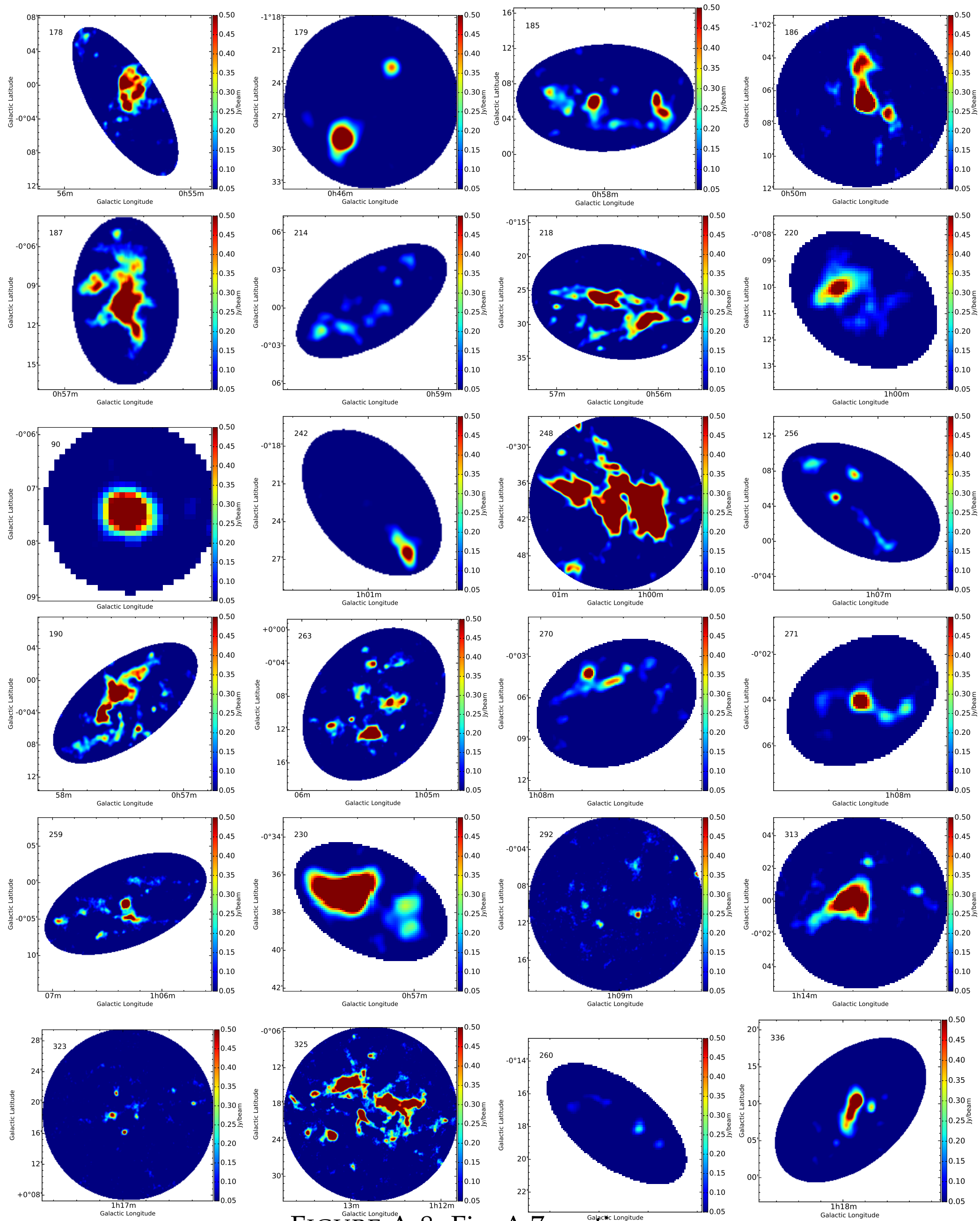

FIGURE A.8: Fig. A.7 continue.

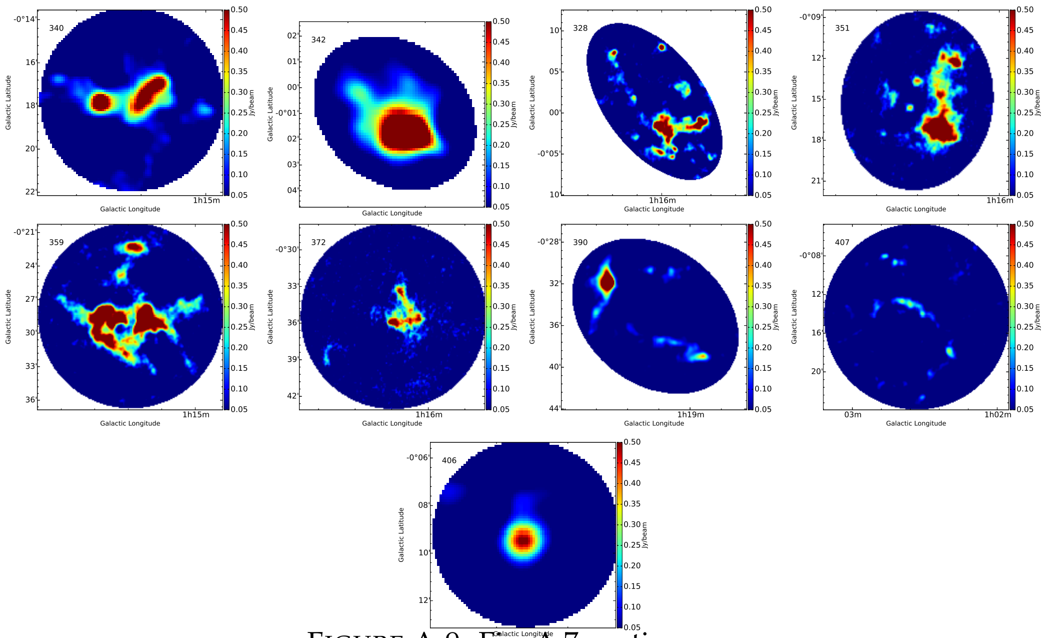

FIGURE A.9: Fig. A.7 continue.

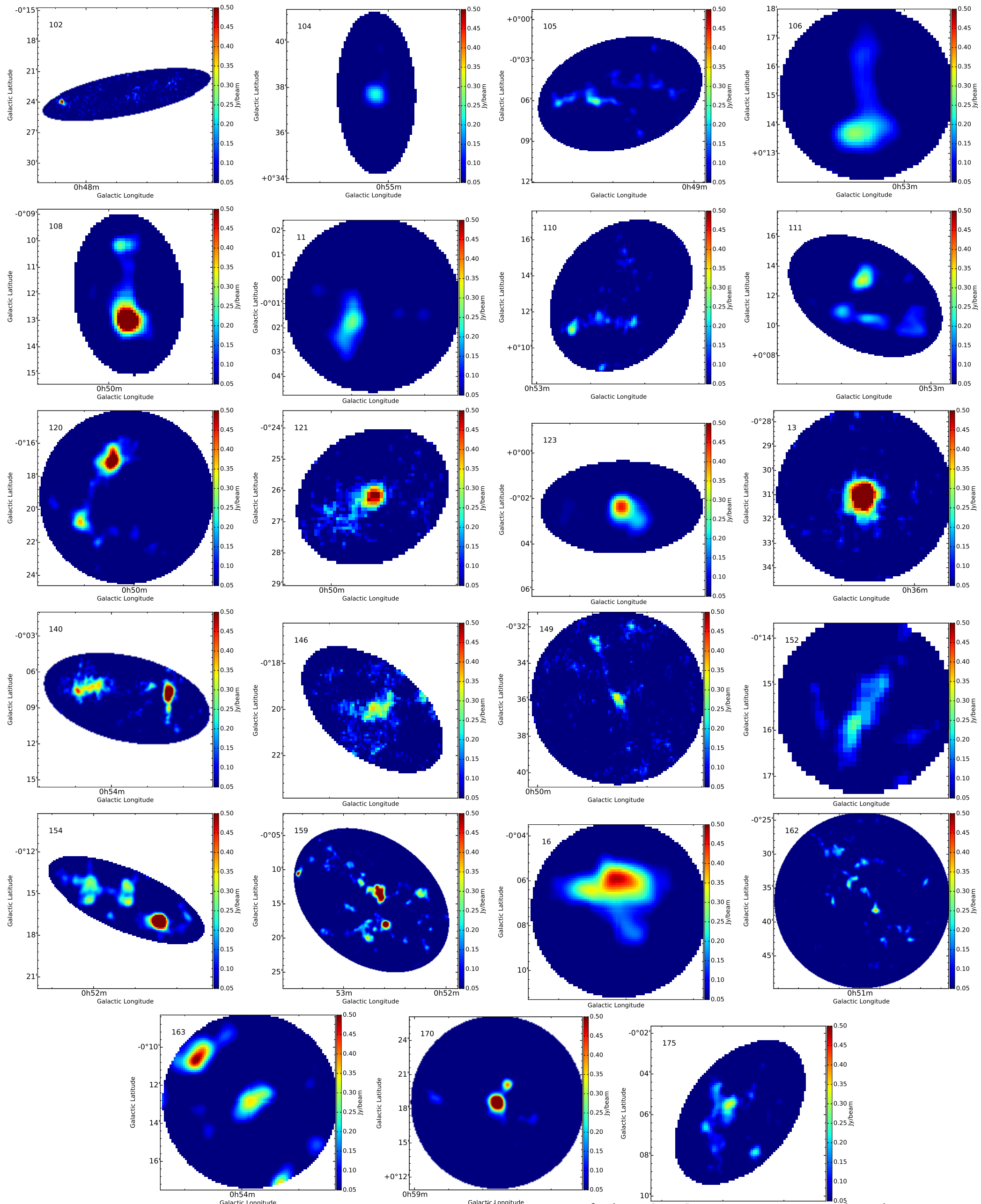

FIGURE A.10: Dust emission, in Jy/beam, of the SFC regions studied.

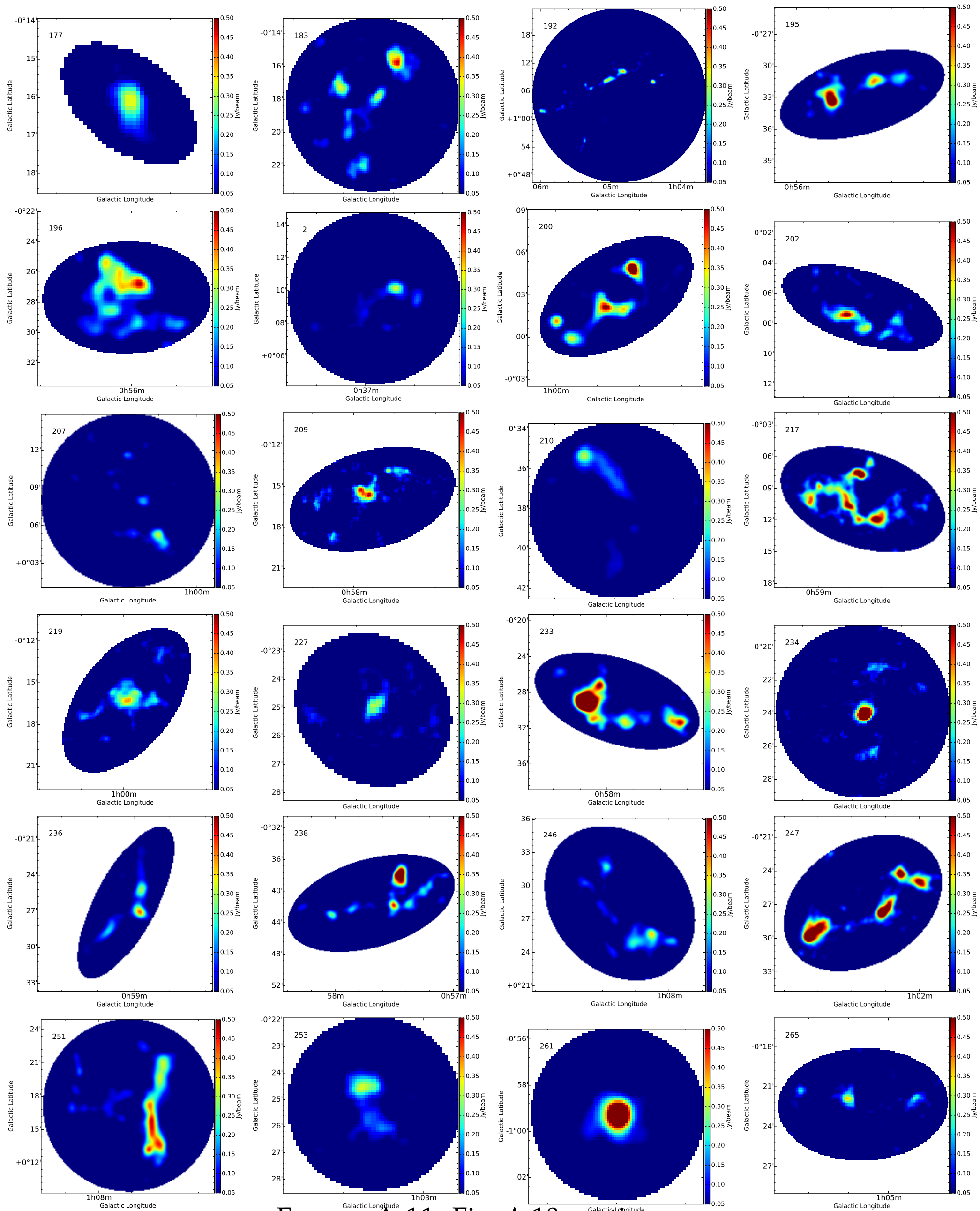

FIGURE A.11: Fig. A.10 continue.

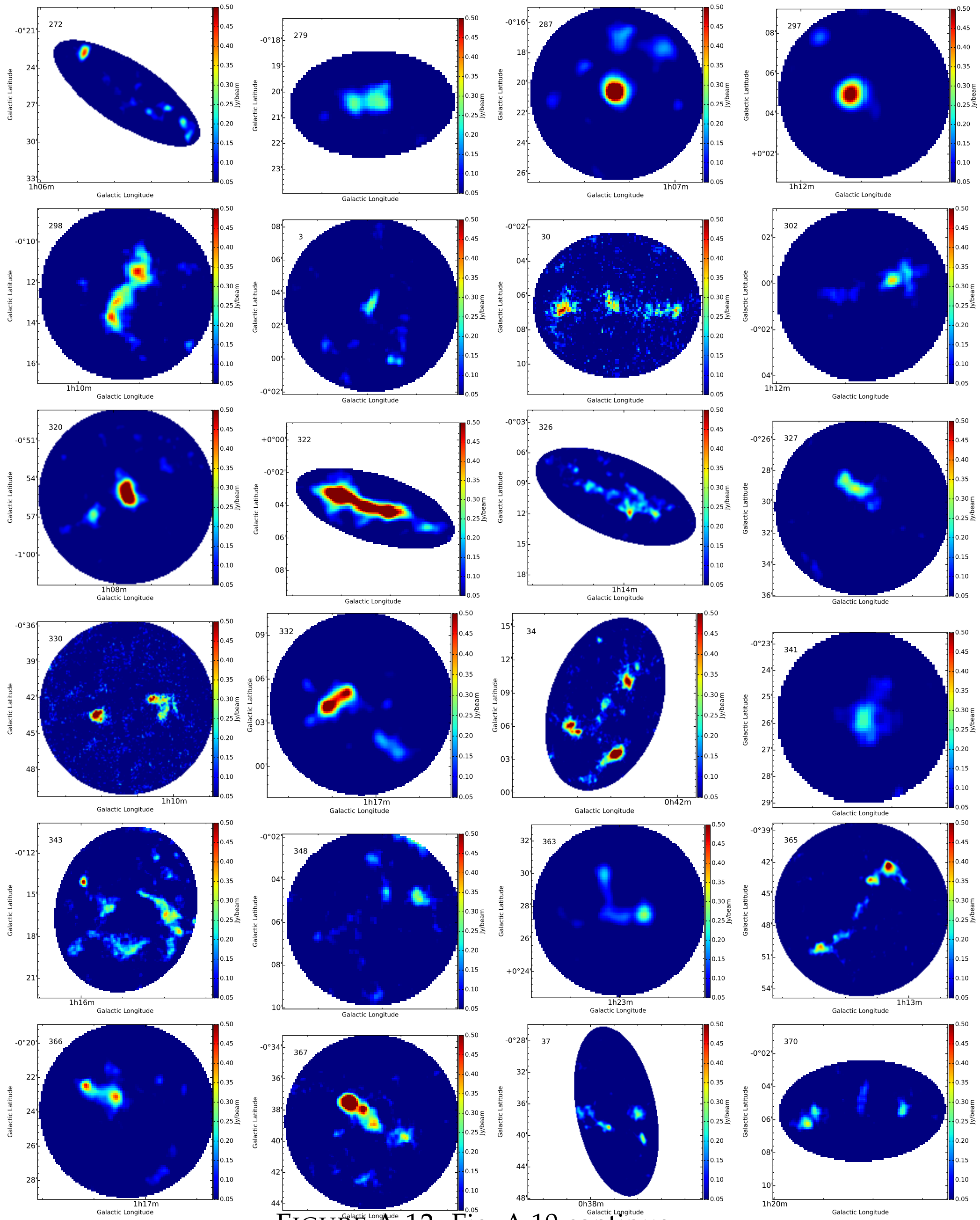

FIGURE A.12: Fig. A.10 continue.

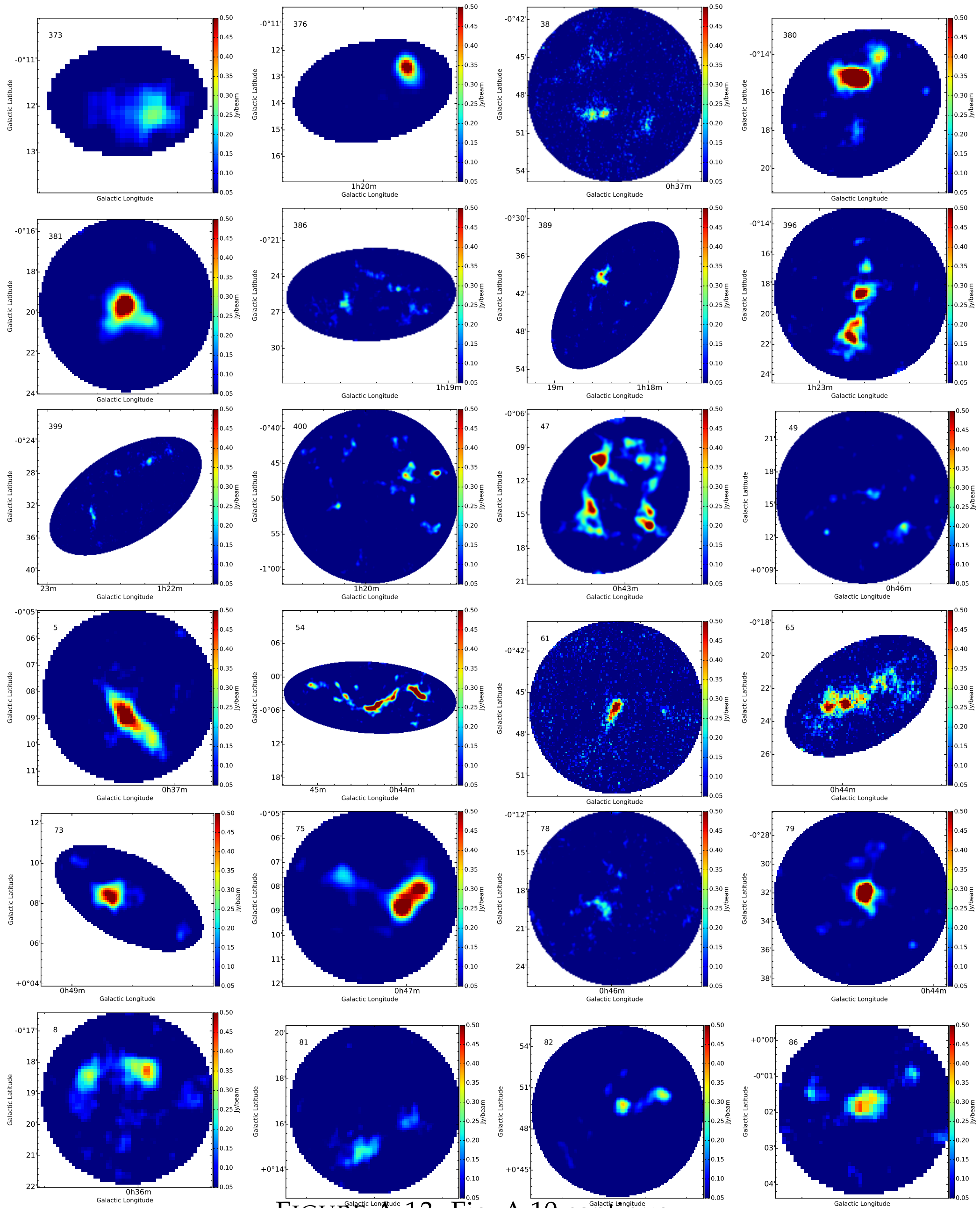

FIGURE A.13: Fig. A.10 continue.

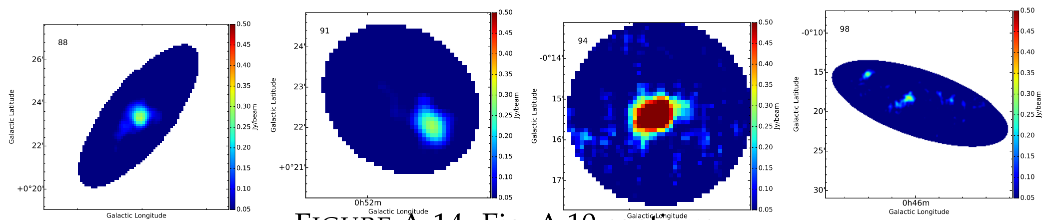

FIGURE A.14: Fig. A.10 continue.

TABLE A.1: Regions studied in this paper

ID	Type	RA (J2000)	DE (J2000)	Radius ($''$)	Maj. Ax ($''$)	Min. Ax ($''$)	Angle ($^\circ$)	d^b (kpc)	σ_D^c (kpc)	Ref.
2	SFC	18:05:35.91	-20:52:28.00	90	—	—	—	3.2	—	1
3	SFC	18:05:47.64	-21:00:32.00	90	—	—	—	4	—	1
4	HII	18:06:15.12	-20:31:36.50	150	—	—	—	5.5	0.4	3
5	SFC	18:06:46.98	-20:59:04.10	180	—	—	—	4.5	—	1
7	HII	18:06:52.03	-21:04:27.35	180	—	—	—	4.8	<0.1	4,6
8	SFC	18:06:53.75	-21:18:46.50	150	—	—	—	4.4	—	1
11	SFC	18:07:34.17	-20:26:03.30	150	—	—	—	2.6	—	1
13	SFC	18:07:42.18	-21:23:02.20	200	—	—	—	4.7	0.3	1
16	SFC	18:07:55.85	-20:28:26.60	220	—	—	—	2.5	—	1
27	HII	18:08:53.62	-18:16:08.10	350	—	—	—	3	0.1	4,2
28	SFC	18:08:59.71	-20:11:29.40	150	—	—	—	2	—	4
29	HII	18:09:23.23	-20:08:38.60	150	—	—	—	3.6	0.1	4,3
31	SFC	18:09:24.38	-20:01:35.70	220	—	—	—	2.3	0.4	1,4
30	HII	18:09:01.33	-19:48:33.30	—	290	250	-60	5.2	—	2
33	HII	18:09:05.33	-19:28:00.80	150	—	—	—	2.5	—	3
36	HII	18:09:37.96	-20:19:16.10	540	—	—	—	1.9	0.2	4
37	SFC	18:09:06.10	-21:03:37.20	420	—	—	—	3.7	0.3	4
38	SFC	18:09:22.35	-21:15:35.70	300	—	—	—	5.2	—	6
44	HII	18:09:29.30	-19:16:19.30	—	620	500	-60	3.4	—	8

TABLE A.1: Continued.

ID	Type	RA (J2000)	DE (J2000)	Radius ($''$)	Maj. Ax ($''$)	Min. Ax ($''$)	Angle ($^\circ$)	d^b (kpc)	σ_D^c (kpc)	Ref.
47	SFC	18:09:54.44	-19:44:46.90	—	450	360	-10	3.5	0.2	1,4,2
49	SFC	18:10:02.27	-18:50:12.00	280	—	—	—	3.4	—	1
50	HII	18:10:05.43	-20:59:11.90	360	—	—	—	3.7^a	—	4,8
51	HII	18:10:12.40	-20:46:22.90	—	800	260	-50	3.7	0.2	4,8
54	SFC	18:10:26.70	-19:20:56.20	—	920	380	-65	3.5	0.2	1,4,3,2,6
55	HII	18:10:54.13	-19:52:35.30	—	860	630	-30	5.2	—	6
60	HII	18:10:51.72	-17:55:57.40	240	—	—	—	2.4	0.3	1,4,6
61	SFC	18:10:54.72	-20:32:50.30	180	—	—	—	5.4	—	6
65	SFC	18:11:05.69	-19:37:05.40	—	300	180	-30	5.2	<0.1	6,2
72	HII	18:11:32.30	-19:30:42.10	300	—	—	—	5.2	<0.1	8,6
73	SFC	18:11:46.63	-18:17:40.40	—	240	120	90	3.8	—	1
74	HII	18:11:43.26	-18:16:54.00	—	480	300	-10	3.6	—	1
75	SFC	18:11:56.19	-18:48:14.50	200	—	—	—	3.2	—	1
78	SFC	18:11:59.63	-19:07:48.50	400	—	—	—	4.6	—	1
79	SFC	18:12:00.81	-19:36:00.90	350	—	—	—	3.2	—	1
81	SFC	18:12:04.07	-17:52:43.80	210	—	—	—	4.3	—	6
82	SFC	18:12:08.63	-16:42:41.60	360	—	—	—	3.4	—	6
83	HII	18:12:12.42	-17:40:52.80	—	450	360	-63	2.2	0.4	4,2,6
86	SFC	18:12:14.29	-18:26:52.00	130	—	—	—	4.8	—	6

TABLE A.1: Continued.

ID	Type	RA (J2000)	DE (J2000)	Radius ($''$)	Maj. Ax ($''$)	Min. Ax ($''$)	Angle (°)	d^b (kpc)	σ_D^c (kpc)	Ref.
88	SFC	18:12:26.51	-17:32:46.30	—	240	90	-10	3.9	—	6
90	HII	18:12:32.90	-18:30:13.00	80	—	—	—	4.2	<0.1	4,3
91	SFC	18:12:32.62	-17:29:16.80	—	120	100	80	3.6	—	1
94	SFC	18:12:41.69	-18:42:58.80	120	—	—	—	5	—	4
98	SFC	18:12:56.03	-19:04:23.40	—	700	250	-80	3.9	—	6
100	HII	18:13:09.20	-18:07:49.70	—	450	250	-40	2.6	<0.1	4,2
102	SFC	18:12:51.72	-18:48:13.50	—	500	120	-50	5	—	-6
103	HII	18:13:12.52	-18:00:07.20	150	—	—	—	2.6	0.1	4,3
104	SFC	18:13:12.15	-16:41:11.40	—	210	100	30	3	—	6
105	SFC	18:13:09.52	-18:15:57.60	—	370	240	-45	3.5	—	1
106	SFC	18:13:30.90	-17:18:06.70	165	—	—	—	2.3	—	1
108	SFC	18:13:38	-18:12:15.20	—	180	120	35	3.6	—	1
110	SFC	18:13:35.59	-17:23:47.20	—	270	210	-10	4.5	—	1
111	SFC	18:13:54.20	-17:16:28.50	—	330	210	90	2.4	—	1
114	HII	18:13:52.96	-18:56:44.90	—	450	300	100	3.9^a	0.3	4,3,8,6
116	HII	18:14:09.82	-17:27:24.20	—	570	220	-45	4.4	0.1	4,3,2
120	SFC	18:14:05.27	-18:14:49.00	300	—	—	—	3.5	—	1
121	SFC	18:14:13.00	-18:20:41.80	—	150	120	-30	5.1	—	6
122	HII	18:14:16.00	-17:57:18.60	—	780	550	-35	4	0.6	4,8,3,2

TABLE A.1: Continued.

ID	Type	RA (J2000)	DE (J2000)	Radius ($''$)	Maj. Ax ($''$)	Min. Ax ($''$)	Angle ($^\circ$)	d^b (kpc)	σ_D^c (kpc)	Ref.
123	SFC	18:14:16.28	-17:14:57.00	—	210	120	-60	2.8	—	1
134	HII	18:14:35.87	-16:45:31.30	—	960	560	-60	4.4	0.3	4
136	HII	18:14:30.50	-17:38:34.00	—	750	400	-65	4.4	0.6	1,4,2,6
140	SFC	18:14:50.37	-17:20:31.50	—	420	210	-75	4.5	—	4
146	SFC	18:14:55.69	-17:46:58.50	—	210	120	80	5.1	—	6
149	SFC	18:14:57.28	-18:27:01.10	270	—	—	—	5	—	6
152	SFC	18:15:01.51	-17:42:22.80	100	—	—	—	4.6	—	6
154	SFC	18:15:11.03	-17:47:21.20	—	360	130	95	3.7	—	1
159	SFC	18:15:46.15	-17:34:20.50	—	750	540	80	3.8	0.4	1,4,2,6
160	HII	18:15:37.51	-17:04:23.50	400	—	—	—	4.1	<0.1	4,3
162	SFC	18:15:38.97	-18:10:42.50	760	—	—	—	3.5	—	2,6
163	HII	18:15:40.22	-17:19:46.70	260	—	—	—	2.6	—	1
165	HII	18:15:45.18	-16:38:58.20	240	—	—	—	5.4	—	3
170	SFC	18:16:00.58	-16:04:53.20	440	—	—	—	2.8	—	4
175	SFC	18:16:12.68	-16:43:53.70	—	240	150	-10	4.3	—	6
177	SFC	18:16:20.00	-17:05:00.90	—	120	70	80	3.7	—	1
178	HII	18:16:31.62	-16:50:59.60	—	600	240	240	3.7	<0.1	4,2
179	HII	18:16:04.39	-19:42:05.20	460	—	—	—	1.6	—	8
183	SFC	18:16:45.65	-17:02:26.90	300	—	—	—	3.7	—	1

TABLE A.1: Continued.

ID	Type	RA (J2000)	DE (J2000)	Radius ($''$)	Maj. Ax ($''$)	Min. Ax ($''$)	Angle ($^\circ$)	d^b (kpc)	σ_D^c (kpc)	Ref.
185	HII	18:16:57.86	-16:15:33.90	—	600	360	-60	2.4	0.3	4,3,2,8
186	HII	18:16:51.62	-18:41:28.30	300	—	—	—	4	—	4
187	HII	18:16:58.96	-16:42:08.70	—	380	240	30	3.6	0.2	4,2,6
190	HII	18:17:11.87	-16:27:00.60	—	630	300	-25	3.7^a	0.1	4,3,2
192	SFC	18:16:18.76	-14:18:57.50	1100	—	—	—	2.2	0.2	4
195	SFC	18:17:27.20	-17:08:58.50	—	480	220	-45	2.7	0.3	1
196	SFC	18:17:21.85	-17:00:48.80	—	330	220	-60	2.3	—	6
200	SFC	18:17:36.02	-15:56:27.60	—	360	200	-30	2.7	0.1	4,7
202	SFC	18:17:31.86	-16:16:59.20	—	330	140	-80	3.7	—	1
207	SFC	18:17:35.93	-15:47:45.70	240	—	—	—	3.1	0.2	1,7
209	SFC	18:17:52.47	-16:29:02.00	—	370	210	-45	4.6	—	1
210	SFC	18:17:55.42	-17:13:05.50	250	—	—	—	2.9	—	6
214	HII	18:17:45.73	-16:01:22.20	—	400	200	-30	2.8	<0.1	7,6
217	SFC	18:17:59.25	-16:15:15.20	—	480	270	100	3.7	0.2	1,2,4
218	HII	18:18:09.85	-16:52:16.80	—	750	500	-70	2.5	0.4	1,2,4
219	SFC	18:18:15.15	-16:04:42.50	—	360	200	-10	3.9	—	7a
220	HII	18:18:16.55	-15:59:13.50	—	180	135	80	4	—	4,3
227	SFC	18:18:46.76	-16:22:29.30	—	170	150	80	4.6	—	1
228	HII	18:18:47.08	-13:32:56.90	—	2000	1200	-60	2	0.4	4,3,8,2,6

TABLE A.1: Continued.

ID	Type	RA (J2000)	DE (J2000)	Radius ($''$)	Maj. Ax ($''$)	Min. Ax ($''$)	Angle ($^\circ$)	d^b (kpc)	σ_D^c (kpc)	Ref.
230	HII	18:18:54.20	-16:48:55.70	—	260	160	90	2.7	0.3	4,2,8
233	SFC	18:19:06.85	-16:33:09.50	—	570	280	100	2.3	0.2	1,4,2
234	SFC	18:19:06.97	-16:11:20.30	300	—	—	—	4.7	<0.1	4
236	SFC	18:19:11.92	-16:18:25.60	—	420	150	—	2.6	—	1
238	SFC	18:19:38.17	-16:42:43.10	—	650	330	-45	2.4	—	1
242	HII	18:19:51.20	-15:55:05.60	200	—	—	—	2.3	—	4
246	SFC	18:20:12.44	-13:51:05.10	—	450	360	70	2.6	<0.1	7,6
247	SFC	18:20:37.42	-15:37:55.10	100	—	—	—	3.6	—	1
248	HII	18:20:27.49	-16:07:40.60	850	—	—	—	2.2	0.2	4,8,3,2
251	SFC	18:20:39.33	-14:02:41.30	450	—	—	—	2.6	—	1
253	SFC	18:20:56.57	-15:24:41.80	180	—	—	—	3.8	<0.1	1,4,6
256	HII	18:21:05.67	-14:17:49.10	—	580	340	90	2.5	—	7
259	HII	18:21:09.17	-14:31:46.20	—	700	350	-40	4.3^a	0.5	4,3,8
260	HII	18:21:10.92	-15:02:42.00	—	300	150	80	3.3	—	3
261	SFC	18:21:12.27	-16:30:08.20	210	—	—	—	2.6	—	1
263	HII	18:21:04.64	-14:46:39.40	—	600	450	-10	3.9	<0.1	4
265	SFC	18:21:44.83	-14:56:52.90	—	380	250	-60	3.9	—	6
270	HII	18:21:59.64	-14:16:11.60	—	360	260	-40	3.6^a	0.2	4,7
271	HII	18:22:04.97	-14:08:55.40	—	210	150	-30	3.6	—	4,3

TABLE A.1: Continued.

ID	Type	RA (J2000)	DE (J2000)	Radius ($''$)	Maj. Ax ($''$)	Min. Ax ($''$)	Angle ($^\circ$)	d^b (kpc)	σ_D^c (kpc)	Ref.
272	HII	18:22:05.14	-14:48:42.90	100	—	—	—	3.8	—	1
279	HII	18:22:22.95	-14:35:35.30	—	190	120	-60	3.8	—	1
287	SFC	18:22:41.01	-14:27:54.20	330	—	—	—	2.4	—	7
292	HII	18:22:52.78	-13:59:26.60	550	—	—	—	4.8	—	6
297	SFC	18:23:18.85	-13:15:50.60	240	—	—	—	2.2	<0.1	5,4,7
298	SFC	18:23:26.37	-13:49:53.30	240	—	—	—	4.3	—	7
301	HII	18:23:35.90	-13:09:28.50	240	—	—	—	6.6	—	5
302	SFC	18:23:37.57	-13:18:52.90	210	—	—	—	4.2	—	5
313	HII	18:24:34.34	-12:52:02.70	300	—	—	—	4	0.3	4,3,8
320	SFC	18:25:07.20	-14:35:12.50	400	—	—	—	3.4	—	4
322	SFC	18:25:09.19	-12:44:38.70	—	300	120	100	3.5	<0.1	1,4
323	HII	18:24:58.83	-12:01:05.50	650	—	—	—	4.5	—	6
325	HII	18:25:16.95	-13:14:13.00	850	—	—	—	4.6	0.5	4,3,8,2,5
326	SFC	18:25:19.61	-12:53:00.50	—	500	230	95	3.9	0.2	1,5,7
327	SFC	18:25:22.32	-13:34:38.30	320	—	—	—	4	0.5	1,7
328	HII	18:25:35.01	-12:20:58.10	—	660	360	65	4.2	0.1	4,2,5
330	SFC	18:25:28.88	-13:58:26.00	420	—	—	—	5.1	—	6
332	SFC	18:25:53.36	-12:06:08.30	360	—	—	—	2.5	<0.1	1
336	HII	18:26:00.56	-11:52:26.90	—	720	440	-20	1.9	—	4,8,3,5

TABLE A.1: Continued.

ID	Type	RA (J2000)	DE (J2000)	Radius (″)	Maj. Ax (″)	Min. Ax (″)	Angle (°)	d^b (kpc)	σ_D^c (kpc)	Ref.
340	HII	18:26:20.45	-12:40:52.20	240	—	—	—	4.6	0.3	4,7,6
341	SFC	18:26:22.16	-12:57:16.60	180	—	—	—	3.6	—	1
342	HII	18:26:24.02	-12:03:09.10	—	200	160	80	2.5	0.2	8,3
343	SFC	18:26:30.07	-12:32:42.00	—	360	300	10	4.7	0.3	7,6
348	SFC	18:26:46.14	-12:03:25.70	230	—	—	—	4.6	—	6
351	HII	18:26:44.64	-12:24:05.30	—	390	330	200	4.5	0.2	4,8,5
359	HII	18:27:03.75	-12:43:48.30	480	—	—	—	4.5	0.3	5,4,2,3
363	SFC	18:27:17.69	-10:36:28.60	300	—	—	—	2.6	0.1	1,7
365	SFC	18:27:09.45	-13:19:49.80	480	—	—	—	4.2	—	5
366	SFC	18:27:35.55	-12:19:14.70	290	—	—	—	4	0.1	1
367	SFC	18:27:45.09	-12:46:41.10	320	—	—	—	4.4	0.2	5,4
370	SFC	18:27:42.08	-11:36:29.60	—	300	180	-60	4.4	—	1
372	HII	18:27:52.09	-12:36:17.50	440	—	—	—	4.9	—	2,5
373	SFC	18:28:06.14	-11:39:09.90	—	100	70	-60	4.2	—	1
376	SFC	18:28:20.95	-11:35:51.60	—	180	110	-50	3.5	<0.1	1,4
380	SFC	18:28:23.18	-11:41:19.00	—	260	220	-30	4.4	0.3	1,4,7
381	SFC	18:28:23.59	-11:47:37.90	240	—	—	—	3.5	0.2	4,5
386	SFC	18:28:48.60	-11:48:40.00	—	420	230	-60	4.6	—	1
389	SFC	18:29:18.34	-12:10:38.60	—	820	430	-10	4.2	—	5

TABLE A.1: Continued.

ID	Type	RA (J2000)	DE (J2000)	Radius ($''$)	Maj. Ax ($''$)	Min. Ax ($''$)	Angle ($^\circ$)	d^b (kpc)	σ_D^c (kpc)	Ref.
390	SFC	18:29:14.36	-11:50:21.70	250	—	—	—	3.4	0.2	4,2,5
396	SFC	18:29:59.97	-11:00:30.50	330	—	—	—	4.2	0.2	1
399	SFC	18:30:30.89	-11:12:11.90	—	630	330	-30	4.7	—	5
400	SFC	18:30:30.81	-11:52:50.40	730	—	—	—	3.5	<0.1	5,7
406	HII	18:18:47.30	-15:48:58.30	220	—	—	—	1.9	—	7
407	HII	18:19:59.95	-15:27:06.90	560	—	—	—	3.7	—	6
26a	SLC	18:08:49.40	-19:40:15.00	80	—	—	—	3.1	<0.1	2,1
30a	SLC	18:09:08.56	-19:45:56.20	60	—	—	—	5.2	—	2
54c	SLC	18:10:40.07	-19:10:40.90	100	—	—	—	3.5	0.2	1,3,2,4
65a	SLC	18:11:09.60	-19:36:32.00	96	—	—	—	5.2	<0.1	2,6
83c	SLC	18:12:19.40	-17:40:12.20	70	—	—	—	2.2	0.4	2,4,6
106a	SLC	18:13:35.58	-17:18:39.60	—	60	35	-50	2.3	—	1
116b	SLC	18:14:13.22	-17:25:15.80	50	—	—	—	4.4	0.1	3,2,4
122b	SLC	18:13:43.80	-17:56:34.00	—	80	60	—	4	0.6	3,2,4,8
185a	SLC	18:16:50.35	-16:21:44.80	—	150	80	60	2.4	0.3	3,2,4,8
203a	SLC	18:17:32.59	-17:06:41.60	120	—	—	—	2.6	—	2
217a	SLC	18:18:02.99	-16:17:23.10	80	—	—	—	3.7	0.2	1,2,4
218b	SLC	18:18:03.23	-16:54:35.50	—	95	60	-80	2.5	0.4	1,2,4
233a	SLC	18:19:02.22	-16:39:59.00	125	—	—	—	2.3	0.2	1,2,4

TABLE A.1: Continued.

ID	Type	RA (J2000)	DE (J2000)	Radius ($''$)	Maj. Ax ($''$)	Min. Ax ($''$)	Angle ($^\circ$)	d^b (kpc)	σ_D^c (kpc)	Ref.
233b	SLC	18:19:13.55	-16:34:57.10	85	—	—	—	2.3	0.2	1,2,4
233e	SLC	18:19:13.36	-16:35:04.20	100	—	—	—	2.3	0.2	1,2,4
247a	SLC	18:20:23.82	-15:38:31.80	—	170	80	95	3.6	—	1
325g	SLC	18:25:23.77	-13:19:04.50	—	125	80	-10	4.6	0.5	2,3,4,5,8
325i	SLC	18:25:22.56	-13:17:13.40	40	—	—	—	4.6	0.5	2,3,4,5,8
328c	SLC	18:25:22.76	-12:23:26.90	100	—	—	—	4.2	0.1	2,4,5
379a	SLC	18:28:18.30	-12:06:26.00	170	—	—	—	4.4	—	2
390b	SLC	18:29:26.67	-11:50:45.60	50	—	—	—	3.4	0.2	2,4,5
159a	SLC	18:16:06.90	-17:36:27.10	65	—	—	—	3.8	0.4	1,2,4,8
162a	SLC	18:15:40.50	-18:13:08.00	75	—	—	—	3.5	<0.1	2,6
160a	SLC	18:15:25.30	-17:05:43.70	90	—	—	—	4.1	<0.1	3,2,4
187f	SLC	18:16:59.68	-16:39:26.80	—	90	70	-40	4	0.2	2,4,6
212a	SLC	18:17:50.60	-15:53:34.00	50	—	—	—	2.7	—	2
212e	SLC	18:17:52.84	-15:55:16.90	50	—	—	—	2.7	—	2
253a	SLC	18:20:55.50	-15:24:05.00	50	—	—	—	3.8	<0.1	1,4,6
329a	SLC	18:25:32.88	-13:01:51.70	120	—	—	—	4.5	—	2
372a	SLC	18:27:43.01	-12:35:42.70	50	—	—	—	4.9	<0.1	2,5
397a	SLC	18:30:02.90	-12:15:51.00	120	—	—	—	3.1	—	2

(1) Ellsworth-Bowers et al. (2013); (2) Tackenberg et al. (2012); (3) Urquhart et al. (2013b); (4) Wienen et al. (2012); (5) Roman-Duval et al. (2009); (6) **2009ApJ...706..727M** (7) Simon et al. (2006); (8) Walsh et al. (1997).

a) These regions have not previous solution for the KDA, but they show shadows against the NIR background radiation, so we located them at the near distance solution. **b)** The distance shown in this table is the result of averaging all the distance estimates available for each source. **c)** The dispersion of all the distance estimates available for each region, when more than one distance estimates are available.

Appendix B

Extra material for GMFs

B.1 Notes on individual GMFs

B.1.1 GMF 307.2-305.4

The GMF 307.2-305.4 can be identified as a mixture of emission and extinction features (see Fig. 4.1). This filament shows the widest velocity range of the sample [-29,-39] km/s. This wide velocity spread can be caused by the location of the filament, close to the tangent point (see also Fig. 4.3), or by the expanding bubble generated by the massive G305 H II complex (Hindson et al., 2010; Davies et al., 2012), that can be identified as emission in the 8 μm image. This H II region has a molecular gas mass of $\sim 6 \times 10^5_\odot$ (Hindson et al., 2010). We find several dense gas clumps in this complex that have velocities consistent with the GMF. GMF 307.2-305.4 lies within the Scutum-Centaurus spiral arm. This is consistent with previous works that relate G 305 to the Scutum-Centaurus arm (Hindson et al., 2010; Davies et al., 2012).

B.1.2 GMF 309.5-308.7

The only GMF aligned perpendicularly to the Galactic plane, it can be seen at 8 μm as a vertical extinction feature connecting a series of strong emitting regions, known to be regions of massive star-forming activity: RCW79 (Saito et al., 2001; Russeil, 2003; Zavagno et al., 2006) in the north, and Gum 48d (Karr, Manoj, and Ohashi, 2009) in the south, the latter connected to the Scutum-Centaurus arm. Previous distance estimates of these H II regions agree with those found in this paper. Some supernova remnants are

TABLE B.1: L–B–V tracks of the filaments

				GMF 307.2-305.4			
l [°]	307.3	306.6	305.8	305.7	305.5	305.2	305.1
b [°]	0.14	-0.12	-0.10	-0.03	-0.03	-0.03	-0.05
v [km/s]	-30	-29	-34	-38	-37	-33	-35
				GMF 309.5-308.7			
l [°]	309.2	309.1	309.0	308.7			
b [°]	-0.48	-0.16	-0.13	0.63			
v [km/s]	-45	-43	-44	-46			
				GMF 319.0-318.7			
l [°]	319.3	318.8	318.5	318.3	318.1	317.7	317.5
b [°]	-0.08	-0.17	-0.23	-0.38	-0.07	0.07	
v [km/s]	-37	-38	-40	-38	-43	-40	-44
				GMF 324.5-321.4			
l [°]	323.9	321.5					
b [°]	-0.46	0.10					
v [km/s]	-32	-32					
				GMF 335.6-333.6			
l [°]	335.2	334.6	332.9	332.3			
b [°]	-0.26	-0.21	-0.50	-0.48			
v [km/s]	-41	-47	-54	-55			
				GMF 335.6-333.6b			
l [°]	332.7	332.5	332.3	331.9	331.6	331.4	
b [°]	-0.23	-0.13	-0.12	-0.11	-0.24	-0.33	
v [km/s]	-45	-47	-50	-50	-46	-48	
				GMF 341.9-337.1			
l [°]	342.2	341.5	340.8	340.3			
b [°]	-0.13	-0.29	-0.23	-0.14			
v [km/s]	-41	-41	-46	-45			
				GMF 343.2-341.7			
l [°]	342.8	342.1	341.9	341.8			
b [°]	0.07	0.19	0.29				
v [km/s]	-42	-41	-43	-43			
				GMF 358.9-357.4			
l [°]	358.4	358.1	357.8	357.5	357.1		
b [°]	-0.48	-0.44	-0.32	-0.32	-0.02		
v [km/s]	4	5	7	5	7		

found within GMF 309.5-308.7 and close to it at lower longitudes, confirming the very active recent massive star-forming activity in the region. Unfortunately, ThruMMS does not fully cover the filament. The southern region has not been observed in either ^{12}CO or ^{13}CO (see red boxes in Fig. B.1). The total molecular mass of the GMF is therefore a lower limit.

B.1.3 GMF 319.0-318.7

We identified the GMF as an extinction feature connecting two star-forming sites. However, a close look to the GMF presents it as two dense filaments, both following extinction features connected by a diffuse envelope (see Fig. B.2). This GMF is located within the predicted Scutum-Centaurus arm.

B.1.4 GMF 324.5-321.4

The most prominent extinction feature is the IRDC 321.71+0.07 (Vasyunina et al., 2009), located at a distance of 2.14kpc. The red box in the bottom-left corner of Fig. B.3 shows that there is no ThruMMS coverage of that area. The red box in the middle of the filament shows a region with very high noise. In this region the east and west ends of GMF 324.5-321.4 are barely connected. Although the ^{12}CO map shows a clear connection between both parts of the filament, we proceed with caution, dividing this GMF in two possible filaments: the whole filament from $l = 321.5\,^{\circ}$ to $l = 324.5\,^{\circ}$, and a shorter version from $l = 321.5\,^{\circ}$ to $l = 322.5\,^{\circ}$ called GMF 324.5-321.4b. All the dense gas mass of this filament is located in IRDC 321.71+0.07, so that the DGMF of GMF 324.5-321.4b is considerably larger than that of the longer GMF 324.5-321.4. This is the only filament showing no velocity gradient along it. GMF 324.5-321.4 and GMF 324.5-321.4b are not connected to any spiral arm.

B.1.5 GMF 335.6-333.6

It harbors one of the best studied H II regions in the southern Galactic hemisphere, G333 or RCW106 (Mookerjea et al., 2004; Roman-Lopes et al., 2009). This H II region is located at 3.6 kpc (in agreement with the distance to our GMF), it has a size of 30×90 pc and a mass of $\sim 2.7 \times 10^5_{\odot}$ (Bains et al., 2006). GMF 335.6-333.6 is seen as an extinction feature connected to RCW106. The

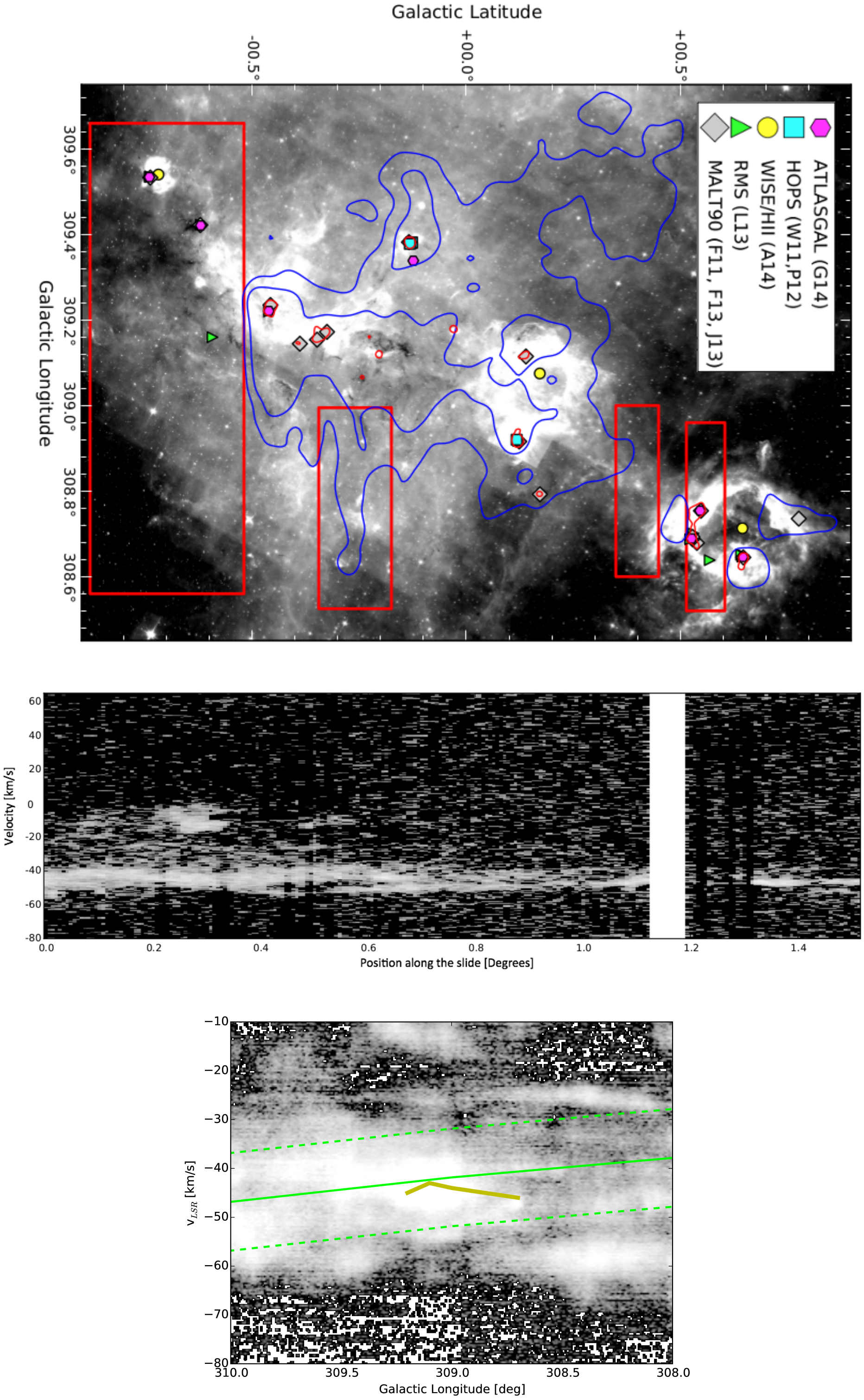

FIGURE B.1: Like Fig. 4.1 for GMF 309.5-308.7.

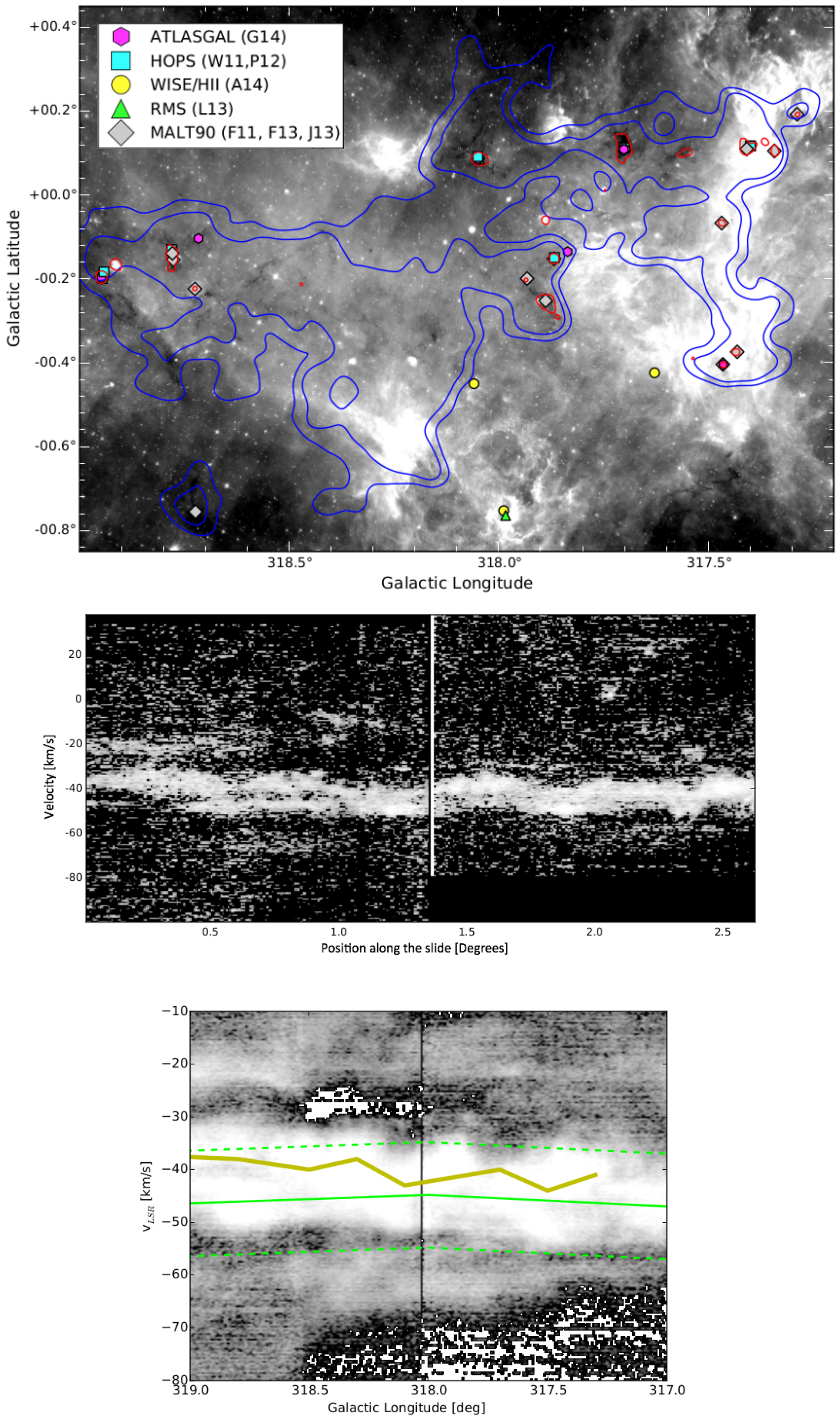

FIGURE B.2: Like Fig. 4.1 for GMF 319.0–318.7.

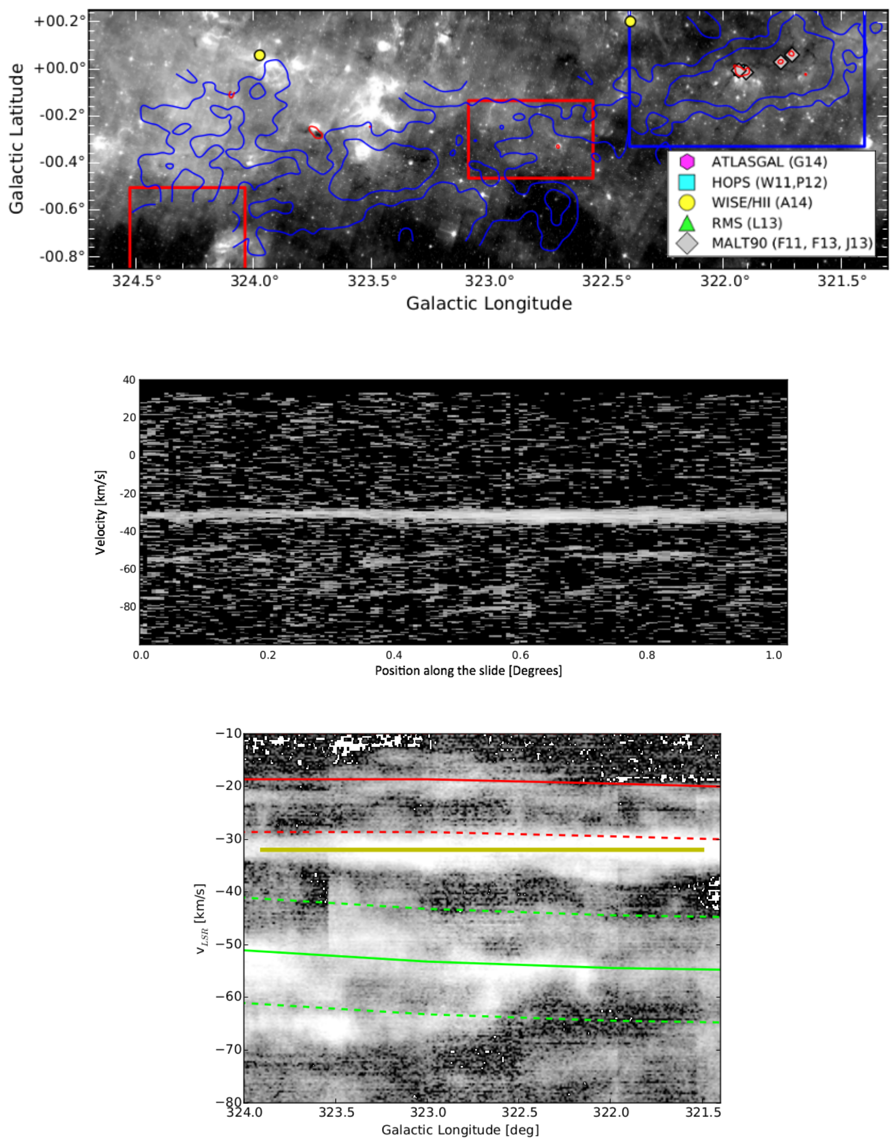

FIGURE B.3: Like Fig. 4.1 for GMF 324.5–321.4.

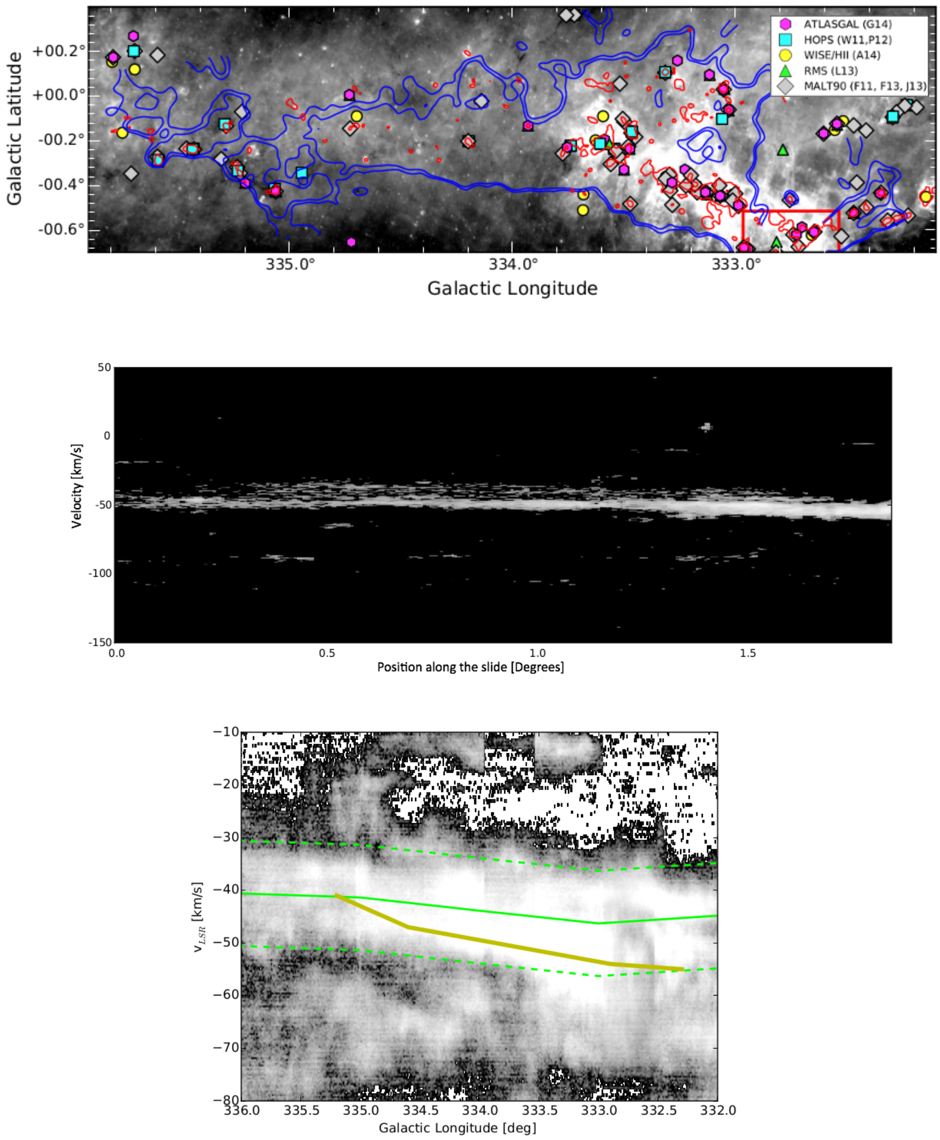

FIGURE B.4: Like Fig. 4.1 for GMF 335.6–333.6.

RCW106 complex is the main cause of the remarkably high DGMF ($\sim 37\%$) measured in GMF 335.6-333.6a. The end at higher galactic longitudes is connected to the S40 bubble. There is a small region of the GMF that is not covered by ThruMMS, as it is shown with the red box in Fig. B.4. This GMF lies in the Scutum-Centaurus arm.

B.1.6 GMF 335.6-333.6b

This filament is very close to GMF 335.6-333.6a and it is recognizable as a prominent extinction feature connecting two star-forming sites. It also has velocity close to that of GMF 335.6-333.6. Although in the first step we included GMF 335.6-333.6b as part of GMF 335.6-333.6, we finally divided them for two reasons: first, because they are not connected in ^{13}CO, and second because their velocities slightly differ. GMF 335.6-333.6b has also been identified as a Milky Way bone (see Sect. 4.4.1) by Zucker, Battersby, and Goodman (2015). GMF 335.6-333.6b lies in the Scutum-Centaurus arm.

B.1.7 GMF 341.9-337.1

GMF 341.9-337.1 has a H II region in its low-longitude end and another one, much more compact, in the middle. An extinction feature connects both star-forming sites and extends towards increasing longitudes. The southern part of the filament is not completely covered by ThruMMS (see the red boxes in Fig. B.6). As shown in Fig. B.6, almost every AGAL clump in this filament has additional kinematic information confirming the location of the dense gas inside GMF 341.9-337.1.

This filament seem to be part of Nessie extended (Goodman et al., 2014). However, GMF 341.9-337.1 does not lie in the Scutum-Centaurus arm, as Nessie extended does, but rather in an inter-arm region (see Fig. B.6). We explore the reasons of this discrepancy below. Figure B.6 shows that the emission of the Scutum-Centaurus arm has velocities of about [-35,-25] km/s, while the velocities of GMF 341.9-337.1 are lower, [-48,-43] km/s. This fact raises the question on whether GMF 341.9-337.1 is connected to Nessie extended.

We integrated the ^{13}CO emission over the expected velocity range of Nessie extended to investigate whether it overlaps with GMF 341.9-337.1. In Fig. B.6 we show that both filaments overlap each other. However, there are extinction features that are only covered by GMF 341.9-337.1 and we also find that most of the star-forming sites known are connected to GMF 341.9-337.1 rather than to Nessie extended. We conclude that there are overlapping extinction features in this region, better matched by GMF 341.9-337.1. This filament lies in an inter-arm region.

B.1.8 GMF 343.2-341.7

Two extinction features separated by a H II region in projection. The high longitude end of the GMF is connected to another smaller H II region. The

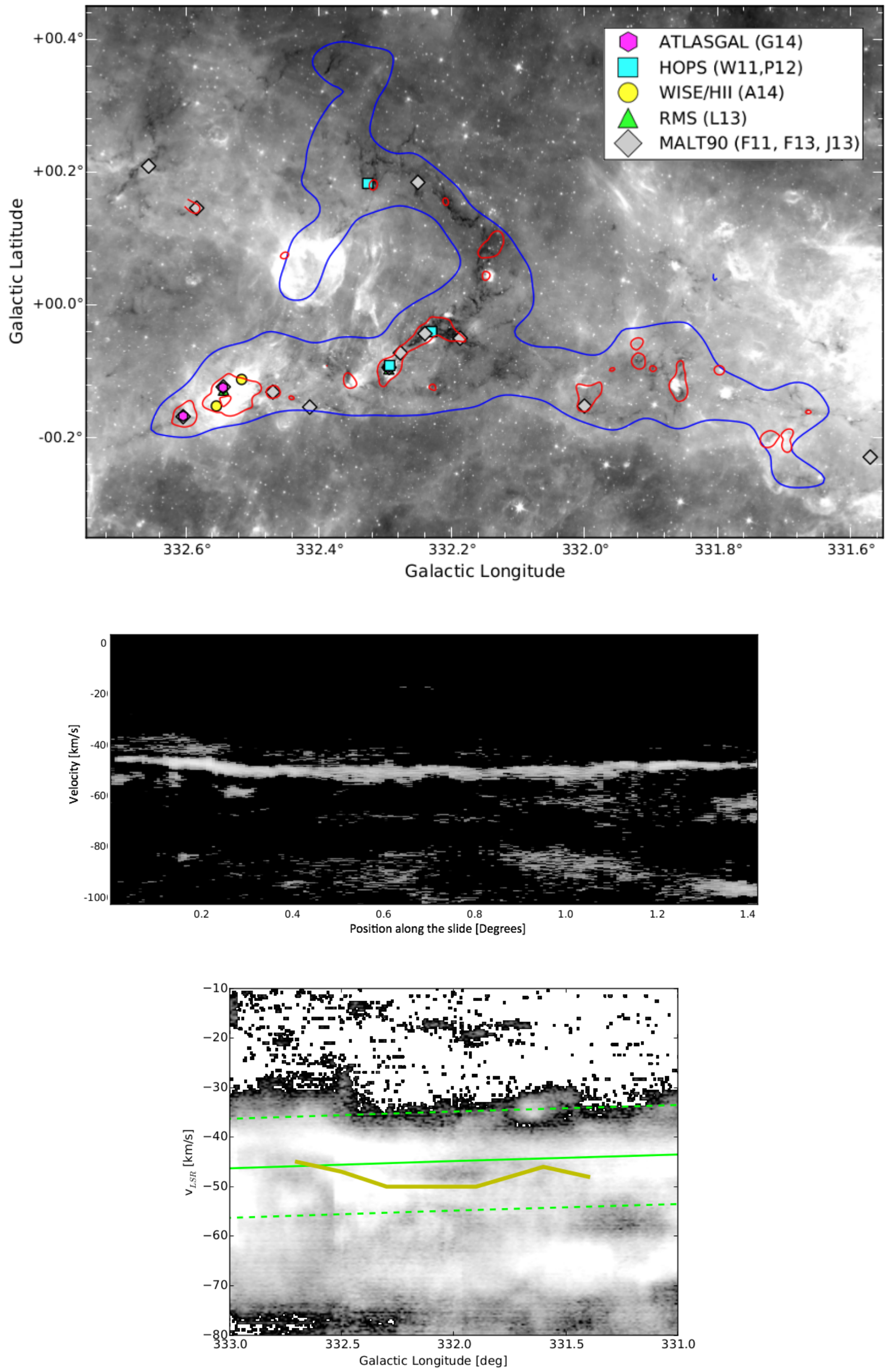

FIGURE B.5: Like Fig. 4.1 for GMF 335.6–333.6b.

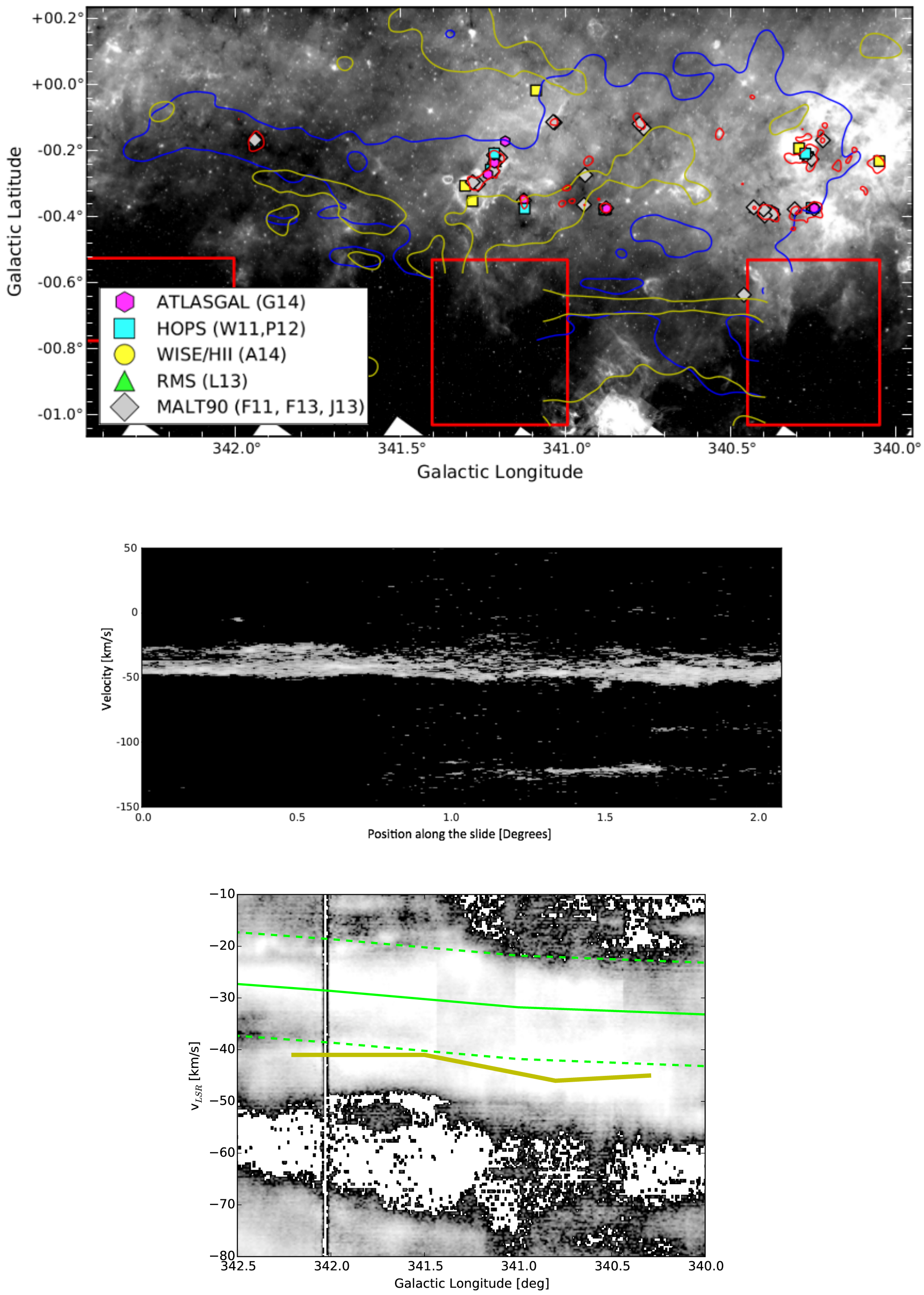

FIGURE B.6: Like Fig. 4.1 for GMF 341.9–337.1.

significant ^{13}CO emission of this filament shows two separated objects, although they are connected by significant ^{12}CO emission. We note that there are high noise features in the ThruMMS data exactly in those ^{13}CO empty regions that could hide a significant connection between the two parts of the ^{13}CO filament (red boxes in Fig. B.7). The high longitude section of the filament shows no dense gas, nor dense clumps connected to GMF 343.2-341.7. The GMF is not connected to any spiral arm, as it is shown in the bottom panel of Fig. B.7.

B.1.9 GMF 358.9-357.4

It lies in a very crowded region. Every spiral arm at these Galactic latitudes has velocities close to 0 km/s. This makes it difficult to isolate single velocity components. The most prominent extinction feature in GMF 358.9-357.4 is the IRDC known as G357 (Marshall, Joncas, and Jones, 2009). After isolating its velocity component we found that it lies inside a much larger ^{13}CO complex. The distance estimates in this region are particularly hard to obtain using the Reid et al. (2014) model. We therefore rejected this model for this filament and instead used the distances from the literature: 3.3 kpc (Marshall, Joncas, and Jones, 2009). This distance estimate places GMF 358.9-357.4 in the Scuttum-Crux arm.

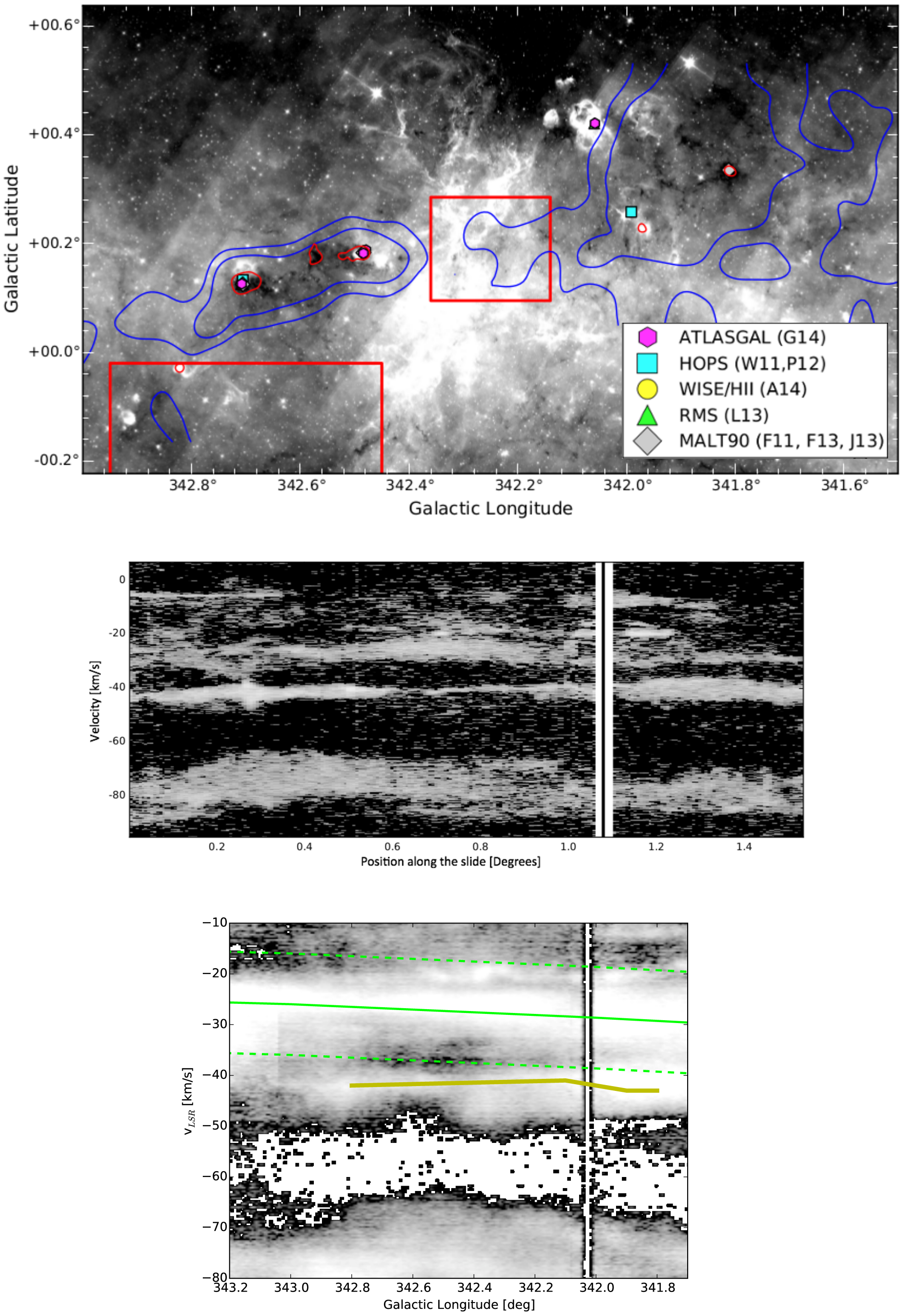

FIGURE B.7: Like Fig. 4.1 for GMF 343.2–341.7.

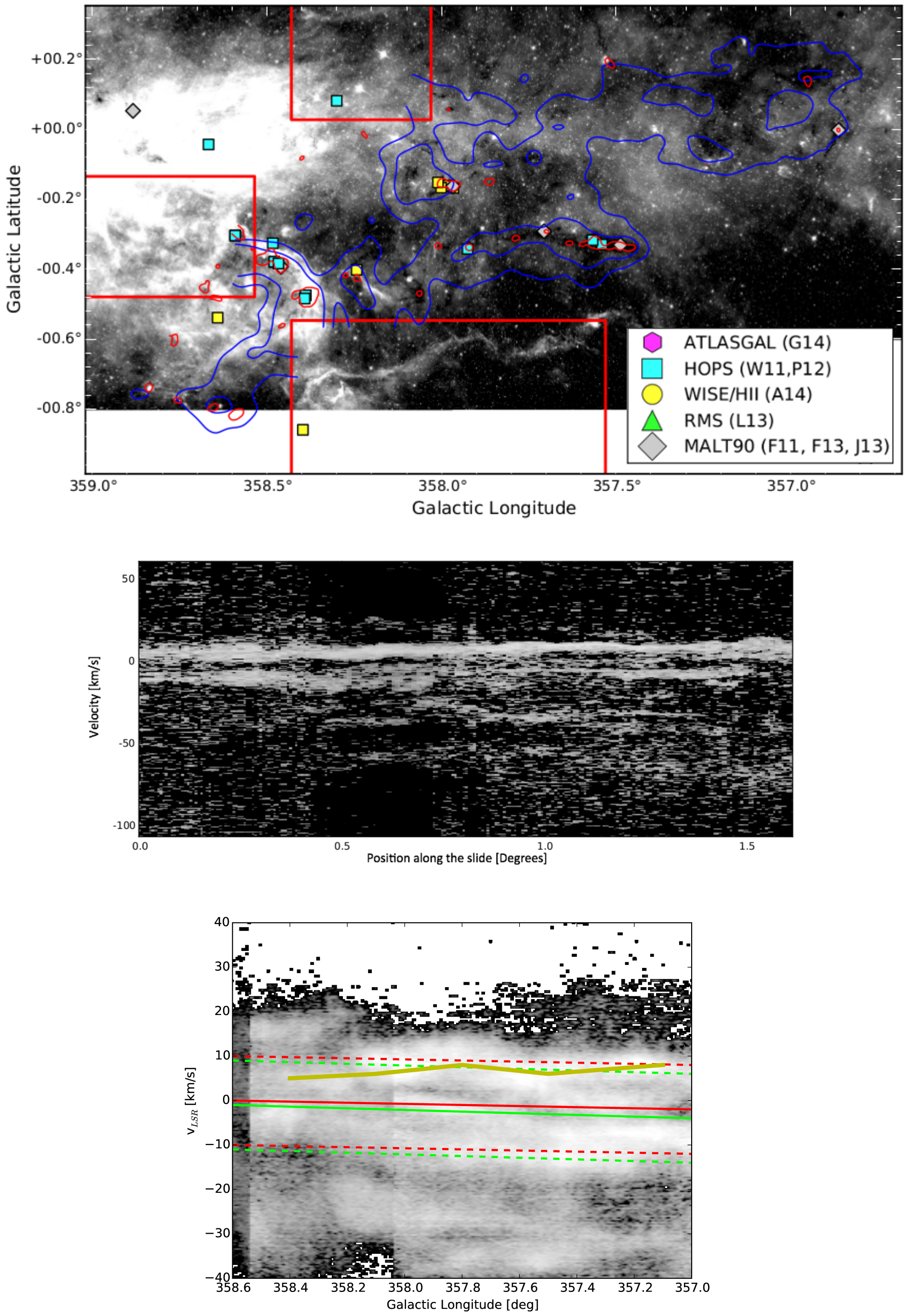

FIGURE B.8: Like Fig. 4.1 for GMF 358.9–357.4.

TABLE B.2: L–B–V tracks of the filaments

			GMF 307.2-305.4				
l [°]	307.3	306.6	305.8	305.7	305.5	305.2	305.1
b [°]	0.14	-0.12	-0.10	-0.03	-0.03	-0.03	-0.05
v [km/s]	-30	-29	-34	-38	-37	-33	-35
			GMF 309.5-308.7				
l [°]	309.2	309.1	309.0	308.7			
b [°]	-0.48	-0.16	-0.13	0.63			
v [km/s]	-45	-43	-44	-46			
			GMF 319.0-318.7				
l [°]	319.3	318.8	318.5	318.3	318.1	317.7	317.5
b [°]	-0.08	-0.17	-0.23	-0.38	-0.07	0.07	
v [km/s]	-37	-38	-40	-38	-43	-40	-44
			GMF 324.5-321.4				
l [°]	323.9	321.5					
b [°]	-0.46	0.10					
v [km/s]	-32	-32					
			GMF 335.6-333.6				
l [°]	335.2	334.6	332.9	332.3			
b [°]	-0.26	-0.21	-0.50	-0.48			
v [km/s]	-41	-47	-54	-55			
			GMF 335.6-333.6b				
l [°]	332.7	332.5	332.3	331.9	331.6	331.4	
b [°]	-0.23	-0.13	-0.12	-0.11	-0.24	-0.33	
v [km/s]	-45	-47	-50	-50	-46	-48	
			GMF 341.9-337.1				
l [°]	342.2	341.5	340.8	340.3			
b [°]	-0.13	-0.29	-0.23	-0.14			
v [km/s]	-41	-41	-46	-45			
			GMF 343.2-341.7				
l [°]	342.8	342.1	341.9	341.8			
b [°]	0.07	0.19	0.29				
v [km/s]	-42	-41	-43	-43			
			GMF 358.9-357.4				
l [°]	358.4	358.1	357.8	357.5	357.1		
b [°]	-0.48	-0.44	-0.32	-0.32	-0.02		
v [km/s]	4	5	7	5	7		

TABLE B.3: Dense gas tracers and star-forming signs associated to our GMFs

l [°]	b [°]	v_{LSR} $[km/s]$	Filament assoc.	Object/line	Survey	Ref.
305.18	0.21	-42.5	3054_ 3072	CO	AGAL	1
304.55	0.34	-42.9	3054_ 3072	NH_3	HOPS	2
305.22	0.21	-39.0	3054_ 3072	H II	WISE	3
304.89	0.64	-36.2	3054_ 3072	YSOs	RMS	4
304.02	0.29	-42.4	3054_ 3072	Several[(a)]	MALT90	5
304.00	0.28	-41.4	3054_ 3072	CH_3OH	AGAL	6
305.14	0.07	-38.4	3054_ 3072	H_2O	HOPS	8
309.34	-0.12	-51.3	3095_ 3087	CO	AGAL	1
309.94	0.40	-41.3	3095_ 3087	CO	AGAL	1
309.38	-0.13	-50.6	3095_ 3087	NH_3	HOPS	2
308.71	0.65	-50.0	3095_ 3087	H II	WISE	3
309.07	0.17	-47.0	3095_ 3087	H II	WISE	3
309.54	-0.72	-43.0	3095_ 3087	H II	WISE	3
308.00	-0.39	-37.6	3095_ 3087	YSOs	RMS	4
308.64	0.57	-44.4	3095_ 3087	YSOs	RMS	4
308.12	-0.34	-47.1	3095_ 3087	Several[(a)]	MALT90	5
308.64	0.65	-47.6	3095_ 3087	Several[(a)]	MALT90	5
308.68	0.54	-44.9	3095_ 3087	Several[(a)]	MALT90	5
308.00	-0.39	-37.6	3095_ 3087	CH_3OH	AGAL	6
308.92	0.12	-50.5	3095_ 3087	H_2O	HOPS	8
332.23	-0.04	-48.0	3356_ 3336	NH_3	HOPS	2
356.66	-0.26	6.6	3589_ 3574	CH_3OH	AGAL	7
357.92	-0.34	3.2	3589_ 3574	CH_3OH	AGAL	7
357.92	-0.34	1.8	3589_ 3574	CH_3OH	AGAL	7
356.47	0.01	1.3	3589_ 3574	H_2O masers	HOPS	8
356.65	-0.32	4.6	3589_ 3574	H_2O	HOPS	8
357.93	-0.34	1.4	3589_ 3574	H_2O	HOPS	8
358.48	-0.33	0.3	3589_ 3574	H_2O	HOPS	8

(1) Giannetti et al. (2014); (2) Purcell et al. (2012); (3) Anderson et al. (2014); (4) Lumsden et al. (2013b); (5) Foster et al. (2011), Foster et al. (2013), and Jackson et al. (2013); (6) Urquhart et al. (2013a); (7) Urquhart et al. (2014); (8) Walsh et al. (2011); [(a)] See Table. 1 in Jackson et al. (2013). **This is a extract of the table A.2 in abreu16 The full table is available online at: http://vizier.cfa.harvard.edu/viz-bin/VizieR?-source=J/A+A/590/A131.**

Bibliography

Abergel, A. et al. (1994). “Comparative analysis of the far-infrared and (13)CO (J = 0-1) emissions of the Taurus complex”. In: *ApJ* 423, pp. L59–L62.

Abreu-Vicente, J. et al. (2015). “Relationship between the column density distribution and evolutionary class of molecular clouds as viewed by ATLASGAL”. In: *A&A* 581, A74, A74.

Aguirre, J. E. et al. (2011). “The Bolocam Galactic Plane Survey: Survey Description and Data Reduction”. In: *ApJS* 192, 4, p. 4.

Alves, J., M. Lombardi, and C. J. Lada (2007). “The mass function of dense molecular cores and the origin of the IMF”. In: *A&A* 462, pp. L17–L21.

— (2014). “2MASS wide-field extinction maps. V. Corona Australis”. In: *A&A* 565, A18, A18.

Anderson, L. D. et al. (2012). “The dust properties of bubble H II regions as seen by Herschel”. In: *A&A* 542, A10, A10.

Anderson, L. D. et al. (2014). “The WISE Catalog of Galactic H II Regions”. In: *ApJS* 212, 1, p. 1.

André, P. et al. (2010a). “From filamentary clouds to prestellar cores to the stellar IMF: Initial highlights from the Herschel Gould Belt Survey”. In: *A&A* 518, L102, p. L102.

— (2010b). “From filamentary clouds to prestellar cores to the stellar IMF: Initial highlights from the Herschel Gould Belt Survey”. In: *A&A* 518, L102, p. L102.

André, P. et al. (2014a). “From Filamentary Networks to Dense Cores in Molecular Clouds: Toward a New Paradigm for Star Formation”. In: *Protostars and Planets VI*, pp. 27–51.

— (2014b). “From Filamentary Networks to Dense Cores in Molecular Clouds: Toward a New Paradigm for Star Formation”. In: *Protostars and Planets VI*, pp. 27–51.

Aniano, G. et al. (2011). “Common-Resolution Convolution Kernels for Space- and Ground-Based Telescopes”. In: *PASP* 123, pp. 1218–1236.

Arzoumanian, D. et al. (2011). “Characterizing interstellar filaments with Herschel in IC 5146”. In: *A&A* 529, L6, p. L6.

Bains, I. et al. (2006). “Molecular line mapping of the giant molecular cloud associated with RCW 106 - I. ^{13}CO”. In: *MNRAS* 367, pp. 1609–1628.

Ballesteros-Paredes, J. et al. (2011). “Gravity or turbulence? - II. Evolving column density probability distribution functions in molecular clouds”. In: *MNRAS* 416, pp. 1436–1442.

Bally, J. et al. (1987). “Filamentary structure in the Orion molecular cloud”. In: *ApJ* 312, pp. L45–L49.

Banerjee, R. et al. (2009). “Clump morphology and evolution in MHD simulations of molecular cloud formation”. In: *MNRAS* 398, pp. 1082–1092.

Barnard, E. E. (1919). “On the dark markings of the sky, with a catalogue of 182 such objects.” In: *ApJ* 49.

— (1927). *Catalogue of 349 dark objects in the sky*.

Barnes, P. et al. (2011). *ThrUMMS (MALT110): the Three-mm Ultimate Mopra Milky way Survey*. ATNF Proposal.

Barnes, P. et al. (2014). *The Three-mm Ultimate Mopra Milky way Survey (MALT110): Completion of Phase II*. ATNF Proposal.

Barnes, P. J. et al. (2015). “The Three-mm Ultimate Mopra Milky Way Survey. I. Survey Overview, Initial Data Releases, and First Results”. In: *ApJ* 812, 6, p. 6.

Battersby, C. and J. Bally (2014). “An 80 pc Long Massive Molecular Filament in the Galactic Mid-Plane”. In: *Astrophysics and Space Science Proceedings* 36, p. 417.

Battisti, A. J. and M. H. Heyer (2014a). “The Dense Gas Mass Fraction of Molecular Clouds in the Milky Way”. In: *ApJ* 780, 173, p. 173.

— (2014b). “The Dense Gas Mass Fraction of Molecular Clouds in the Milky Way”. In: *ApJ* 780, 173, p. 173.

Benjamin, R. A. et al. (2003). “GLIMPSE. I. An SIRTF Legacy Project to Map the Inner Galaxy”. In: *PASP* 115, pp. 953–964.

Bergin, E. A. and M. Tafalla (2007). “Cold Dark Clouds: The Initial Conditions for Star Formation”. In: *ARA&A* 45, pp. 339–396.

Bernard, J.-P. et al. (2010). “Dust temperature tracing the ISRF intensity in the Galaxy”. In: *A&A* 518, L88, p. L88.

Beuther, H. et al. (2002). “High-Mass Protostellar Candidates. II. Density Structure from Dust Continuum and CS Emission”. In: *ApJ* 566, pp. 945–965.

Beuther, H. et al. (2007). “The Formation of Massive Stars”. In: *Protostars and Planets V*, pp. 165–180.

Beuther, H. et al. (2011). “The Coalsack near and far”. In: *A&A* 533, A17, A17.

Bigiel, F. et al. (2008). “The Star Formation Law in Nearby Galaxies on Sub-Kpc Scales”. In: *AJ* 136, pp. 2846–2871.

Bohlin, R. C., B. D. Savage, and J. F. Drake (1978). “A survey of interstellar H I from L-alpha absorption measurements. II”. In: *ApJ* 224, pp. 132–142.

Bok, B. J. and E. F. Reilly (1947). “Small Dark Nebulae.” In: *ApJ* 105, p. 255.

Bolatto, A. D., M. Wolfire, and A. K. Leroy (2013). “The CO-to-H_2 Conversion Factor”. In: *ARA&A* 51, pp. 207–268.

Bolatto, A. D. et al. (2008). “The Resolved Properties of Extragalactic Giant Molecular Clouds”. In: *ApJ* 686, 948-965, pp. 948–965.

Bronfman, L., L.-A. Nyman, and J. May (1996). “A CS(2-1) survey of IRAS point sources with color characteristics of ultra-compact HII regions.” In: *A&AS* 115, p. 81.

Brunt, C. M. (2010). “The density variance - Mach number relation in the Taurus molecular cloud”. In: *A&A* 513, A67, A67.

Brunt, C. M., C. Federrath, and D. J. Price (2010). “A method for reconstructing the variance of a 3D physical field from 2D observations: application to turbulence in the interstellar medium”. In: *MNRAS* 403, pp. 1507–1515.

Burkert, A. and L. Hartmann (2004). “Collapse and Fragmentation in Finite Sheets”. In: *ApJ* 616, pp. 288–300.

Caselli, P. et al. (2002). “Dense Cores in Dark Clouds. XIV. N_2H^+ (1-0) Maps of Dense Cloud Cores”. In: *ApJ* 572, pp. 238–263.

Chini, R. et al. (1997). “Dust Filaments and Star Formation in OMC-2 and OMC-3”. In: *ApJ* 474, pp. L135–L138.

Commerçon, B. et al. (2011). “Radiative, magnetic and numerical feedbacks on small-scale fragmentation”. In: *Computational Star Formation*. Ed. by J. Alves et al. Vol. 270. IAU Symposium, pp. 227–230.

Csengeri, T. et al. (2014a). “The ATLASGAL survey: a catalog of dust condensations in the Galactic plane”. In: *A&A* 565, A75, A75.

— (2014b). “The ATLASGAL survey: a catalog of dust condensations in the Galactic plane”. In: *A&A* 565, A75, A75.

Csengeri, T. et al. (2016). “The ATLASGAL survey: distribution of cold dust in the Galactic plane. Combination with Planck data”. In: *A&A* 585, A104, A104.

Cyganowski, C. J. et al. (2008). "A Catalog of Extended Green Objects in the GLIMPSE Survey: A New Sample of Massive Young Stellar Object Outflow Candidates". In: *AJ* 136, 2391, pp. 2391–2412.

Dame, T. M., D. Hartmann, and P. Thaddeus (2001). "The Milky Way in Molecular Clouds: A New Complete CO Survey". In: *ApJ* 547, pp. 792–813.

Dame, T. M. et al. (1986). "The largest molecular cloud complexes in the first galactic quadrant". In: *ApJ* 305, pp. 892–908.

Dame, T. M. et al. (1987). "A composite CO survey of the entire Milky Way". In: *ApJ* 322, pp. 706–720.

Davies, B. et al. (2012). "The G305 star-forming complex: the central star clusters Danks 1 and Danks 2". In: *MNRAS* 419, pp. 1871–1886.

Dempsey, J. T., H. S. Thomas, and M. J. Currie (2013). "CO (3 - 2) High-resolution Survey of the Galactic Plane: R1". In: *ApJS* 209, 8, p. 8.

di Francesco, J. et al. (2007). "An Observational Perspective of Low-Mass Dense Cores I: Internal Physical and Chemical Properties". In: *Protostars and Planets V*, pp. 17–32.

Dobbs, C. L. and A. Burkert (2012). "The myth of the molecular ring". In: *MNRAS* 421, pp. 2940–2946.

Dobbs, C. L. et al. (2014). "Formation of Molecular Clouds and Global Conditions for Star Formation". In: *Protostars and Planets VI*, pp. 3–26.

Draine, B. T. (2011a). *Physics of the Interstellar and Intergalactic Medium*.

— (2011b). *Physics of the Interstellar and Intergalactic Medium. Princeton University Press, 2011. ISBN: 978-0-691-12214-4*.

Draine, B. T. et al. (2007). "Dust Masses, PAH Abundances, and Starlight Intensities in the SINGS Galaxy Sample". In: *ApJ* 663, pp. 866–894.

Draine, B. T. et al. (2014). "Andromeda's Dust". In: *ApJ* 780, 172, p. 172.

Dunham, M. K. et al. (2011). "A Mid-infrared Census of Star Formation Activity in Bolocam Galactic Plane Survey Sources". In: *ApJ* 731, 90, p. 90.

Dunham, M. M. et al. (2014). "The Evolution of Protostars: Insights from Ten Years of Infrared Surveys with Spitzer and Herschel". In: *Protostars and Planets VI*, pp. 195–218.

Eden, D. J. et al. (2012). "Star formation towards the Scutum tangent region and the effects of Galactic environment". In: *MNRAS* 422, pp. 3178–3188.

Eden, D. J. et al. (2013). "Star formation in Galactic spiral arms and the interarm regions". In: *MNRAS* 431, pp. 1587–1595.

Egusa, F., J. Koda, and N. Scoville (2011). "Molecular Gas Evolution Across a Spiral Arm in M51". In: *ApJ* 726, 85, p. 85.

Ellsworth-Bowers, T. P. et al. (2013). "The Bolocam Galactic Plane Survey. VIII. A Mid-infrared Kinematic Distance Discrimination Method". In: *ApJ* 770, 39, p. 39.

Elmegreen, B. G. (2002a). "Star Formation from Galaxies to Globules". In: *ApJ* 577, pp. 206–220.

— (2002b). "Star Formation from Large to Small Scales". In: *Ap&SS* 281, pp. 83–95.

— (2011). "On the Initial Conditions for Star Formation and the Initial Mass Function". In: *ApJ* 731, 61, p. 61.

Enoch, M. L. et al. (2008). "The Mass Distribution and Lifetime of Prestellar Cores in Perseus, Serpens, and Ophiuchus". In: *ApJ* 684, 1240-1259, pp. 1240–1259.

Evans, N. (2008). "Panel Discussion I: What is a Massive Protostar? Theoretical Definitions, Observational Criteria, and Evolutionary Sequence". In: *Massive Star Formation: Observations Confront Theory*. Ed. by H. Beuther, H. Linz, and T. Henning. Vol. 387. Astronomical Society of the Pacific Conference Series, p. 425.

Falgarone, E. and T. Passot, eds. (2003). *Turbulence and Magnetic Fields in Astrophysics*. Vol. 614. Lecture Notes in Physics, Berlin Springer Verlag, pp. 3–26.

Falgarone, E., J. Pety, and T. G. Phillips (2001). "Filamentary Structure and Helical Magnetic Fields in the Environment of a Starless Dense Core". In: *ApJ* 555, pp. 178–190.

Federrath, C. and R. S. Klessen (2013). "On the Star Formation Efficiency of Turbulent Magnetized Clouds". In: *ApJ* 763, 51, p. 51.

Fiege, J. D. and R. E. Pudritz (2000a). "Helical fields and filamentary molecular clouds - I". In: *MNRAS* 311, pp. 85–104.

— (2000b). "Helical fields and filamentary molecular clouds - II. Axisymmetric stability and fragmentation". In: *MNRAS* 311, pp. 105–119.

Fischera, J. and P. G. Martin (2012a). "Estimating distance, pressure, and dust opacity using submillimeter observations of self-gravitating filaments". In: *A&A* 547, A86, A86.

— (2012b). "Physical properties of interstellar filaments". In: *A&A* 542, A77, A77.

Forster, J. R. and J. L. Caswell (2000). “Radio Continuum Emission at OH and H_2O Maser Sites”. In: *ApJ* 530, pp. 371–386.

Foster, J. B. et al. (2011). “The Millimeter Astronomy Legacy Team 90 GHz (MALT90) Pilot Survey”. In: *ApJS* 197, 25, p. 25.

Foster, J. B. et al. (2013). “Characterisation of the MALT90 Survey and the Mopra Telescope at 90 GHz”. In: *PASA* 30, e038, p. 38.

Foyle, K. et al. (2010). “Arm and Interarm Star Formation in Spiral Galaxies”. In: *ApJ* 725, pp. 534–541.

Fritz, J. et al. (2012). “The Herschel Exploitation of Local Galaxy Andromeda (HELGA). I. Global far-infrared and sub-mm morphology”. In: *A&A* 546, A34, A34.

Garay, G. et al. (1993). “VLA Observations of Strong IRAS Point Sources Associated with Compact H II Regions”. In: *ApJ* 418, p. 368.

Giannetti, A. et al. (2014). “ATLASGAL-selected massive clumps in the inner Galaxy. I. CO depletion and isotopic ratios”. In: *A&A* 570, A65, A65.

Girichidis, P. et al. (2014). “On the Evolution of the Density Probability Density Function in Strongly Self-gravitating Systems”. In: *ApJ* 781, 91, p. 91.

Glover, S. C. O. and P. C. Clark (2012). “Is molecular gas necessary for star formation?” In: *MNRAS* 421, pp. 9–19.

Glover, S. C. O. and R. J. Smith (2016). “CO-dark gas and molecular filaments in Milky Way-type galaxies - II. The temperature distribution of the gas”. In: *MNRAS* 462, pp. 3011–3025.

Goldreich, P. and J. Kwan (1974). “Molecular Clouds”. In: *ApJ* 189, pp. 441–454.

Gómez, G. C. and E. Vázquez-Semadeni (2014). “Filaments in Simulations of Molecular Cloud Formation”. In: *ApJ* 791, 124, p. 124.

Goodman, A. A., J. E. Pineda, and S. L. Schnee (2009). “The ”True” Column Density Distribution in Star-Forming Molecular Clouds”. In: *ApJ* 692, pp. 91–103.

Goodman, A. A. et al. (1998). “Coherence in Dense Cores. II. The Transition to Coherence”. In: *ApJ* 504, p. 223.

Goodman, A. A. et al. (2014). “The Bones of the Milky Way”. In: *ApJ* 797, 53, p. 53.

Gordon, K. D. et al. (2010). “Determining dust temperatures and masses in the Herschel era: The importance of observations longward of 200 micron”. In: *A&A* 518, L89, p. L89.

Gratier, P. et al. (2010). "Molecular and atomic gas in the Local Group galaxy M 33". In: *A&A* 522, A3, A3.

Grenier, I. A., J.-M. Casandjian, and R. Terrier (2005). "Unveiling Extensive Clouds of Dark Gas in the Solar Neighborhood". In: *Science* 307, pp. 1292–1295.

Gressel, O. (2010). "Supernova-driven Turbulence and Magnetic Field Amplification in Disk Galaxies". PhD thesis. PhD Thesis, 2010.

Griffin, M. J. et al. (2010). "The Herschel-SPIRE instrument and its in-flight performance". In: *A&A* 518, L3, p. L3.

Gutermuth, R. A. et al. (2011a). "A Correlation between Surface Densities of Young Stellar Objects and Gas in Eight Nearby Molecular Clouds". In: *ApJ* 739, 84, p. 84.

— (2011b). "A Correlation between Surface Densities of Young Stellar Objects and Gas in Eight Nearby Molecular Clouds". In: *ApJ* 739, 84, p. 84.

Hacar, A. et al. (2013). "Cores, filaments, and bundles: hierarchical core formation in the L1495/B213 Taurus region". In: *A&A* 554, A55, A55.

Hartmann, L., J. Ballesteros-Paredes, and F. Heitsch (2012). "Rapid star formation and global gravitational collapse". In: *MNRAS* 420, pp. 1457–1461.

Heiderman, A. et al. (2010a). "The Star Formation Rate and Gas Surface Density Relation in the Milky Way: Implications for Extragalactic Studies". In: *ApJ* 723, 1019, pp. 1019–1037.

— (2010b). "The Star Formation Rate and Gas Surface Density Relation in the Milky Way: Implications for Extragalactic Studies". In: *ApJ* 723, 1019, pp. 1019–1037.

Heitsch, F. (2013a). "Gravitational Infall onto Molecular Filaments". In: *ApJ* 769, 115, p. 115.

— (2013b). "Gravitational Infall onto Molecular Filaments. II. Externally Pressurized Cylinders". In: *ApJ* 776, 62, p. 62.

Heitsch, F., J. Ballesteros-Paredes, and L. Hartmann (2009). "Gravitational Collapse and Filament Formation: Comparison with the Pipe Nebula". In: *ApJ* 704, pp. 1735–1742.

Heitsch, F. et al. (2008). "Cooling, Gravity, and Geometry: Flow-driven Massive Core Formation". In: *ApJ* 674, 316-328, pp. 316–328.

Hennebelle, P. (2013). "On the origin of non-self-gravitating filaments in the ISM". In: *A&A* 556, A153, A153.

Hennebelle, P. and G. Chabrier (2008). "Analytical Theory for the Initial Mass Function: CO Clumps and Prestellar Cores". In: *ApJ* 684, pp. 395–410.

— (2009). "Analytical Theory for the Initial Mass Function. II. Properties of the Flow". In: *ApJ* 702, pp. 1428–1442.

Hennebelle, P. and E. Falgarone (2012). "Turbulent molecular clouds". In: *A&A Rev.* 20, p. 55.

Henning, T. et al. (2010a). "The seeds of star formation in the filamentary infrared-dark cloud G011.11-0.12". In: *A&A* 518, L95, p. L95.

— (2010b). "The seeds of star formation in the filamentary infrared-dark cloud G011.11-0.12". In: *A&A* 518, L95, p. L95.

Hernandez, A. K. et al. (2012). "A Virialized Filamentary Infrared Dark Cloud". In: *ApJ* 756, L13, p. L13.

Heyer, M. et al. (2009). "Re-Examining Larson's Scaling Relationships in Galactic Molecular Clouds". In: *ApJ* 699, pp. 1092–1103.

Hily-Blant, P. and E. Falgarone (2007). "Dissipative structures of diffuse molecular gas. II. The translucent environment of a dense core". In: *A&A* 469, pp. 173–187.

Hindson, L. et al. (2010). "The G305 star-forming complex: wide-area molecular mapping of NH_3 and H_2O masers". In: *MNRAS* 408, pp. 1438–1451.

Hollenbach, D. et al. (2009). "Water, O_2, and Ice in Molecular Clouds". In: *ApJ* 690, pp. 1497–1521.

Hollenbach, D. J. and A. G. G. M. Tielens (1997). "Dense Photodissociation Regions (PDRs)". In: *ARA&A* 35, pp. 179–216.

Hughes, A. et al. (2013). "Probability Distribution Functions of $^{12}CO(J = 1 - 0)$ Brightness and Integrated Intensity in M51: The PAWS View". In: *ApJ* 779, 44, p. 44.

Inutsuka, S.-I. and S. M. Miyama (1992). "Self-similar solutions and the stability of collapsing isothermal filaments". In: *ApJ* 388, pp. 392–399.

Jackson, J. M. et al. (2006). "The Boston University-Five College Radio Astronomy Observatory Galactic Ring Survey". In: *ApJS* 163, pp. 145–159.

Jackson, J. M. et al. (2010). "The "Nessie" Nebula: Cluster Formation in a Filamentary Infrared Dark Cloud". In: *ApJ* 719, pp. L185–L189.

Jackson, J. M. et al. (2013). "MALT90: The Millimetre Astronomy Legacy Team 90 GHz Survey". In: *PASA* 30, e057, p. 57.

Johnston, K. G. et al. (2009). "Ionized Gas toward Molecular Clumps: Physical Properties of Massive Star-Forming Regions". In: *ApJ* 707, pp. 283–309.

Kainulainen, J., C. Federrath, and T. Henning (2013). "Connection between dense gas mass fraction, turbulence driving, and star formation efficiency of molecular clouds". In: *A&A* 553, L8, p. L8.

— (2014). "Unfolding the Laws of Star Formation: The Density Distribution of Molecular Clouds". In: *Science* 344, pp. 183–185.

Kainulainen, J. and J. C. Tan (2013). "High-dynamic-range extinction mapping of infrared dark clouds. Dependence of density variance with sonic Mach number in molecular clouds". In: *A&A* 549, A53, A53.

Kainulainen, J. et al. (2009a). "Probing the evolution of molecular cloud structure. From quiescence to birth". In: *A&A* 508, pp. L35–L38.

— (2009b). "Probing the evolution of molecular cloud structure. From quiescence to birth". In: *A&A* 508, pp. L35–L38.

Kainulainen, J. et al. (2011a). "Mass reservoirs surrounding massive infrared dark clouds. A view by near-infrared dust extinction". In: *A&A* 536, A48, A48.

— (2011b). "Mass reservoirs surrounding massive infrared dark clouds. A view by near-infrared dust extinction". In: *A&A* 536, A48, A48.

Kainulainen, J. et al. (2011c). "Probing the evolution of molecular cloud structure. II. From chaos to confinement". In: *A&A* 530, A64, A64.

Kainulainen, J. et al. (2013a). "High-fidelity view of the structure and fragmentation of the high-mass, filamentary IRDC G11.11-0.12". In: *A&A* 557, A120, A120.

— (2013b). "High-fidelity view of the structure and fragmentation of the high-mass, filamentary IRDC G11.11-0.12". In: *A&A* 557, A120, A120.

— (2013c). "High-fidelity view of the structure and fragmentation of the high-mass, filamentary IRDC G11.11-0.12". In: *A&A* 557, A120, A120.

Kainulainen, J. et al. (2016). "Fragmentation of high line-mass filaments as revealed by ALMA: the integral shaped filament in Orion A". In: *ArXiv e-prints*.

Karr, J. L., P. Manoj, and N. Ohashi (2009). "Gum 48d: An Evolved H II Region with Ongoing Star Formation". In: *ApJ* 697, pp. 133–147.

Kaufman, M. J. et al. (1999). "Far-Infrared and Submillimeter Emission from Galactic and Extragalactic Photodissociation Regions". In: *ApJ* 527, pp. 795–813.

Kawamura, A. et al. (2009). "The Second Survey of the Molecular Clouds in the Large Magellanic Cloud by NANTEN. II. Star Formation". In: *ApJS* 184, pp. 1–17.

Kennicutt Jr., R. C. (1998). "The Global Schmidt Law in Star-forming Galaxies". In: *ApJ* 498, pp. 541–552.

Kirk, H. et al. (2013a). "Filamentary Accretion Flows in the Embedded Serpens South Protocluster". In: *ApJ* 766, 115, p. 115.

Kirk, J. M. et al. (2013b). "First results from the Herschel Gould Belt Survey in Taurus". In: *MNRAS* 432, pp. 1424–1433.

Klessen, R. S. (2000). "One-Point Probability Distribution Functions of Supersonic Turbulent Flows in Self-gravitating Media". In: *ApJ* 535, pp. 869–886.

Klessen, R. S. and A. Burkert (2000). "The Formation of Stellar Clusters: Gaussian Cloud Conditions. I." In: *ApJS* 128, pp. 287–319.

Koda, J. et al. (2009). "Dynamically Driven Evolution of the Interstellar Medium in M51". In: *ApJ* 700, pp. L132–L136.

Könyves, V. et al. (2010). "The Aquila prestellar core population revealed by Herschel". In: *A&A* 518, L106, p. L106.

Könyves, V. et al. (2015). "A census of dense cores in the Aquila cloud complex: SPIRE/PACS observations from the Herschel Gould Belt survey". In: *A&A* 584, A91, A91.

Kramer, C. et al. (2010). "PACS and SPIRE photometer maps of M 33: First results of the HERschel M 33 Extended Survey (HERM33ES)". In: *A&A* 518, L67, p. L67.

Kritsuk, A. G., M. L. Norman, and R. Wagner (2011). "On the Density Distribution in Star-forming Interstellar Clouds". In: *ApJ* 727, L20, p. L20.

Krumholz, M. R. (2007). "Turbulence, feedback, and slow star formation". In: *Triggered Star Formation in a Turbulent ISM*. Ed. by B. G. Elmegreen and J. Palous. Vol. 237. IAU Symposium, pp. 378–383.

Krumholz, M. R., A. Dekel, and C. F. McKee (2012). "A Universal, Local Star Formation Law in Galactic Clouds, nearby Galaxies, High-redshift Disks, and Starbursts". In: *ApJ* 745, 69, p. 69.

Krumholz, M. R. and C. F. McKee (2005). "A General Theory of Turbulence-regulated Star Formation, from Spirals to Ultraluminous Infrared Galaxies". In: *ApJ* 630, pp. 250–268.

Krumholz, M. R., C. F. McKee, and J. Tumlinson (2009). "The Star Formation Law in Atomic and Molecular Gas". In: *ApJ* 699, pp. 850–856.

Lada, C. J. and E. A. Lada (2003). “Embedded Clusters in Molecular Clouds”. In: *ARA&A* 41, pp. 57–115.

Lada, C. J., M. Lombardi, and J. F. Alves (2009). “The California Molecular Cloud”. In: *ApJ* 703, pp. 52–59.

— (2010a). “On the Star Formation Rates in Molecular Clouds”. In: *ApJ* 724, pp. 687–693.

— (2010b). “On the Star Formation Rates in Molecular Clouds”. In: *ApJ* 724, pp. 687–693.

Lada, C. J. et al. (2012a). “Star Formation Rates in Molecular Clouds and the Nature of the Extragalactic Scaling Relations”. In: *ApJ* 745, 190, p. 190.

— (2012b). “Star Formation Rates in Molecular Clouds and the Nature of the Extragalactic Scaling Relations”. In: *ApJ* 745, 190, p. 190.

Langer, W. (1976). “The carbon monoxide abundance in interstellar clouds”. In: *ApJ* 206, pp. 699–712.

Langer, W. D., J. L. Pineda, and T. Velusamy (2014). “The scale height of gas traced by [C ii] in the Galactic plane”. In: *A&A* 564, A101, A101.

Langer, W. D. et al. (1989). “Dust and gas emission in Barnard 5”. In: *ApJ* 337, pp. 355–381.

Larson, R. B. (1981). “Turbulence and star formation in molecular clouds”. In: *MNRAS* 194, pp. 809–826.

— (1985). “Cloud fragmentation and stellar masses”. In: *MNRAS* 214, pp. 379–398.

Launhardt, R. et al. (2013a). “The Earliest Phases of Star Formation (EPoS): a Herschel key project. The thermal structure of low-mass molecular cloud cores”. In: *A&A* 551, A98, A98.

— (2013b). “The Earliest Phases of Star Formation (EPoS): a Herschel key project. The thermal structure of low-mass molecular cloud cores”. In: *A&A* 551, A98, A98.

Leroy, A. K. et al. (2008). “The Star Formation Efficiency in Nearby Galaxies: Measuring Where Gas Forms Stars Effectively”. In: *AJ* 136, pp. 2782–2845.

Leroy, A. K. et al. (2011). “The CO-to-H_2 Conversion Factor from Infrared Dust Emission across the Local Group”. In: *ApJ* 737, 12, p. 12.

Li, G.-X. et al. (2013). “A 500 pc filamentary gas wisp in the disk of the Milky Way”. In: *A&A* 559, A34, A34.

Lockman, F. J. (1989). “A survey of radio H II regions in the northern sky”. In: *ApJS* 71, pp. 469–479.

Lockman, F. J., D. J. Pisano, and G. J. Howard (1996). “Detection of 130 “Diffuse” Galactic H II Regions”. In: *ApJ* 472, p. 173.

Lombardi, M. (2009). “nicest, a near-infrared color excess method tailored to small-scale structures”. In: *A&A* 493, pp. 735–745.

Lombardi, M. and J. Alves (2001). “Mapping the interstellar dust with near-infrared observations: An optimized multi-band technique”. In: *A&A* 377, pp. 1023–1034.

Lombardi, M., J. Alves, and C. J. Lada (2006). “2MASS wide field extinction maps. I. The Pipe nebula”. In: *A&A* 454, pp. 781–796.

— (2010). “Larson’s third law and the universality of molecular cloud structure”. In: *A&A* 519, L7, p. L7.

— (2015). “Molecular clouds have power-law probability distribution functions”. In: *A&A* 576, L1, p. L1.

Lombardi, M. et al. (2014). “Herschel-Planck dust optical-depth and column-density maps. I. Method description and results for Orion”. In: *A&A* 566, A45, A45.

Lumsden, S. L. et al. (2013a). “The Red MSX Source Survey: The Massive Young Stellar Population of Our Galaxy”. In: *ApJS* 208, 11, p. 11.

— (2013b). “The Red MSX Source Survey: The Massive Young Stellar Population of Our Galaxy”. In: *ApJS* 208, 11, p. 11.

Mac Low, M.-M. and R. S. Klessen (2004). “Control of star formation by supersonic turbulence”. In: *Reviews of Modern Physics* 76, pp. 125–194.

Machida, M. N., S.-i. Inutsuka, and T. Matsumoto (2008). “High- and Low-Velocity Magnetized Outflows in the Star Formation Process in a Gravitationally Collapsing Cloud”. In: *ApJ* 676, 1088-1108, pp. 1088–1108.

Marshall, D. J., G. Joncas, and A. P. Jones (2009). “Distribution and Characteristics of Infrared Dark Clouds Using Genetic Forward Modelling”. In: *ApJ* 706, pp. 727–737.

Matzner, C. D. and C. F. McKee (2000). “Efficiencies of Low-Mass Star and Star Cluster Formation”. In: *ApJ* 545, pp. 364–378.

McKee, C. F. and E. C. Ostriker (2007). “Theory of Star Formation”. In: *ARA&A* 45, pp. 565–687.

Meidt, S. E. et al. (2015). “Short GMC Lifetimes: An Observational Estimate with the PdBI Arcsecond Whirlpool Survey (PAWS)”. In: *ApJ* 806, 72, p. 72.

Meisner, A. M. and D. P. Finkbeiner (2015). “Modeling Thermal Dust Emission with Two Components: Application to the Planck High Frequency Instrument Maps”. In: *ApJ* 798, 88, p. 88.

Meixner, M. et al. (2010). “HERschel Inventory of The Agents of Galaxy Evolution (HERITAGE): The Large Magellanic Cloud dust”. In: *A&A* 518, L71, p. L71.

Milam, S. N. et al. (2005). “The $^{12}C/^{13}C$ Isotope Gradient Derived from Millimeter Transitions of CN: The Case for Galactic Chemical Evolution”. In: *ApJ* 634, pp. 1126–1132.

Molinari, S. et al. (2010a). “Clouds, filaments, and protostars: The Herschel Hi-GAL Milky Way”. In: *A&A* 518, L100, p. L100.

Molinari, S. et al. (2010b). “Hi-GAL: The Herschel Infrared Galactic Plane Survey”. In: *PASP* 122, pp. 314–325.

Molinari, S. et al. (2014a). “The Milky Way as a Star Formation Engine”. In: *Protostars and Planets VI*, pp. 125–148.

— (2014b). “The Milky Way as a Star Formation Engine”. In: *Protostars and Planets VI*, pp. 125–148.

Mookerjea, B. et al. (2004). “The Giant Molecular Cloud associated with RCW 106. A 1.2 mm continuum mapping study”. In: *A&A* 426, pp. 119–129.

Moore, T. J. T. et al. (2012). “The effect of spiral arms on star formation in the Galaxy”. In: *MNRAS* 426, pp. 701–707.

Motte, F., P. Andre, and R. Neri (1998). “The initial conditions of star formation in the rho Ophiuchi main cloud: wide-field millimeter continuum mapping”. In: *A&A* 336, pp. 150–172.

Motte, F. and P. Hennebelle (2009). “Our knowledge of high-mass star formation at the dawn of Herschel”. In: *EAS Publications Series*. Ed. by L. Pagani and M. Gerin. Vol. 34. EAS Publications Series, pp. 195–211.

Motte, F. et al. (2010). “Initial highlights of the HOBYS key program, the Herschel imaging survey of OB young stellar objects”. In: *A&A* 518, L77, p. L77.

Motte, F. et al. (2012). “The HOBYS Key Program: When Herschel links high-mass star formation to cloud structure”. In: *SF2A-2012: Proceedings of the Annual meeting of the French Society of Astronomy and Astrophysics*. Ed. by S. Boissier et al., pp. 45–50.

Myers, P. C. (2009). “Filamentary Structure of Star-forming Complexes”. In: *ApJ* 700, pp. 1609–1625.

Nutter, D. et al. (2008). “SCUBA and Spitzer observations of the Taurus molecular cloud - pulling the bull’s tail”. In: *MNRAS* 384, pp. 755–763.

Offner, S. S. R. et al. (2009). “The Effects of Radiative Transfer on Low-Mass Star Formation”. In: *ApJ* 703, pp. 131–149.

Ossenkopf, V. and T. Henning (1994a). “Dust opacities for protostellar cores”. In: *A&A* 291, pp. 943–959.

— (1994b). “Dust opacities for protostellar cores”. In: *A&A* 291, pp. 943–959.

Ostriker, E. C., C. F. McKee, and A. K. Leroy (2010). “Regulation of Star Formation Rates in Multiphase Galactic Disks: A Thermal/Dynamical Equilibrium Model”. In: *ApJ* 721, pp. 975–994.

Ostriker, E. C., J. M. Stone, and C. F. Gammie (2001). “Density, Velocity, and Magnetic Field Structure in Turbulent Molecular Cloud Models”. In: *ApJ* 546, pp. 980–1005.

Ott, S. (2010). “The Herschel Data Processing System - HIPE and Pipelines - Up and Running Since the Start of the Mission”. In: *Astronomical Data Analysis Software and Systems XIX*. Ed. by Y. Mizumoto, K.-I. Morita, and M. Ohishi. Vol. 434. Astronomical Society of the Pacific Conference Series, p. 139.

Padoan, P., B. J. T. Jones, and A. P. Nordlund (1997). “Supersonic Turbulence in the Interstellar Medium: Stellar Extinction Determinations as Probes of the Structure and Dynamics of Dark Clouds”. In: *ApJ* 474, p. 730.

Padoan, P. and Å. Nordlund (2002). “The Stellar Initial Mass Function from Turbulent Fragmentation”. In: *ApJ* 576, pp. 870–879.

— (2011). “The Star Formation Rate of Supersonic Magnetohydrodynamic Turbulence”. In: *ApJ* 730, 40, p. 40.

Padoan, P. et al. (2001). “Turbulent Fragmentation and the Initial Conditions for Star Formation”. In: *From Darkness to Light: Origin and Evolution of Young Stellar Clusters*. Ed. by T. Montmerle and P. André. Vol. 243. Astronomical Society of the Pacific Conference Series, p. 279.

Padoan, P. et al. (2014). “The Star Formation Rate of Molecular Clouds”. In: *Protostars and Planets VI*, pp. 77–100.

Padoan, P. et al. (2016). “Supernova Driving. I. The Origin of Molecular Cloud Turbulence”. In: *ApJ* 822, 11, p. 11.

Palmeirim, P. et al. (2013). “Herschel view of the Taurus B211/3 filament and striations: evidence of filamentary growth?” In: *A&A* 550, A38, A38.

Passot, T., A. Pouquet, and P. Woodward (1988). “The plausibility of Kolmogorov-type spectra in molecular clouds”. In: *A&A* 197, pp. 228–234.

Penzias, A. A. et al. (1972). "Carbon Monoxide Observations of Dense Interstellar Clouds". In: *ApJ* 174, p. L43.

Peretto, N. and G. A. Fuller (2009). "The initial conditions of stellar protocluster formation. I. A catalogue of Spitzer dark clouds". In: *A&A* 505, pp. 405–415.

— (2010). "A Statistical Study of the Mass and Density Structure of Infrared Dark Clouds". In: *ApJ* 723, pp. 555–562.

Pilbratt, G. L. et al. (2010a). "Herschel Space Observatory. An ESA facility for far-infrared and submillimetre astronomy". In: *A&A* 518, L1, p. L1.

— (2010b). "Herschel Space Observatory. An ESA facility for far-infrared and submillimetre astronomy". In: *A&A* 518, L1, p. L1.

Pineda, J. L. et al. (2010). "The Relation Between Gas and Dust in the Taurus Molecular Cloud". In: *ApJ* 721, pp. 686–708.

Planck Collaboration et al. (2014a). "Planck 2013 results. I. Overview of products and scientific results". In: *A&A* 571, A1, A1.

— (2014b). "Planck 2013 results. I. Overview of products and scientific results". In: *A&A* 571, A1, A1.

Planck Collaboration et al. (2014c). "Planck 2013 results. VII. HFI time response and beams". In: *A&A* 571, A7, A7.

Planck Collaboration et al. (2014d). "Planck 2013 results. XI. All-sky model of thermal dust emission". In: *A&A* 571, A11, A11.

Poglitsch, A. et al. (2010a). "The Photodetector Array Camera and Spectrometer (PACS) on the Herschel Space Observatory". In: *A&A* 518, L2, p. L2.

— (2010b). "The Photodetector Array Camera and Spectrometer (PACS) on the Herschel Space Observatory". In: *A&A* 518, L2, p. L2.

Pokhrel, R. et al. (2016). "AHerschel-SPIRE survey of the Mon R2 giant molecular cloud: analysis of the gas column density probability density function". In: *MNRAS* 461, pp. 22–35.

Polychroni, D. et al. (2013). "Two Mass Distributions in the L 1641 Molecular Clouds: The Herschel Connection of Dense Cores and Filaments in Orion A". In: *ApJ* 777, L33, p. L33.

Price, D. J., T. S. Tricco, and M. R. Bate (2012). "Collimated jets from the first core". In: *MNRAS* 423, pp. L45–L49.

Purcell, C. R. et al. (2012). "The H_2O Southern Galactic Plane Survey: NH_3 (1,1) and (2,2) catalogues". In: *MNRAS* 426, pp. 1972–1991.

Ragan, S. et al. (2012a). "The Earliest Phases of Star Formation (EPoS): a Herschel key program. The precursors to high-mass stars and clusters". In: *A&A* 547, A49, A49.

— (2012b). "The Earliest Phases of Star Formation (EPoS): a Herschel key program. The precursors to high-mass stars and clusters". In: *A&A* 547, A49, A49.

Ragan, S. E., T. Henning, and H. Beuther (2013). "APEX/SABOCA observations of small-scale structure of infrared-dark clouds . I. Early evolutionary stages of star-forming cores". In: *A&A* 559, A79, A79.

Ragan, S. E. et al. (2014). "Giant molecular filaments in the Milky Way". In: *A&A* 568, A73, A73.

Ragan, S. E. et al. (2015). "Fragmentation and kinematics of dense molecular cores in the filamentary infrared-dark cloud G011.11-0.12". In: *A&A* 573, A119, A119.

Reid, M. J. et al. (2014). "Trigonometric Parallaxes of High Mass Star Forming Regions: The Structure and Kinematics of the Milky Way". In: *ApJ* 783, 130, p. 130.

Robitaille, T. P. et al. (2007). "Interpreting Spectral Energy Distributions from Young Stellar Objects. II. Fitting Observed SEDs Using a Large Grid of Precomputed Models". In: *ApJS* 169, pp. 328–352.

Robitaille, T. P. et al. (2008). "Intrinsically Red Sources Observed by Spitzer in the Galactic Midplane". In: *AJ* 136, pp. 2413–2440.

Rohlfs, K. and T. L. Wilson (2004). *Tools of radio astronomy*.

Röllig, M. et al. (2007). "A photon dominated region code comparison study". In: *A&A* 467, pp. 187–206.

Roman-Duval, J. et al. (2009). "Kinematic Distances to Molecular Clouds Identified in the Galactic Ring Survey". In: *ApJ* 699, pp. 1153–1170.

Roman-Duval, J. et al. (2011). "The Turbulence Spectrum of Molecular Clouds in the Galactic Ring Survey: A Density-dependent Principal Component Analysis Calibration". In: *ApJ* 740, 120, p. 120.

Roman-Duval, J. et al. (2016). "Distribution and Mass of Diffuse and Dense CO Gas in the Milky Way". In: *ApJ* 818, 144, p. 144.

Roman-Lopes, A. et al. (2009). "GEMINI near-infrared spectroscopic observations of young massive stars embedded in molecular clouds". In: *MNRAS* 394, pp. 467–478.

Roussel, H. (2013). "Scanamorphos: A Map-making Software for Herschel and Similar Scanning Bolometer Arrays". In: *PASP* 125, pp. 1126–1163.

Rudolph, A. L. et al. (2006). "Abundance Gradients in the Galaxy". In: *ApJS* 162, pp. 346–374.

Russeil, D. (2003). "Star-forming complexes and the spiral structure of our Galaxy". In: *A&A* 397, pp. 133–146.

Russeil, D. et al. (2013). "The Herschel view of the massive star-forming region NGC 6334". In: *A&A* 554, A42, A42.

Sadavoy, S. I. et al. (2013). "The Herschel and JCMT Gould Belt Surveys: Constraining Dust Properties in the Perseus B1 Clump with PACS, SPIRE, and SCUBA-2". In: *ApJ* 767, 126, p. 126.

Sadavoy, S. I. et al. (2014). "Class 0 Protostars in the Perseus Molecular Cloud: A Correlation Between the Youngest Protostars and the Dense Gas Distribution". In: *ApJ* 787, L18, p. L18.

Saito, H. et al. (2001). "The Most Massive $C^{18}O$ Molecular Complex in Centaurus and Star Formation Therein". In: *PASJ* 53, pp. 1037–1051.

Sanders, D. B., P. M. Solomon, and N. Z. Scoville (1984). "Giant molecular clouds in the Galaxy. I - The axisymmetric distribution of H2". In: *ApJ* 276, pp. 182–203.

Scalo, J. et al. (1998). "On the Probability Density Function of Galactic Gas. I. Numerical Simulations and the Significance of the Polytropic Index". In: *ApJ* 504, p. 835.

Schinnerer, E. et al. (2013a). "The PdBI Arcsecond Whirlpool Survey (PAWS). I. A Cloud-scale/Multi-wavelength View of the Interstellar Medium in a Grand-design Spiral Galaxy". In: *ApJ* 779, 42, p. 42.

— (2013b). "The PdBI Arcsecond Whirlpool Survey (PAWS). I. A Cloud-scale/Multi-wavelength View of the Interstellar Medium in a Grand-design Spiral Galaxy". In: *ApJ* 779, 42, p. 42.

Schmalzl, M. et al. (2010). "Star Formation in the Taurus Filament L 1495: From Dense Cores to Stars". In: *ApJ* 725, pp. 1327–1336.

Schmidt, M. (1959). "The Rate of Star Formation." In: *ApJ* 129, p. 243.

Schneider, N. et al. (2010). "Dynamic star formation in the massive DR21 filament". In: *A&A* 520, A49, A49.

Schneider, N. et al. (2012a). "Cluster-formation in the Rosette molecular cloud at the junctions of filaments". In: *A&A* 540, L11, p. L11.

— (2012b). "Cluster-formation in the Rosette molecular cloud at the junctions of filaments". In: *A&A* 540, L11, p. L11.

Schneider, N. et al. (2013a). "What Determines the Density Structure of Molecular Clouds? A Case Study of Orion B with Herschel". In: *ApJ* 766, L17, p. L17.

— (2013b). "What Determines the Density Structure of Molecular Clouds? A Case Study of Orion B with Herschel". In: *ApJ* 766, L17, p. L17.

Schneider, N. et al. (2014). "Understanding star formation in molecular clouds II. Signatures of gravitational collapse of IRDCs". In: *ArXiv e-prints*.

Schneider, N. et al. (2015a). "Detection of two power-law tails in the probability distribution functions of massive GMCs". In: *MNRAS* 453, pp. 41–45.

Schneider, N. et al. (2015b). "Understanding star formation in molecular clouds. I. Effects of line-of-sight contamination on the column density structure". In: *A&A* 575, A79, A79.

— (2015c). "Understanding star formation in molecular clouds. I. Effects of line-of-sight contamination on the column density structure". In: *A&A* 575, A79, A79.

— (2015d). "Understanding star formation in molecular clouds. I. Effects of line-of-sight contamination on the column density structure". In: *A&A* 575, A79, A79.

Schneider, S. and B. G. Elmegreen (1979). "A catalog of dark globular filaments". In: *ApJS* 41, pp. 87–95.

Schruba, A. et al. (2012). "Low CO Luminosities in Dwarf Galaxies". In: *AJ* 143, 138, p. 138.

Schuller, F. et al. (2009a). "ATLASGAL - The APEX telescope large area survey of the galaxy at 870 μm". In: *A&A* 504, pp. 415–427.

— (2009b). "ATLASGAL - The APEX telescope large area survey of the galaxy at 870 μm". In: *A&A* 504, pp. 415–427.

Ségransan, D. (2007). "Observability and UV coverage". In: *New A Rev.* 51, pp. 597–603.

Shirley, Y. L. et al. (2005). "Modeling the Physical Structure of the Low-Density Pre-Protostellar Core Lynds 1498". In: *ApJ* 632, pp. 982–1000.

Shirley, Y. L. et al. (2011). "Observational Constraints on Submillimeter Dust Opacity". In: *ApJ* 728, 143, p. 143.

Shu, F. H., F. C. Adams, and S. Lizano (1987). "Star formation in molecular clouds - Observation and theory". In: *ARA&A* 25, pp. 23–81.

Simon, R. et al. (2006). "A Catalog of Midcourse Space Experiment Infrared Dark Cloud Candidates". In: *ApJ* 639, pp. 227–236.

Siringo, G. et al. (2009). “The Large APEX BOlometer CAmera LABOCA”. In: *A&A* 497, pp. 945–962.

Skrutskie, M. F. et al. (2006). “The Two Micron All Sky Survey (2MASS)”. In: *AJ* 131, pp. 1163–1183.

Smith, R. J. et al. (2014). “CO-dark gas and molecular filaments in Milky Way-type galaxies”. In: *MNRAS* 441, pp. 1628–1645.

Sodroski, T. J. et al. (1997). “A Three-dimensional Decomposition of the Infrared Emission from Dust in the Milky Way”. In: *ApJ* 480, pp. 173–187.

Solomon, P. M. and A. R. Rivolo (1989). “A face-on view of the first galactic quadrant in molecular clouds”. In: *ApJ* 339, pp. 919–925.

Solomon, P. M. et al. (1987). “Mass, luminosity, and line width relations of Galactic molecular clouds”. In: *ApJ* 319, pp. 730–741.

Stanimirovic, S. (2002). “Short-Spacings Correction from the Single-Dish Perspective”. In: *Single-Dish Radio Astronomy: Techniques and Applications*. Ed. by S. Stanimirovic et al. Vol. 278. Astronomical Society of the Pacific Conference Series, pp. 375–396.

Stark, A. A. and Y. Lee (2006). “Giant Molecular Clouds Are More Concentrated toward Spiral Arms than Smaller Clouds”. In: *ApJ* 641, pp. L113–L116.

Steigman, G. (2007). “Primordial Nucleosynthesis in the Precision Cosmology Era”. In: *Annual Review of Nuclear and Particle Science* 57, pp. 463–491.

Stutz, A. et al. (2010a). “Dust-temperature of an isolated star-forming cloud: Herschel observations of the Bok globule CB244”. In: *A&A* 518, L87, p. L87.

— (2010b). “Dust-temperature of an isolated star-forming cloud: Herschel observations of the Bok globule CB244”. In: *A&A* 518, L87, p. L87.

Stutz, A. M. and A. Gould (2016). “Slingshot mechanism in Orion: Kinematic evidence for ejection of protostars by filaments”. In: *A&A* 590, A2, A2.

Stutz, A. M. and J. Kainulainen (2015). “Evolution of column density distributions within Orion A”. In: *A&A* 577, L6, p. L6.

Stutz, A. M. et al. (2009). “Spitzer and Heinrich Hertz Telescope Observations of Starless Cores: Masses and Environments”. In: *ApJ* 707, pp. 137–166.

Stutz, A. M. et al. (2013). "A Herschel and APEX Census of the Reddest Sources in Orion: Searching for the Youngest Protostars". In: *ApJ* 767, 36, p. 36.

Tackenberg, J. et al. (2012). "Search for starless clumps in the ATLASGAL survey". In: *A&A* 540, A113, A113.

Tackenberg, J. et al. (2013). "Triggered/sequential star formation? A multi-phase ISM study around the prominent IRDC G18.93-0.03". In: *A&A* 550, A116, A116.

Takahashi, S. et al. (2013). "Hierarchical Fragmentation of the Orion Molecular Filaments". In: *ApJ* 763, 57, p. 57.

Tan, J. C. (2007). "Massive star and star cluster formation". In: *IAU Symposium*. Ed. by B. G. Elmegreen and J. Palous. Vol. 237. IAU Symposium, pp. 258–264.

Tan, J. C. et al. (2014). "Massive Star Formation". In: *Protostars and Planets VI*, pp. 149–172.

Tang, N. et al. (2016). "Physical properties of CO-dark molecular gas traced by C^{+}". In: *A&A* 593, A42, A42.

Tasker, E. J. (2011). "Star Formation in Disk Galaxies. II. The Effect Of Star Formation and Photoelectric Heating on the Formation and Evolution of Giant Molecular Clouds". In: *ApJ* 730, 11, p. 11.

Tasker, E. J. and J. C. Tan (2009). "Star Formation in Disk Galaxies. I. Formation and Evolution of Giant Molecular Clouds via Gravitational Instability and Cloud Collisions". In: *ApJ* 700, pp. 358–375.

Tassis, K. (2007). "The star formation law in a multifractal ISM". In: *MNRAS* 382, pp. 1317–1323.

Tassis, K. et al. (2010). "Do lognormal column-density distributions in molecular clouds imply supersonic turbulence?" In: *MNRAS* 408, pp. 1089–1094.

Teixeira, P. S. et al. (2016). "Two-level hierarchical fragmentation in the northern filament of the Orion Molecular Cloud 1". In: *A&A* 587, A47, A47.

Testi, L. and A. I. Sargent (1998). "Star Formation in Clusters: A Survey of Compact Millimeter-Wave Sources in the Serpens Core". In: *ApJ* 508, pp. L91–L94.

Thomas, G. (1986). "Infrared Astronomical Satellite (IRAS)." In: *Rutherford Appleton Laboratory Report* 63, pp. 1–1.

Tielens, A. G. G. M. (2005). *The Physics and Chemistry of the Interstellar Medium*.

Tóth, L. V. et al. (2014). "The AKARI Far-Infrared Surveyor young stellar object catalog". In: *PASJ* 66, 17, p. 17.

Tremblin, P. et al. (2014). "Ionization compression impact on dense gas distribution and star formation. Probability density functions around H II regions as seen by Herschel". In: *A&A* 564, A106, A106.

Trumpler, R. J. (1930). "Absorption of Light in the Galactic System". In: *PASP* 42, p. 214.

Uchida, Y. et al. (1991). "Evidence for a rotating helical filament in L1641, part of the Orion cloud complex". In: *Nature* 349, pp. 140–142.

Urquhart, J. S. et al. (2013a). "ATLASGAL - environments of 6.7 GHz methanol masers". In: *MNRAS* 431, pp. 1752–1776.

Urquhart, J. S. et al. (2013b). "ATLASGAL - properties of compact H II regions and their natal clumps". In: *MNRAS* 435, pp. 400–428.

Urquhart, J. S. et al. (2014). "ATLASGAL - towards a complete sample of massive star forming clumps". In: *MNRAS* 443, pp. 1555–1586.

Vallée, J. P. (2008). "New Velocimetry and Revised Cartography of the Spiral Arms in the Milky Way-A Consistent Symbiosis". In: *AJ* 135, 1301, pp. 1301–1310.

Van Loo, S., M. J. Butler, and J. C. Tan (2013). "Kiloparsec-scale Simulations of Star Formation in Disk Galaxies. I. The Unmagnetized and Zero-feedback Limit". In: *ApJ* 764, 36, p. 36.

Vasyunina, T. et al. (2009). "Physical properties of Southern infrared dark clouds". In: *A&A* 499, pp. 149–161.

Vazquez-Semadeni, E. (1994). "Hierarchical Structure in Nearly Pressureless Flows as a Consequence of Self-similar Statistics". In: *ApJ* 423, p. 681.

Vázquez-Semadeni, E. and N. García (2001). "The Probability Distribution Function of Column Density in Molecular Clouds". In: *ApJ* 557, pp. 727–735.

Vázquez-Semadeni, E. et al. (2006). "Molecular Cloud Evolution. I. Molecular Cloud and Thin Cold Neutral Medium Sheet Formation". In: *ApJ* 643, pp. 245–259.

Vázquez-Semadeni, E. et al. (2007). "Molecular Cloud Evolution. II. From Cloud Formation to the Early Stages of Star Formation in Decaying Conditions". In: *ApJ* 657, pp. 870–883.

Vázquez-Semadeni, E. et al. (2009). "High- and Low-Mass Star-Forming Regions from Hierarchical Gravitational Fragmentation. High Local Star

Formation Rates with Low Global Efficiencies”. In: *ApJ* 707, pp. 1023–1033.

Vázquez-Semadeni, E. et al. (2011). “Molecular cloud evolution - IV. Magnetic fields, ambipolar diffusion and the star formation efficiency”. In: *MNRAS* 414, pp. 2511–2527.

Walker-LaFollette, A. et al. (2014). “Kinematic Results From a Systematic Search for Infall Signatures Towards the Starless Core Population in the Perseus Molecular Cloud”. In: *American Astronomical Society Meeting Abstracts*. Vol. 223. American Astronomical Society Meeting Abstracts, p. 454.

Walsh, A. J. et al. (1997). “Studies of ultracompact HII regions - I. Methanol maser survey of IRAS-selected sources”. In: *MNRAS* 291, pp. 261–278.

Walsh, A. J. et al. (2011). “The H_2O Southern Galactic Plane Survey (HOPS) - I. Techniques and H_2O maser data”. In: *MNRAS* 416, pp. 1764–1821.

Wang, K. et al. (2015). “Large-scale filaments associated with Milky Way spiral arms”. In: *MNRAS* 450, pp. 4043–4049.

Ward-Thompson, D. et al. (2007). “An Observational Perspective of Low-Mass Dense Cores II: Evolution Toward the Initial Mass Function”. In: *Protostars and Planets V*, pp. 33–46.

Wienen, M. et al. (2012). “Ammonia from cold high-mass clumps discovered in the inner Galactic disk by the ATLASGAL survey”. In: *A&A* 544, A146, A146.

Wilking, B. A., M. Gagné, and L. E. Allen (2008). “Star Formation in the ρ Ophiuchi Molecular Cloud”. In: *Handbook of Star Forming Regions, Volume II*. Ed. by B. Reipurth, p. 351.

Wilson, R. W., K. B. Jefferts, and A. A. Penzias (1970). “Carbon Monoxide in the Orion Nebula”. In: *ApJ* 161, p. L43.

Wolfire, M. G., D. Hollenbach, and C. F. McKee (2010). “The Dark Molecular Gas”. In: *ApJ* 716, pp. 1191–1207.

Wolfire, M. G., A. G. G. M. Tielens, and D. Hollenbach (1990). “Physical conditions in photodissociation regions - Application to galactic nuclei”. In: *ApJ* 358, pp. 116–131.

Wood, D. O. S. and E. Churchwell (1989). “The morphologies and physical properties of ultracompact H II regions”. In: *ApJS* 69, pp. 831–895.

Zamora-Avilés, M. and E. Vázquez-Semadeni (2014). “An Evolutionary Model for Collapsing Molecular Clouds and their Star Formation Activity. II. Mass Dependence of the Star Formation Rate”. In: *ApJ* 793, 84, p. 84.

Zamora-Avilés, M., E. Vázquez-Semadeni, and P. Colín (2012). "An Evolutionary Model for Collapsing Molecular Clouds and Their Star Formation Activity". In: *ApJ* 751, 77, p. 77.

Zari, E. et al. (2016). "Herschel-Planck dust optical depth and column density maps. II. Perseus". In: *A&A* 587, A106, A106.

Zavagno, A. et al. (2006). "Triggered massive-star formation on the borders of Galactic H II regions. II. Evidence for the collect and collapse process around RCW 79". In: *A&A* 446, pp. 171–184.

Zucker, C., C. Battersby, and A. Goodman (2015). "The Skeleton of the Milky Way". In: *ArXiv:1506.08807*.